THE UNIVERSITY OF MICHIGAN

INDUSTRY PROGRAM OF THE COLLEGE OF ENGINEERING

A STUDY OF THE STRUCTURE AND ATOMIC MOTIONS OF VITREOUS SILICA BY THERMAL NEUTRON SCATTERING TECHNIQUES

John D. Sutton

A dissertation submitted in partial fulfillment
of the requirements for the degree of
Doctor of Philosophy in the
(Nuclear Engineering)
University of Michigan
1971

March, 1971

IP-837

TABLE OF CONTENTS

LIST OF TABLES

LIST OF FIGURES

CHAPTER I

1.1 THE PROBLEM

At the present time we know relatively little about the structures and the atomic motions in glassy materials. This situation is perhaps best illustrated by considering the vitreous phase of silicon dioxide. No glass has been studied more extensively than vitreous silica and yet, even the short range orientations of the atoms in this substance remain in doubt. For a description of its long range structure one can choose from a variety of vaguely-worded theories which seem to have one common characteristic - a strong aversion to quantitative detail. Attempts to describe the dynamics of the atoms in vitreous silica have been fustrated by a number of factors: i.) the uncertainty about the structure of the glass, ii.) unsatisfactory and, in some instances, contradictory data from Raman, infrared, and neutron scattering studies, and iii.) the lack of an adequate theoretical treatment of the dynamics of a noncrystalline solid.

The following work is a study of the structure and the atomic motions in vitreous silica by neutron scattering techniques.

1.2 THE DEFINITION OF A GLASS

There are many different definitions of glass in the literature. For example, Morey (1) defines glass as "an inorganic substance in a condition which is continuous with, and analogous to, the liquid state of that substance, but which, as the result of being cooled from a fused condition, has attained so high a degree of viscosity as to be for all practical purposes rigid." The same ideas are expressed more concisely in the American Society for Testing Materials (2) definition: "Glass is an inorganic product of fusion which has cooled to rigid condition without crystallizing." Although these statements convey the idea that glass is a solid, there is no description of the structure of this substance.

One also finds thermodynamically oriented definitions (3)(4) which omit any reference to the geometry of the atoms in the system. Stevels (5) suggests that glass may be defined as "a solid system obtained from a liquid system without first order phase transitions." This can be demonstrated with an entropy-temperature relationship of the type shown in Figure 1. Starting at the high temperature end of the diagram one can see that as the liquid is cooled through the freezing point (T_f) it may either freeze into a crystalline solid, with a discontinuous or "first order" transition at this temperature, or it may continue as a supercooled liquid below T_f. This means that

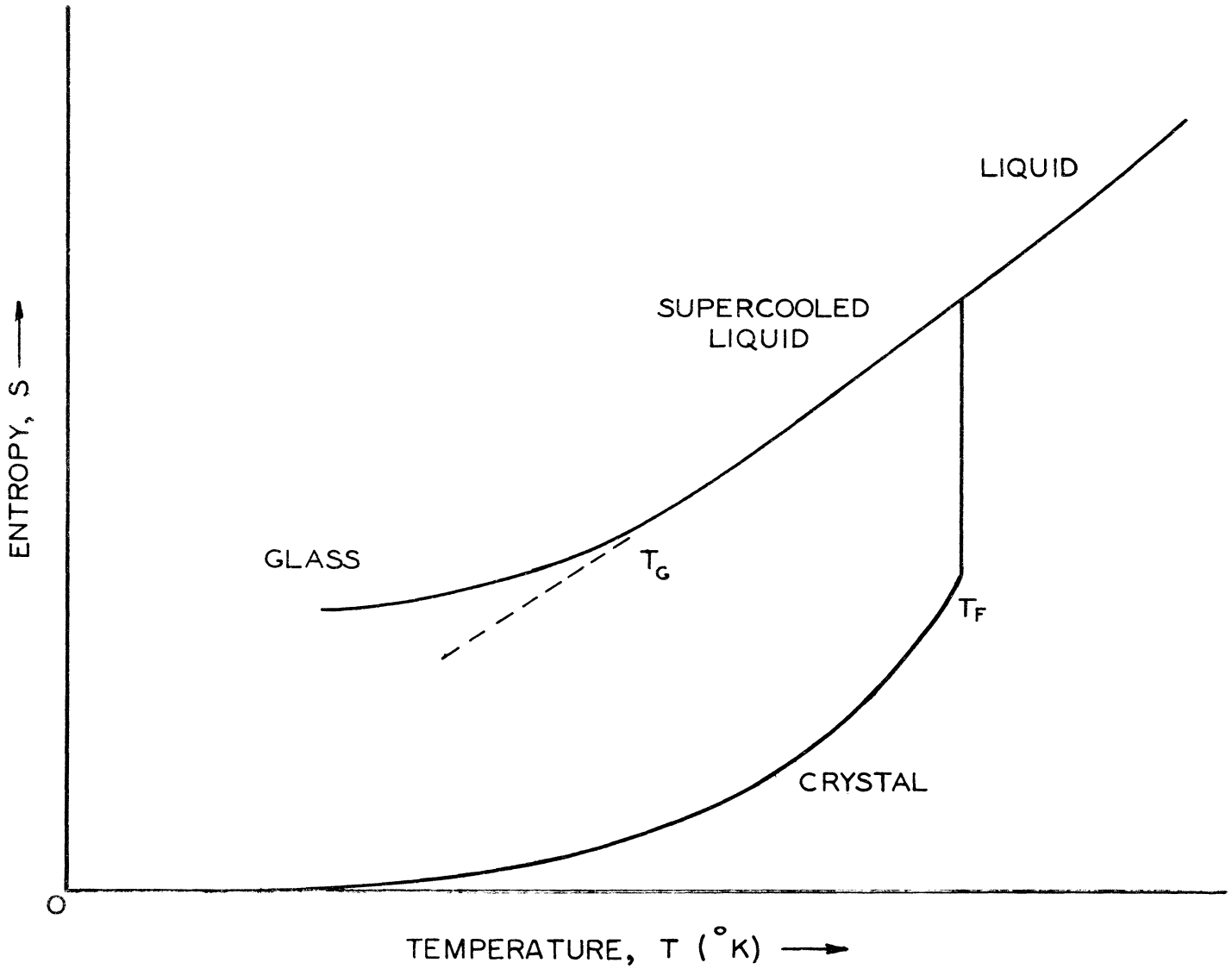

Figure 1. Entropy as a function of temperature for the liquid, supercooled liquid, vitreous solid, and crystalline solid states.

the system still has the features of a liquid, but from a thermodynamic point of view, it is metastable. In the supercooled region the temperature is still so high that the rate of change in the configuration of the system is still large compared with the rate of cooling.

If the cooling proceeds along the liquidus line, the supercooled liquid then passes the stiffening or glass point T_g (having attained a viscosity of the order of $10^{13} - 10^{14}$ poise) and is hence called a stabilized glass, provided the cooling is slow enough to guarantee continuation of the metastable thermodynamic equilibrium. The rate of change in the configuration of the system is then small compared to the rate of cooling; the configuration is said to be "frozen in" and the system shows the typical features of a solid.

According to Mackenzie (6), the above definitions are unsatisfactory because a.) they are restricted to inorganic materials only and thus automatically rule out the glassy organic polymers, and b.) they are restricted to a single method for the preparation of a glass, namely, from the cooling of a liquid. Although the cooling of a liquid in the absence of crystallization is the most common method of preparing a glass, it is well known that glasses may also be formed by the direct condensation of a vapor and other techniques such as shock wave treatment and neutron bombardment of crystals (7).

The definition proposed by Mackenzie (6) appears to be the most relevant to the following discussion since it deals specifically with the nature of the structure of a glass: "any isotropic material, whether it be inorganic or organic, in which three-dimensional atomic periodicity is absent and the viscosity of which is greater than about 10^{14} poise, may be described as a glass. By three-dimensional periodicity we imply a long-range order, dependent on the material in question, of greater than say, 20 angstrom units (Å)."

Since this work is confined to the study of one of the multitude of materials covered by the above definitions, in the following pages it has been convenient to use the term "glass" as a synonym for vitreous silica.

1.3 THE STRUCTURE OF VITREOUS SILICA

1.3.1 INTRODUCTION

Although the current concepts of the atomic structure of vitreous silica are derived from a variety of experimental data, no single body of data has had a greater impact on the development of the various models and hypotheses which will be discussed in the following pages than that obtained by the x-ray diffraction technique. During the first quarter of this century, prior to the discovery of the x-ray diffraction phenomena and its development as an investigative tool, speculations concerning the structure of glass were based on similarities between glasses and other systems such as colloids, crystals, and solutions. Since little or no detailed knowledge of the atomic arrangement in these systems was available at the time, it is hardly surprising that the results of such comparisons were ambiguous and led to erroneous conclusions. Attempts to infer the structure of vitreous silica from the results of thermodynamic measurements were equally unproductive since such data was expressed in terms of a few simple variables and susceptible to many different interpretations. The x-ray diffraction investigations provided the first direct experimental structure data. Although it has not been possible to translate this data into a precisely defined model, the nature of the short range atomic order in vitreous silica has been clarified.

The phenomena of x-ray diffraction by crystals was

discovered in 1912 by Max von Laue (8) and his colleagues. This discovery, which was cited as proof of the wave nature of x-rays, was soon applied to the study of the structures of crystalline solids by W.H.Bragg (9) and his followers. Shortly thereafter, in 1915, Debye (10) and Ehrenfest (11) independently postulated that noncrystalline systems should also possess characteristic diffraction patterns from which certain conclusions concerning the distribution of the electrons in these systems could be drawn. However, in the following decade, most of those working in this field concentrated on investigations of crystalline solids and the relatively few studies of noncrystalline systems were confined mostly to liquids.

In the late 1920's x-ray diffraction studies of vitreous silica were reported by Parmelee, Clark, and Badger (12) and Clark and Amberg (13). Parmelee, et.al. argued that the diffuse, liquid-like diffraction pattern of vitreous silica which they observed was indicative of an incipient crystallization. Clark and Amberg interpreted similar data as indicating that the SiO_2 molecule is the unit of structure in vitreous silica, the molecules being arranged end to end in long chains, the chains grouped into bundles. Both of these interpretations were of a highly speculative nature and totally devoid of any quantitative information.

The results of diffraction studies of the crystalline silicas, which began around 1926, forced investigators to

abandon the established idea that the silicas, crystalline and vitreous, were made up of individual SiO_2 molecules. In spite of the variety and apparent complexity of the crystalline silicas, the diffraction studies indicated that every silicon atom in the crystalline silicas has the same environment, four nearest neighbor oxygen atoms arranged in a tetrahedral configuration. Furthermore, it was determined that the SiO_4 tetrahedra (with one exception) are joined together at the vertices by means of Si-O-Si bridges and that the crystalline polymorphs of silica differ only in the relative arrangement of the neighboring tetrahedra in space (14).

The crystallographic data provided the basis for the two major models of the structure of vitreous silica, the crystallite model and the continuous random network model. The development of these two models, which took place in the ten year period between 1930 and 1940, is detailed in the following pages.

1.3.2 THE DISCRETE CRYSTALLITE MODEL (1930)

The early photographic records of the scattering of x-rays by vitreous silica consisted of ill-defined and unsymmetrical shadow-bands. (The intensity of the x-ray scattering was determined by a microphotometer measurement of the film.) The x-ray diffraction pattern of vitreous silica obtained by Randall, Rooksby, and Cooper (15) consisted primarily of a broad diffuse band centered at a momentum transfer of 1.5 Å^{-1}. A second barely discernible band was observed at a larger momentum transfer.

In their analysis the authors noted that the dominant feature of their vitreous diffraction pattern was observed at very nearly the same momentum transfer as the intense (111) Bragg reflection of the crystalline silica low cristobalite. This correspondence suggested a connection between the crystalline and glassy states. Since it was well known that the breadth of the lines in the diffraction pattern of a powdered crystal increase as the size of the powder particles decrease, Randall, et.al. concluded that the broad diffuse diffraction band of vitreous silica could be attributed to the presence of extremely small crystals (crystallites) of cristobalite. In fact, it was suggested that these cristobalite crystallites make up approximately eighty percent of the total volume of vitreous silica.

The average linear dimension of the crystallites was estimated by means of the Scherrer (16) line width-particle

size relationship:

$$I\text{-}1 \qquad W_{\frac{1}{2}} = \frac{2\sqrt{(\ln 2)/\pi}\ \lambda}{L \cos\theta}$$

where $W_{\frac{1}{2}}$ is the width of the diffraction maximum at half maximum intensity, λ is the wavelength of the monochromatic x-rays, θ, one half of the scattering angle, and L is the length of the edge of the averaged sized particle in the scattering system. (The particles are assumed to be cubical in shape and to belong to the cubic system.) The application of Equation I-1 to Randall's data indicated that the average crystallite dimension was 15 - 20 Å.

The fact that tridymite, another crystalline polymorph of silica, had a diffraction pattern very similar to that of cristobalite was noted. However, since tridymite is rarely found in the natural state and is not easily produced by artificial means, the authors concluded that it was unlikely that the crystallites would have this structure.

Other factors cited in favor of the cristobalite-like structure included (a) the fact that cristobalite is the stable form of silica in the temperature range in which glassy SiO_2 stiffens and (b) when vitreous silica is held at a temperature of approximately 1200°C, the devitrification product is invariably cristobalite.

Russian authors commonly credit the origin of the crystallite hypothesis to A. A. Lebedev (17). In 1921, Lebedev observed anomalies in such properties as refraction

and the thermal expansion of glass. This led him to advance the hypothesis that glass contains crystallites in a state of great dispersion. However, a different crystalline polymorph of silica was favored in this analysis. In concluding his paper, Lebedev formulated his views as follows: "... glass consists of an aggregation of highly disperse crystals, among which are crystals of quartz, in all probability not in pure form, but as solid solutions with some other substance ..."

1.3.3 ZACHARIASEN'S CONTINUOUS RANDOM NETWORK MODEL (1932)

Shortly after the appearance of Randall's crystallite hypothesis, W. H. Zachariasen (18) formulated a set of rules governing the formation of oxide glasses. According to Zachariasen, if an oxide is to occur in the vitreous state, its space lattice must satisfy the following conditions:

1.) Every oxygen ion must be bound to not more than two cations.

2.) The number of oxygen ions surrounding the same cation must be three or four.

3.) The oxygen polyhedra adjacent to each other must have common corners but no common edges or faces.

4.) Each oxygen polyhedron must share at least three corners with neighboring polyhedra.

The description of the atomic arrangement in glass derived from these rules is known as the continuous random network model.

Zachariasen's basic argument is contained in the following excerpt from his paper: "Since the mechanical properties of glasses are directly comparable with those of crystals over a wide range of temperatures, it is logical to assume that the atoms in glass are linked together by forces essentially the same as in crystals and that the atoms are oscillating about definite equilibrium positions. As in crystals, the atoms in glasses must form extended

three dimensional networks. While the network is not periodic and symmetrical as in crystals, it is not entirely random due to the fact that the inter-nuclear distances do not sink below a given minimum value. In the terminology of crystals, the network in glass is characterized by an infinitely large unit cell containing an infinite number of atoms. Because of the lack of periodicity no two atoms in the glass are structurally equivalent, while in a crystal lattice like that of sodium chloride all the sodium atoms are equivalent as are the chlorine atoms."

Zachariasen observed that in the crystalline forms of the oxides A_mO_n, the oxygen atoms invariably form polyhedra of one kind or another around the A atoms. Having postulated that the interatomic forces in a crystal and a glass are essentially the same and that the energy of a glass is comparable with that of the crystal, the logical conclusion was that one should find essentially the same polyhedra of oxygen atoms around the atoms A in the glass network.

In order to prevent the regular lining up of the polyhedra when building the network, Zachariasen argued that the linking of the polyhedra occurs only at the corners (as opposed to the sides or faces of the polyhedra) and the oxygen atoms are shared by no more than two polyhedra. Furthermore, since the network is three-dimensional, he argued that at least three corners of each oxygen polyhedra must be shared.

As noted in the introduction, in the crystalline polymorphs of silica the quadrivalent Si^{+4} cation is surrounded by four oxygen atoms in a tetrahedral configuration. Therefore, according to Zachariasen's argument, the network in vitreous silica is made up of SiO_4 tetrahedra. The tetrahedra share corners with each other in such a manner that an oxygen atom is linked to two silicon atoms, and it is assumed that the relative orientations of the tetrahedra may vary within rather wide limits.

One of the attractive features of this model was that it seemed to provide an explanation of the remarkable tendency of silicon dioxide to vitrify. The argument was as follows: the fact that each oxygen must be shared between two cations results in the formation of complex aggregates in the melt. The atoms are already bound rather tightly in these complex aggregates and on rapid cooling there is not time for the atoms to disentangle themselves and get properly ordered for forming a regular crystalline structure. The sharing of each oxygen between only two cations permits a great deal of flexibility in the joining together of the tetrahedral groups and as a result, the random network is almost as stable as a crystalline arrangement.

Perhaps the most unsatisfactory feature of the Zachariasen model is that it is so vague in describing the manner in which large numbers of the SiO_4 groups link

together. For example, nothing is said about the nature of the distribution or the mean value of the Si-O-Si bond angles in the random network. Morey (19) took note of this fact when he remarked: "This picture of the structure of glass (Zachariasen's) seems much more probable than that of Randall, Rooksby, and Cooper but after all does it do much more than to say in the language of x-ray structure that glass is an undercooled liquid?"

1.3.4 WARREN'S X-RAY STUDY OF THE STRUCTURE OF VITREOUS SILICA (1934)

Zachariasen's model received strong support from B. E. Warren (20). Warren, like Randall, based his analysis on the results of x-ray diffraction measurements and although there was no discernible difference in the data published by the two authors, Randall's crystallite interpretation was rejected.

If glass is heated to a temperature between ~1000°C and 1723°C, it will begin to crystallize to cristobalite. This crystallization is commonly called "devitrification", as it usually results in converting the transparent homogeneous glass into a white chalky mass of minute crystals (21). In his paper Warren pointed out the apparent difficulty of interpreting the devitrification of glass in terms of the crystallite model. He argued that if the crystallite description were valid, the tiny cristobalite crystals in a heated sample of vitreous silica would act as nucleation centers and slowly increase in size; the growth of the crystallites would in turn be observed in a gradual narrowing of the glass's characteristic broad diffraction band. However, in his experiments Warren observed that the transition from the broad diffraction band of vitreous silica to the sharp (111) line of cristobalite in the devitrification process was very abrupt.

Warren also suggested that because of the tiny size

postulated for the crystallites, one would expect that the width of the diffraction band should be extremely sensitive to heat treatment and the origin of the sample. He found, however, that glass samples of different origin and those subjected to heat treatment as drastic as possible without producing devitrification, all showed broad diffraction bands of the same width. Although other criticisms of the crystallite hypothesis were voiced, those cited above were considered to be the most serious.

Warren concluded that the most attractive alternative for the interpretation of his data was Zachariasen's random network model. His method of analysis was to choose a particular spatial distribution of atoms, calculate the corresponding theoretical scattering intensity curve, and then compare the results of the calculation with the experimental curve. The choice of the theoretical atom distribution was governed by Zachariasen's argument that the interatomic spacings and coordinations in vitreous silica are essentially the same as those found in the crystalline silicas. Therefore, the result of this analysis was a model or spatial distribution in which each silicon atom is surrounded by four oxygen atoms at a distance of 1.6 Å and each oxygen is shared between two silicon atoms. It was assumed that each oxygen lies very nearly on the straight line between the two silicons to which it is bonded, i.e. the distance between the nearest neighbor

silicon atoms is 3.20 Å. The relative orientations of the SiO_4 groups about the 180° Si-O-Si bonds linking them together were described as being completely random. Warren thus carried the continuous random network model beyond Zachariasen's description by becoming the first author to specify a specific mean value for the tetrahedra linking angles. Although no mention was made of the distribution of the Si-O-Si angles about this mean value, one was left with the impression that any deviations from 180° were small.

The atom spacings and coordinations in Warren's model are listed in Table I-1. The agreement between his experimental diffraction data and the diffraction pattern calculated from this model was so satisfactory, Warren concluded that he had completely substantiated the random network hypothesis.

TABLE I-1 Radial Distribution of Atoms in the Warren Model (1934)

From O to:		From Si to:		Atom Pair Spacing (Å)
No.	Kind	No.	Kind	
2	Si	4	O	1.60
6	O			2.62
		4	Si	3.20
6	Si	12	O	4.00
		12	Si	5.20

1.3.5 THE MODERN CRYSTALLITE THEORY (1936)

Warren's interpretation of his data and criticisms of the crystallite hypothesis were disputed by N. N. Valenkov and E. A. Porai-Koshits (22). Inprovements in the resolution of the experimental apparatus and extension of the x-ray measurements to larger scattering angles enabled these authors to detect previously unobserved maxima in the diffraction patterns of glasses. The presence of the diffraction maxima at the larger scattering angles was attributed to a greater degree of order in the glass structures than indicated by the random network hypothesis. Valenkov and Porai-Koshits also reported that there was a distinct difference in the diffraction pattern of a glass which they prepared from a melt of low-quartz and one prepared from low-cristobalite. The observation that the structure of glass (and hence its diffraction pattern) depends on the method of preparation appeared to be compatible with the crystallite hypothesis and refuted Warren's contention that all glasses of a given chemical composition have the same structure regardless of their origin and subsequent heat treatment.

In their analysis Valenkov and Porai-Koshits argued that the Zachariasen-Warren hypothesis erroneously suggested the existence of a sharp boundry between the crystalline and glassy states. For example, to explain the rapid nature of the devitrification event it was necessary

to conceive of a process in which the continuous atomic (ionic) network suddenly ruptures with each piece of the original network forming a crystallization center. Valenkov and Porai-Koshits offered a different interpretation based on the crystallite model: "The process of devitrification (i.e. of crystallite growth) progresses very slowly at first owing to the great viscosity of the glass and therefore has small effect on the diffraction pattern; yet when the crystallites have attained a certain limiting size, the growth of the crystallites is much accelerated and therefore the diffraction pattern in this period is changing if not suddenly, still within a very short span of time." Thus, in this interpretation there is no marked boundry between the glassy and crystalline states because the growth of the crystallites is continuous without any previous breaking-up of the atomic network.

Valenkov and Porai-Koshits's criticisms of the random network model by no means indicated acceptance of the crystallite model as postulated by Randall, et. al. The suggestion that the structure of vitreous silica consists of a jumble of tiny crystals with sharp external boundaries was considered to be as unrealistic as the Zachariasen-Warren model (Randall (23) himself had by this time abandoned his original interpretation in favor of the random network hypothesis.) The Valenkov - Porai-Koshits version of the crystallite hypothesis, which is summarized in the

following excerpt from their paper, was significantly different: " in vitreous silica crystallites of cristobalite are present whose 'inner dimensions' are somewhat higher than 10-12 Å and whose outer portions are strongly distorted producing diffuse maxima of higher orders as a result of diffuse scattering." Therefore, rather than picturing the crystallites as extremely tiny crystals with sharp external boundaries, the crystallites were considered to be regions of a continuous space network interconnected by their gradually distorting external portions.

Unfortunately, Valenkov and Porai-Koshits, like Randall, et. al., chose to identify their model as the crystallite theory of glass. This has created a great deal of confusion in the literature since it is often difficult to determine just which version of the crystallite theory is being discussed in a given paper. Eckstein (24) explains that this difficulty probably arises from the fact that the term "crystallite" has different meanings in the Russian and English languages; in Russian the term denotes merely a relatively well-ordered ("crystalloidic") region. The suggestion by Urnes (25) that the Valenkov - Porai-Koshits model be denoted as the "modern" crystallite theory has been adopted in this work.

1.3.6 WARREN'S 1936-1938 PUBLICATIONS

Warren was not swayed by the arguments of Valenkov and Porai-Koshits and in subsequent papers reaffirmed his support of the random network hypothesis (26)(27)(28).

Using the Bragg particle size equation (29) and the width of the most prominent peak in his diffraction data, Warren calculated an average crystallite dimension of 7.7 Å. This result, he contended, demonstrated the fallacy of the crystallite hypothesis: "High cristobalite is cubic and low cristobalite, pseudocubic, the cube edge of the unit cell of both being 7.0 to 7.1 Å. The particle-size determination then demands that, on the basis of the crystallite theory, we postulate that the major part of the material is in the form of cristobalite crystals scarcely larger than one unit cell. Since the term "crystal" means a form of matter in which some unit of structure repeats itself identically at regular intervals in three dimensions, it is stretching the term so far that it loses all meaning to apply it to volumes of the order of one unit cell. It is pointless, furthermore, to argue that the true crystals are larger than 8 Å but that the outer parts are sufficiently distorted to give the lower experimental value. What one calculates from the particle-size equation is the size of crystal sufficiently undistorted to be called a crystal. It must be concluded from the particle-size study that the use of the term "crystal" in connection with vitreous silica is an extension

of the term beyond the point where it has any simple meaning or significance."

The question of the bonding scheme in vitreous silica was then considered: "For the sake of argument let us continue to assume that vitreous silica consists of small crystals of cristobalite. The next question to be answered has to do with how these assumed crystallites join onto one another. Is the glass an aggregation of these small crystals with some kind of break in bonding between them or is the scheme of bonding perfectly continuous with no breaks or voids?" Warren argued that the nature of the bonding scheme in vitreous silica could be determined by a study of the x-ray scattering intensity at small angles: "Intense small-angle scattering is characteristic of materials made up of small discrete particles with gaps and voids between them. The absence of small-angle scattering is a direct indication of a continuous medium."

Warren's measurements of the small angle diffraction intensities of vitreous silica and dried silica gel are shown in Figure 2. (Dried silica gel (SiO_2) has a highly porous structure which is characterized by the uniformity of the size and arrangement of the pores. The average diameter of the pores is estimated to be 40 Å (30).) The intensity of scattering by the vitreous silica appears to decrease almost monotonically with decreasing momentum transfer. This behavior is confirmed by more recent measurements by

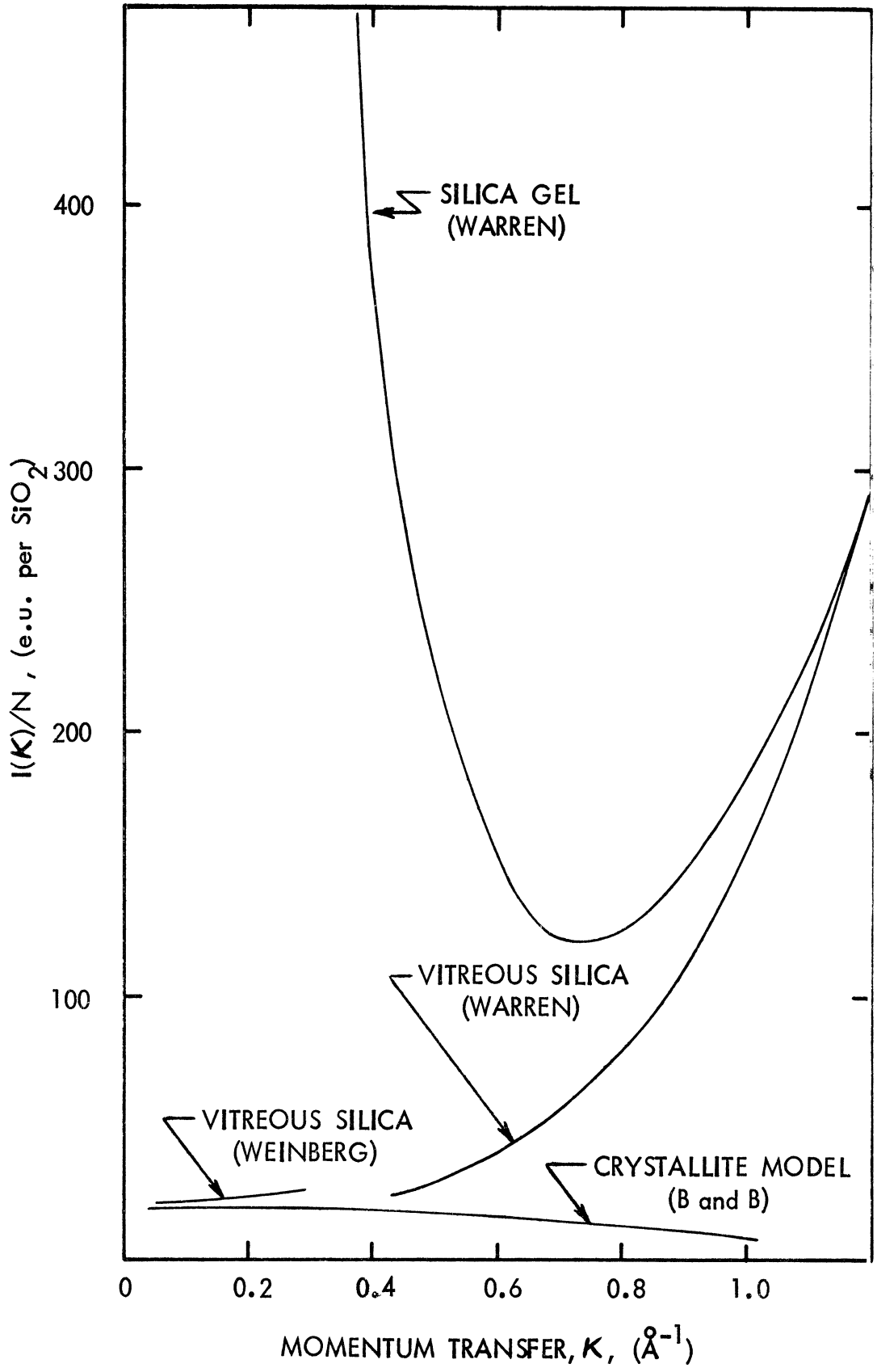

Figure 2. Small angle x-ray diffraction intensities of vitreous silica and dried silica gel. (From Bienenstock and Bagley (36).)

Weinberg (31). By way of contrast, the scattering intensity from the silica gel passes through a mimimum at a momentum transfer of approximately 0.8 $\mathring{A}^{-1}$ and then sharply increases to values higher than those observed at larger momentum transfers, Therefore, Warren concluded: "The absence of small angle scattering means that glass is a continuous medium with no discrete particles or breaks in the scheme of bonding." (It should be noted here that this criticism applies only to the Randall version of the crystallite model and is not applicable to the modern crystallite hypothesis of Valenkov and Porai-Koshits in which it is assumed that there is a continuous bonding scheme between regions with different degrees of ordering.)

Although the theoretical diffraction pattern derived in his earlier paper agreed quite well with the experimental data, Warren was troubled by the question of the uniqueness of the assumed model. Obviously what was needed was a method of extracting structure information directly from the diffraction data, a means of analysis independent of any assumption as to the structure of the sample.

In the late 1920's Debye and Menke (32) and Zernike and Prins (33) had shown that the radial distribution of atoms in a liquid could be obtained from a Fourier integral analysis of the liquid diffraction pattern. In 1936 Warren and his colleagues (27) demonstrated that the Fourier inversion method could be generalized to make it applicable to the

analysis of the diffraction pattern of a polyatomic amorphous solid.

The radial distribution curve for vitreous silica which Warren obtained from the inversion of his diffraction data is shown in Figure 3. For a polyatomic system such as silicon dioxide, this curve can be interpreted as a distribution of pairs of different atom types. The position of a peak gives the atom pair spacing, the area under the peak gives the number of atom pairs. In practice, the identification of the particular atom pairs which give rise to a given peak in the distribution curve is greatly aided by correlation of the observed spacing with the spacings of the atoms in crystalline forms of the same substance. For example, the first peak in Figure 3 is identified with the nearest neighbor silicon and oxygen atoms. The observed 1.62 Å spacing is quite close to the silicon-oxygen spacings found in the crystalline silicas.

Warren was gratified to find that the results of the Fourier analysis of his diffraction data agreed almost exactly with his earlier synthesized model (Table I-1). However, he added the following note of caution to his remarks: "It should be emphasized that the x-ray study of a glass gives information only on average quantities, it tells nothing about the fine details of the structure and the possibility of small variations in the structure. Secondary structural features such as those which change

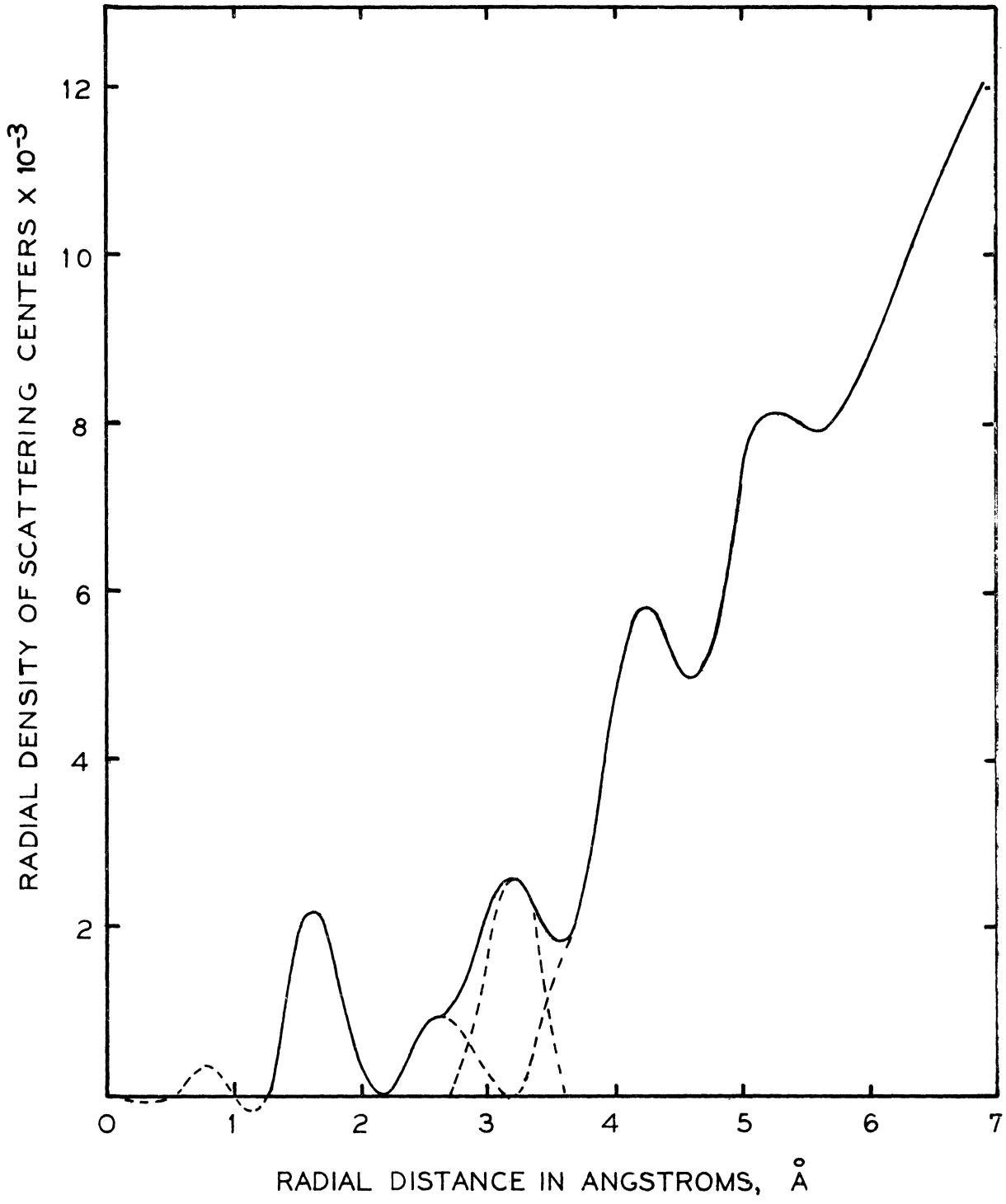

Figure 3. Atom pair correlation function of vitreous silica derived from x-ray diffraction data. (From Warren, Krutter, and Morningstar (27).)

with annealing or conditioning, do not affect the x-ray pattern sufficiently to be recognized. The x-ray studies of glass might be said to establish the first order approximation to a picture of the structure and the fine details must be filled in from other kinds of measurements."

1.3.7 CRITICISMS OF WARREN'S WORK

A number of authors have questioned Warren's interpretation of his small-angle scattering data. Normally, the small-angle scattering from particles whose dimensions are less than a few thousand angstroms is observed as a result of the relative isolation of the particles, i. e. one observes the scattering from individual particles and the interparticle interference may be neglected. In his analysis, Warren contrasted the small-angle scattering of vitreous silica with that of silica gel. Since the particles in silica gel are relatively well separated, the intense small-angle scattering by this substance is not surprising. However, the structure of silica gel has little in common with the structure model of vitreous silica proposed by Randall, et. al.

Debye (34) and Fournet (35) have shown that the intensity of scattering at small angles decreases quite markedly as the density of the particles of a powder increases towards the limit of a compressed solid. The densities of most amorphous phases of a given substance are only slightly less than those of the corresponding crystalline phases, e.g. the densities of vitreous silica and low-cristobalite are 2.20 g/cm^3 and 2.30 g/cm^3 respectively. Bienenstock and Bagley (36) point out that the high relative density of the amorphous phase of silica indicates that the crystallites, if they exist, must be

in close contact with their neighbors. Therefore, intercrystallite interference may be expected to play an important role in the determination of the small-angle scattering intensity.

Bienenstock and Bagley have calculated the intensity of small-angle x-ray scattering from two crystallite models which are designed to indicate the upper limits to the actual scattering intensity. In each model it is assumed that the electrons are all concentrated within the crystallites so that there is the greatest possible difference between the electron density within the crystallites and the space (or voids) between the crystallites. In one model the voids consist of randomly packed, non-overlapping spherical shells, i.e. the void is distributed more or less uniformly around each crystallite. The other model recognizes the possibility that a very large portion of the surface of any crystallite can be in contact with other crystallites. In this case, the voids are considered to be spherical cavities rather than spherical shells.

The following results were reported: (a) for each model, the scattered intensity per crystallite was very much less than the scattering from an isolated crystallite, (b) at high packing densities the marked decrease in scattering intensity with increasing density was due only to the diminuation of the total void volume. The arrangement

of voids and therefore the particular model have little influence on the order of magnitude of the scattering, and (c) in the particular case of vitreous silica, the calculated upper limits to the scattering from an array of crystallites were of the same order of magnitude or less than the scattering intensities measured by Warren and Weinberg. The calculated scattering intensity for a model in which crystallites with the density of low-cristobalite and an average linear dimension of 8 Å are packed to the density of vitreous silica is shown in Figure 2.

Although Bienenstock and Bagley concluded that the failure to observe small-angle scattering from vitreous silica does not invalidate a discrete crystallite model, they noted that their calculation does not, on the other hand, offer any evidence for the existence of discrete crystallites.

As noted in Section 1.3.6, Warren's application of the Fourier inversion method provides the short range atom spacings and coordination numbers independent of any model assumptions. However, there are many potential sources of error in this calculation.

The atom pair distribution curve shown in Figure 3 is obtained by evaluating the integral

$$\text{I-2} \qquad \frac{2r}{\pi} \int_0^\infty K \frac{I(K)}{f_e^2} \sin Kr \, dK$$

where K is the momentum transfer in the scattering event,

$I(K)$ is the structure dependent coherent scattering intensity, and f_e is the average structure factor per electron. (The derivation of this expression is omitted since the comparable expression for the neutron scattering experiment will be derived in Chapter II.) There are many problems involved in obtaining an accurate $I(K)$ function from the experimental data. The measurement of the intensity of the x-ray scattering from an amorphous substance of medium-to-low scattering power such as vitreous silica presents some difficulty, especially since strictly monochromatic radiation must be employed. Cartz (37) has noted that filtered x-rays, which are never perfectly monochromatic, have been used in many of the glass studies. Another problem is that at large angles the scattering is very weak, but it must be measured very accurately in order to normalize the scattering intensities.

Assuming that there are no problems such as fluoresence in the sample, the raw data must be corrected for polarization effects, multiple scattering, and absorption of the incident and scattered radiation in the sample. Even with these corrections, the data still include the contributions from the incoherent (or Compton) scattering.

The incoherent contributions are removed and the coherent scattering intensity is normalized in the following manner (38): The intensities of the structure independent

coherent scattering and the incoherent scattering, identified as $f(K)^2$ and I_{inc} respectively, are computed from tabulated atomic scattering factors (39). It is assumed that for large momentum transfers the corrected experimental data, I_{exp} , will approximate the total structure independent scattering contribution, $f(K)^2 + I_{inc}$, because the interatomic interference effects are no longer significant. Thus, the experimental scattering data is normalized to an absolute intensity scale by matching the calculated $f(K)^2 + I_{inc}$ curve with I_{exp} at the larger scattering angles. Once this normalization is accomplished, one obtains the coherent structure dependent contribution from the relationship:

$$I(K) = I_{exp} - f(K)^2 - I_{inc} \qquad \text{I-3}$$

There are several sources of error in this normalization. Consider, for example, the calculation of the total structure independent scattering. The atomic scattering factor, $f(K)$, is a function of the electron density of the atom. Since the exact density function is known only for the hydrogen atom, the scattering factors for all other atoms must be approximated in some manner. Various methods of approximating the total wave function (and hence the electron density function) of an atom are discussed in the literature; no less than six different methods of calculation are cited in the International

Tables for X-ray Crystallography (39). An accurate estimate of the electron distribution is also required to calculate the incoherent (Compton) scattering contribution.

The actual curve fitting process is not without difficulties. Henninger, et.al. (40) report that their x-ray scattering intensity curve for vitreous silica oscillates at the larger scattering angles and as a result, it is hard to obtain a satisfactory match with the smoothly varying $f(K)^2 + I_{inc}$ curve.

Other problems arise in the computation of the Fourier transform (Equation I-2). The accuracy of the $I(K)$ function almost always varies over the range of momentum transfers for which it is measured. This is due to differences in the counting statistics, angle dependent multiple scattering, ect.. However, the integration indicated in Equation I-2 ignores this problem and employs the scattering data in an indiscriminant manner. An error in the measurement of the scattering intensity at a momentum transfer of K_e will produce a ripple in the atom pair distribution curve with a period of $2\pi/K_e$. The presence of the K term in the integrand of I-2 indicates that errors at the larger scattering angles where the scattering intensity is low are magnified.

If the integration indicated in I-2 does not include all K's for which the integrand is non-zero, as is usually the case, the resulting function will have a number of

spurious maxima and minima. These spurious features may be suppressed by multiplying the integrand of I-2 by a suitable weighting function. The function $\exp(-\eta K^2)$ is often used for this purpose, with the coefficient η chosen so that the integrand has a negligible value beyond K_{max}, the upper limit of the experimental measurement. However, the use of this convergence factor can remove real as well as spurious features from the pair distribution curve.

The preceding is intended only to indicate some of the problems the experimentalist faces in attempting to derive an accurate pair distribution function from his scattering data. Detailed discussions of the sources and consequences of various errors in the inversion process are found in works by Finbak (41), Klug and Alexander (42), Grjotheim (43) and Riley (38).

The difficulty of obtaining an error-free distribution function is not the only criticism of the Fourier inversion method. A number of authors, especially the proponents of the crystallite hypotheses, emphasize that even if there are no errors, the calculation provides only a spherical average of the distribution of atom pairs in the sample. Petrashen and Porai-Koshits (44) have argued that the derivation of the Fourier transform relationship presupposes a random structure and therefore, a choice between the random network theory and the crystallite hypothesis cannot be based on results obtained by the use of this method.

1.3.8 THE SYNTHESIS OF THE CRYSTALLITE AND RANDOM NETWORK THEORIES

Most of the supporters of the random network and crystallite hypotheses have recognized that neither model in its more extreme form is consistent with the available experimental data. Each is valid only to a certain degree, and explains only some of the properties and characteristics of glass.

In 1941, Warren (45) reviewed his work of the previous decade and acknowledged that "it would be incorrect to say that the present random network theory of the structure of glass has been uniquely established." It has been difficult for the proponents of the random network theory to ignore the results of numerous experimental measurements which seem to indicate the presence of a greater degree of order in the structure of vitreous silica than the original version of the Zachariasen hypothesis would suggest. Westbrook (46), for example, has studied the variation of penetration hardness with temperature and found that vitreous silica obtained from a melt of cristobalite shows an irregularity near the high-low cristobalite inversion (~272^{o}C), while vitreous silica made from a melt of quartz shows a similar irregularity near 573^{o}C, the high-low inversion temperature of quartz. German (47) reports that the measurement of the dielectric constant of a sample of vitreous silica as a function of temperature

shows clear, reproducible steps at temperatures corresponding to the high-low quartz, the high-low tridymite, and the high-low cristobalite transitions. According to Eckstein (48), the anomalies which German observes are too marked to be caused by traces of devitrification in the sample and she suggests that they can be explained by "the apparent coexistence of regions of cristobalite and low-quartz, or high-quartz and tridymite structure (i.e. of paracrystalline configurations corresponding to these lattices) in silica." Evstropyev (49) notes that similar anomalies are observed in the refractive index, the viscosity, and the thermal expansion coefficient of vitreous silica at the temperatures corresponding to the polymorphic transition points of the crystalline silicas.

On the other hand, the results of the diffraction experiments and physical properties such as the absence of a definite melting point and the viscosity-temperature relationship can not be satisfactorily explained if vitreous silica is assumed to be an aggregation of minute crystals.

Valenkov and Porai-Koshits (Section 1.3.5) were the first authors to suggest the logical and rather obvious step of combining the features of both a crystallite and a random structure in a single model. The presence of regions with crystal-like order could explain the correlations observed between the physical properties of the vitreous and crystalline phases of silica and yet, as Valenkov and Porai-Koshits observed, the synthesis of the crystallite and

random network concepts in the modern crystallite theory is not diametrically opposed to the Zachariasen-Warren model. According to Lebedev (50), the difference between the modern crystallite theory and the random network theory is merely one of degree: "It is easy to see that such a gradual transition may be imagined between these theories that their juxtaposition becomes meaningless. On the basis of the continuous network concept we can always imagine that at some points in the network the orientations of the atoms may go so far that such regions can be quite justly termed crystallites; on the other hand, on the basis of the (modern) crystallite theory we must visualize the individual crystallites as being so small that we cannot speak of the existence of completely defined crystals with sharp boundaries, as it is evident that between the grains there should be transition zones with irregular distribution of the particles, while the lattice of the grains themselves may be considerably distorted owing to the extremely small size of the crystals."

The original version of the modern crystallite theory has been modified in more recent papers. Valenkov and Porai-Koshits, like Randall, et.al., employed the Scherrer line width-particle size relationship (Equation I-1) to estimate the average size of the crystal-like regions in the sample. Porai-Koshits (51) has recently conceded that no significance can be attached to this calculation since

the derivation of the Scherrer formula presupposes the existence of a much more ordered structure than can possibly exist in vitreous silica. The idea that there are crystallites that very much resemble crystals has therefore been abandoned.

Stevels (5) offers a representative version of the updated modern crystallite theory: "It is very likely that there are regions (which may be of the order of 100 Å, but also larger) in which networks as described by Zachariasen-Warren exist, with the restriction that the randomness is not complete; or perhaps: where deviations from order are not too great. These regions are bound together by means of other regions where the degree of randomness is much higher, and where the Zachariasen-Warren theory also virtually holds. Here, relatively higher concentrations of the missing bridges, vacancies and perhaps (in cases like fused silica) also "impurities will be found. These regions may be the boundaries of the first-mentioned ones and thus account for the grainlike structure found with the electron microscope. In other words, this synthesis accounts for the experimentally found microinhomogeneity of glass."

As noted by Stevels, the results of studies with the electron microscope appear to support the concept of coexisting regions with differing degrees of order. Oberlies (52) and Prebus and Michener (53), among others, have detected inhomogeneities in samples of vitreous silica with this instrument. Warshaw (54) reports that electron

microscopy of fractured and polished surfaces of glass shows the presence of inhomogeneities ranging in size from 30 Å to 150 Å in diameter. In his analysis he argues that if the bonding within the inhomogeneities is random, and if the inhomogeneities are distributed in a random manner throughout the glass, his observations are in no way incompatible with the pair distribution curve obtained by Warren.

Zarcycki and Mezard (55) have reported that they have obtained electron transmission micrographs of vitreous silica which exhibit a fine granularity in the 50 Å to 100 Å range. They offer the following interpretation of this data: the observed pattern is attributed to the mutual mis-orientation of domains. The degree of order inside of these domains should be sufficient for it to be possible to speak of mis-orientation - in other words to be able to define the orientation of one domain in relation to its neighbors. But on the other hand, their dimensions being approximately 100 Å, the domains must be sufficiently disorganized not to give rise to the sharp diffraction pattern which would be expected of a perfect crystal of that size. It is thought that the image of the glass network could be best described by using a 'para-crystalline' model. The degree of order in the domains would thus be intermediate between that of a perfect crystal and of an amorphous lattice. These domains would in turn be arranged

in a superlattice which can exhibit various degrees of order from completely amorphous to increasingly para-crystalline.

Zarcycki and Mezard conclude that this model is consistent with the results of the low-angle x-ray diffraction experiments since the electron diffraction is completely independent of the internal structure of the domains and depends only on their external shapes.

1.3.9 RING STRUCTURES IN VITREOUS SILICA

Several authors (57) (58) have observed that the structures of the crystalline forms of silica may be described in terms of rings of SiO_4 tetrahedra. The rings in the silica crystals are regularly repetitive and the types of rings in the immediate neighborhood of each atom are limited. For example, the structures of cristobalite (both high and low temperature forms), quartz, and tridymite contain only hexagonal rings of SiO_4 tetrahedra. King (58) describes the hexagonal rings in cristobalite as "chair-shaped" and those in tridymite as "chair-shaped" and "boat-shaped". The structures of coesite and keatite, two of the denser crystalline polymorphs of silica, consist of rings of four and five tetrahedra respectively.

The concept of rings of SiO_4 tetrahedra has also been adopted by a number of authors to describe the structure of vitreous silica. Bernal (59) was one of the first to suggest that vitreous silica could be pictured as "a network of linked four-coordinated molecules forming rings of four, five, six, seven, or even more molecules arranged in various sets of random order, and consequently, complexly responsive to temperature and pressure changes, leading to anomalous expansion at low temperature."

Dean (60) has suggested the possibility of a ring structure in vitreous silica formed from three tetrahedra. The three silicon atoms and three of the oxygen atoms in

these tetrahedra form a planar ring with Si-O-Si angles of 130^{o}. Dean argues that if the force field for this configuration can be represented by a nearest neighbor central force model, his analysis shows that there exist two normal modes of vibration which are strictly localized to the six atoms of the planar ring and involve no displacements from equilibrium of other atoms in the network. In one mode the adjacent atoms vibrate out of phase and a simple order of magnitude calculation indicates that this motion might account for the band observed at ~ 950 cm^{-1} in the infrared spectrum of vitreous silica (61). The other mode is described as an infinitesimal ring rotation in which the atoms all move in phase with an extremely low frequency.

The results of x-ray and neutron scattering measurements, which are discussed in Section 1.3.13, indicate that the Si-O-Si angle suggested by Dean is unrealistically low. If the three-membered SiO_4 rings are one of a number of different ring configurations in vitreous silica, they could account for only a very small percentage of the ring types in the structure or the density of the structure would be too high.

Cartz (62) has measured the x-ray diffraction pattern of vitreous silica and reports that the theoretical diffraction pattern calculated from a model consisting of a mixture of non-planar rings of five, six, seven, and eight SiO_4 tetrahedra is in excellent agreement with this data.

In each of these rings the Si-O-Si angle is 150°, the Si-O bond length is 1.60 Å, and the tetrahedra are assumed to be regular. The distribution of ring-sizes is shown in Table I-2.

Table I-2 Ring Size Distribution in the Cartz Model Of Vitreous Silica

Non-planar Ring-size Distribution: Percentage of number of rings containing n tetrahedra					
n=4	5	6	7	8	9
0	24	48	20	8	0

King (58) has investigated the ring configurations in the random network model which she and Evans have constructed (63). She finds that her model contains rings of five, six, and seven SiO_4 tetrahedra. The distribution of these ring types is as follows: five-membered rings - 46%, six-membered rings - 38%, and seven-membered rings - 16%. (The King and Evans model is discussed in greater detail in Chapter V.)

On the other hand, Oberlies and Dietzel (64) report that the most satisfactory match with the pair distribution function derived from their x-ray diffraction data is provided by a model composed almost entirely of six-membered SiO_4 rings similar to those found in cristobalite.

1.3.10 TILTON'S PENTAGONAL-DODECAHEDRAL MODEL (THE VITRON)

In 1957 Tilton (65) suggested the possibility of a pentagonal-dodecahedral model for the structure of glass. The unit cell in this model, which is constructed of five-membered rings of symmetrical tetrahedra, is a regular pentagonal-dodecahedral element (12 faces, each face five sided) containing 20 SiO_4 tetrahedra with 20 silicon atoms at their centers, 30 oxygen atoms at interconnected corners, and 20 "external" oxygen atoms which form bridges for the addition of neighboring unit cells. The radial distribution of the atoms in this unit cell is given in Table I-3.

According to Tilton, this structure arises from a high temperature arrangement of connected silicon-oxygen tetrahedra which is frozen by the rapid increase in rigidity as the glass cools. As a result, the configuration of the connected tetrahedra is such that the structure will have minimum density, i.e. the Si-O-Si bond angle is 180° and the rings, if any, are circular and planar so that the tetrahedra can have maximum distention. These conditions favor the formation of pentagonal rings since the interior angle of a regular tetrahedron, $109^{\circ}28'$, differs so little from the interior angle of a regular pentagon, 108°. The growth of Tilton's structure proceeds uniquely in six directions from an initial tetrahedron to form a network containing dodecahedral holes or cavities, each separated

TABLE I-3 Radial Distribution of Atoms in the Tilton Pentagonal Dodecahedra

From O to:		From Si to:		Atom Pair Spacing (Å)
No.	Kind	No.	Kind	
2	Si	4	O	1.60
6	O			2.60
		4	Si	3.20
6	Si	12	O	4.00
6	O			4.19
3	Si	6	O	4.92
12	O			4.99
		12	Si	5.18
12	O			5.93
12	Si	24	O	6.14
12	O			6.79
12	O			7.14
6	Si	12	O	7.15
12	O			7.3
		24	Si	7.33
12	Si	24	O	7.71
12	O			8.04
3	O	12	Si	8.38
		24	Si	8.4
6	Si	12	O	8.54
18	O			8.6
		4	Si	8.97

from its twelve somewhat distorted neighboring cavities by twelve planar interfaces of very slightly stressed penta rings. A stressed network cluster of such dodecahedral cages is designated a vitron.

The most important property of this model is that its fivefold symmetry precludes the formation of a crystalline structure. In the words of Tilton: "Just as penta tiles fail where hexagons succeed in covering a floor, so do regular penta dodecahedra fail to fill space completely and extensively." The bonding of the dodecahedra is described as follows: "The interior dihedral angle of a dodecahedron is 116.6°, and thus not far from 120°, which would be exactly right for filling space without stress and distortion. If one regular dodecahedron is attached or joined on each face to 12 like structures, none in the outer shell can touch any of its five neighbors. By radial compression these neighbors may meet and the requisite tangential tension in the peripheral bonds may not be excessive for the first shell. Further increase in cluster size by the addition of 32 cages in the second shell would require much higher tensions in the outermost bonds, and some defective attachments or broken bonds might result in order for bonds to hold elsewhere on the periphery. Thus the great strength of the silicon-oxygen bond is the factor that should cause, and automatically limit, the growth in size of vitrons. The automatically limited ability to grow, and a

distribution of stresses localized and balanced within each vitron, are features that may distinguish a vitreous substance from a crystal."

The balance of Tilton's paper is devoted to a detailed geometrical classification of possible vitrons and an attempt first, to correlate the model with experimental diffraction data, and second, to interpret a number of physiochemical properties of glass, e.g., gaseous diffusion, viscosity, density, coefficient of thermal expansion, etc.. For example, the observed low tensile strength of silica glass is attributed to the fact that there are fewer bonds per unit cross section in the interstitial connective "matrix" between the vitrons than within them. Changes in the interstitial matrix's structure and volume, both of which are rather arbitrary parameters in this model, are credited with producing the observed anomalies in the thermal behavior of vitreous silica with respect to its viscosity, compressibility, volume, and elastic moduli.

One of the weakest features of the vitron model appears to be the low density of this structure. The calculated density of a vitron is 2.00 g/cm^3, which is about 10% lower than the known density of vitreous silica, 2.20 g/cm^3. To explain this discrepancy the author is forced to argue for either a decrease in the unit volume of the outer and distorted cages of vitrons or throw the burden of raising the average density upon the relatively small volume of interstitial material between the vitrons.

As noted previously, Warren's analysis of his x-ray diffraction data in the 1930's indicated that the Si-O-Si angle is approximately linear. This result is consistent with Tilton's model: in the five-membered planar ring of SiO_4 tetrahedra, the Si-O-Si angle is approximately 177°. However, a number of more recent diffraction measurements suggest that this angle is considerably less than 180°. (The Si-O-Si angles calculated from the results of a number of x-ray and neutron diffraction measurements are listed in Table I-7.) Furthermore, the larger interatomic spacings in the unit cell of Tilton's model do not agree very well with the spacings indicated in the radial distribution curves obtained from recent neutron diffraction measurements (Table I-6).

Hicks (66) has argued, on the basis of configurational entropy considerations, that local regions in vitreous silica are far more likely to have a cristobalite structure than a pentagonal dodecahedra structure. He considers the number of bonds required to form the six-membered rings characteristic of the cristobalite structure and a pentagonal dodecahedra and estimates that the relative probability of the formation of the two configurations is 520,000 to 1 in favor of cristobalite.

1.3.11 ROBINSON'S PENTAGONAL-DODECAHEDRAL MODEL

A modified version of the pentagonal dodecahedra model has been suggested in a paper by Robinson (67). In the words of the author: "The vitreous silica model network arrived at in this paper can be described as textured pentagonal dodecahedral. This means that on the average the network can be conceived of as an assemblage of individual grains, each grain consisting of stacked pentagonal dodecahedra (pd). The individual pd are, however, badly distorted and in fact no two pd will be exactly alike in shape. Furthermore, there will surely be imperfections in the sense that some of the pentagons (pentagonal rings) forming the sides of the dodecahedra will undoubtably be replaced by hexagons or rings containing other numbers of Si atoms. It is not known at this time what percentage of the total rings are other than pentagonal but the evidence derived from the density and the admittedly non-precise diffraction data shows that it cannot be large."

The distortion or puckering of the faces of the pentagonal dodecahedra has the advantage of decreasing the size of the unit cell and hence increasing the density of the model to a more reasonable value. The puckering also introduces a dispersion among the bond lengths and the 'same' interatomic distances vary somewhat from position to position in the ring. (The calculated interatomic distances for the puckered pentagons which make up this structure are

listed in Table I-4.) Although the smaller number of repeating interatomic spacings in this model makes it more compatible with the x-ray diffraction results (Table I-5, Section 1.3.13) than Tilton's model, it certainly does not predict or explain the larger interatomic spacings indicated in the atom pair distribution curves obtained from neutron diffraction data (Table I-6, Section 1.3.13).

It should also be noted that Hick's (66) determination of the relative probability of forming a cristobalite-like structure and pentagonal dodecahedra applies to the Robinson model as well as Tilton's model since the same number of bonds are required to form the pentagonal dodecahedral unit cell regardless of whether the unit is distorted or regular in shape.

TABLE I-4 Radial Distribution of Atoms in the Robinson Distorted Pentagonal Dodecahedra

From O to:		From Si to:		Atom Pair Spacing (Å)
No.	Kind	No.	Kind	
2	Si	4	O	1.615
6	O			2.67
		4	Si	3.226
6	Si	12	O	3.97
6	O			4.17
3	Si	6	O	4.85
		12	Si	4.98

1.3.12 TEMPERATURE-PRESSURE DEPENDENT COEXISTING STRUCTURES IN VITREOUS SILICA

Babcock, Barber, and Fajans (68) have attacked the structure question from still another point of view. The primary concern of these authors is to explain the anomalous thermal properties of vitreous silica: "The very small and nearly constant (thermal expansion) coefficient of vitreous silica between 300° and 1250°K and the fact that it becomes negative below 200°K is unique among homogeneous solid substances. A minimum occurs not only for the volume, but (according to Doborzynski (69)) also for the dielectric constant of vitreous silica. No satisfactory explanation of these facts has been offered and they cannot be understood from the viewpoint of a single continuous network which, with increasing temperature, would show merely the effects of the anharmonicity of atomic vibrations."

Babcock, et.al. suggest that these anomalies are the direct result of temperature and pressure dependent structural changes in the glass. Two possible descriptions of the mechanics of the structural transformations are offered:

a.) The change in bond angles and distances occurs more or less continuously throughout the vitreous phase.

b.) Two (or more) well-defined ionic arrangements, "structures" I and II, coexist within the glass.

> Each structure has a normal positive thermal expansion coefficient, but their relative concentrations, which are in equilibrium with each other within the homogeneous phase, change continuously with temperature and pressure.

Although the authors concede that the data presented in their article does not allow a clear-cut decision between the two hypotheses, they favor the coexisting structure hypothesis.

The properties of the coexisting structures in the Babcock, et.al. model are as follows:

1.) At a given temperature, the specific volume of I is greater than that of II.

2.) An increase in temperature shifts the equilibrium from I toward II, i.e., the conversion I $\longrightarrow$ II is endothermic. The lower the temperature the greater is the amount of the spacious structure I which is available for conversion into the denser structure II.

3.) The interconversion of I and II is rapid and reversible even at low temperatures.

4.) Increased pressure shifts the equilibrium from I toward II.

Therefore, according to this hypothesis, the thermal expansion behavior of vitreous silica is the result of the small positive expansions of both I and II coupled with the

volume contraction which accompanies the conversion of I (low temperature form, low density) into II (high temperature form, high density) on heating.

The fact that the mean compressibility of vitreous silica increases with increasing pressure and decreasing temperature is also interpreted in terms of the conversion I $\rightarrow$ II. According to properties 1 and 4, the coefficient of compressibility can be expected to be relatively large because the conversion I $\rightarrow$ II causes contraction. At increased temperatures structure II is favored; the high pressure applied during the measurement of compressibility at elevated temperatures causes smaller amounts of the conversion I $\rightarrow$ II and therefore decreases the apparent compressibility.

The possibility of coexisting structures in vitreous silica was noted in Section 1.3.8. However, the results of an x-ray scattering study by Zarcycki (70) provides the basis for a very telling criticism of the Babcock, et.al. hypothesis. According to Babcock, structure I predominates in vitreous silica at a temperature of approximately - 73^{o}C and the total conversion of structure I to structure II takes place over a range of about 1000^{o}C. Zarcycki has observed the x-ray scattering by vitreous silica at temperatures of 20^{o}C and 1600^{o}C. Although it was necessary to replace the 1600^{o}C specimen with a new one every fifteen minutes because of its progressive devitrification, he

found that the interatomic spacings at the two temperatures were practically the same. A proponent of the Babcock hypothesis might well argue that at a given temperature the differences in the interatomic spacings of structures I and II could not be resolved in the Fourier analysis of the diffraction data; however, it is difficult to believe that the change which one would expect in the relative concentrations of the two structures at these widely separated temperatures would not be observed through a shift in the mean values of the interatomic spacings.

1.3.13 EXPERIMENTAL DIFFRACTION DATA

Most of the models of the structure of vitreous silica are based on the results of x-ray, neutron, and, to a lesser extent, electron diffraction studies. The following survey of these measurements will perhaps indicate why the structure of vitreous silica remains the subject of so much controversy.

As indicated in the discussion of Warren's work, there are two possible ways of analyzing the experimental diffraction data. One method is based on the calculation of the theoretical diffraction patterns for various models; the other method starts with the observed diffraction curve and transforms it into a radial distribution curve characteristic of the average atom pair density in the sample. Comparison between theory and experiment is made by means of the diffraction curves in the first method and pair distribution curves in the second. Although the two methods are equivalent in principle, they each have their limitations and in practice there are situations where one method is more appropriate than the other.

Intuitively it would seem that the most straightforward and satisfactory method of analysis is that which requires the least manipulation of the experimental data. The fact that there is a much wider variation in the reported pair distribution curves than in the diffraction patterns from which they are derived lends added weight to this argument.

However, few of those who have suggested models have either calculated a theoretical diffraction curve or provided the necessary information to do so. In lieu of this information, the experimentalist has no physically meaningful way in which to present his results other than in the form of an atom pair distribution curve. There is also the question of the uniqueness of the diffraction pattern calculated from a particular model. For example, Bagdyk'yants and Alekseev (71) report that the theoretical diffraction curves for a random network model and a model consisting of cristobalite crystallites (2 x 2 x 1 unit cells in size) both agree quite well with the electron diffraction pattern for vitreous silica which they have measured. The possibility that radically different structures may produce the same diffraction pattern (homometric structures) has also been demonstrated by Patterson (72). Therefore, for the reasons cited above, the comparison between theory and experimental results is usually made on the basis of atom pair distribution curves.

The use of electron diffraction techniques for the study of amorphous systems has been discussed in detail by Bauer (73). Electron diffraction investigations of vitreous silica have been rather limited. This is due, in part, to the low penetrating power of an electron beam and the resulting experimental difficulties associated with the need to use very fine powders or films. Surface effects

such as the interaction of the samples with moisture in the air hinder the measurement of reliable diffraction patterns. The high cross section for electron scattering also creates serious multiple scattering problems.

Bauer (73) suggests that the low penetrating power of the electron beam might be a definite advantage in the investigation of the structure of a non-crystalline solid: "As is well known, the radial distribution function involves an averaging, over all points in a sample, of the product of the density of electric potential or scattering matter at each point by the density contained in a shell of radius r. Clearly, up to a certain size the magnitude of the sample affects the average. Conceivably, if one were to illuminate small enough regions of the sample, he could obtain a much more sensitive measure of local order than is generally observed; but corrections will have to be made for diffraction effects due to small sample size." However, the results of the electron diffraction measurements to date do not appear to support this argument.

Electron diffraction studies of vitreous silica have been reported by Ackermann (74), Bagdyk'yants and Alekseev (71), König (75), Maxwell and Mosely (76), McClurg (77), and Shishakov (78). There is one consistent feature of all of these studies: the interatomic distances which are deduced from this data are smaller than those determined from the x-ray and neutron diffraction data. McClurg, for example, has obtained a pair distribution

from the Fourier inversion of his diffraction data which shows well-defined peaks at spacings of 1.3, 2.2, 3.0, 4.0, and 4.5 Å. In comparison, the spacings of the peaks in the pair distribution curve which Warren obtained from his x-ray data are 1.62, 2.65, 3.2, 4.3, and 5.2 Å. McClurg concludes that the discrepancies in the interatomic spacings obtained by the two different methods are not the result of experimental error; and therefore, that the bulk structure of vitreous silica must be different from the structure of the surface layer. Weyl and Marboe (79) suggest that the difference in the bulk and surface structures arises from the fact that the SiO_4 tetrahedra in the surface have to be distorted in order to assume a structure that does not contain unscreened Si^{4+} ions.

Shishakov claims that the sharp interference effects which he observes in his electron diffraction pattern are proof of the existence of flat networks or one and two dimensional chains. However, Porai-Koshits (80) attributes these effects to the partial crystallization of the glass during its preparation for the investigation.

The paramount role of the x-ray diffraction studies of vitreous silica in the development of the various theories and models of the structure has been detailed in the foregoing pages. The results of a number of these studies, in the form of atom pair spacings, are listed in Table I-5.

A brief comment concerning the atom pair spacings

TABLE I-5. Interatomic Spacings in Vitreous Silica (Å) Obtained from X-ray Diffraction Data

Separation	Warren (27)	Hartlief (81)	Simon (82)	Zarzycki (83)	Norman (84)	Warren (85)	Henninger (40)
Si-O	1.62	1.7	1.61	1.60	1.62	1.64	1.56
O-O	2.65	2.7	-	-	2.62	2.68	2.54
Si-Si	3.20	3.1	3.03	3.00	3.05	3.14	3.065
Si-(2)O	4.2	4.1	4.19	4.0	4.08	4.2	3.94
	4.5	-	-	-	-	4.5	-
	5.2	5.3	5.4	5.0	5.02	5.2	-

reported in the literature is in order here. Even if the diffraction data are inverted with a minimum number of errors, the accurate determination of the atom pair spacings from the resulting pair distribution curves is still a very difficult proposition. Consider, for example, the analysis of Warren's pair distribution curve (Figure I-3). The second and third peaks in Warren's curve are unresolved. (The same is true for all of the other pair distributions obtained from x-ray measurements.) Warren has indicated that the unresolved distribution curve can be separated into two relatively symmetric peaks in this region. However, the arbitrary separation of unresolved peaks is a very questionable procedure and obviously leads to a great deal of inaccuracy in the determination of the pair spacings and densities. In addition to the problem of unresolved peaks, at the larger spacings (>3.2 Å) the identification of a peak in the distribution curve with a particular atom pair is a matter of considerable uncertainty. In one paper Warren concludes that the peak at 4.3 Å can be attributed to two different silicon-oxygen pairings which are unresolved in the Fourier analysis (26); yet, in another paper he indicates that this same peak arises from a combination of silicon-oxygen and oxygen-oxygen pairings (27).

In recent years there have been several neutron diffraction studies of vitreous silica. The major advantage of this technique lies in the fact that neutron scattering

by an isolated nucleus is isotropic. In the x-ray diffraction experiment the scattering intensity is determined by the electron density distribution in the sample. Since the wavelength of the x-rays is of the same order of magnitude as the atomic radii, interference occurs between waves scattered by different electrons within the same atom. This destructive interference decreases the intensity of scattering as the scattering angle increases and limits the range of momentum transfers in which it is possible to observe diffraction maxima. The independence of the neutron scattering from this effect has led to the discovery of diffraction maxima at momentum transfers well beyond the effective range of the x-ray experiments.

The results of those who have transformed their neutron diffraction data into atom pair distribution curves are listed in Table I-6. The smaller pair spacings derived from the neutron measurements agree quite well with those obtained from the x-ray data. The advantage of being able to obtain diffraction data at larger momentum transfers is reflected in the fact that previously undetected longer-range atom pair spacings are observed in the neutron results. However, the information in Table I-6 must be viewed with the same degree of caution as that in Table I-5 since the interpretation of the pair distribution curves obtained from the neutron data is subject to the same difficulties as the interpretation of the x-ray results

TABLE I-6. Interatomic Spacings in Vitreous Silica (Å) Obtained From Neutron Diffraction Data

Separation	Milligan (86)	Breen (87)	Carraro (88)	Henninger (40)	Lorch (89)
Si-O	1.58	1.6	1.61	1.59	1.60
O-O	2.56	2.6	2.59	2.62	2.60
Si-Si	3.02	3.3	-	3.22	3.05
Si-(2)O	4.0	3.9	4.05	4.09	3.60
	-	4.5	-	-	4.05
	5.1	5.3	5.0	5.03	5.02
	5.9	-	-	-	
	6.6	6.3	6.3	6.2	
	7.4	7.2	7.3		
	-	8.2	-		
	9.0	9.1	8.7		
	9.7	10.2	9.8		

(unresolved peaks and the uncertainty as to whether a given peak represents one or more types of atom pairing).

Henninger, Buschert, and Heaton (40) have suggested that the question of whether a particular peak in the pair distribution curves represents a single type of atom pairing can be resolved by combining the results of the x-ray and neutron diffraction measurements. (Assuming, of course, that the same sample is used for both measurements.)

The distribution function obtained by the Fourier inversion of an x-ray or neutron diffraction pattern is not a direct distribution of atoms; rather, it is a sum of the distributions of each type of atom pair weighted by the effective scattering amplitudes and atom concentrations. The appearances of the pair distributions obtained from the x-ray and the neutron measurements differ considerably. This follows, in part, from the fact that the x-rays scatter with greater intensity from silicon atoms than from oxygen atoms while the reverse is true for the neutron scattering. (The ratio of the nuclear scattering lengths Si/O for neutrons is 0.65 (90); the ratio of the scattering factors Si/O for x-rays is 1.5 (39).)

According to Henninger, et.al., the ratio of the distribution functions obtained from the x-ray and neutron data, R(r), may be equated to the following expression:

$$\text{I-3} \qquad R(r) = \frac{m_O K_O^2 \rho_{O-O}(r) + m_{Si} K_{Si}^2 \rho_{Si-Si}(r) + m_O K_O K_{Si} \rho_{O-Si}(r) + m_{Si} K_{Si} K_O \rho_{Si-O}(r)}{m_O b_O^2 \rho_{O-O}(r) + m_{Si} b_{Si}^2 \rho_{Si-Si}(r) + m_O b_O b_{Si} \rho_{O-Si}(r) + m_{Si} b_{Si} b_O \rho_{Si-O}(r)}.$$

where m_i is the fraction of the total number of atoms which are of type i, $\rho_{i-j}(r)$ is the average density of j-type atoms at a distance r from i-type atoms, b_i is the neutron coherent scattering length of an i-type atom, and K_i is the x-ray scattering amplitude of an i-type atom divided by the average scattering factor per electron.

If the near neighborhood of each atom is highly ordered, the ratio R(r) derived from the experimental data will indicate the correlation of atom types. For example, if an oxygen atom has only oxygen neighbors at distance r_1, and no silicon-silicon pairs exist with a spacing of r_1, the ratio should be $R_{O-O}(r_1) = K_O^2/b_O^2 = 147$ since $\rho_{Si-O}(r_1) = \rho_{O-Si}(r_1) = \rho_{Si-Si}(r_1) = 0$. The other possible isolated correlations would give $R_{Si-Si}(r) = 1450$ and $R_{Si-O}(r) = 463$. When there is no preferential pairing, as in a random mixing, $\rho_{Si-O} = 2\rho_{Si-Si} = \rho_{O-O} = 2\rho_{O-Si}$ and therefore, $R_{mix}(r) = 364$. At large separations r, beyond the region of short-range order, the ratio should approach this value.

The experimental R(r) curve which Henninger et.al. computed from the results of their x-ray and neutron measurements is shown in Figure 4. According to the authors, this calculation verifies that each of the first three peaks in the pair distribution curves represent a single type of atom pairing: Si-O pairs with a 1.61 Å spacing, O-O pairs at 2.62 Å, and Si-Si pairs at 2.95 Å. Furthermore, they claim that the peaks in the pair distribution curves at larger spacings represent mixtures

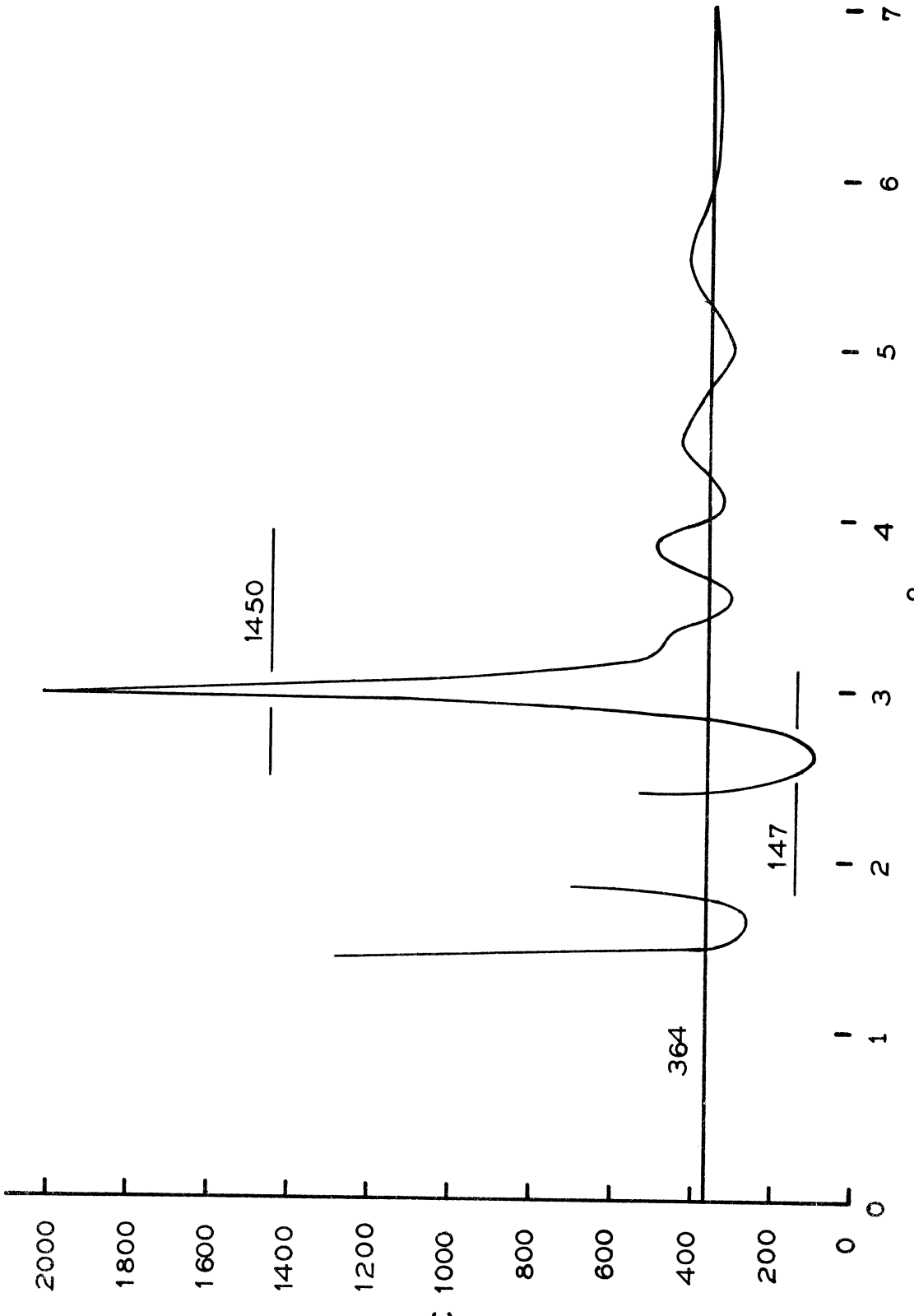

Figure 4. Ratio of the atom pair correlation function of vitreous silica derived from x-ray diffraction data to that derived from neutron diffraction data. (From Henninger, Buschert, and Heaton (40).)

of all three types of pairing. (This last assertion is difficult to reconcile with their R(r) curve. The two maxima in the R(r) curve at r = 3.85 Å and r = 4.4 Å are certainly much closer to R_{Si-O}= 463 than the value for mixed pairings R_{mix}= 364.)

The successful application of the ratio analysis obviously requires accurate computation of the two atom pair distribution curves. Since three of the ratios of pairings (R_{O-O}= 147, R_{mix}= 364, and R_{Si-O}= 463) are quite close in value there is not much of a margin for error. The fact that Henninger's experimental R(r) curve overshoots the calculated extreme values for each of the first three atom pairings would seem to indicate that his pair distribution curves are not sufficiently accurate for the analysis of the peaks at the larger spacings.

It is extremely difficult to assess the relative quality of the atom pair distribution curves reported in the literature. As noted previously, the sources of error in the measurement and in the inversion of the diffraction data are numerous. The problem is further complicated by the fact that the authors' attempts, if any, to correct for the experimental and inversion difficulties are rarely discussed in any detail. As a result, there are many instances where the reader has been led to believe that spurious peaks are real and real features of the pair distribution curve have either been altered or completely

removed. The diffraction studies by Carraro (88) and Henninger (40) provide a typical example of the confusion created by this problem. Each of these authors has measured the neutron diffraction pattern of vitreous silica and transformed his data into a pair distribution curve. Although the positions and relative intensities of the maxima in the two diffraction patterns are in excellent agreement, there is a significant difference in their pair distribution curves. Henninger's results show a prominent, well-resolved peak at 3.22 Å; Carraro's analysis, on the other hand, indicates that this peak is a spurious feature and his pair distribution curve actually passes through a minimum at this point. Although Henninger provides a more detailed description of his computation than Carraro, neither author provides sufficient information to determine which interpretation is correct.

An equally troublesome omission in most of the papers is an adequate description of the sample itself. According to Sosman (91): "The structure of any given fragment of vitreous silica is a composite inheritance from all of the temperatures through which it has passed since it last attained a thermodynamic equilibrium. Its properties therefore depend, to a limited extent, upon its thermal and mechanical history." In the discussion of the crystallite model it was noted that various measurements of the physical properties of vitreous silica suggest that there is a correlation between the structure of the glass

and the crystalline form of silica from which it was prepared. Douglas and Isard (92) report that the quenching of vitreous silica from temperatures that vary between 1000°C and 1500°C produces samples with substantial differences in density at room temperature. All of these factors indicate that if a pair distribution function is to have any significance, the sample from which it is obtained must be adequately described.

Since the diffraction studies cited in this report suffer in varying degrees from the abovementioned errors and omissions, let us discuss exactly what we can learn about the structure of vitreous silica from the atom pair spacings in Tables I-5 and I-6.

There is almost universal agreement that the results of the diffraction experiments confirm that the basic unit of the vitreous silica structure is the SiO_4 tetrahedron. The mean value of the O-Si-O angle is

$$\beta(\text{O-Si-O}) = \arccos\left[\frac{2R^2_{\text{Si-O}} - R^2_{\text{O-O}}}{2R^2_{\text{Si-O}}}\right] \qquad \text{I-4}$$

where $R_{\text{Si-O}}$ and $R_{\text{O-O}}$ are the silicon-oxygen and oxygen-oxygen pair spacings respectively. If the silicon atom is surrounded by four oxygen atoms in a regular tetrahedral configuration, this angle will be 109°28'. As shown in Table I-7, the O-Si-O angles calculated from the experimentally derived pair spacings lie within a few degrees of this value.

TABLE I-7. Bond Angles in Vitreous Silica Calculated from Diffraction Data

Author	Method	β (O-Si-O)	$\ominus$ (Si-O-Si)
Warren	X-ray	109°	162°
Hartlief	X-ray	104°	130°
Simon	X-ray	-	140°
Zarzycki	X-ray	-	$143° \pm 17°$ [a]
Norman	X-ray	107°	140°
Warren	X-ray	109°	146°
Henninger	X-ray	108°	158°
Milligan	Neutron	107°	145°
Breen	Neutron	108°	~180° [b]
Carraro	Neutron	106°	-
Henninger	Neutron	110°	~180° [b]
Lorch	Neutron	109°	145°
Henninger	X-ray/Neutron	103°	132°

(a) Zarzycki is one of the few authors who has calculated the Si-O-Si angle from his data and is the only one who has estimated the error in the angle determination.

(b) Both Breen and Henninger report Si-Si atom spacings which are more than twice the Si-O atom spacings.

As the spacings between the atoms increase, there is a corresponding decrease in the reliability of the information which can be obtained from the pair distribution curves. Consider, for example, the calculation of the mean angle of the Si-O-Si bond linking the SiO_4 tetrahedra. The Si-O-Si angle is given by the expression

$$\text{I-5} \qquad \ominus (\text{Si-O-Si}) = \arccos \left[\frac{2R^2_{\text{Si-O}} - R^2_{\text{Si-Si}}}{2R^2_{\text{Si-O}}} \right]$$

Using the Si-O and Si-Si pair spacings listed in Tables I-5 and I-6, one finds that estimates of the mean Si-O-Si angle vary from 130° to 180° (Table I-7).

It should be remembered that the x-rays are scattered by the electron distribution in the sample whereas the neutrons are scattered by the nuclei. Unless the electron distribution about each atom is spherically symmetric, there is no reason to expect that the Si-O-Si angles calculated from the neutron and x-ray data will be very nearly equal. However, it is almost inconceivable that the 32° range in values calculated from the x-ray data and the comparable 35° variation in the neutron results is a true reflection of the degree to which the short range order of vitreous silica varies from sample to sample. There is evidence, furthermore, that even if the mean value of the Si-O-Si angle is strongly sample dependent, the limits indicated in Table I-7 are unreasonable. Bell and Dean (93) have constructed a physical model of the vitreous silica

structure, based on the random network concept, in which the mean Si-O-Si bond angle is $139^{\circ}24'$. They find that the density of this model is approximately 25% greater than the measured density of vitreous silica. On the other hand, a model in which the mean Si-O-Si angle is approximately 180° has a density 10% lower than the measured density (65).

The most likely explanation of the wide range in the Si-O-Si angles is the extreme sensitivity of the angle calculation to small variations in the Si-O and Si-Si atom spacings. A plot of the Si-O-Si angle as a function of these pair spacings is shown in Figure 5. We see, for example, if a fixed Si-O pair spacing of 1.60 Å is assumed, a decrease in the Si-Si spacing from 3.20 Å to 3.15 Å decreases the Si-O-Si angle by 20°. Lorch (89) estimates an error of ±0.05 Å in the Si-O pair spacing which he has derived from his neutron diffraction study. Again referring to Figure 5, we see that if a fixed Si-Si atom pair spacing of 3.15 Å is assumed, an increase in R_{Si-O} from 1.58 Å to to 1.60 Å, a change of only 0.02 Å, gives rise to a 12° increase in $\ominus$(Si-O-Si). Perhaps the difficulty of obtaining an accurate estimate of $\ominus$ explains why there has not been a satisfactory interpretation of the other maxima ($r > 3.2$ Å) in the pair distribution functions of vitreous silica.

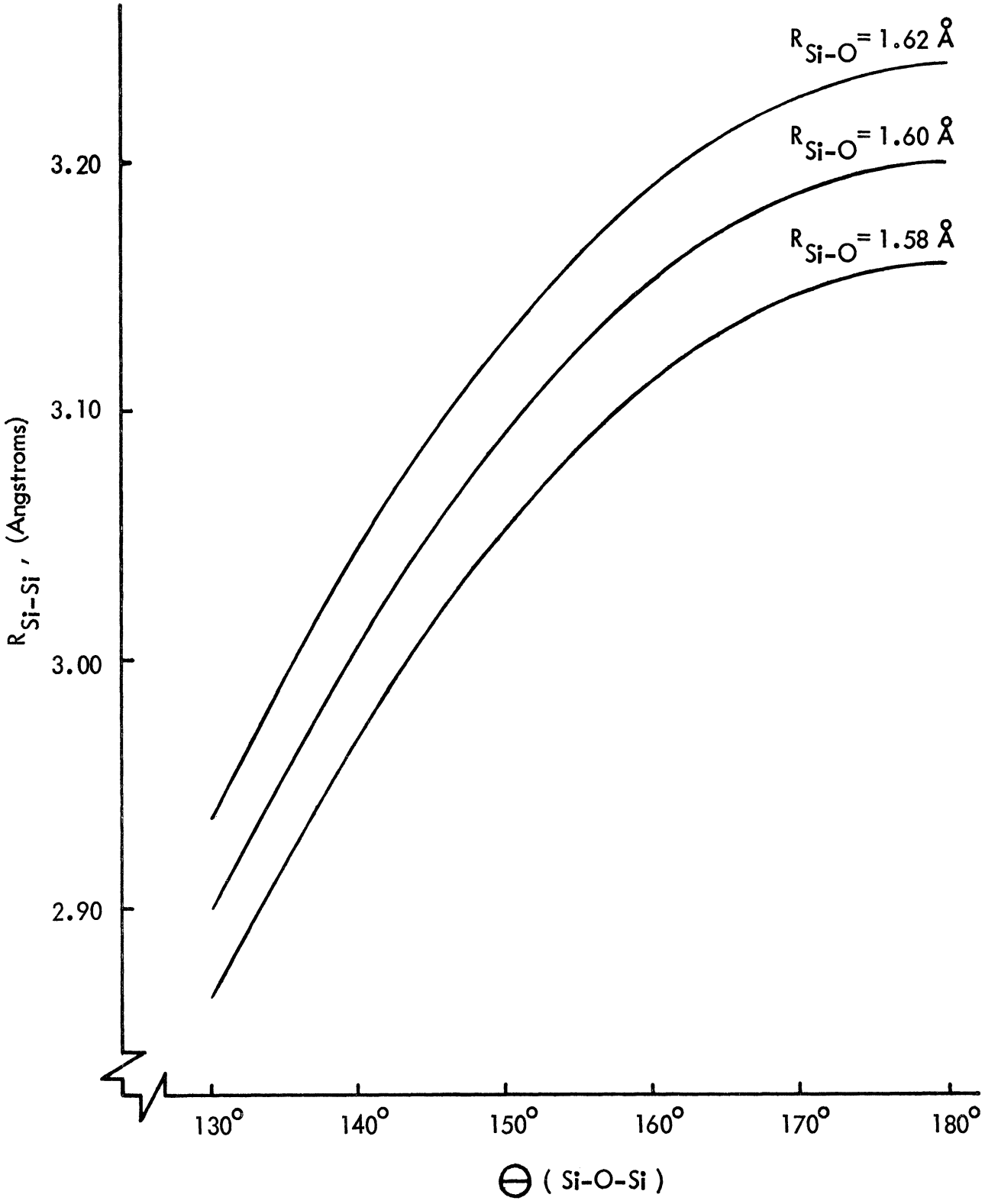

Figure 5. The tetrahedra linking angle, (Si-O-Si), as a function of the silicon-oxygen and silicon-silicon spacings.

1.4 THE DYNAMICS OF THE VITREOUS SILICA STRUCTURE

1.4.1 INTRODUCTION

The foregoing discussion of the various models of the structure of vitreous silica dealt with what may be classified as the structural statics, i.e. the interatomic spacings, bond angles, and the coordination (atom pair densities) of the structure. A complete description of vitreous silica must also include a description of its characteristic vibrations and the nature of the forces which give rise to them. The most direct experimental evidence of the dynamical properties of vitreous silica is obtained from measurements of its infrared, Raman, and more recently, inelastic neutron scattering spectra. The measurements and interpretations of these spectra are reviewed in the following pages.

1.4.2 INFRARED AND RAMAN SPECTRA OF VITREOUS SILICA

Infrared properties of glass have been studied since the beginning of infrared spectroscopy more than sixty years ago (94)(95) and the first attempts to investigate Raman spectra in glass date back to 1928 (96)(97)(98)(99). As a result, a reasonably large body of data has been accumulated by both techniques. The apparatus and the methods employed to obtain the infrared absorption and reflection spectra of glasses are detailed in a review article by Simon (100). A similar discussion of the Raman measurements is provided by Bobovich and Tulub (101). Therefore, the following remarks will be confined to a few special problems connected with the specific nature of the infrared and Raman interactions in glass and their bearing on the reliability of the data obtained by the two techniques.

The principal problem in the infrared spectroscopy of vitreous silica lies with the type of sample required for the measurements. Absorption in the regions of the fundamental bands is so strong that layers of vitreous silica a few microns thick absorb the incident light completely. In order to obtain a useful transmission spectrum, one has to resort to very thin films blown as bubbles from molten glass or fine powders in oil suspensions or mixed with dry KBr powder and pressed into pellets. Since the strength and shape of absorption bands in powdered materials depend critically on the particle size, it is questionable if the data obtained from this type of sample is truly representative of the bulk

structure of vitreous silica. A similar objection applies to the data obtained from the thin films. The infrared spectrum can be obtained by reflection from a polished surface of a larger glass sample. However, the reflection measurement is generally insensitive for weak bands.

The Raman effect in vitreous silica is very weak and generally produces broad diffuse bands. Difficulties in the Raman measurements arise from the parasitic scattering from sample defects such as knots, bubbles, devitrified particles, etc.. The high pressure mercury lamps which have commonly been used as the exciting source for these measurements, produce spectra containing a continuous background in addition to sharp lines which greatly hinders the detection and interpretation of the weak scattering spectrum of glass. The use of low-pressure mercury lamps in more recent studies has helped to reduce the background problems. Also, the more modern technique of using a laser as the exciting source is just beginning to be employed in the study of glasses.

The results of a number of infrared studies of vitreous silica are compiled in Table I-8. The number of absorption or reflection bands reported by a particular author is not significant in that the measurements cover widely different ranges of frequencies, e.g. Reitzel's (108) study includes only the 400 cm^{-1} to 600 cm^{-1} region whereas the measurement of Lippencott, et.al. (106) extends from 300 cm^{-1} to 4000 cm^{-1}. What will be described as the consensus inrared spectrum of vitreous silica is listed in the last column of Table I-8.

TABLE I-8. Infrared Bands of Vitreous Silica

Gross & Romanov (102)	Markin (103)	Barnes (104)	Simon & McMahon (105)	Lippincott (106)	Mattossi & Bluschke (107)	Reitzel (108)	Su (109)	Florinskaya Pechenkina (110)	Consensus
		76							
		85							
		116							
							207		
							226		
							250		
							280		
373									
495				468	478	465	469;476		475 (s)
685									
794	788		800	805	783		803	797	795 (m)
			950						
1124	1120		1100	1108	1136		1099;1030	1093	1100 (vs)
1205			1190	1200					1200 (ms)

Key: vs- very strong, s- strong, ms- moderately strong, m- moderate

The criterion for the inclusion of a band in the consensus spectrum is that it must have been observed in at least three different measurements.

The nature of the low frequency region ($\nu < 400$ cm^{-1}) of the infrared spectrum of vitreous silica is a matter of considerable controversy. The weak absorption bands at 76 cm^{-1}, 85 cm^{-1}, and 116 cm^{-1} which Barnes (104) observed in his 1932 measurements have not been confirmed by subsequent measurements. Plendel and Mansur (111) report that they have observed a very weak absorption band at $\sim$143 cm^{-1} but nothing below this band in a measurement that extends down to at least 65 cm^{-1}. Su, et.al. (109) report the presence of four absorption bands between 207 and 280 cm^{-1}. However, it is interesting to note that there is no evidence of this absorption in the transmission curve shown in their paper. Hanna (112) also reports an infrared band at about 200 cm^{-1}. Plendel and Mansur (111), on the other hand, observe no absorption in this region. Gross and Romanov (102) claim to have observed a moderately strong infrared band at about 373 cm^{-1}. Lippencott (106), Su (109), and Hanna (112) observe no absorption in this region of their spectra.

In summary, if there are infrared bands in the low frequency end of the vitreous silica spectrum, they are obviously quite weak and/or very sample-dependent. The many discrepancies noted above point up this fact and indicate that more intensive studies of this region of

the infrared spectrum are required.

The 475 cm^{-1}, 790 cm^{-1}, and 1100 cm^{-1} bands of the consensus spectrum are all quite strong. Although these bands are relatively broad (>50 cm^{-1} at room temperature), their positions in the spectrum are well established. For example, if the older data of Gross and Romanov (102) is ignored, the variation in the reported positions of the infrared bands in the 475 cm^{-1} region of experimental spectra is only 10 cm^{-1}; in the 790 cm^{-1} region, 19 cm^{-1}. If the 1030 cm^{-1} band which Su, et.al.(109) observed in their reflection spectrum is discounted, the range in the reported positions of the bands in the 1100 cm^{-1} region is ~ 30 cm^{-1}. This relatively large range, in comparison to the other two bands, probably is due to the presence of a band at $\sim$ 1200 cm^{-1} which appears as a shoulder on the high frequency side of the 1100 cm^{-1} band and distorts its shape. No bands have been observed in the infrared data in the region beyond 1300 cm^{-1}.

The results of a number of Raman scattering studies of vitreous silica are compiled in Table I-9. The dominant feature of the Raman spectrum of vitreous silica is an intense continuum extending from the exciting line out to a sharp cut-off at $\sim$ 560 cm^{-1}. (The criterion of three observations for the inclusion of a band in the consensus experimental spectrum has been relaxed in this instance since there have been only two serious attempts to measure the extreme low frequency region of the Raman scattering

TABLE I-9. Raman Bands of Vitreous Silica (cm^{-1})

Gross & Kolesova (113)	Gross & Romanov (114)	Kujumzelis (115)	Krishnan (116)	Harrand (117)	Bobovich & Tulub (101)	Lord (118)	Flubacher (119)	Consensus
			~30-120	95			~10-560	~10
	213							
250-450	263	230-450	285	275-500				
	323							
	370		370					
	444		430					
490	500	500	495	500	500			500(vs)
595	625	607	635	595-612	595-600			595-620(w)
690	667	720	660					685(w)
750	741							
780-820	800-833	780-840	775-805	795-826	800	790-850	760-850	780-830(s)
820-850			810-845	860				830-850(m)
900-990		915	885-940	910				915(vw)
1030-1100	1031-1087	1030-1090	1022-1098	1020-1100	1065	1000-1080	1013-1093	1020-1095(ms)
1130-1230	1190-1235	1160-1230	1140-1245	1150-1250	1200	1150-1235	1115-1245	1150-1240(w)
1350-1400		1390						

Key: vs- very strong, s- strong, ms- moderately strong, m- moderate, w- weak, vw- very weak

spectrum of vitreous silica.) According to Flubacher, et.al. (119), the continuum is characterized by two broad intensity maxima at 48 cm^{-1} and 432 cm^{-1} and a sharper peak at 489 cm^{-1}. Krishnan (116) reports a strong Raman band at $\sim$ 370 cm^{-1}. Gross and Romanov (114) report some six different maxima in this region. Simon (100) suggests the possibility of two strong bands at approximately 95 cm^{-1} and 275 cm^{-1}. Thus, it is interesting to note that one finds discrepancies in the low frequency Raman data similar to those in the low frequency infrared data.

The higher frequency end of the Raman spectrum of vitreous silica appears as follows: two fairly weak bands are observed at 595 - 620 cm^{-1} and 685 cm^{-1}. The most intense band in the spectrum after the low frequency continuum appears at 780 - 830 cm^{-1} with a moderate intensity shoulder at 830 - 850 cm^{-1}. A very weak band is observed at 915 cm^{-1} and a moderately strong band is observed between 1020 - 1095 cm^{-1} with a weak shoulder at about 1150 - 1240 cm^{-1}. There have been no reports of Raman bands beyond 1300 cm^{-1}.

Knowledge of the degree of polarization of the Raman bands should be helpful for band assignments. According to a study of the state of polarization of the Raman spectrum by Harrand (117), the continuum is strongly polarized at $\sim$ 200 - 500 cm^{-1} but depolarized at $\sim$ 100 cm^{-1}. The bands at 595 - 620 cm^{-1}, 780 - 830 cm^{-1}, and 915 cm^{-1} are polarized; all of the other bands are depolarized.

Attempts to assign the various features of the infrared and Raman spectra to particular motions of the atoms in vitreous silica are discussed in Section 1.4.4.

1.4.3 INELASTIC NEUTRON SCATTERING SPECTRA OF VITREOUS SILICA

The inelastic neutron scattering measurement offers several significant advantages over both the infrared and Raman techniques. In Section 1.4.2 it was noted that the high absorption of the incident radiation in the infrared measurements requires the use of thin films or powder samples. Since the mean free path of a neutron in vitreous silica is approximately 4 to 5 centimeters (Chapter IV), it is possible to use a much larger sample and thus obtain data which is more truly representative of the bulk structure. Also, the sample does not have to have the high optical quality required in the Raman measurement. However, the greatest advantage of the neutron scattering experiment is that the neutrons can interact with all of the vibrational modes of the target whereas the infrared and Raman experiments are sensitive only to optically active modes.

To date, only Egelstaff (120) and Leadbetter (121) have studied the inelastic neutron scattering properties of vitreous silica. Both experiments were performed at the cold neutron-chopper facility at the Dido reactor, Harwell. In each case, the energy of the neutrons in the incident beam was 3 meV (25 cm^{-1}) and therefore, only energy gain spectra were observed.

Egelstaff's measurements were performed at temperatures of 20°C and 350°C. He reports that he observes three major

peaks and a fourth peak of low intensity in the inelastic scattering spectra. The energies of these peaks are given as 39 meV (315 cm^{-1}), 13 meV (105 cm^{-1}), 4 meV (32 cm^{-1}), and approximately 2 meV (16 cm^{-1}). (The energies of the scattered neutrons are determined by measuring their time-of-flight over a 1.28 meter flight path.) Three of the spectra, one of the 20°C measurements and two of the 350°C measurements, are reproduced in his paper. The scatter of the data points and the lack of error bars makes it extremely difficult to observe the reported maxima. Only the 39 meV and 13 meV peaks in one of the 350°C spectra are readily apparent. Judged on the basis of the three spectra shown, the presence of the other two peaks is highly questionable.

In Leadbetter's study, the coherent inelastic neutron scattering by a sample of vitreous silica at a temperature of $\sim 17^{\circ}C$ was observed at six scattering angles between 20° and 90°. The spectrum observed at the 75° scattering angle is reproduced in Figure 6. Leadbetter claims that the coherent inelastic neutron scattering spectra of his glass sample and a powder sample of low-cristobalite are almost identical for the region $\omega > 50$ cm^{-1}. The location of the maxima in the low-cristobalite spectra (for $\omega > 50$ cm^{-1}) are given as ~ 85 cm^{-1}, ~ 150 cm^{-1}, and between 200 and 500 cm^{-1}. In the low frequency region of the spectra ($\omega < 50$ cm^{-1}), Leadbetter notes that a peak observed at ~ 40 cm^{-1} in the low-cristobalite spectra is almost

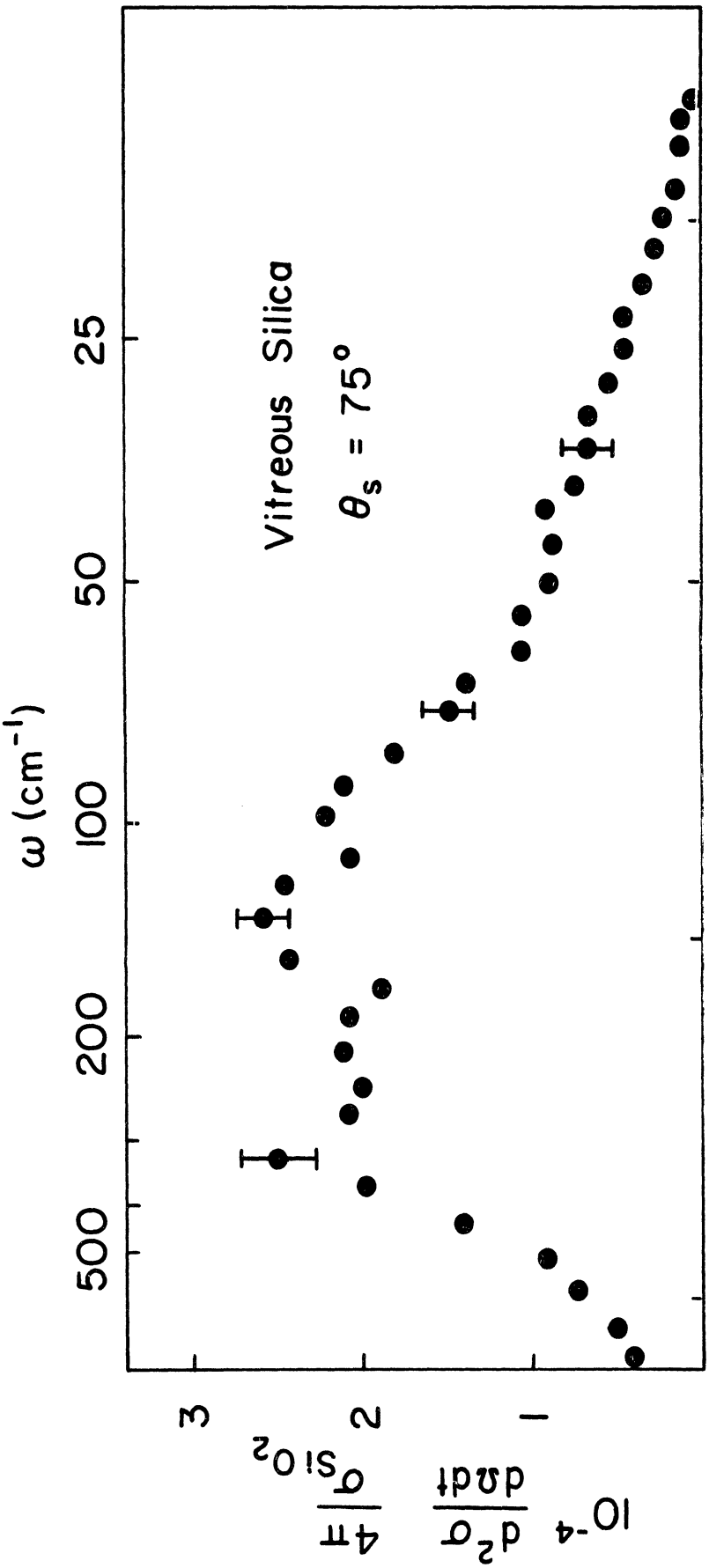

Figure 6. Neutron scattering spectrum of vitreous silica. (From Leadbetter (121).)

completely smeared out in the vitreous silica results where it exists only as an ill-defined shoulder.

Although Leadbetter states that his results are in good agreement with those of Egelstaff, there are a number of discrepancies in the positions of the maxima reported by the two authors. This can be attributed in part to the difficulty of accurately determining the centers of the relatively broad bands of the neutron scattering spectra. However, with better counting statistics it might be possible to determine if there is one band centered at 105 cm^{-1} as reported by Egelstaff, or bands at $\sim$ 85 cm^{-1} and $\sim$ 150 cm^{-1} as reported by Leadbetter, and to resolve the question of the presence or absence of peaks in the low frequency region of the spectra.

1.4.4 INTERPRETATION OF THE VIBRATIONAL SPECTRA OF VITREOUS SILICA

At the outset it can be stated that the problem of interpreting the spectra obtained from the inelastic neutron scattering, Raman, and infrared measurements of vitreous silica remains as yet unsolved. The techniques commonly employed in the analysis of the molecular vibrations of free molecules and the lattice dynamics of crystalline solids are not strictly applicable in this case. The problem of interpreting the dynamics of the disordered glass lattice is of course further complicated by the uncertainty as to the nature of even the short range order in the structure.

As a first step in the interpretation of the observed spectra, one might consider a general classification of the vibrational modes of the polymorphs of SiO_2 suggested by Lippencott, et.al. (106). It is noted that a SiO_2 group in a rigid framework has 3N-3 or six vibrational degrees of freedom. Recognizing the fact that there is some ambiguity as to how the corresponding modes of vibration should be classified in terms of bond stretching, bond bending, and bond distortion types, Lippencott, et. al. somewhat arbitrarily associate a bond stretching and a bond bending mode with each oxygen atom. It is assumed that the O-stretching mode corresponds to the highest observed frequencies in the spectra. Two vibrational modes are assigned to the Si atom, one of which is a stretching mode corresponding approximately to motions of the Si atom between the two O atoms. The

remaining mode is assigned to what is described as a low frequency distortion or Si-O bending mode.

For each SiO_2 group which is added to the first to make up the unit cell, nine vibrational degrees of freedom are added. These nine modes are classified as the following types: because each added SiO_2 group adds four bonds, four of the nine modes correspond to bond stretching frequencies, two involving displacements associated with the O atoms and two for the Si atom. (Using another description, these would correspond to two antisymmetric stretching modes of the type ← Si O→←Si, and two symmetric stretching modes of the type ←Si O Si →.) Two more of the nine modes may be classified as bending motions associated with the bending of the Si-O-Si angle. The remaining three modes are associated with low frequency bending or distortion modes. Table I-10 summarizes this classification of the modes of vibration for various numbers of SiO_2 groups per unit cell. Lippencott, et.al. emphasize that their classification of vibrational modes is only approximate and that in general, a given mode will be a mixture of stretching, bending, and distortion types.

In the case of vitreous silica, one obviously cannot speak in terms of a unit cell comparable to that found in a crystalline lattice. However, the identification of the infrared, Raman, and neutron bands of vitreous silica in a given frequency range with the modes indicated in Table I-10 is justified to some extent by the argument that the

TABLE I-10 Descriptive Classification of the Modes of Vibration of SiO_2 Groups Proposed by Lippincott, et. al. (106)

	SiO_2 groups per unit cell						Spectral region assigned for polymorphs of SiO_2
	1	2	3	4	6	8	
Number of Si-O stretching modes involving motion primarily associated with the oxygen atoms	2	4	6	8	12	16	1200 to 1000 cm^{-1}
Number of stretching modes involving motion primarily associated with the silicon atoms	1	3	5	7	11	15	825 to 600 cm^{-1}
Si-O Bending Modes	2	4	6	8	12	16	600 to 390 cm^{-1}
Distortion Modes	1	4	7	10	16	22	380 to 100 cm^{-1}
Total Modes	6	15	24	33	51	69	

vibrational spectra of glasses are determined largely by the nearest neighbor interactions and thus are essentially similar to the spectra of crystals of the same composition and possessing the same type of short range order.

Since it is generally recognized that the SiO_4 group is the basic structural unit of the disordered glass lattice, several authors (122) (123) have suggested that it would be reasonable to attempt to relate the observed spectra of vitreous silica to the normal frequencies of a free SiO_4 tetrahedron. Support for this argument comes from the fact that tetrahedral SiO_4 groups are the main structure elements in the crystal lattices of silicates and the infrared reflection spectra of all silicates contain two reflection maxima near 1000 cm^{-1} and 500 cm^{-1}. These maxima have been attributed to the two infrared active frequencies of a tetrahedral point group.

The four normal modes of vibration of a free tetrahedral molecule of the type XY_4 are shown in Figure 7. The first mode (Species A_1) is Raman active, producing completely polarized lines, and inactive in the infrared. The second mode (Species E) is also Raman active and infrared inactive. The Raman lines for this mode are depolarized. The other two modes (Species F_2) are both Raman and infrared active. The Raman lines for both modes are depolarized (124).

As noted by Simon (100), the calculation of the normal frequencies of the SiO_4 tetrahedron is not completely

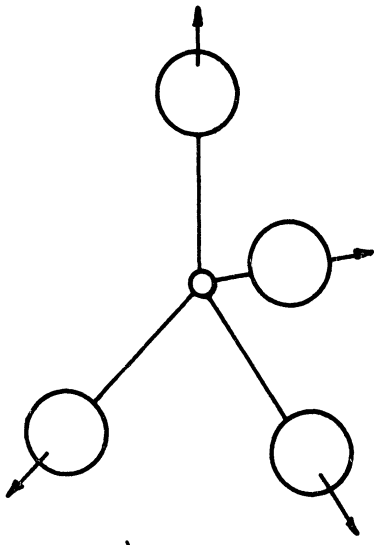

ν_1, TYPE A
SYMMETRIC

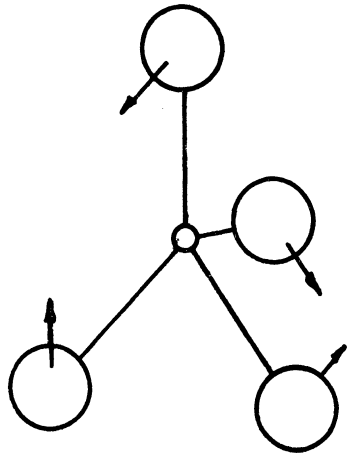

ν_2, TYPE E
DOUBLY DEGENERATE

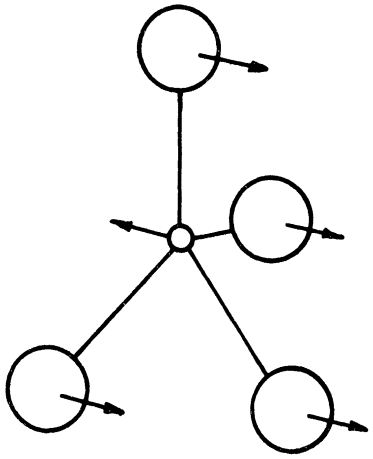

ν_3, TYPE F

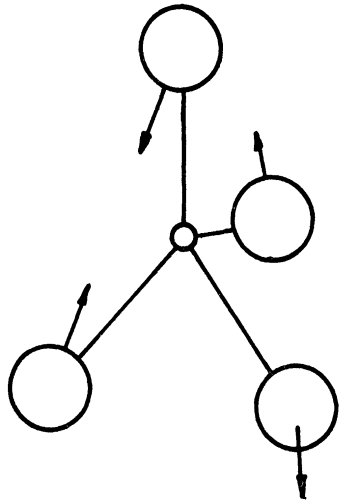

ν_4, TYPE F

BOTH TRIPLY DEGENERATE

Figure 7. The four normal modes of a tetrahedral molecule of the type XY_4 . (From Simon (100).)

straightforward. A detailed analysis by group theoretical methods indicates that there are seven individual force constants to be considered in an XY_4 molecule (125). Those who have calculated the normal frequencies of the free SiO_4 tetrahedron have assumed that a number of these force constants are negligibly small. Matossi (124) has used three force constants in the central force formulas of Dennison and Schaefer (126) to obtain the following frequencies for the SiO_4 tetrahedron: ν_1 = 770 cm^{-1}, ν_2 = 260 cm^{-1}, ν_3 = 924 cm^{-1}, ν_4 = 450 cm^{-1}. Saksena (127) obtains frequencies of ν_1 = 729 cm^{-1}, ν_2 = 473 cm^{-1}, ν_3 = 1031 cm^{-1}, and ν_4 = 493 cm^{-1} through the use of three force constants in the formulas given by Herzberg (128).

The calculated frequencies and the polarizations predicted for the Raman lines of the free tetrahedron agree reasonably well with the stronger features of the consensus experimental infrared and Raman spectra (Tables I-8 and I-9). The relatively strong polarized band observed at 780-830 cm^{-1} in the consensus Raman spectrum might well be associated with the ν_1 mode. Although this mode is supposedly inactive in the infrared, a strong band is observed at 790 cm^{-1} in the experimental infrared spectrum. The predicted ν_2 mode in the Raman spectra would lie in the intense, depolarized continuum observed in the low frequency region of the Raman spectrum. The 1100 cm^{-1} band of the consensus infrared spectrum and the moderately strong depolarized band observed at 1020-1095 cm^{-1} in the Raman spectrum agree well with the

predicted frequencies and polarizations of the ν_3 mode. The 475 cm^{-1} band in the infrared spectrum agrees quite well with the calculated frequencies of the ν_4 mode and the Raman scattering is also quite strong in this region of the frequency spectrum. However, the Raman line for the ν_4 mode of the free SiO_4 tetrahedron is depolarized while Harrand (117) reports that the experimental data in this region is strongly polarized.

Since the SiO_4 tetrahedra in vitreous silica are partially or completely bound to each other by the common oxygen atoms, it is apparent that the foregoing identification of bands of the experimental spectra with the normal frequencies of the free SiO_4 tetrahedron must be considered to be only an extremely crude approximation. The discrepancies between the observed and predicted results confirm this point and indicate the need for a more sophisticated model.

Su, Borrelli, and Miller (129) and Wadia and Balloomal (130) have attempted to simulate the effect of the linkage of the SiO_4 group to the rest of the glass lattice with models in which the tetrahedral unit is bonded to four atoms of infinite weight located at the neighboring silicon sites. In both papers it is assumed that the bond angle is straight (Si-O-Si = 180°) so that the tetrahedral symmetry (T_d) of the free SiO_4 unit is retained. The frequency spectra calculated for this model are of dubious value since the model as described, is hardly an adequate representation of the actual

bonding scheme and completely ignores the effect of the vibrational motions of the lattice. This perhaps explains the fact that the results of both of these calculations are relatively insensitive to the authors' choice of force constants for the model.

As noted previously, the tetrahedral configuration of the oxygen atoms about a central silicon atom is also observed in the lattices of the crystalline silicates. The linkage of the tetrahedra in these lattices occurs in many different forms. Crystals such as enstatite ($MgSiO_3$) and diopside ($CaMg(SiO_3)_2$), for example, form lattices in which the SiO_4 groups share only two corners with other SiO_4 tetrahedra. This interlinkage leads to infinitely extended $(SiO_3)_x$ chains which are held together by Mg^{2+} and Ca^{2+} ions. In other lattices such as those of some clay minerals and micas, the SiO_4 tetrahedra share three of their four corners and form infinitely extending sheets. Connection of SiO_4 groups so as to form rings of tetrahedra occurs in crystals of benitoite ($BaTiSi_3O_9$) and beryl ($Al_2Be_3Si_6O_{18}$). Matossi (124), Saksena (127), and Stepanov and Prima (131), among others, have calculated the vibrational spectra for these different groupings of the SiO_4 tetrahedra.

Since one would expect that the groupings of SiO_4 tetrahedra in the silicate lattices would provide a more realistic approximation of the vitreous silica lattice than the model of a single fixed tetrahedron, it is tempting to

look for correlations between their calculated vibrational spectra and the experimental spectra of vitreous silica. However, there are serious problems in attempting such an analysis. In the three papers cited above, the authors caution that their calculations are of an approximate nature and therefore, not too much importance can be attached to the numerical values which they have obtained for the frequencies of the various vibrational modes. (Even in the simplest case, the free SiO_4 tetrahedron, Saksena's and Matossi's calculations of the frequencies of the normal modes vary by as much as 200 cm^{-1}.) The question as to how the interaction of the various groupings of the tetrahedra with their surroundings is to be taken into account remains unsolved since the abovementioned calculations are for completely isolated systems. Even after this gross simplification of the problem, other assumptions were required for these calculations. In the work of Stepanov and Prima (131), for example, only valence vibrations were considered; this reduces the number of force constants in the calculation to two and in the published part of the work to only one. Furthermore, the lack of long-range order in vitreous silica prevents the symmetry properties of the different molecular groups from manifesting themselves in the optical properties of the bulk solid. Under these circumstances the group theoretical selection rules for the infrared and Raman activity of the various vibrations are no longer strictly valid and it becomes difficult, if not

impossible, to make reliable assignments of the observed frequencies (100).

In recent years there has been an increased interest in adapting the methods employed in the calculation of the vibrational frequency spectra of crystalline lattices to the problem of the disordered glass lattice. Dean (132), Anderson (133), Dyson (134), and Schmidt (135), among others, have considered this problem. The greater portion of this work has been devoted to the study of the physically unrealistic model of a one dimensional chain of harmonic oscillators. However, as Lieb and Mattis (136) have pointed out in their review of this subject, until the one dimensional model is thoroughly understood, it is rather pointless to consider the much more complicated two and three dimensional disordered arrays.

Bell, Bird, and Dean (137) have calculated vibrational frequency spectra for the physical model of the glass structure constructed by Bell and Dean (93). (As noted in Section 1.3.13, this model is based on the random network concept with a mean Si-O-Si bond angle of $\sim 140^{\circ}$.) The spectra calculations were based on a numerical technique originally used by Dean and Bacon (138) in work on the spectra of two component lattices and the assumption that central and non-central forces act between nearest neighbors in the model. Zarzycki and Naudin's (139) estimate of 4.0×10^5 dynes/cm was adopted for the central force constant and the non-central force constant was taken to be

3/17 times the central force constant; this is in close agreement with Saksena's (127) suggested ratio for the force constants in SiO_2.

Two types of boundry conditions were considered in the calculations: the fixed-end condition in which the non-bridging oxygen atoms at the model surface are regarded as fixed, and the free-end condition in which these surface oxygen atoms are free to vibrate. Since the model is finite in size, there are a finite number of degrees of freedom - 1227 when the fixed-end condition is imposed and 1509 with the free-end condition.

The spectrum calculated for the fixed-end boundry condition shows prominent peaks at 410 cm^{-1}, 730 cm^{-1}, and 1040 cm^{-1}. (The three strong bands in the consensus experimental infrared spectrum are observed at 470 cm^{-1}, 795 cm^{-1}, and 1100 cm^{-1}.) From a study of the atomic motions associated with these frequencies, the authors propose the following tentative assignments. The band at 1040 cm^{-1} is associated with a 'bond-stretching' vibration in which the bridging oxygen atoms move in the opposite direction to their Si neighbors and roughly parallel to the Si-Si lines. The peak at 730 cm^{-1} is assigned to a 'bond-bending' vibration in which the oxygen atoms move approximately at right angles to the Si-Si lines and in the Si-O-Si planes; these are the so-called 'Si-stretching' modes described by Lippencott, et.al. (106). The large peak at 410 cm^{-1} in the calculated spectrum is attributed to a 'bond-rocking'

vibration in which the oxygen atoms move roughly perpendicular to the Si-O-Si planes. According to Bell, et.al., the modes in these bands are not localized to just a few atoms, nor, on the other hand, are they typical of the extended wave-like modes which occur in crystalline solids; they appear to be complicated vibrations intermediate between the two extreme types. Furthermore, there is a tendency for the higher frequency modes to be more localized than modes at low frequencies.

The major difference in the spectra derived from the fixed-end and free-end boundry conditions was that a band gap observed between the 730 cm^{-1} and 1040 cm^{-1} peaks of the fixed-end spectrum was replaced by a new and fairly intense band at about 850 cm^{-1} in the frequency spectrum of the free-end model. A study of the atomic displacement eigenvectors for modes in the region of the new band indicated that this band could be attributed to highly localized Si-O stretching vibrations involving the surface, i.e. non-bridging, oxygen atoms. The non-bridging oxygens also give rise to another less marked shoulder at about 330 cm^{-1} in the free-end spectrum.

Bell, et. al. note that if they accept Saksena's (127) suggestion that the central force constant for the non-bridging oxygens is 5.0×10^5 dynes/cm (as opposed to 4.0×10^5 dynes/cm for bridging oxygens) the peak at 850 cm^{-1} should move to a higher frequency, probably around 950 cm^{-1}. Simon and McMahon (Table I-8, ref. (105)) report that they

have observed a band in this region of the infrared spectrum of vitreous silica. In a more recent paper, Simon (140) confirms the presence of a structure sensitive (i.e. its intensity varies from sample to sample of glass) infrared band at about 950 cm^{-1} which he likewise attributes to the presence of non-bridging oxygen atoms. However, there is another possible explanation of this band. Weyl and Marboe (141) report that the observation of this band in the infrared spectra of some samples of vitreous silica has been attributed to the presence of OH^- ions. This band is absent in powdered quartz but can be developed when finely powdered quartz (grain size ~1 micron) is brought into contact with water. Water itself does not have this band.

Bell, et.al. conclude their paper with the following statement: "We must emphasize the point that the frequency spectrum (as computed in our work) is not equivalent to the infrared or Raman spectrum, even for a glass where one does not encounter strict selection rules forbidding optical activity in certain modes. However, one expects each of the main bands in the frequency spectrum to have a counterpart in the infrared or the Raman spectrum, or both." The three most prominent peaks in their calculated spectra do indeed agree quite well with the strong bands observed in both the Raman and infrared spectra. Furthermore, Leadbetter (121) claims that there is excellent agreement between the Bell, et.al. spectra and his inelastic neutron scattering results for frequencies greater than 100 cm^{-1}.

The discussion to this point has dealt with attempts to correlate the experimental data with calculated frequency spectra. The difficulties arising from the lack of an adequate model of the structure, the approximate character of the proposed force systems, and the sensitivity of the calculations to the choice of force constants, indicate the need for supplementary methods of analysis. Vlasov (141) has discussed the problem of interpreting the experimental spectra and has come to the conclusion that at the present time the only promising direction for studies of the characteristic vibrations of the glass lattice lies in the comparison of the experimental glass spectra with the measured spectra of the crystalline silicas. An analysis of this nature is , of course, attractive to proponents of the modern crystallite theory of the structure.

(Before discussing the crystalline data, a brief word is required about the notation used to identify the high- and low-temperature modifications of the various crystalline forms of silica. In the literature it is a common practice to give the designation α to the low-temperature modification and β to the high-temperature modification.)

A major problem in attempting to find correlations in the various spectra of vitreous silica and the crystalline polymorphs is that there is neither sufficient quantity or quality of data for the crystalline silicas. Only in the case of α-quartz are the Raman, infrared, and inelastic neutron scattering spectra relatively well established.

The Raman and neutron scattering spectra of α-cristobalite have each been measured once. Neither of these measurements have been performed for α-tridymite.

A comparison of the Raman data for α-quartz and the consensus Raman spectra of vitreous silica is presented in Table I-11. Although there are some similarities, there are also a number of obvious discrepancies. The major difference appears to be in the low frequency end of the spectra: the lowest frequency line in the α-quartz spectrum is observed at 128 cm^{-1} while the intense continuum in the glass spectrum extends down almost to the exciting line of the source.

Harrand (146) is the only author who has reported a measurement of the Raman spectrum of α-cristobalite. She notes that she had great difficulty in obtaining any scattering of useful intensity but did observe a moderately sharp line at 470 cm^{-1} and weak bands at 100 cm^{-1} and 150 - 200 cm^{-1}. Since α-cristobalite is usually opaque (147), it is surprising that such a measurement was possible.

The results of numerous measurements of the infrared spectrum of α-quartz are compiled in Table I-12. It is interesting to note that in some instances the vitreous silica measurements appear to be more precise than the α-quartz measurements. For example, in Section 1.4.2 it was observed that the reports of the position of the band in the 475 cm^{-1} region of the glass spectrum differ by only 10 cm^{-1}; the reported positions of the corresponding band in in the α-quartz data vary by as much as 26 cm^{-1}. A likely

TABLE I-11. Comparison of the Raman Spectra of α- Quartz and Vitreous Silica

α- Quartz					Vitreous Silica
Krishnan (142)	Saksena (143)	Scott & Porto (144)	Shapiro (145)	Consensus	
					10 ↓
128	128	128	128	128 (s)	
		145	147	146 (vw)	
207	207	207	207	207 (s)	
266	267	265	264	265 (ms)	
356	358	356	355	356 (m)	
394	391	394	394	394 (m)	
403	403	401	403	403 (m)	
	452	450	452	451 (m)	
466	466	464	466	466 (vs)	
	505	509	508	508 (m)	550 (vs)
					595-620 (w)
695	695	697	698	697 (w)	685 (w)
796	795	795	798	796 (w)	780
809	806	807	811	808 (m)	↓
					830 (s)
					↓
					850 (m)
					915 (vw)
1063	1063	1072	1067	1066 (w)	1020
1082	1082	1085	1081	1082 (vw)	↓ 1095 (ms)
1160	1160	1162	1161	1161 (w)	1150
1227	1228	1235	1233	1233 (vw)	↓ 1240 (w)

Key: s- strong, m- moderate, w- weak, v- very

TABLE I-12. Comparison of the Infrared Spectra of α- Quartz and Vitreous Silica

α- Quartz (cm^{-1})								Vitreous Silica (cm^{-1})
Plendl & Mansur (111)	Spitzer & Kleinman (148)	Simon & McMahon (105)	Lippincott (106)	Reitzel (108)	Saksena (143)	Florinskaya Pechenkina (110)	Consensus	
129			128		128		128 (w)	
266			265		264		265 (w)	
			374		364		369 (m)	
385	394		397		384		390 (m)	
476	450		462-475	455	476		465 (vs)	475 (s)
			513	500-550	508		515 (s)	
690	697	695	696		695		695 (w)	
		780	780		775	778	778 (m)	
	797	795			787	797	795 (s)	795 (m)
800		802	801		812		801 (s)	
1111	1072	1065	1097		1047	1093	1081 (vs)	1100 (vs)
	1163	1162	1150-1176		1176		1165 (m)	1200 (ms)
	1227	1230			1235		1230 (w)	

Key: vs- very strong, s- strong, ms- moderately strong, m- moderate, w- weak

explanation of this lack of precision in the quartz data is that unlike cristobalite, tridymite, and vitreous silica, the scattering of light by quartz is not isotropic. While quartz may be considered as fairly isotropic far enough from strong dispersion bands, this is not the case within the bands. According to Simon and McMahon (105), strong dichroisim is usually observed within the bands and the methods commonly used to analyses the data fail to yield consistent results near the band centers.

From Table I-12 one can see that the prominent bands of the consensus infrared spectrum of the vitreous silica match up quite well with intense bands in the α-quartz data. However, the correlations are no worse for the much less often measured spectra of α-cristobalite and α-tridymite. (See Tables I-13 and I-14.) A brief review of some of the papers cited in Tables I-12, I-13, and I-14 indicates that there are indeed many different opinions as to which of the spectra of the crystalline silicas more nearly resembles that of vitreous silica.

Simon and McMahon (105) studied the 700 to 1400 cm^{-1} region of the infrared spectra of α-quartz, α-cristobalite, and vitreous silica. In one measurement the samples were held at a temperature of 80°K in order to minimize the line broadening effect of thermal motions. Comparing the widths of the strongest band in the spectra of the three samples (1055 cm^{-1} in α-quartz, 1085 cm^{-1} in α-cristobalite, and 1100 cm^{-1} in vitreous silica), it was noted that the widths

TABLE I-13. Comparison of the Infrared Spectra of ∝- Cristobalite and Vitreous Silica

∝ - Cristobalite (cm^{-1})						Vitreous Silica (cm^{-1})
Florinskaya Pechenkina (110)	Reitzel (108)	Lippincott (106)	Simon & McMahon (105)	Plendl & Mansur (111)	Consensus	
				143		
				298		
				383		
	493	485		488	488 (s)	475 (s)
		515				
		620		617	618 (w)	
793		798	800	800	798 (ms)	795 (m)
1105		1104	1085	1070	1095 (s)	1100 (vs)
		1160				
		1204	1192	1219	1205 (ms)	1200 (ms)

Key: vs- very strong, s- strong, ms- moderately strong, m- moderate, w- weak

TABLE I-14. Comparison of the Infrared Spectra of ∝- Tridymite and Vitreous Silica

∝ - Tridymite (cm^{-1})				Vitreous Silica (cm^{-1})
Florinskaya Pechenkina (110)	Lippincott (106)	Plendl & Mansur (111)	Consensus	
		143		
		298		
		315		
	478	488	483 (s)	475 (s)
	508			
		617		
787	792	800	793 (m)	795 (m)
1105	1109	1070	1105 (s)	1100 (vs)
	1175	1219	1197 (ms)	1200 (ms)

Key: vs- very strong, s- strong, ms- moderately strong, m- moderate

of the quartz and cristobalite bands were identical, while the width of the vitreous silica band was only slightly greater (27 cm^{-1} as compared with 22 cm^{-1}). The fact that the width of the band for the glass sample was only 5 cm^{-1} greater than those for the crystalline samples was interpreted as an indication that the motion giving rise to this band must be associated with a feature of the silica structures which persists even in the absence of long range order. Simon and McMahon identified the motion as a valence streching mode ($\leftarrow$ Si O$\rightarrow\leftarrow$Si) of neighboring Si-O ions. Furthermore, they claimed that the spectrum of vitreous silica corresponds more nearly to that of α-cristobalite than α-quartz.

Lippencott, et.al. (106) have measured the infrared spectra of α-quartz, α-tridymite, α-cristobalite, coesite, and vitreous silica. They conclude that the infrared spectrum of vitreous silica resembles that of tridymite in that each has the same number of observed frequencies.

Florinskaya and Pechenkina (110), like Simon and McMahon (105), have investigated the 700 to 1400 cm^{-1} region of the silica spectra. Their experiment, however, included a measurement of the α-tridymite spectrum in addition to the α-quartz, α-cristobalite, and vitreous silica spectra. They report that the bands of the glass spectrum coincide with the bands of the quartz spectrum. This result is attributed to the presence of quartz crystallites in the glass structure and it is suggested that the crystallites

are probably larger than the sizes estimated from x-ray data.

Both Egelstaff (120) and Leadbetter (121) report that there is little similarity in the neutron scattering spectra which they have measured for vitreous silica and α-quartz. The differences in the spectra are most apparent in the low frequency region ($\omega < 50$ cm^{-1}). Leadbetter's claim of excellent agreement between the neutron scattering spectra of α-cristobalite and vitreous silica for $\omega > 50$ cm^{-1} was noted in Section 1.4.3.

In the foregoing discussion there is no mention of spectra measurements for the high-temperature modifications of the crystalline silicas. Since these are the crystalline forms existing at the temperatures at which glass solidifies, this data is potentially of great interest. Unfortunately, because of the difficulty of these measurements, very little high temperature data has been reported. Some of the more recent work includes studies of the Raman spectrum of β-quartz by Scott and Porto (144) and Shapiro (145), and measurements of the high frequency region (700 to 1400 cm^{-1}) of the infrared spectra of β-quartz and β-cristobalite by Simon and McMahon (105). Unfortunately, the bands which are observed in these spectra are so broadened by the thermal motions of the crystal lattices that they are of little practical value for comparisons with other spectra.

1.5 THE ANOMALOUS LOW TEMPERATURE HEAT CAPACITY OF VITREOUS SILICA

The inelastic neutron scattering data appearing in this work provides new information about the low frequency region of the vibrational spectrum of glass. In the concluding pages of this introduction, several physical properties of vitreous silica which are directly related to the low frequency motions will be examined. The acoustic and dielectric attenuations in glass and its low temperature heat capacity are of special interest because they differ quite markedly from the corresponding properties of at least one of the crystalline silicas, low-quartz. Of course, one hopes that an examination of these properties will provide added insights into the nature of the glass structure and the factors which differentiate the crystalline and vitreous state.

The thermodynamic properties of a solid, as is well known, are determined by the characteristic vibrations of its atoms. The problem of computing the complete vibrational spectrum of a solid from its microscopic force constants is quite difficult and has been attempted only for crystalline forms; however, important simplifications occur in the low temperature limit.

At low temperatures, only the lowest frequency vibrational modes of a solid are excited. Because of the periodic symmetry of its lattice, the normal modes of a

crystal may be represented as traveling plane waves characterized by a wavevector $\bar{q}_i$ and a frequency ω_i. At very low frequencies where the wavelength $2\pi/q$ is large compared with the interatomic spacing, the vibrational behavior of the crystal lattice is similar to that of an elastic continuum; the phase velocity ω/q and the group velocity, $d\omega/dq$, of the lattice waves are identical and equal to the velocity of sound. The properties of these waves can therefore be computed from the bulk properties of the crystal, i.e. from the macroscopic elastic constants, without regard for the detailed atomic forces.

A glass has no long range order and hence no periodic symmetry. Although its atomic vibrations may still be resolved (in the harmonic approximation) into normal modes, these will, in general, no longer be plane waves. However, in the long wavelength limit, where the detailed atomic structure in a small region is unimportant, the glass will also behave as an elastic continuum and the properties of the "elastic" or "acoustic" waves in the glass can also be determined from the measurements of its macroscopic elastic constants (149) (150). If these "elastic" modes are the only low frequency vibrations in the glass, one can compute the low temperature heat capacity directly from its macroscopic elastic constants.

It can be shown (151) that the low frequency vibrational spectrum of an insulator has the form:

I-5 $G(\omega) = \alpha\omega^2 + \beta\omega^4 + \gamma\omega^6 + \ldots$

According to Debye (152), the first term of the above expression represents the frequency distribution of an elastic continuum; the higher order terms arise from dispersion of the lattice waves.

In the quasi-harmonic approximation (151) (153), the constant volume heat capacity of a solid at temperature T is

I-6 $$C_v(T) = k_B \int_0^{\omega_{max}} G(\omega) \frac{(\hbar\omega/k_BT)^2 \exp(-\hbar\omega/k_BT)}{(\exp(-\hbar\omega/k_BT) - 1)^2} d\omega$$

The frequency distribution given in Equation I-5 would therefore give rise to a heat capacity of the form

I-7 $C_v(T) = aT^3 + bT^5 + cT^7 + \ldots$

The heat capacity is also often expressed in terms of a Debye temperature $\theta(T)$. The Debye temperature is defined as the cut-off $(\hbar\omega_{max}/k_B)$ of the Debye distribution, $G(\omega) = \alpha\omega^2$, which would give the experimental heat capacity at the specified sample temperature T.

The limiting value of the Debye temperature at 0° K is defined to be

I-8 $$\theta_o = (12 N k_B \pi^4 / 5 a)^{1/3}$$

where N is the total number of atoms in the sample (154). The parameter a in the above expression is obtained from the experimental heat capacity data by plotting $C_v(T)/T^3$ versus T^2 and extrapolating the resulting curve to $T^2 = 0$.

The Debye temperature may also be defined in terms of the macroscopic elastic properties of the sample:

$$\text{I-9} \qquad \theta(\text{elastic}) = \frac{\hbar}{k_B}\left[\frac{3N}{4\pi V}\right]^{1/3} v_m$$

where v_m is the mean velocity of sound obtained by averaging the elastic constants in all directions of the sample and V is the volume of the sample (149). The parameter a, defined in terms of the elastic data, is then

$$\text{I-10} \qquad a = (16/5)\pi^5 (k_B/\hbar^3) V v_m^{-3}$$

If the only low frequency vibrations in the sample (crystalline or noncrystalline) are the harmonic, long wavelength acoustic lattice vibrations, then the Debye temperature computed from the elastic constants, θ(elastic), should be equal to the Debye temperature obtained from the calorimetric measurement, θ_o, within the experimental error. (Anderson (155) has shown that the comparison of θ_o and θ(elastic) is independent of any assumptions regarding the size of the vibrating unit.)

The low temperature heat capacity of vitreous silica has been measured by Flubacher, Leadbetter, Morrison, and Stoicheff (119) for a sample annealed at 1100°C and by

Westrum (156) for samples annealed at 1070°C and 1300°C. The results of Flubacher's glass measurements and Westrum's data for quartz and cristobalite are shown in Figure 8.

Anderson (155) extrapolated the vitreous silica and quartz data to $T^2 = 0$ and found that

$$\theta_o = 395^\circ \text{ K for vitreous silica}$$

and

$$\theta_o = 620^\circ \text{ K for quartz}$$

From a calculation based on the elastic constant data of Koga (157), Anderson estimated that

$$\theta(\text{elastic}) = 600^\circ \text{ K for quartz}$$

whereas the low temperature elastic constant data of McSkimin (158) indicated that

$$\theta(\text{elastic}) = 495^\circ \text{ K for vitreous silica}$$

The agreement between the two θ's for quartz is satisfactory while the θ_o for vitreous silica appears to be less than $\theta(\text{elastic})$ by about 20%. According to Anderson and Dienes (159), if the non-acoustic contribution to the heat capacity of vitreous silica is estimated by subtracting a Debye function from Westrum's data, over half the heat capacity up to 35° K arises from non-acoustic vibrations.

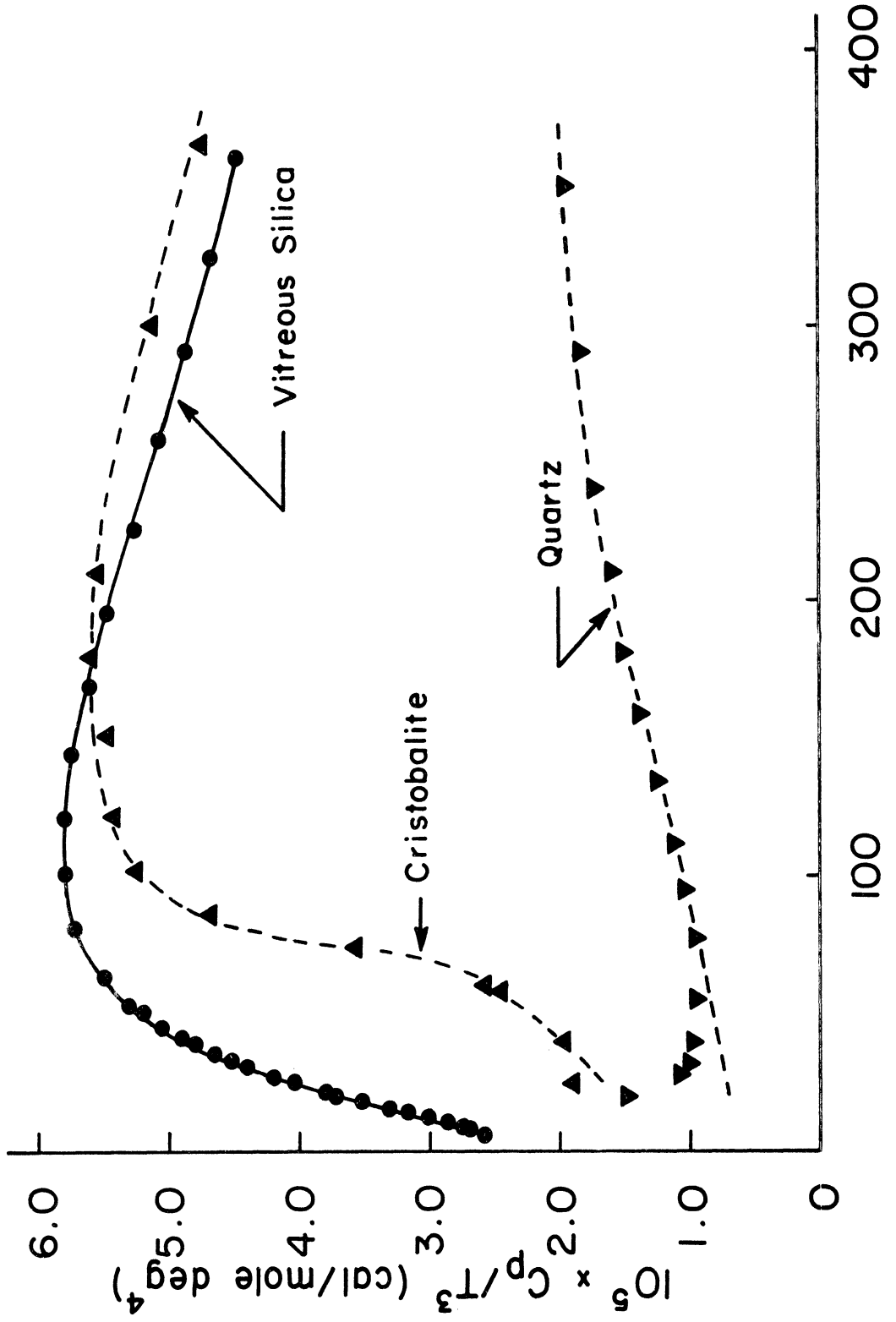

Figure 8. C_p/T^3 as a function of T^2 for vitreous silica, cristobalite, and quartz. (From Leadbetter and Morrison (168).)

There appears to be no question that the discrepancy in the vitreous silica θ's is not the result of experimental errors. The elastic wave velocities obtained by McSkimin have been confirmed by Fine (160) and Flubacher, et.al. (119). McSkimin's and Fine's data were obtained from ultrasonic measurements while the results of Flubacher, et.al. were determined from measurements of the Brillouin spectra of vitreous silica. The calorimetric measurements of Flubacher, et.al. and Westrum extend down to temperatures of 2.3° K and 5° K respectively. Flubacher, et.al. estimate an accuracy of ± 2 per cent at the lowest temperatures of their measurements. The data is consistent with more recent measurements of the heat capacity of vitreous silica which extend down to 1.3° K and indicate that at these very low temperatures C/T^3 is actually increasing with decreasing temperature (161).

The source of the excess heat capacity is a matter of considerable speculation. Rosenstock (150), for instance, suggests that it is reasonable to expect "extra" low frequency vibrations in a noncrystalline solid: "Cavities in the structure are likely to occur in the disordered lattice, and such cavities may possibly contain one atom weakly bound to only one of the other atoms. Such a weakly bound atom will vibrate with low frequency and thus contribute strongly to the specific heat at low temperatures; but it will in no way affect the motion of the rest of the lattice. The vibration is strictly a local

one and will therefore not show up in any measurement of elastic waves." Anderson and Dienes (159) suggest that the explanation lies in the presence of a low frequency optical branch or a highly disperse acoustic mode. Flubacher, Leadbetter, Morrison and Stoicheff (119) have supported the theory that the excess arises from low frequency optical modes. Their observation of the low frequency continuum in the Raman spectrum of vitreous silica is cited in support of this interpretation. However, Leadbetter (121) has more recently suggested that the excess heat capacity is produced by a very highly disperse acoustic mode. This conclusion is based on the results of his neutron scattering study (Section 1.4.3).

As yet, no one has attempted to obtain the low frequency vibrational spectrum of vitreous silica by inversion of the heat capacity data. On the other hand, there have been a number of attempts to reproduce the heat capacity data with calculations based on specific models of the structure and vibrational properties of the glass lattice.

Smyth, Skogan, and Harsell (162) have calculated the heat capacity from a model in which it is assumed that the atoms in vitreous silica can be regarded as independent harmonic oscillators. The heat capacity is represented as the sum of three Einstein functions:

$$\text{I-11}\quad C_v(T) = R\left[3E(\hbar\omega_{Si}/k_BT) + 4E(\hbar\omega_T/k_BT) + 2E(\hbar\omega_L/k_BT)\right]$$

$$\text{where}\quad E(\hbar\omega/k_BT) = \frac{(\hbar\omega/k_BT)^2 \exp(\hbar\omega/k_BT)}{(\exp(\hbar\omega/k_BT) - 1)^2}$$

Smyth, et.al. assume that the silicon atom is in a fairly symmetric field and therefore assign the same frequency, ω_{Si}, to each of its three possible modes of vibration. Each oxygen atom is assumed to lie at midpoint of a line joining two silicon atoms and is assigned two equal transverse frequencies, ω_T, and one longitudinal frequency ω_L. The oxygen ion finds itself in a very unsymmetrical field because vibrations along the Si-O bond encounter the strong field of the silicon, while vibrations transverse to the Si-O bond encounter little if any, repulsive force. Consequently, the restoring force of this mode of vibration is low, leading to a small frequency. Smyth, et.al. conclude that the transverse mode of the oxygen ion accounts for most of the low temperature specific heat.

Dank and Barber (163) have fitted the specific heat data between 5° K and 30° K with a function similar to those derived theoretically (164) (165) for layer-like solids such as graphite:

$$\text{I-12}\quad C_v(T) = \frac{C_2(\theta_2/T) - y^2 C_2(\theta_3/T) + y^3 C_3(\theta_3/T)}{1 - y^2 + y^3}$$

where $C_2(\theta_n/T) = 6\ R\ (T/\theta_n)^2 \int_0^{\theta_n/T} \frac{x^3 \exp(x)}{(\exp(x) - 1)^2}\, dx$

$$\theta_n = (\hbar\omega_n/k_B);\ x = (\hbar\omega/k_BT);\ y = (\theta_3/\theta_2) = \omega_3/\omega_2$$

The functions in Equation I-12 are described as follows: "the function $C_2(\theta_n/T)$ represents the heat capacities of idealized two-dimensional continua, while $C_3(\theta_n/T)$ is the well-known Debye function. The characteristic temperature θ_2 is assumed to correspond to the maximum ω_2, of a class of frequencies consisting of translations normal to the "layer" and rotational oscillation about axes in the "layer", while θ_3 is assumed to correspond to a maximum, ω_3, in a class of relatively low frequencies which because of interactions between "layers" in real laminar solids, are characteristic of isotropic solids." From their analysis, Dank and Barber conclude that (a) the best fit of the experimental heat capacity data is obtained by assuming that the smallest group of atoms which vibrate as a unit is Si_3O_6 and, (b) at low temperatures, the structure of vitreous silica is highly anisotropic.

Flubacher, et.al. (119) fit their specific heat data in the range between 2^oK and 15^oK with the expression

$$\text{I-13}\quad C_v(T) = 1.155 \times 10^{-5}T^3 + 1.5 \times 10^{-8}T^5 + 1 \times 10^{-10}T^7 + 1.36 \times 10^{-3}\, E(13/T) + 3.51 \times 10^{-2}\, E(32/T) + 2.62 \times 10^{-1}\, E(58/T)\ \text{cal./mole degree K}$$

This expression has the form of Equation I-7 with the

addition of three Einstein terms. As indicated, the characteristic temperatures, $\frac{\hbar\omega}{k_B}$, of the Einstein terms are $13^{\circ}K$, $32^{\circ}K$, and $58^{\circ}K$ and represent 0.008, 0.2, and 1.4% of the total number of vibrational modes in the sample. The idea of using a combination of Debye and Einstein spectra to fit experimental heat capacity data was previously introduced by Nernst (165). His viewpoint is that the Einstein terms represent the contribution from the optical branches of spectra for polyatomic crystals.

The value of the heat capacity calculations and the conclusions which are drawn from them is questionable. In each of the three papers cited above, the calculated heat capacity agrees quite well with the experimental data. This apparent insensitivity to the choice of model indicates that the heat capacity data alone cannot provide the detailed shape of the low frequency spectrum of glass.

The question arises as to whether the anomalous or excess heat capacity is characteristic of the vitreous state. On the basis of a study of the low temperature heat capacities of a number of crystalline and vitreous substances, Leadbetter (149) has concluded that: " at low frequencies there are no appreciable differences in the frequency distributions of crystals and glasses which are attributable simply to the lack of periodicity characteristic of all glasses." Evidence that the excess heat capacity need not occur as a direct result of a disordered structure is provided by the fact that the value

of θ(elastic) calculated from the measured elastic wave velocities of vitreous germania agrees quite well with the value of θ_o derived from the T = 0 intercept of its measured heat capacity (167).

The fact that the low temperature heat capacity of cristobalite appears to be more nearly like that of vitreous silica than that of quartz (Figure 8) is also suggestive. The question of comparing the values of θ_o and θ(elastic) for cristobalite is not resolved since the elastic constants of cristobalite have not been measured. Although this problem is usually circumvented by arguing that the elastic properties of cristobalite and vitreous silica should be quite similar since their densities differ by only $\sim 5\%$, there are also disagreements concerning the interpretation of the thermal data. According to Anderson (155), the values of θ_o for vitreous silica and cristobalite are close. (This comparison is based on Westrum's data.) He argues that in order for the anomaly to be absent in cristobalite, its elastic constants would have to be about 30% less in magnitude than those of vitreous silica. On the other hand, Leadbetter and Morrison (168) suggest that Anderson has misread Westrum's data; they assert that it is very likely that the elastic and extrapolated thermal results for cristobalite will agree in the low temperature limit.

1.6 THE ACOUSTIC AND DIELECTRIC LOSSES IN VITREOUS SILICA

Acoustic measurements by a number of observers (169)(170)(171)(172) indicate that there is a large internal friction effect in vitreous silica at low temperatures (30° to 50°K) and high frequencies (60 kc to 20 mc per second). The term 'internal friction' includes all phenomena which lead to an irreversible generation of heat from mechanical energy. Although there are several possible sources of internal friction in glasses (e.g. thermoelastic effects, viscous flow, phase transformations, static (or elastic) hysteresis) the temperature and frequency behavior of the data strongly suggests a structural relaxation (172).

Structural relaxation at low temperatures and high frequencies should be indicated by effects other than the internal friction; in particular, a dielectric loss should occur at roughly the same frequency and temperature as the observed acoustic loss. Stevels (173) has measured a dielectric absorption peak for a silicate glass which is in the kilocycle-to-megacycle frequency range and which appears to have a maximum near 60°K. Furthermore, in this experiment the evidence for a shift of the peak to higher temperatures for higher frequencies (as one would expect for a structural relaxation) is quite marked.

Corresponding losses, both acoustic (174) and dielectric (175), have been observed in quartz. However, these effects are generally attributed to the presence of lattice defects and impurities in the quartz samples. By way of comparison,

the acoustic losses in vitreous silica are about three orders of magnitude larger than in natural quartz (159).

The dielectric and acoustic losses in vitreous silica are characterized by the following features:

(a) The loss curves for vitreous silica are quite broad, requiring a wide distribution of relaxation times. Anderson and Bommel (172) have demonstrated that a distribution of six activation energies, each of which is associated with a relaxation, could account for the shapes of their experimental loss curves. On the other hand, the losses in quartz are relatively sharp, and they approximate a single relaxation mechanism. The heights and widths of the internal friction peaks show that a great deal more heat is generated from the lattice waves in the non-crystalline phase than in the crystalline phase. (See Table I-15).

(b) It can be shown that the angular relaxation frequency ω_0 satisfies the expression $\omega_0 = \omega_{max} \exp(-q/k_B T_m)$ where ω_{max} is the Debye frequency calculated from the elastic constants, q is the activation energy, and T_m is the temperature at which the loss is a maximum for a given frequency ω_0. According to Dienes and Anderson (159), the fact that the pre-exponential factor is equal to the Debye frequency indicates that there is essentially no entropy of activation; consequently, the relaxation proceeds with no reorganization of the structure surrounding the relaxing species.

(c) The activation energy, q , is very small in comparison with the energy required for relaxation processes associated with the diffusion of ions in silica, or for a molecular rotation (such as, for example, the SiO_4 tetrahedron). Values of q and the internal friction, Q^{-1}, are listed in Table I-15 (159).

TABLE I-15 Experimental Parameters for the Dielectric and Acoustic Losses in Vitreous Silica

Sample	q (cal/mole)	Max Q^{-1}
Vitreous Silica	1030 (acoustic)	2×10^{-3}
Vitreous Silica	1320 (dielectric)	1×10^{-4}
Quartz	1600 (acoustic)	2×10^{-6}
Quartz	1900 (dielectric)	2×10^{-5}

The values listed above are intended only to show the order of magnitude. The maximum value of the internal friction depends to some extent on the sample and the frequency. In the case of vitreous silica, the value of q represents the most probable value of the activation energy for the relatively broad distribution.

(d) Although the acoustic loss results from the propagation of both longitudinal and transverse (or shear) waves, a comparison of McSkimin's data for the longitudinal waves and the data of Fine and Anderson and Bommel for the shear waves, indicates that most of the loss is traceable to the shear waves, i.e. the loss is most probably associated with a transverse vibration.

(e) Accompanying the acoustic loss is a 2% relaxation of the shear modulus. The small change in modulus indicates that only a small fraction of the relaxation species are relaxing at any one time.

Anderson and Bommel (172), who are responsible for collecting much of the information cited above, have proposed a model in which the lateral motion of the oxygen atom perpendicular to the Si-O-Si bond is responsible for the internal friction. The mean Si-O-Si bond angle is assumed to be 180° and the argument proceeds as follows: "The gradual change from the close range ordered structure to distant disordered structure is a result of the small variation in bond angles. A kinked Si-O-Si bond angle corresponds to the oxygen atom in a higher than average energy state. For every kinked bond there is, however, another almost equivalent state which is the mirror image of the kinked bond. If the oxygen is to pass from one state to the mirror image, the two adjacent silicons must be pushed apart. Thermal energy can make the oxygen atom take up these equivalent positions alternately. A shear ultrasonic wave can bias one of the energy states with respect to the other, thus altering the time in each state. The time lag for equilibrium to be reached is the source of the relaxation."

"Such vibrations of the oxygen atom would exert a strong dipole moment since the motion Si-O-Si is a transverse optical vibration. This vibration would require virtually no reorganization of the structure thus satisfying the

condition of zero entropy of activation. The number of bent bonds would determine the magnitude of the loss and the value of the relaxation strength. The spread of relaxation times would depend upon the variability of the bond angle."

Mason (176) has suggested the following simple calculation to show that the activation energy, which he claims is mainly the energy required to push the two silicon atoms apart as the oxygen goes from one position to the other, is consistent with the measured values. There are about 2.2×10^{22} molecules per cubic centimeter, and twice as many Si-O bonds. The expansion caused by a bond angle flexing from an angle of $(\pi - \phi)$ to π (in radians) is

$$\text{I-14} \qquad \delta l/l = (1 - \cos\phi) \approx \phi^2/2$$

The energy is approximately the expansion multiplied by Young's modulus, or

$$\text{I-15} \qquad q = \frac{E\,N\,(\delta l/l)}{J\,(4.4 \times 10^{22})} = 2.05 \times 10^{5}\,\phi^2 \text{ cal/mole}$$

where E is Young's modulus (7.80×10^{11}), N is Avogadro's number (0.603×10^{24}), and J is the conversion factor between ergs and calories (4.18×10^{7}). The estimated activation energies which he obtains for various angles are listed in Table I-16.

TABLE I-16 Energy Required to Flex a Si-O-Si Bond

(degrees)	1°	2°	3°	4°	5°	6°
q (cal/mole)	62.5	250	562	1000	1560	2240

One can see that a change in bond angle of the order of 4^{o} to 5^{o} would be consistent with the measured activation energies.

Strakna (177) has suggested a model in which the relaxation loss is attributed to the motion of oxygen atoms in elongated Si-O-Si bonds. In this model the oxygen atoms have two equivalent stable positions which are alternately occupied due to thermal activation. The ultrasonic signal biases one of these positions with respect to the other and changes the relative population of these sites. When the time of readjustment to the equilibrium distribution is comparable to the period of the biasing ultrasonic signal, energy is returned to it out of phase, resulting in a decrease of amplitude. The relaxation time associated with this loss mechanism is dependent upon the height of the energy barrier between the alternate oxygen positions. Strakna calculates the barrier energy as a function of Si-Si separation by assuming that the interaction energy of the bridging oxygen atom within the two silicon atoms can be approximated by the sum of two Morse potentials. He estimates that an exceptionally large proportion (20 to 30%) of the total number of Si-O-Si bonds in vitreous silica are anomalous (elongated).

A number of authors have attempted to associate the observed ultrasonic absorption phenomena with the excess heat capacity. Mason (176) and Leadbetter and Morrison (168) suggest that the motion of the oxygen atom proposed by

Anderson and Bommel (172) might well account for both effects.

Clark and Strakna (178) have calculated the excess specific heat on the basis of the elongated Si-O-Si bond model. Solution of the one-dimensional Schroedinger equation for the vibrational motion of the oxygen atom in this bond leads to a system of split energy levels. Using the Si-Si bond lengths obtained in Strakna's ultrasonic study, the excess specific heat contribution of the extended bonds due to the spacing between the two lowest energy levels was calculated. It was assumed that for each elongated Si-Si bond distance, R_i' , the excess specific heat per mole was:

$$\text{III-16} \qquad C_i(T) = \frac{R_m \left(\Delta E_i/R_m T\right)^2 \exp\left(\Delta E_i/R_m T\right)}{\left(1 + \exp\left(\Delta E_i/R_m T\right)\right)^2}$$

where R_m is the gas constant per mole and ΔE_i is the energy difference between the two lowest energy levels for bond lengths with spacing R_i'. The total excess specific heat is then simply $C(T) = (1/N) \sum_i N_i C_i(T)$ where N_i is the relative number of Si-Si bonds with spacings between R_i' and R_{i+1}', and $N = \sum_i N_i$. Clark and Strakna conclude that 10-20% of all of the Si-O-Si bonds in vitreous silica must be elongated in order to fit the heat capacity data with this model.

It should be noted that the agreement between the heat capacity data and Clark and Strakna's calculation is not very good. While it is possible that the excess heat capacity might be fitted satisfactorily with this model, it appears that the required distribution of elongated bonds must differ markedly from the distribution derived from the

ultrasonic attenuation data.

There is other evidence which suggests that the ultrasonic attenuation and the excess heat capacity are unrelated. Primak (179) has studied the changes in the properties of vitreous silica irradiated in intense fast neutron beams. Irradiation of a vitreous silica sample reduced its excess heat capacity by about 50% while the ultrasonic attenuation was reduced by about 85%. This result suggests that the ultrasonic attenuation and the excess heat capacity depend on somewhat different features of the glass structure. It should also be noted that even though the low temperature acoustic absorption is observed in Pyrex glass, there is no excess heat capacity (149).

The measurements of the acoustic and dielectric losses and the low temperature heat capacity have provided strong evidence of unusual low frequency atomic motions in vitreous silica. They have, in fact, provided valuable insights into the nature of these anomalies. However, in the final analysis, the development of convincing models and/or explanations of these phenomena requires more precise knowledge of the microscopic properties of vitreous silica - information such as that which can be obtained from diffraction and spectra measurements. This is not to imply that the neutron scattering results will provide all of the answers to the many questions raised in the preceding pages. They should, however, fill some serious gaps in our present knowledge of the structure and atomic motions of glass.

CHAPTER II

2.1 INTRODUCTION

The relationship between the structure and dynamics of an atomic system and its neutron scattering cross sections will be discussed in this chapter. For detailed derivations of the cross section formulae which are presented here the reader is referred to the texts of authors such as Lomer and Low (180), Turchin (181), and Summerfield, Carpenter, and Lurie (182).

In the neutron scattering experiment we assume that a neutron with wave vector $\underline{k}_o$ impinges on the target system, scatters through an angle ϕ, and leaves the target with wave vector $\underline{k}$. In this interaction of the neutron and the scattering system there is a momentum transfer of

$$\text{II-1} \qquad \hbar\underline{K} = \hbar(\underline{k}_o - \underline{k})$$

and an energy transfer of

$$\text{II-2} \qquad \hbar\omega = \frac{\hbar^2}{2m_n}(k_o^2 - k^2)$$

The scalar momentum transfer is related to the angle of scattering by the equation

$$\text{II-3} \qquad \hbar^2 K^2 = \hbar^2(k_o^2 + k^2 - 2k_o k \cos\phi)$$

Fermi (183) has shown that if one introduces a special potential to represent the interaction between a neutron and the target nuclei, the probability of the scattering of thermal energy neutrons by a system of bound nuclei can be

calculated by means of the first Born approximation. Since the range of the nuclear forces ($\sim 10^{-12}$ cm) is small in comparison to both the wavelength of a thermal neutron and the interatomic distances in the scattering system ($\sim 10^{-8}$ cm), the neutron-nuclear interaction can be characterized as a "localized impact". The interaction potential is therefore represented in the form of a delta function, the so-called Fermi pseudopotential:

$$\text{II-4} \qquad V = \frac{2\pi\hbar}{m_n} \, b \, \delta(\underline{r} - \underline{R}(t))$$

where m_n is the neutron mass and b is the bound atom scattering length of the nucleus located at position $\underline{R}$ at time t. The form of the Fermi pseudopotential is chosen so as to guarantee that in the high energy limit ($E_o > ev$) the first Born approximation will give the correct total scattering cross section for a free atom: $\sigma_T = 4\pi a^2$ where a is the experimentally determined free atom scattering length. (The relationship between the bound and free atom scattering lengths is $b = (m_n + M)\, a/M$ where M is the mass of the scattering atom.)

The formal expression for the differential scattering cross section per unit solid angle and unit interval of energy, is

$$\text{II-5} \qquad \frac{d^2\sigma}{d\Omega dE} = b^2 \, \frac{k}{\hbar k_o} \, S(\underline{\kappa},\omega)$$

where

$$\text{II-6} \quad S(\underline{K},\omega) = (2\pi)^{-1} N \iint \exp i(\underline{K}\cdot\underline{r} - \omega t)\ G(\underline{r},t)\ d\underline{r}\ dt$$

It is assumed here that the scattering system consists of N nuclei of the same type with zero spin. The function $S(\underline{K},\omega)$, the so-called scattering law, is independent of the mass and energy of the scattered neutron as well as the interaction potential - it depends solely on the physical properties of the scattering system. $G(\underline{r},t)$, described by Van Hove (184) as the space-time correlation function of the system, is defined to be

$$\text{II-7} \quad G(\underline{r},t) = \frac{(2\pi)^{-3}}{N} \sum_{1}^{N} \sum_{j}^{N} \int d\underline{K}\ e^{-i\underline{K}\cdot\underline{r}} \left\langle e^{-i\underline{K}\cdot\underline{R}_1(0)}\ e^{i\underline{K}\cdot\underline{R}_j(t)} \right\rangle$$

or the equivalent expression

$$\text{II-8} \quad G(\underline{r},t) = \frac{1}{N} \left\langle \sum_{1}^{N} \sum_{j}^{N} \int d\underline{r}'\ \delta\left[\underline{r} + \underline{R}_1(0) - \underline{r}'\right]\ \delta\left[\underline{r}' - \underline{R}_j(t)\right] \right\rangle$$

$\underline{R}_1(0)$ and $\underline{R}_j(t)$ are Heisenberg position operators for the nuclei. In the usual scattering experiment the atoms of the scattering system are not initially in any one given energy eigenstate, rather, there is a thermal distribution of energy eigenstates in the system. The angular brackets in the above expressions indicate a thermal averaging of the expectation values of the enclosed operators over the different states of the system at a given temperature.

If the target can be described as a classical system, $G(\underline{r},t)d\underline{r}$ is readily interpreted as the probability of

finding one of the target nuclei in the neighborhood $d\underline{r}$ of the point $\underline{r}$ at time t given that a nucleus was at the origin at t = 0. However, in a quantum system $G(\underline{r},t)$ is generally complex and this simple interpretation is no longer adequate. The physical interpretation of the real and imaginary parts of $G(\underline{r},t)$ is discussed in detail by Van Hove (184).

If the scattering system can be regarded as being composed of distinguishable particles (i.e., the particles obey Boltzman statistics), the space-time correlation function can be separated into two components: $G_s(\underline{r},t)$, the self-correlation function which describes the correlation between the positions of the same particle at different times, and the function $G_d(\underline{r},t)$ which describes the correlation between pairs of distinct particles. Thus,

$$\text{II-9} \quad G(\underline{r},t) = G_s(\underline{r},t) + G_d(\underline{r},t)$$

where

$$\text{II-10} \quad G_s(\underline{r},t) = \frac{1}{N}\left\langle \sum_1^N \int d\underline{r}' \, \delta(\underline{r} + \underline{R}_1(0) - \underline{r}') \, \delta(\underline{r}' - \underline{R}_1(t)) \right\rangle$$

and

$$\text{II-11} \quad G_d(\underline{r},t) = \frac{1}{N}\left\langle \sum_{1\neq j}^N \int d\underline{r}' \, \delta(\underline{r} + \underline{R}_1(0) - \underline{r}') \, \delta(\underline{r}' - \underline{R}_j(t)) \right\rangle$$

In systems in which the scattering length differs among isotopes or in which the spin dependent scattering lengths for a given isotope differ, incoherent scattering

takes place. These factors can be taken into account by replacing $b^2G(\underline{r},t)$ by

$$\text{II-12} \quad b^2G(\underline{r},t) \longrightarrow b^2_{inc}G_s(\underline{r},t) + b^2_{coh}G_d(\underline{r},t)$$

where

$$\text{II-13} \quad b^2_{inc} = \langle b^2 \rangle - \langle b \rangle^2$$

$$\text{II-14} \quad b^2_{coh} = \langle b \rangle^2$$

The angular brackets represent averaging first over the spin states of the system consisting of the neutron and the given isotope and second, over all the isotopes of the given chemical element. Equation II-5 is replaced by the following expressions for the coherent and incoherent differential scattering cross sections of a monatomic scattering system:

$$\text{II-15} \quad \frac{d^2\sigma^{coh}}{d\Omega dE} = \frac{Nb^2_{coh}}{2\pi\hbar}\frac{k}{k_o}\iint d\underline{r}\, dt\, e^{i(\underline{K}\cdot\underline{r} - \omega t)}\, G(\underline{r},t)$$

$$\text{II-16} \quad \frac{d^2\sigma^{inc}}{d\Omega dE} = \frac{Nb^2_{inc}}{2\pi\hbar}\frac{k}{k_o}\iint d\underline{r}\, dt\, e^{i(\underline{K}\cdot\underline{r} - \omega t)}\, G_s(\underline{r},t)$$

2.2 THE STRUCTURE FACTOR AND THE STATIC PAIR DENSITY FUNCTION

The structure factor of an atomic system is defined as the integral of the scattering law over all energy transfers occurring in the interaction of the atoms and the particles which they scatter:

$$\text{II-17} \quad \int S(\underline{K},\omega)\, d\omega = \frac{N}{2\pi} \int d\omega \iint d\underline{r}\, dt\; e^{i(\underline{K}\cdot\underline{r} - \omega t)}\, G(\underline{r},t)$$

Since $\int d\omega\; e^{-i\omega t} = 2\pi\delta(t)$, the above expression reduces to

$$\text{II-18} \quad \int S(\underline{K},\omega)\, d\omega = N \int d\underline{r}\; e^{i\underline{K}\cdot\underline{r}}\, G(\underline{r},0)$$

From Equation II-8 we see that $G(\underline{r},0)$, the space-time correlation function at time 0, is

$$\text{II-19} \quad G(\underline{r},0) = \frac{1}{N} \sum_{l,j}^{N} \int d\underline{r}' \left\langle \delta(\underline{r} + \underline{R}_l(0) - \underline{r}')\, \delta(\underline{r}' - \underline{R}_j(0)) \right\rangle$$

Since $\underline{R}_l(0)$ and $\underline{R}_j(0)$ commute, in this instance it is possible to perform the $d\underline{r}'$ integration:

$$\text{II-20} \quad G(\underline{r},0) = \frac{1}{N} \sum_{l,j}^{N} \left\langle \delta(\underline{r} + \underline{R}_l(0) - \underline{R}_j(0)) \right\rangle$$

Separating out the diagonal terms of the summation over the indices l and j, one finds that

$$\text{II-21} \quad G_s(\underline{r},0) = \delta(\underline{r})$$

$$G(\underline{r},0) = \delta(\underline{r}) + g(\underline{r})$$

where

$$\text{II-22} \qquad g(\underline{r}) = \frac{1}{N} \sum_{1 \neq j=1}^{N} \left\langle \delta(\underline{r} + \underline{R}_1(0) - \underline{R}_j(0)) \right\rangle$$

The function $g(\underline{r})$ is the well known static pair correlation function - the average density of atoms in a unit volume located at position $\underline{r}$ as seen from an atom located at the origin. The substitution of the above expression for $G(\underline{r},0)$ in Equation II-18 gives

$$\text{II-23} \qquad \int S(\underline{K},\omega)\, d\omega = N \left(1 + \int e^{i\underline{K}\cdot\underline{r}}\, g(\underline{r})\, d\underline{r} \right)$$

We see that in order to determine $g(\underline{r})$ one does not require detailed knowledge of the scattering law itself; the integral of the scattering law, i.e., the structure factor, is sufficient. Unfortunately, the data obtained in the normal diffraction measurement cannot be directly related to the structure factor of the scattering system without employing certain approximations.

The conventional diffraction experiment generally provides a measure of the coherent angular scattering cross section:

$$\text{II-24} \qquad \frac{d\sigma}{d\Omega}^{coh} = \int \frac{d\sigma}{d\Omega dE}^{coh} dE = b_{coh}^2 \int \frac{k}{k_o}\, S(\underline{K},\omega)\, d\omega$$

The k/k_o factor in the integrand of the above expression depends on the energy transfers in the scattering process. Furthermore, $\underline{K}$ varies with ω and the integration is limited to energy transfers between $-\infty$ and E_o/h. Since the indicated integration is automatically performed in the

experimental measurement, the value of $(d\sigma^{coh}/d\Omega)$ which one obtains is not a direct measure of the system's structure factor.

If the energy transfers in a diffraction measurement are negligible in comparison to the energies of the incident photons, electrons, or neutrons, then $k/k_o \approx 1$, the locus of the experimental measurement in $\underline{K}$-ω space satisfies the constant $\underline{K}$ condition required in the definition of the structure factor, and the range of integration is effectively infinite. This is the so-called static approximation. If this approximation is valid, then it follows that

$$\text{II-25} \qquad \frac{d\sigma^{coh}}{d\Omega} = N\, b_{coh}^2 \left(1 + \int e^{i\underline{K}\cdot\underline{r}}\, g(\underline{r})\, d\underline{r} \right)$$

In an x-ray diffraction measurement, the ratio of the incident energy of the photons to the energy transfers is of the order of $\sim 10^6$. For electrons with a wavelength of ~ 1 Å, the incident energy - energy transfer ratio is $\sim 10^4$. Therefore, the static approximation is quite accurate for x-ray and electron measurements. It is also common practice to assume that the static approximation is reasonably well satisfied for neutron diffraction experiments. However, since the energies of thermal neutrons are generally of the same order of magnitude as the energy transfers when they are scattered, the applicability of the static approximation in the analysis of the neutron data is by no

means as obvious as in the x-ray and electron diffraction experiments. This point will be discussed in greater detail in Chapter III; for the remainder of this discussion, it will be assumed that Equation II-25 is valid for the neutron diffraction experiment.

It is useful at this point to note some of the general characteristics of the $g(\underline{r})$ function. Regardless of whether the scattering system is liquid, gaseous, or solid, the repulsive forces between the electron distributions of the atoms in the system will cause the static pair density function to go to zero in some finite region around $\underline{r} = 0$. (In Chapter IV it will be shown that this property of the $g(\underline{r})$ function can be used to normalize the diffraction data if the determination of the absolute scattering intensity is not feasible.) For an ideal gas, the $g(\underline{r})$ function assumes a constant value in the region beyond this minimum distance of approach for a pair of atoms. In strongly ordered systems such as polycrystals, the $g(\underline{r})$ function will exhibit distinct, well-resolved peaks at distances corresponding to the separations of the nearest atom neighbors, the next nearest neighbors, ect.. In a substance such as vitreous silica, where what order there is in the structure is relatively short-ranged, the peaks in the $g(\underline{r})$ function are less distinct and become progressively broader at large $\underline{r}$'s. Eventually, $g(\underline{r})$ approaches a constant value equal to the average density of the system.

II-26 $$\lim_{r \to \text{large}} g(\underline{r}) = n = N/V$$

The fact that the static pair density function assumes a constant value at large $\underline{r}$ leads to singular behavior of the cross section in the forward scattering direction. If the asymptotic value of $g(\underline{r})$ is added to and subtracted from Equation II-25, then

II-27 $$\frac{d\sigma^{coh}}{d\Omega} = Nb_{coh}^2 \left(1 + (2\pi)^2 \delta(\underline{K})n + \int e^{i\underline{K}\cdot\underline{r}} (g(\underline{r})-n)\, d\underline{r} \right)$$

The second term in this expression represents the forward scattering contribution. Since the forward scattering contribution cannot be measured, it is ignored.

To this point in the discussion it has been assumed that the scattering system is monatomic. For a polyatomic system such as silicon dioxide, Equation II-27 becomes

II-28 $$\frac{d\sigma^{coh}}{d\Omega} = \sum_t N_t b_t^2 + \sum_t b_t \sum_{t'} N_{t'} b_{t'} \int d\underline{r}\, e^{i\underline{K}\cdot\underline{r}} (g_{t't}(\underline{r}) - n_t)$$

where $\sum_t$ is the summation over atoms of type t, b_t is the coherent scattering length of an atom of type t, N_t is the number of atoms of type t in the system, and n_t is the average density of the type t atoms, $n_t = N_t/V$. The function $g_{t't}(\underline{r})$ is a new static pair correlation function giving the density of atoms of type t about atoms of type t':

II-29 $$g_{t't}(\underline{r}) = \frac{1}{N_{t'}} \sum_{n,n'} \left\langle \delta(\underline{r} + \underline{R}_{t',n'} - \underline{R}_{t,n})(1 - \delta_{t't}\delta_{nn'}) \right\rangle$$

where $\sum_{n,n'}$ represents the double sum over the N_t atoms of

type t and the $N_{t'}$ atoms of type t'. The factor $(1 - \delta_{t't}\delta_{nn'})$ is included to insure that only the contribution of distinct atom pairs is included in the sum.

If the polyatomic scattering system can be assumed to be isotropic, then $g_{t't}(\underline{r})$ will depend only on the magnitude of $\underline{r}$ and Equation II-28 will reduce to the following expression:

$$\text{II-30} \quad \frac{d\sigma^{coh}}{d\Omega} = \sum_t N_t b_t^2 + \sum_t b_t \sum_{t'} N_{t'} b_{t'} \int_0^\infty 4\pi r^2 (g_{t't} - n_t) \frac{\sin Kr}{Kr} \, dr$$

Dividing Equation II-30 by $\sum_t N_t b_t^2$, which is the limiting value of $(d\sigma^{coh}/d\Omega)$ at large momentum transfers, we have

$$\text{II-31} \quad \frac{1}{\sum_t N_t b_t^2} \frac{d\sigma^{coh}}{d\Omega} - 1 = \frac{\sum_t b_t \sum_{t'} N_{t'} b_{t'} \int_0^\infty 4\pi r^2 (g_{t't} - n_t) \frac{\sin Kr}{Kr} \, dr}{\sum_t N_t b_t^2}$$

The Fourier transform of Equation II-31 gives the following expression:

$$\text{II-32} \quad 4\pi r^2 (\bar{g}(r) - g_o) = \frac{2r}{\pi} \int_0^\infty i(K) \cdot K \cdot \sin Kr \, dK$$

where $$i(K) = \frac{1}{\sum_t N_t b_t^2} \frac{d\sigma^{coh}}{d\Omega} - 1$$

$$g(r) = \sum_t b_t \sum_{t'} N_{t'} b_{t'} g_{t't}(r) / \sum_t N_t b^2{}_t$$

$$g_o = \sum_t b_t \sum_{t'} N_{t'} b_{t'} n_t / \sum_t N_t b^2{}_t$$

2.3 INTERPRETATION OF THE INELASTIC NEUTRON SCATTERING SPECTRUM

In the introductory remarks in Section 2.1 it was noted that knowledge of the scattering law function, $S(\underline{\kappa}, \omega)$, enables one, in principle, to derive the space- and time-dependent pair correlation function of the scattering system:

$$\text{II-33} \quad G(\underline{r},t) = (2\pi)^{-3} N^{-1} \int \exp i(\omega t - \underline{\kappa}\cdot\underline{r})\, S(\underline{\kappa}, \omega)\, d\underline{\kappa}\, d\omega$$

Unfortunately, it is rarely possible to obtain an experimental measurement of the scattering law with sufficient range in $\underline{\kappa}$-ω space and statistical accuracy to allow one to evaluate the four-dimensional Fourier integral. Even in studies of isotropic scattering systems, in which case the above expression reduces to a two-dimensional Fourier integral, there have been few attempts to obtain the G(r,t)function by inversion of the experimental data. One must therefore consider alternative methods of data analysis to determine the dynamical properties of the scattering system.

For crystalline solids there is the detailed theory of lattice vibrations on which to base the interpretation of the experimental data. It is well known that if the vibrations of the N atoms in a solid are harmonic, these motions may be described by a superposition of 3N independent normal vibrational modes. The periodic symmetry of a crystal lattice enables one to represent these modes as traveling plane waves - each wave characterized by a wave vector $\underline{q}$, a frequency ω, and a polarization index s. If the unit cell

of the crystal lattice contains n nuclei, the polarization index s will assume 3n values and there will be 3n vibrational branches for each wave vector $\underline{q}$. For each branch s, there is a three dimensional dispersion relation $\omega = \omega_s(\underline{q})$. If the crystal in question scatters neutrons coherently, the experimental determination of these dispersion relations is relatively straightforward.

When only one phonon participates in the scattering of a neutron, i.e. the quantum number of one of the normal modes of the crystal is increased or decreased by one, characteristic peaks are observed in the coherent inelastic scattering spectrum. (The cross sections for multiphonon processes are generally small in comparison to the single phonon cross section.) The coherent double differential cross section for one phonon processes in a crystal can be written as follows (185):

$$\text{II-34}\quad \frac{d^2\sigma}{d\Omega d\epsilon}^{coh} = \frac{\hbar k}{2k_0 N} \sum_j \sum_{j'} b_j b_{j'} e^{-(W_j+W_{j'})} e^{i\underline{K}\cdot(\underline{\rho}_j - \underline{\rho}_{j'})}$$
$$\times \frac{1}{\sqrt{M_j M_{j'}}} \frac{(2\pi)^3}{V} \sum_s^{3N} \frac{(\underline{K}\cdot\underline{\alpha}_j^s)(\underline{K}\cdot\underline{\alpha}_{j'}^s)^*}{\omega_s(\exp(\hbar\omega_s/k_BT) - 1)} \begin{bmatrix} \exp(\hbar\omega_s/k_BT) \\ 1 \end{bmatrix}$$
$$\times \delta(\underline{K} \pm \underline{q} - 2\pi\underline{\tau})\, \delta(\epsilon \pm \hbar\omega_s)$$

The upper signs refer to phonon creation and the lower signs to phonon annihilation processes. The j-th atom of the unit cell of the crystal has a coherent scattering length b_j^{coh}, mass M_j, Debye-Waller factor W_j, and its equilibrium position within the cell is located at $\underline{\rho}_j$. The s index identifies the normal mode. The amplitudes, directions and phases of

the motions of the atoms within the unit cell are specified by the polarization vectors $\underline{\alpha}_j^s$.

The energy and momentum conservation conditions for the neutron - phonon interaction,

$$\text{II-35} \qquad \epsilon = \mp \hbar\omega_s(\underline{q}) = \frac{\hbar(k^2 - k_o^2)}{2m_n}$$

and

$$\underline{K} = \underline{k} - \underline{k}_o = 2\pi\underline{\tau} \mp \underline{q}$$

are incorporated in Equation II-34 in the delta functions. Therefore, each peak observed in the coherent inelastic scattering spectra yields a pair of values of ω and $\underline{q}$ belonging to a dispersion relation. An accurate measurement of the absolute scattering intensity of the individual phonon peaks enables one, in principle, to determine the polarization vectors.

The extraction of the polarization vector information from experimental data is a difficult undertaking which has been attempted for only the simplest crystals. However, as indicated above, the dispersion relations are deduced simply from energy and momentum conservation considerations without recourse to any very complicated theory or analysis of the data. Furthermore, the determination of the phonon peak positions in $\underline{K}$-ω space requires nowhere near as much detail or statistical accuracy in the experimental measurement as would be required to obtain the Van Hove space-time correlation function.

In a polycrystalline target the direction of a given reciprocal lattice vector $\underline{\tau}$ is randomly distributed and as a result, the sharp peaks found in the coherent inelastic scattering spectra of single crystals are generally no longer observed. However, there remain characteristic sharp breaks in the energy distribution of the scattered neutrons which can be related to an average dispersion relation for the target.

One-phonon coherent scattering from a polycrystal can occur only if K lies in the range

II-36 $$2\pi\tau - q \leq K \leq 2\pi\tau + q$$

q is the wave number of the phonon in question and τ is the modulus of an arbitrary reciprocal lattice vector. The cross section for the one-phonon event in a polycrystal is obtained from Equation II-34 by summing over all orientations of $\underline{q}$ with respect to $2\pi\underline{\tau}$ and then averaging this result over all orientations of $\underline{K}$ with respect to $2\pi\underline{\tau}$ (186). The general shape of the scattering spectrum is determined by the factor $\left[(\underline{K}\cdot\underline{\alpha}^s_j)(\underline{K}\cdot\underline{\alpha}^s_{j'})^*\right]$ in the cross section expression. If, as a limiting case, it is assumed that all lattice waves are either pure longitudinal or pure transverse waves, i.e., $\underline{\alpha}^L$ and $\underline{\alpha}^T$ are taken to be unit vectors parallel and at right angles, respectively, to the phonon wave vector, the resulting polarization factors will appear as shown in Figure 9. The contribution from the longitudinal mode is

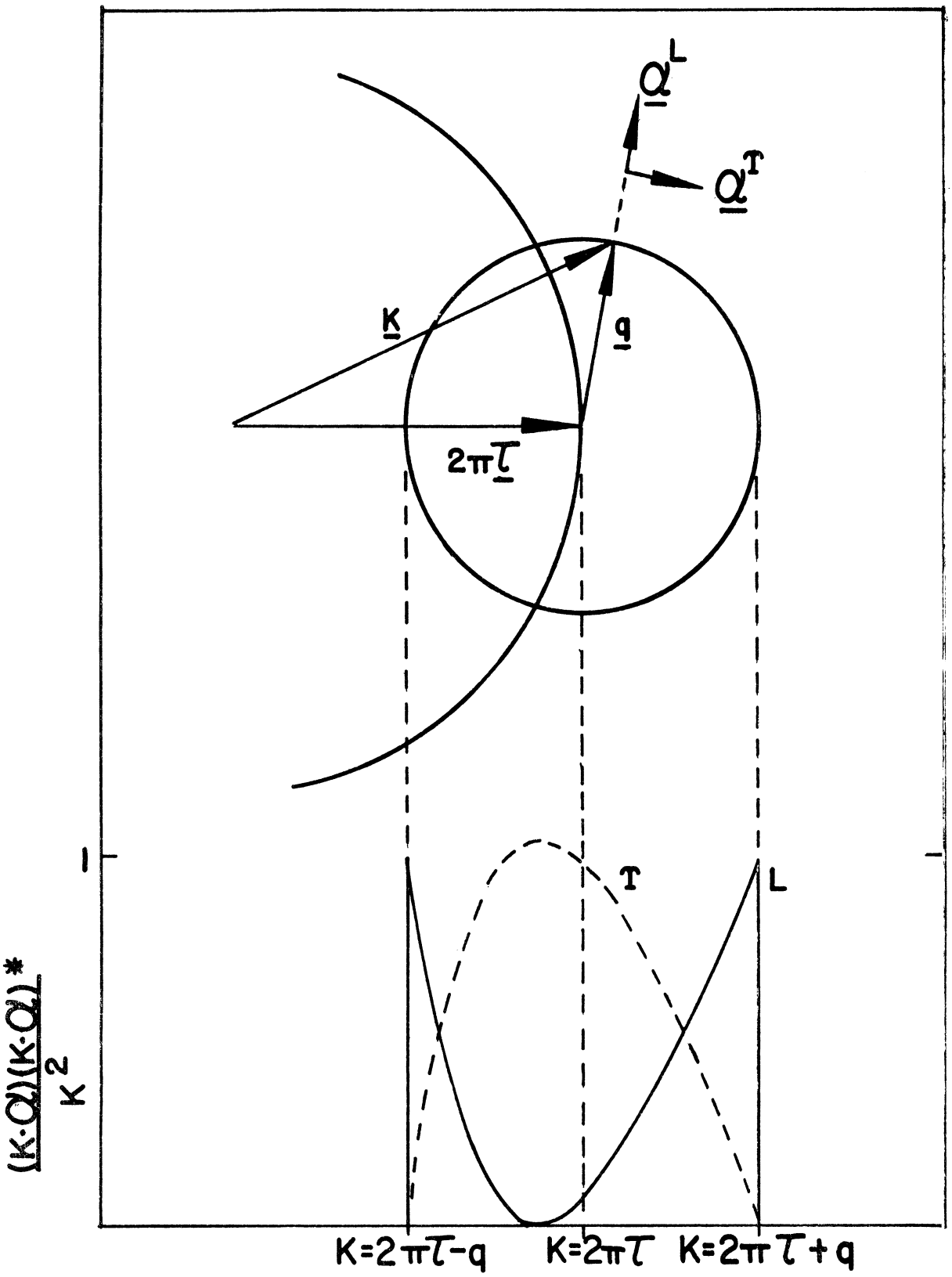

Figure 9. Vector diagram for a coherent one-phonon process in a polycrystal and the resulting polarization factors. (From Skold and Larsson (193).)

seen to peak at $K = 2\pi\tau \pm q_L$ and fall to zero for $K = 2\pi\tau$. On the other hand, the contribution from the transverse modes has a broad maximum at $K \approx 2\pi\tau$ and falls to zero at $K = 2\pi\tau \pm q_T$.

Because of the nature of the longitudinal and transverse polarization factors, the sharp breaks in the scattering spectra of polycrystalline solids are generally associated with longitudinal phonon effects. The contribution from the transverse modes, which is usually obscured by the longitudinal contribution, is well defined only in situations where the transverse frequency coincides with a peak in the density of vibrational states. The average longitudinal frequency - wave number relationship is determined from the positions of the discontinuities in the coherent scattering spectrum. At a fixed energy transfer $\epsilon = \hbar\omega$, the distance between the two breaks in the scattering spectrum is $\Delta K = 2q$ - thus we obtain the $\omega = \omega(q)$ relationship.

The coherent structure in the inelastic scattering spectra of a polycrystal is generally restricted to the smaller momentum and energy transfers. At large momentum transfers many different reciprocal lattice points can contribute to the scattering and as a result, the momentum and energy conservation conditions for the neutron - phonon interaction can be satisfied at most points in K - space. The observation of coherent structure at large energy transfers is hindered by the fact that the inelastic

scattering cross section generally tends to decrease with increasing energy transfers.

Is it reasonable to attempt to analyze the inelastic scattering spectrum of vitreous silica on the basis of theories and cross section formulae developed for polycrystalline systems? Vitreous silica is more nearly like a liquid in that there is no long range regularity of the equilibrium positions of its atoms. Even if the modern crystallite model of its structure (Section 1.3.8) is correct, a comparison of the diffraction patterns of vitreous silica and the polycrystalline silicon dioxides clearly indicates that the range of order in vitreous silica is nowhere near as extensive as that in the polycrystalline samples. On the other hand, the silicon and oxygen atoms in glass and the polycrystalline silicon dioxides lack the mobility of the atoms in a liquid.

Because of the lack of long-range regularity of the equilibrium positions of the atoms in liquids and noncrystalline solids it is questionable if the description of their vibrational motions in terms of phonons with well-defined frequency-wave vector relationships is appropriate. Nevertheless, we know that some of the atomic motions in these systems can be characterized as waves: solids support both longitudinal and transverse acoustic waves regardless of the degree of order in their structure and liquids are known to support longitudinal acoustic waves.

The similarity of the polycrystal and liquid phase coherent inelastic neutron scattering spectra of a number of substances suggests that in some instances a phonon-like description of the collective motions is meaningful for the liquid state. To cite an example, Cocking and Guner (187) report that the same discontinuities which they observe in the coherent neutron scattering spectrum of polycrystalline tin are also found in their liquid tin data. Experimental evidence of the existence of dispersion relations for liquid aluminum (188), lead (189) (190), potassium (191), sodium (192), and argon (193) has also appeared in the literature. Both Singwi (194) and Egelstaff (195) have employed the idea of phonon-like modes to describe near-neighbor correlations of the atomic motions in liquids. Singwi's model introduces the concept of a finite range of phonon-like excitations while Egelstaff takes some account of the polarization of the modes. Cocking (196) has shown that the introduction of polarized modes is required to explain the observed results of coherent neutron scattering by liquid metals and his results agree with the conclusions of Sköld and Larsson (193) for liquid argon.

Considering the success of adapting the concepts of phonon-like motions and the cross section formulae of polycrystalline systems to the interpretation of liquid scattering spectra, it seems reasonable to conclude that the neutron scattering spectrum of vitreous silica can be

interpreted in a like manner - especially since the scattering spectrum of a solid is not complicated by contributions from the diffusive motions one finds in a liquid.

In the discussion of the anomalous specific heat of vitreous silica (Section 1.5) it was noted that the equilibrium thermodynamic properties of a solid can be determined from a knowledge of the frequency spectrum of the system's normal vibrations. The normal frequency distribution function, $g(\omega)$, is an integral characteristic of the dynamics of a crystal which can in principle be generated from the dispersion relations. The foregoing discussion has indicated that the most that one could hope to obtain from the analysis of the structure in the coherent scattering spectra of a polycrystalline target or a less ordered solid such as vitreous silica would be an average dispersion relation. This result could hardly be expected to provide the required detail to generate an accurate $g(\omega)$ function. However, Egelstaff (197) has suggested an alternative method of extracting the frequency spectrum information from the scattering data of polycrystalline targets in which the nuclei have large coherent scattering amplitudes.

The differential scattering cross section for a polycrystalline target is written in the following form

$$\text{II-37}\quad \frac{d^2\sigma}{d\Omega dE} = \frac{Nk}{k_o}\left[b_{inc}^2\, S_s(K,\omega) + b_{coh}^2\left[S_s(K,\omega) + S_d(K,\omega)\right]\right]$$

Since the silicon and oxygen atoms are coherent scatterers there will be no contribution from the first term in this expression. $S_s(K,\omega)$ has the following property (for processes in which the neutron gains energy on scattering.)

$$\text{II-38} \quad \lim_{K\to 0}\left[\frac{S_s(K,\omega)}{K^2}\right] = \frac{1}{2M\omega}\,\frac{g(\omega)}{3N^2}\left[\exp(\hbar\omega/k_BT) - 1\right]^{-1}$$

$S_d(K,\omega)$ represents an interference contribution, the explicit form of which is unimportant. The important point is that as K increases this function should tend to zero. Thus, for sufficiently large ,

$$\text{II-39} \quad b_{coh}^2\left[S_s(K,\omega) + S_d(K,\omega)\right] \longrightarrow b_{coh}^2\, S_s(K,\omega)$$

The sum of $S_s(K,\omega)$ and $S_d(K,\omega)$ plotted as a function of K^2 is quite similar in appearance to the decay curve (in activity versus time) of a mixture of two radioactive species with different half-lives: $S_d(K,\omega)$ corresponds to the contribution from the shorter-lived component while $S_s(K,\omega)$ is similar in appearance to the contribution of the longer-lived component.

The Egelstaff analysis proceeds as follows: at a fixed energy transfer ϵ , the ratio

$$\text{II-40} \quad \frac{d^2\sigma}{d\Omega dE} \Big/ K^2 \Big|_{\epsilon = \text{constant}}$$

is formed from the experimental data and plotted as a function of K^2. The resulting curve is extrapolated to

$K = 0$ from the region of large K where the incoherent approximation is valid and the contribution from $S_d(K,\omega)$ is negligible. The extrapolation yields

$$\text{II-41} \quad \lim_{K\to 0}\left[\frac{d^2\sigma}{d\Omega dE} K^{-2}\right] = b_{coh}^2 \frac{k}{k_0 6NM\omega} \frac{g(\omega)}{\exp(\hbar\omega/k_B T) - 1}$$

i.e., the magnitude of $g(\omega)$ for a given $\omega = \epsilon/\hbar$. The frequency spectrum is generated by repeating this process for a range of values of ϵ.

If there is more than one type of atom in the scattering system, one must be cautious in interpreting the results of this mode of analysis. Although this point has often been ignored, the $g(\omega)$ function obtained by the Egelstaff extrapolation technique is the true phonon frequency spectrum function only if the target has a Bravais lattice with cubic symmetry. For a monatomic lattice with a basis, the relationship between the experimentally determined and true $g(\omega)$ functions can be established to within the Debye-Waller factor. However, a direct relationship no longer exists for lattices containing different atom types. In this instance the extrapolation technique does not produce the true $g(\omega)$ but a product of this function and a sum including Debye-Waller factors and the squares of the moduli of the phonon polarization vectors of the scattering system. Because of the dependence of the polarization vectors on ϵ, the experimentally derived function may be quite different in form from the true $g(\omega)$. It is only when the dependence

of the polarization vectors on ϵ is sufficiently smooth that the experimental $g(\omega)$ will resemble the true frequency spectrum. This problem is discussed in detail by Gurevich and Tarasov (198) and Kagan (199).

CHAPTER III

3.1 THE VITREOUS SILICA TARGETS

The targets used in this study were 4" x 2" x 0.290" samples of Corning Glass Works' Code 7940 vitreous silica. This is an ultrapure glass manufactured from noncrystalline materials. The maximum total impurities, other than water, do not exceed 0.01 wt. percent. The water content of this silica is estimated to be about 0.1 wt. percent. (The parts per million of the sample contaminants are listed in Table III-1 (200).)

Complete details of the physical properties of the Code 7940 glass are provided in Corning's product information bulletin FS-5 (January 15, 1965). Briefly, its thermal properties are as follows:

Average Expansion Coefficient per ^{o}C:	
0 - 300^{o}C	5.6×10^{-7}
300^{o} - 600^{o}C	4.0×10^{-7}
600^{o} - 900^{o}C	3.6×10^{-7}
Softening Point (±40^{o}C)	1585^{o}C
Annealing Point (±25^{o}C)	1075^{o}C
Strain Point (±25^{o}C)	990^{o}C
Specific Heat at 25^{o}C, cal/gm(^{o}C)	0.17
Thermal Diffusivity at 25^{o}C, cm^2/sec	0.008
Thermal Conductivity at 25^{o}C, cal/(sec)(cm^2)(^{o}C/cm)	0.0032

Some of the more important mechanical properties of the glass are:

Elastic Modulus, 25°C	10.6×10^6 psi
Shear Modulus, 25°C	4.55×10^6 psi
Poisson's Ratio, 25°C	0.17
Modulus of Rupture, Abraded, 25°C	7160 psi
Density, gm/cm^3	2.202

As noted above, the thickness of each target obtained from Corning was 0.290". In order to test for multiple scattering effects in our measurements, one target was ground down to a thickness of 0.164". Grinding operations are quite capable of generating a very large amount of heat and producing some local devitrification in the sample. To prevent this from occurring, the sample was immersed in a coolant during the grinding operation and the material was removed in steps of 0.002" with frequent pauses to dissipate any heat buildup.

TABLE III-1

Purity of CORNING Ultrapure Vitreous Silica, Code 7940

ELEMENT	PARTS PER MILLION
Sodium	0.01 - 2.0
Potassium	0.01 - 0.1
Copper	0.01 - 0.05
Magnesium	0.01 - 0.1
Calcium	0.1 - 1.0
Zinc	0.05 - 0.5
Boron	0.05 - 0.5
Aluminum	0.05 - 5.0
Chlorine	10.0 - 100.0
Titanium	0.1 - 10.0
Phosphorus	0.01 - 0.1
Arsenic	0.001 - 0.005
Antimony	0.001 - 0.005
Bismuth	0.01 - 0.1
Vanadium	0.01 - 0.1
Chromium	0.001 - 0.05
Manganese	0.001 - 0.01
Iron	0.1 - 5.0

According to Corning, the above analysis is considered to be typical of all of their Code 7940 glass. Different techniques were used for different impurities in order to obtain the most accurate values.

3.2 THE PHASED-CHOPPER MECHANICAL MONOCHROMATOR

The inelastic neutron scattering measurements reported in this work were performed with the University of Michigan's phased chopper mechanical monochromator. A schematic diagram of this facility, which is located at beam port "J" of the Ford Nuclear Reactor, is shown in Figure 10. The system is similar to the facility constructed at Chalk River by Egelstaff, et.al. (201) and has been described in references (202), (203), and (204). The following description will draw on these sources to provide a brief explanation of the operation of the system. This information will also provide the necessary background for the description of a two rotor modification of the system which was used to measure the total neutron cross section and the diffraction pattern of the vitreous silica target.

The major components of the mechanical monochromator facility are four time-phased slotted rotors which define the energy and direction of the incident neutron beam, and a detector-time-of-flight analyzer system which determines the energies and directions of the scattered neutrons.

The neutron source for the monochromator is the leakage spectrum of the two megawatt Ford Nuclear Reactor (205). The facility's beam port is extended through the water of the reactor pool by means of a nitrogen-filled stainless steel bellows and looks directly at a D_2O tank mounted next to the reactor core (206). A helium filled collimator in the beam port helps to optimize the neutron beam incident on

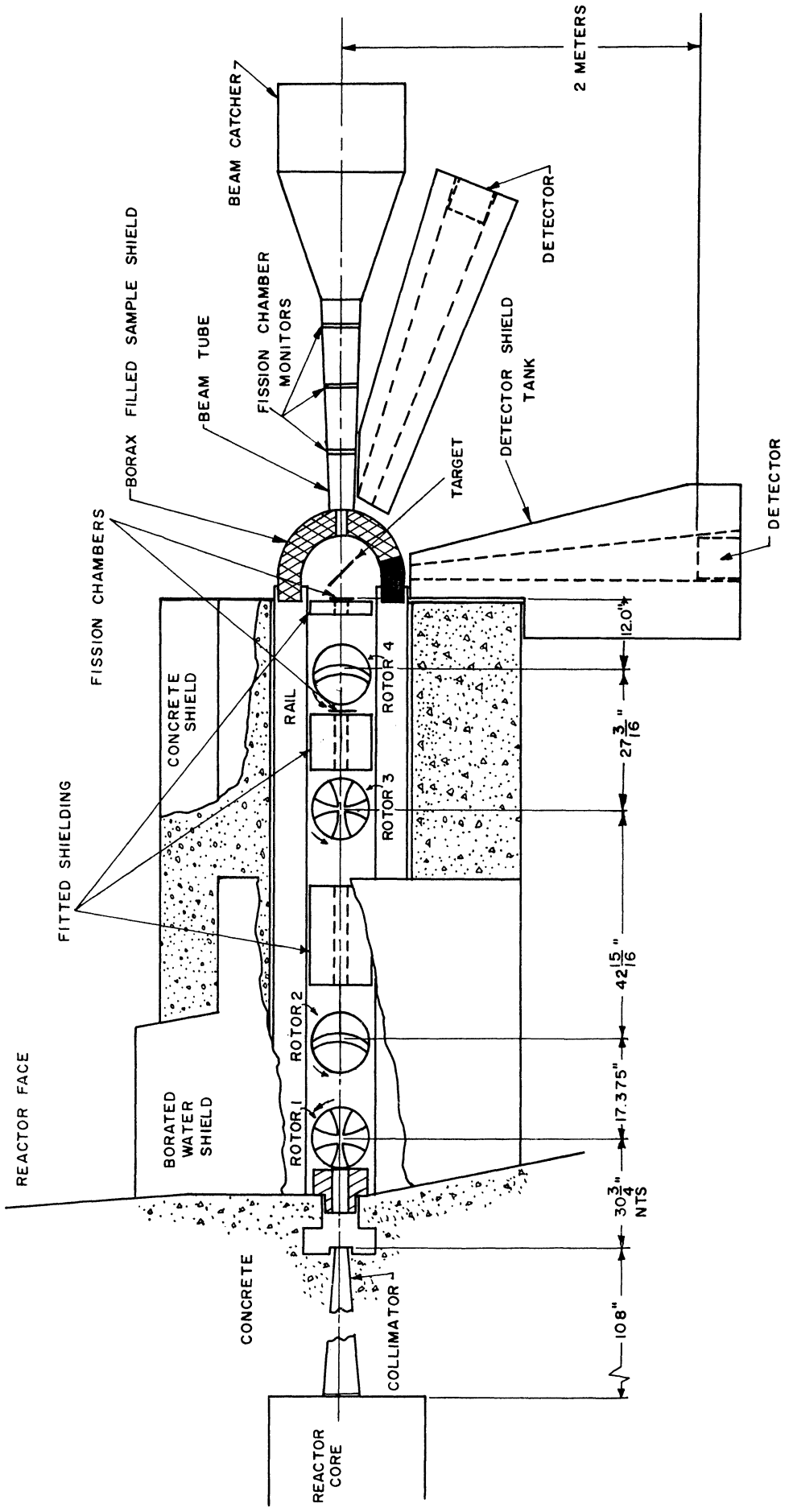

Figure 10. Schematic drawing of the four-rotor mechanical monochromator.

rotor 1.

The four rotor units are housed along the beam path in a concrete shield. Additional shielding in the form of water tanks, polyethylene, masonite, and borated paraffin is fitted around each unit to reduce the background from the scattering of neutrons and gamma radiation by the rotors.

The two types of rotors used in the system are shown in Figure 11. The rotors at positions 1 and 3 (Figure 10) are made of a fibreglass-resin mixture. The wide, divergent slits in these rotors are designed to transmit a relatively broad pulse of both thermal and fast neutrons. The rotors at positions 2 and 4 are made of a high strength Mg-Zn alloy containing 10% cadmium for neutron attenuation. The narrow, curved slits of these rotors produce relatively short bursts of thermal neutrons. Since the total cross section of cadmium drops from a value of ~7600 barns at 0.176 ev to less than ~20 barns at 1.0 ev (207), fast neutrons pass through these rotors with minimal attenuation.

The range of neutron energies transmitted by a rotor is a function of its speed of rotation and the curvature of its slits. The ratio of the optimum transmitted neutron speed (NS) to the rotor tip speed (TS) is commonly used to characterize the slit curvature of the rotor. For the cadmium rotor shown in Figure 11, NS/TS = 8. The ratio for the fibreglass-resin rotors, NS/TS = 24, is higher since they are designed to operate at lower angular velocities. For a detailed discussion of rotor transmission characteristics

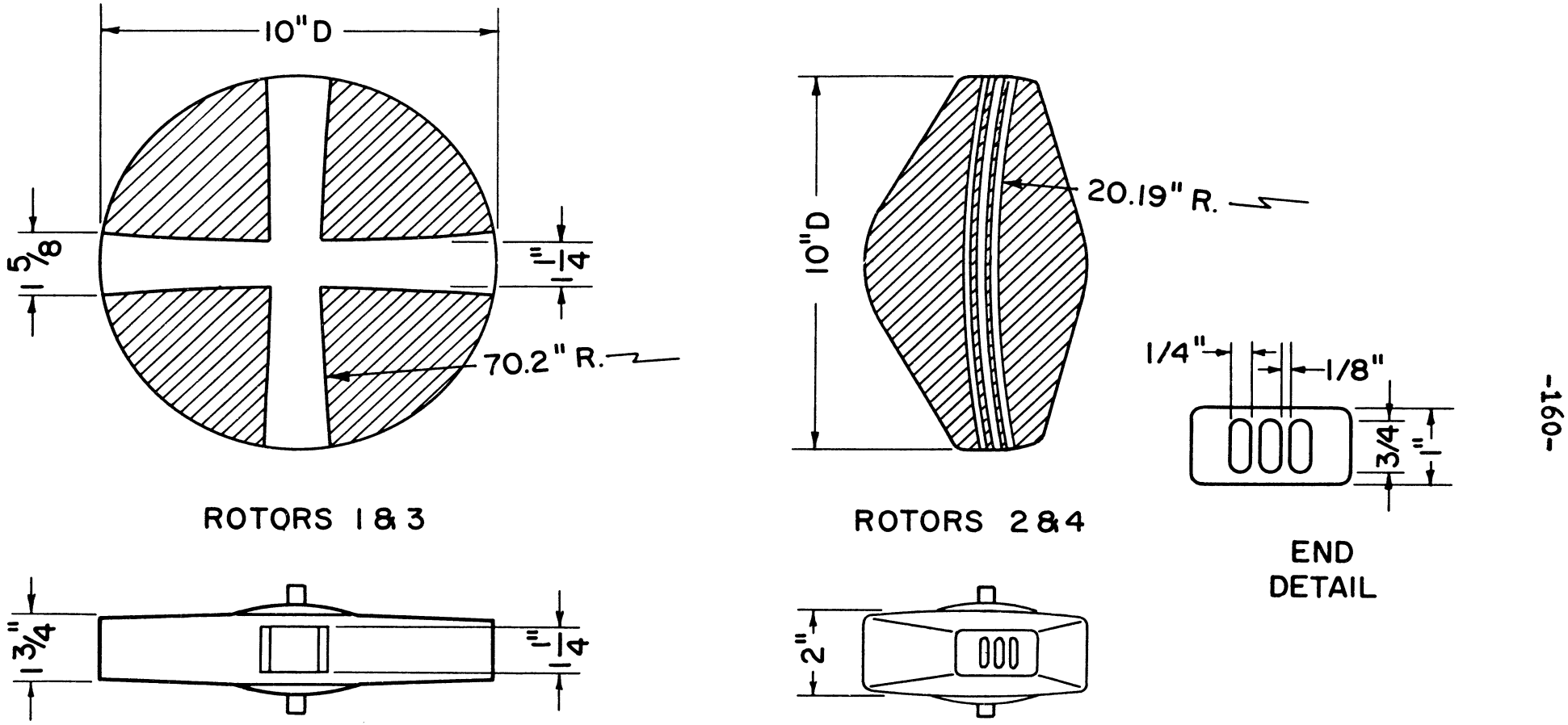

Figure 11. Schematic drawing of the mechanical monochromator rotors.

the reader is referred to the works of Carpenter (208) and Marseguerra and Pauli (209).

The system which drives the rotors was designed at AERE, Harwell and is described in reference (210). Briefly, the drive unit is designed around a standard 60 watt hysteresis motor. The shaft runs in air bearings and is supported by a magnetic thrust bearing in order to minimize energy losses. The motors are driven in pairs from a common power supply-amplifier combination controlled by a set of tuning fork oscillators. The fibreglass-resin rotors, which produce four neutron bursts per revolution, are driven at one fourth the speed of the cadmium rotors which produce only one burst per revolution. The cadmium rotors may be driven at speeds of 240, 280, 320, 360, 400, 440, or 480 cycles per second.

The neutron transmission properties of a system of slotted rotors depends on the angular relationship or phase between the slits of the individual rotors. A magnetic pickup mounted on each drive unit generates a signal at the approximate moment when the rotor slit is in the open position relative to the beam path. As indicated in Figure 12, these signals are routed to the phase monitor which is basically a gated clock registering the elapsed time between the arrival of the open signals from any given pair of rotors. Measurements to determine the timing errors which arise from differences between the true opening time of a rotor slit and the signal from the magnetic pickup are

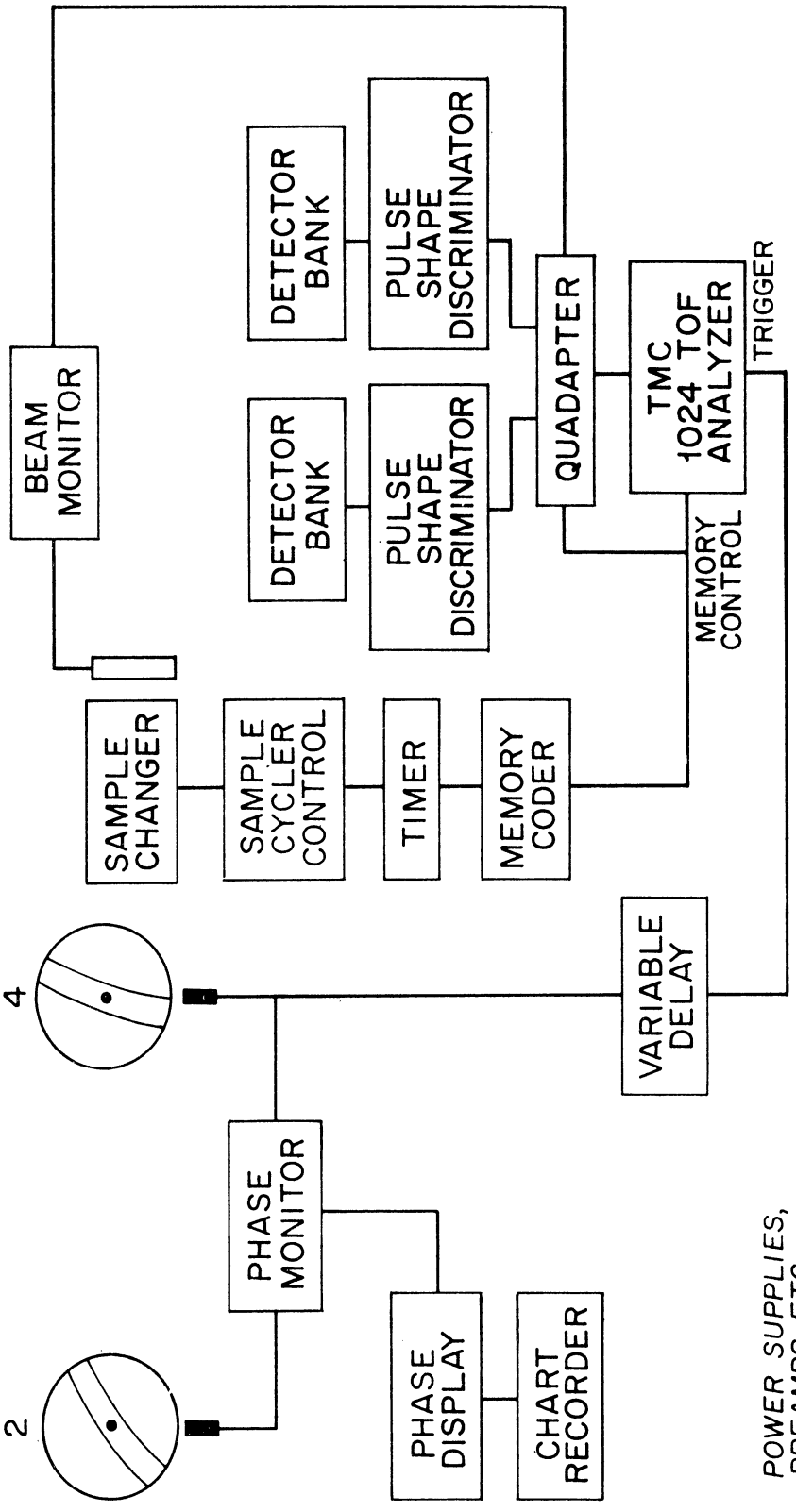

Figure 12. Block diagram of the time-of-flight spectrometer.

described by Straker (202). The phase between a pair of rotors is altered by means of a small stepping motor in each drive unit which changes the angular orientation of the drive motor's stator.

The monochromation of the neutron beam by the four rotors is illustrated in Figure 13. In the first step, the collimated neutron beam is chopped into discrete pulses (or bursts) by the fibreglass-resin rotor at position 1 (Figure 10). The pulse formed by rotor 1 moves along the beam path to the second rotor position where the cadmium rotor opens briefly to transmit a fraction of the thermal neutrons in the incident pulse. As noted above, the fast neutrons pass through rotor 2 with virtually no attenuation. In the space between rotors 2 and 3 it is observed that each pulse produced by rotor 1 and chopped by rotor 2 has been separated into two pulses. One pulse, composed of fast neutrons, is of relatively long duration while the other is a shorter pulse of thermal neutrons.

In discussing a multi-velocity neutron pulse formed by a rotor it is important to distinguish between the velocity spread of the neutrons in the pulse and the time spread. The neutron velocity spread is fixed when the pulse is formed and remains constant. The time spread, however, depends both on the velocity spread and on the distance the pulse has traveled from its point of origin. Therefore, if the neutron pulses could be observed in flight between rotor 2 and rotor 3, one could see that the fast neutrons are

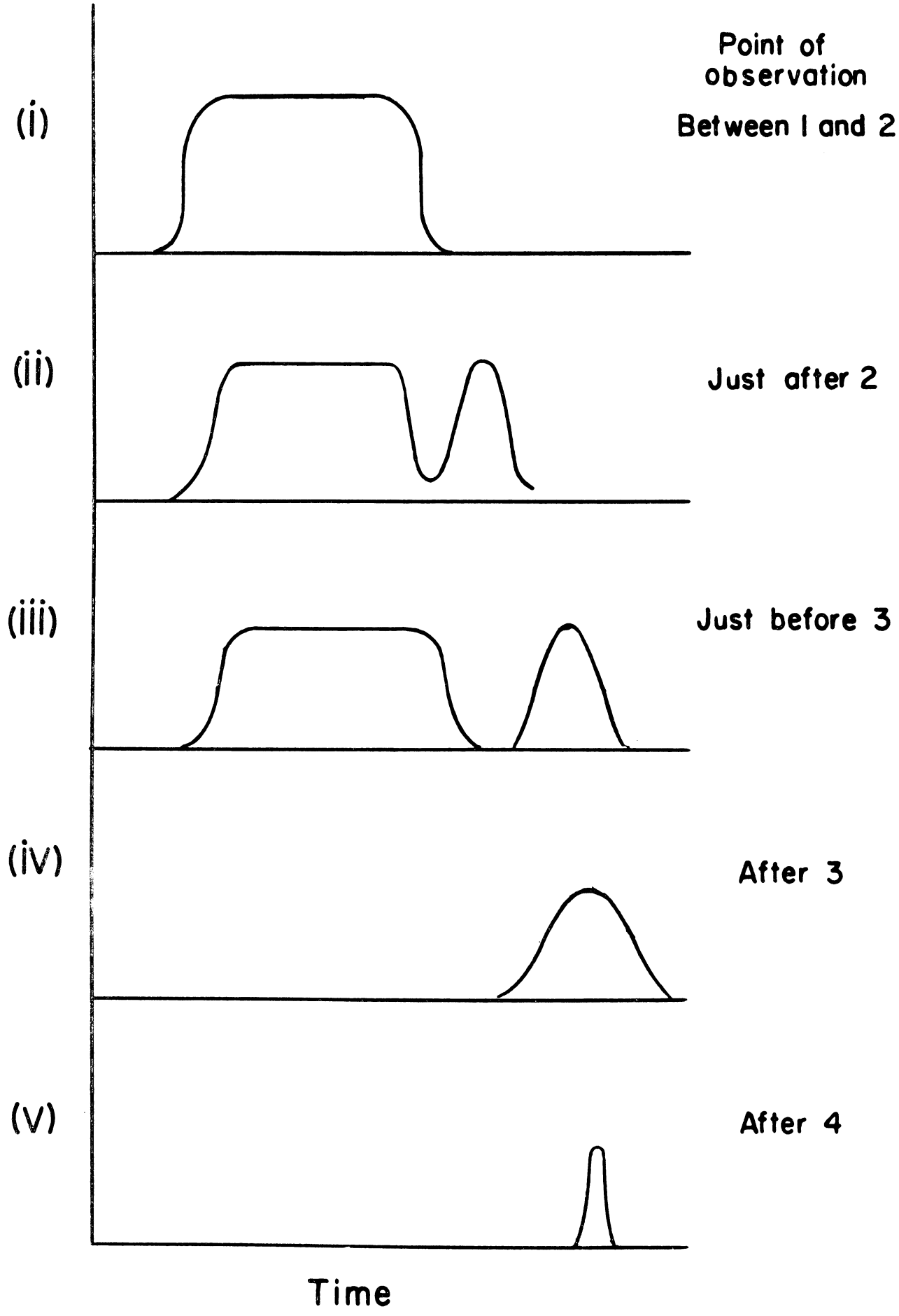

Figure 13. Steps in the monochromation of a polychromatic neutron beam.

drawing away from the thermal neutrons and the width of each pulse is increasing (Steps ii and iii, Figure 13).

The function of the fibreglass-resin rotor at position 3 is to attenuate the epi-cadmium neutrons in the beam. This is accomplished by adjusting the phase of the rotor so that it is open only when the thermal neutron pulse arrives. The monochromation of the thermal neutron pulse transmitted by rotor 3 takes place in the final step. If neutrons of velocity v are desired for an experiment, the phase time between rotor 2 and rotor 4 is adjusted to $t = L_{24}/v$, where L_{24} is the distance from the centerplane of rotor 2 to the centerplane of rotor 4. The rotor at position 4 opens to the neutrons with velocities in a narrow range centered about the desired velocity and rejects all others.

The cooperative chopping action of the rotors described above produces a nearly monokinetic beam approximately 1" high by 1½" wide at the target position. The transmission properties of the four rotor system as a function of neutron energy and rotor speed are shown in Figure 14.

The neutron scattering characteristics of a target are determined by measuring the scattered neutron energy distribution as a function of the scattering angle. In its present form the system permits simultaneous collection of scattering data at two different angles. The energies of the scattered neutrons are determined by time-of-flight analysis.

The time-of-flight analysis rests on the simple premise

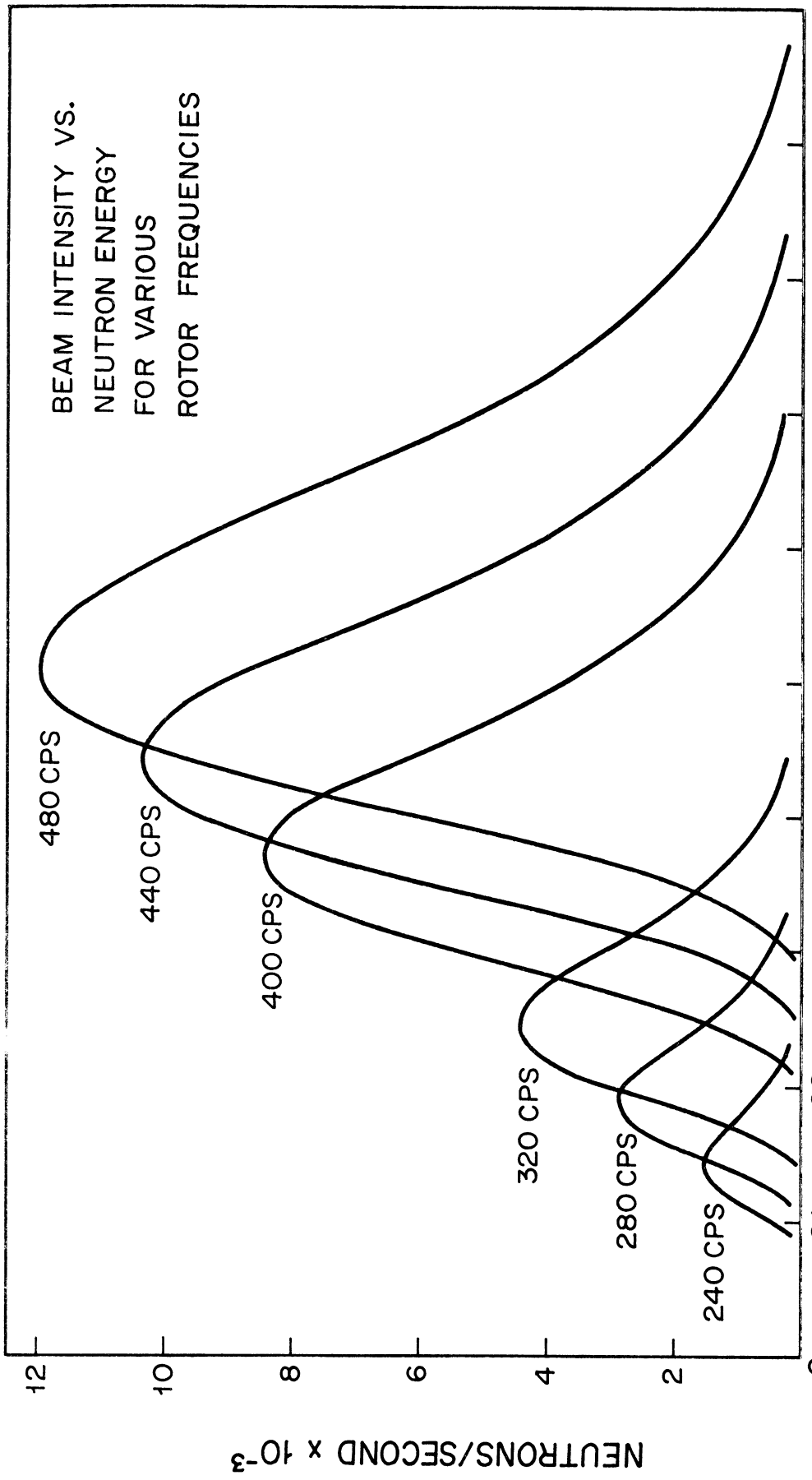

Figure 14. Beam intensity versus neutron energy at various rotor frequencies.

that if the time required by a neutron to travel a known distance can be measured, then the speed of the neutron is known. If the target is positioned at a distance L_{4T} from rotor 4, a neutron of velocity v_o will arrive at a time L_{4T}/v_o after rotor 4 opens. If the velocity of a neutron scattered by the target is v_f, it will arrive at a detector located at a distance L_{TD} from the target, at a time L_{TD}/v_f after being scattered. For each time-of-flight analyzer channel N of time width Δt, there will be a corresponding neutron time-of-flight per unit path length, $\tau_f = 1/v_f$, where $\tau_f = (N\Delta t - L_{4T}/v_o)/L_{TD}$. Thus, for a fixed initial neutron velocity, the distribution in time of neutrons arriving at the detectors positioned at a given scattering angle is a measure of the scattered neutron time-of-flight spectrum. Since the neutron pulses incident on the target are not truly monokinetic, it is necessary to place the target as close as possible to rotor 4. The closer the target is to rotor 4, the smaller the time spread of the neutron pulse. This in turn improves the resolution of the measurement.

The resolution of the neutron scattering measurements has been determined from the theoretical work of Royston (211) and the experimental measurements of Sampson (212). In Figure 15, the resolution functions for the monochromator facility are shown for the special case where the neutron energies selected by the rotors are near the optimum of the rotor transmission function.

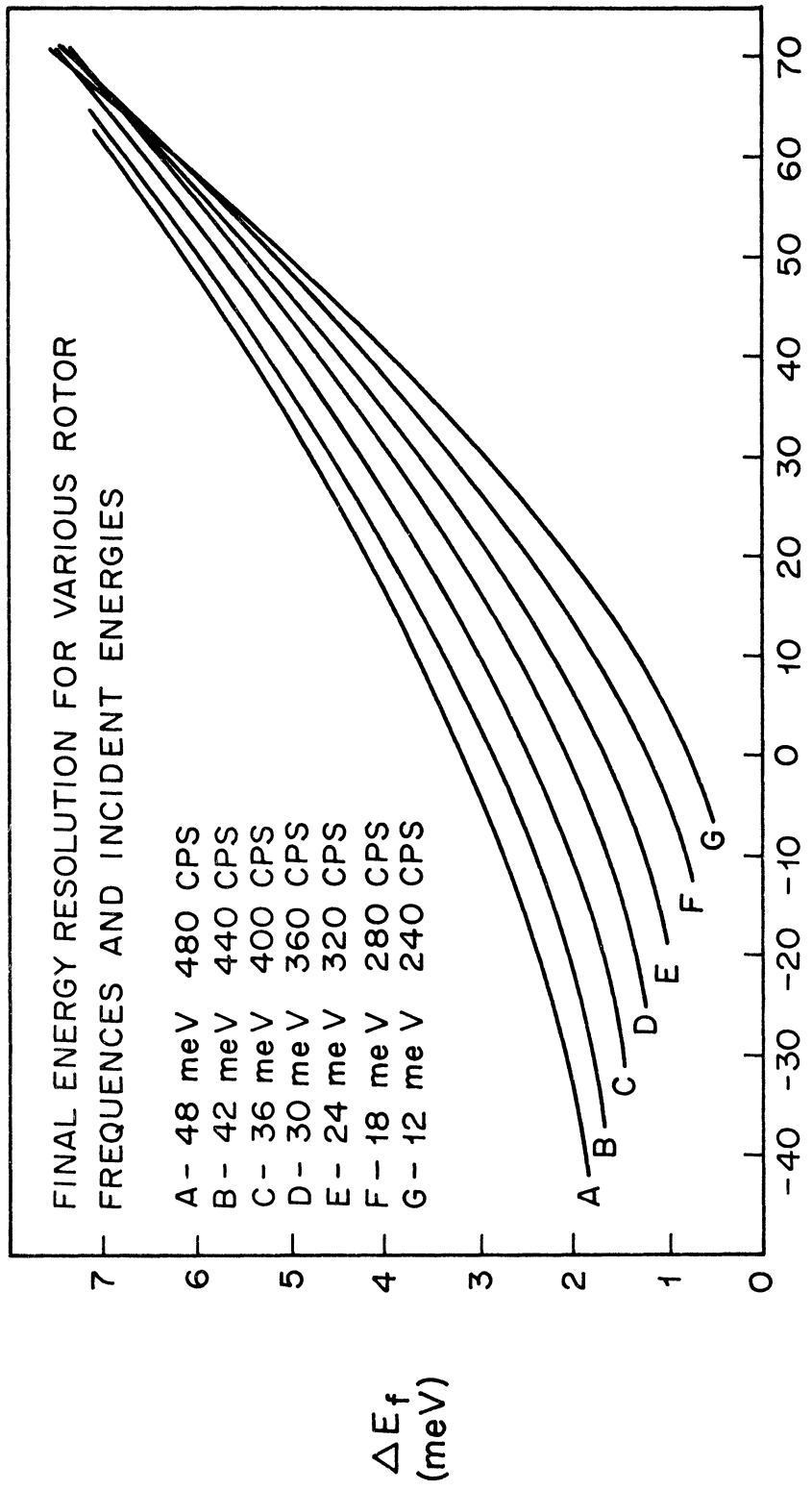

Figure 15. Final energy resolution as a function of neutron energy transfer for various incident energies.

A schematic diagram of the system which measures the neutron time-of-flight is shown in Figure 12. In addition to providing a signal for the phase monitor, the magnetic pickup on the drive unit of rotor 4 provides the trigger signal which activates the multi-channel time-of-flight analyzer. The signal from rotor 4 is first passed through a variable delay unit which is capable of retarding the trigger signal for a time between 1 and 2047 microseconds. The purpose of the variable trigger delay is to allow the scattered neutron spectrum to be properly positioned on the multi-channel analyzer's time scale.

The scattered neutrons are detected by two banks of Li^6F-ZnS(Ag)-polymethylmethacrylate scintillation detectors (213) mounted on a radius two meters from the target. Each detector has a surface area 5" x 5" and subtends a solid angle, with respect to a point scatterer, of 4.0×10^{-3} steradians. Seven of these detectors are fixed in a bank at a scattering angle of 90° and a smaller bank of three detectors may be positioned at any scattering angle between 21° and 75°. The efficiency of the detectors (214) is

$$\text{III-1} \qquad \eta(E) = \left(0.066 + \frac{2.79}{\sqrt{E}} - \frac{3.41}{E}\right)\left(1 - \frac{20}{E^2}\right)$$

(E is the neutron energy in units of millielectronvolts and III-1 is applicable only for neutron energies > 10 meV.) One of the desirable features of these detectors is that they are very thin (2 mm) and thus, their contribution to

the resolution of the time-of-flight measurement is negligible. Also, the neutron induced scintillations in these detectors have significantly longer decay times than those arising from gamma, cosmic rays, etc.. The use of a pulse length discriminator (215) which accepts only those pulses with decay times greater than three microseconds reduces the non-neutron background by a factor of 10.

The output signal from the pulse length discriminator is passed through a "quadapter" (216) (217), a unit which divides the time-of-flight analyzer's 1024 channels into separate groups in such a manner as to require no internal modification to the analyzer itself. The pulses originating at a given detector bank are routed to the appropriate portion of the analyzer's memory reserved for that data. As indicated by its name, the unit is designed to simultaneously distribute the total signal and background data from four different sets of detectors.

There are several other components of the facility indicated in Figure 12 which require brief comment. The target is mounted in a sample changer (218), a mechanical device which moves the target and a dummy target holder (if required) into and out of the neutron beam. The motion of the sample changer is controlled by the sample cycler which is essentially a timing device. The sample cycler is interconnected with the quadapter and the time-of-flight analyzer in order to direct the scattering data from the target and the background data to their appropriate locations

in the analyzer memory. For the inelastic scattering measurements reported here, the period of a complete cycle of the changer was set at eight minutes. Three fourths of the cycle time was devoted to data accumulation with the target in the beam and one fourth of the cycle to the measurement of the background. The purpose of the continuous cycling process is to remove uncertainties in the experimental measurements due to fluctuations in the incident beam intensity.

A low efficiency, high transmission parallel plate fission chamber (219) is mounted in the beam path before rotor 4 to monitor the beam intensity. If the observed intensity drops below a preset level, the time-of-flight analysis is automatically terminated.

3.3 THE TWO ROTOR FACILITY

The four rotor system described in the preceding pages was modified to produce polychromatic neutron bursts. The modification consisted of removing rotor 4 from the beam path and driving only rotors 1 and 2. Rotor 3 remained in the system at rest and acted as a fixed collimator. The size of the neutron beam was reduced by the introduction of a single slit collimator, 5" in length, between rotor 3 and the target. The dimensions of the slit were $\frac{1}{4}$" wide by $1\frac{1}{4}$" high; the front face of the collimator was 12" from the centerline of the sample changer.

Each cycle of the two rotors produces a fast neutron burst and a thermal neutron burst similar to those shown in step ii of the monochromation process (Figure 13). The trigger pulse for the time-of-flight analyzer, in this case provided by rotor 2, is delayed for an appropriate interval of time so that only the thermal energy neutrons are observed in the time-of-flight measurement. The thermal neutron transmission characteristics of the two rotor configuration are shown in Figure 16.

One of the major advantages in using the two rotor configuration is that it is possible to measure the total neutron cross section or the single differential cross section of a target over an extended range of neutron energies in a single measurement. For example, at a rotor speed of 400 cycles per second, a thermal neutron burst

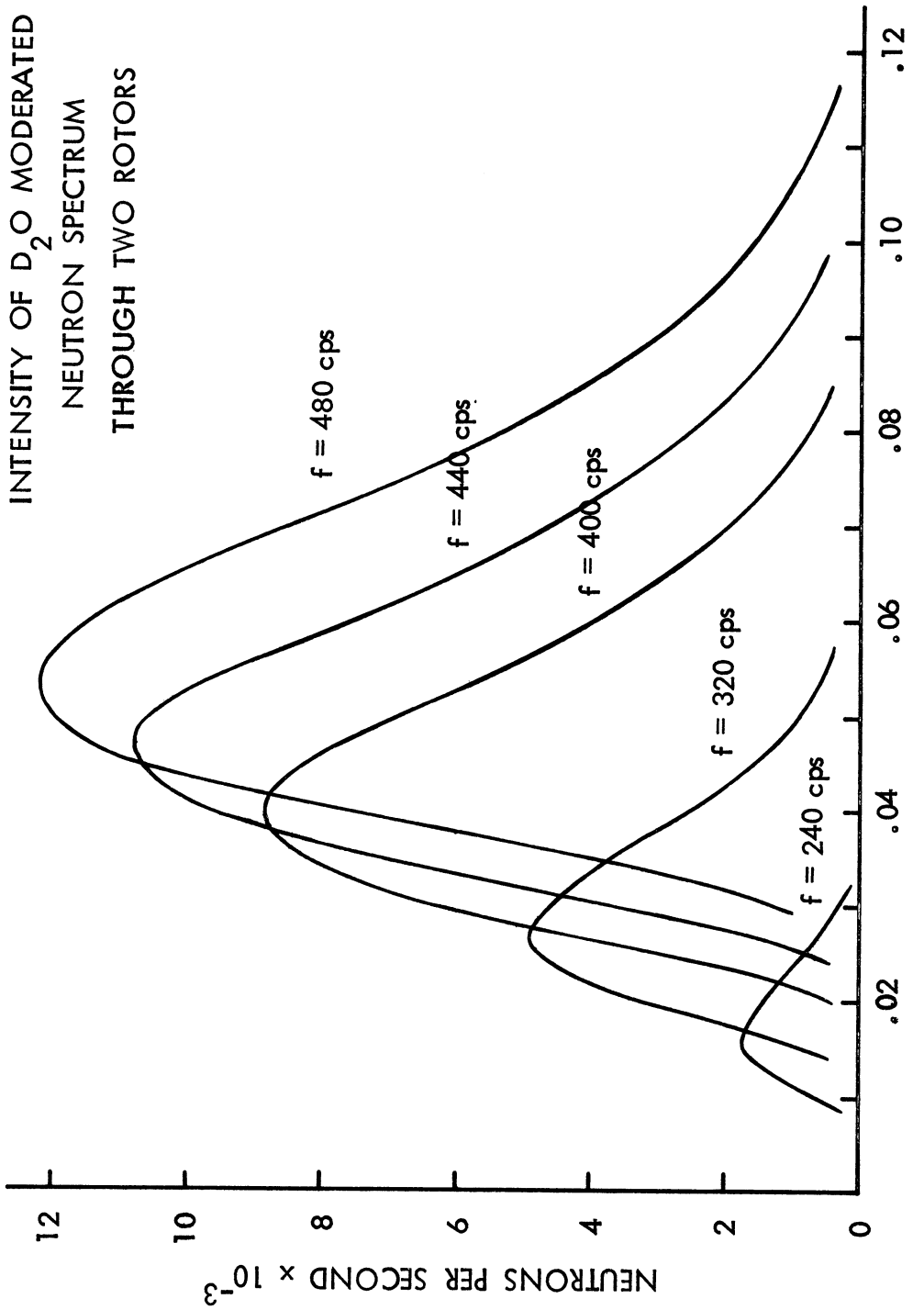

Figure 16. Neutron transmission characteristics of the two rotor configuration.

produced by the two rotors includes neutrons with energies ranging from 20 meV to 80 meV. By comparison, similar measurements with the monochromator system are extremely inefficient due to the low beam intensity and the limitation of the measurement to a single neutron energy per run.

3.3.1 THE TIME-OF-FLIGHT DIFFRACTION EXPERIMENT

In the time-of-flight diffraction experiment, neutrons in the polychromatic pulses produced by the two rotor configuration were scattered from a target to banks of detectors at scattering angles of 21.1° and 90°. The relationship between the scattered neutron intensity observed at each of these scattering angles and the single differential cross section of the target will be developed in the following discussion. (The general formulation of this problem is found in the work of Zweifel and Carpenter (220).)

The scattered neutron intensity is recorded as a function of t, the time of arrival of the neutrons at the point of their detection. A neutron of mass m and energy E in a pulse formed at rotor 2 travels a distance L to the target in a time $L/(2E/m)^{\frac{1}{2}}$. If in collision with the target the neutron energy is changed to E' and the neutron then travels the distance L' to a bank of detectors at a scattering angle θ_s, the elapsed time between pulse formation and the arrival of the neutron at the detector is

$$\text{III-2} \qquad t = \frac{L}{(2E/m)^{\frac{1}{2}}} + \frac{L'}{(2E'/m)^{\frac{1}{2}}}$$

In the following expression for the scattered neutron count rate observed at time t, it will be assumed that the target is thin and multiple scattering will be treated only as an attenuation effect. Also, resolution effects are

ignored. With these simplifications in mind, the count rate observed at scattering angle θ_s at the time of arrival t is

$$\text{III-3}\quad C(t) = N_o \frac{T}{\cos\beta} A_b \Delta\Omega \int dE \int dE' \, \phi(E) \frac{\partial^2\sigma}{\partial\Omega\partial E'}(E,E',\theta_s) \times F(E,E') \eta(E') \delta\left[t - \frac{L}{(2E/m)^{\frac{1}{2}}} - \frac{L'}{(2E'/m)^{\frac{1}{2}}}\right] \Delta t$$

where N_o = the number of scattering units in the target

T = the thickness of the target

β = the angle between the direction of the incident beam and the normal to the target surface

A_b = the area of the incident neutron beam

$\Delta\Omega$ = the solid angle subtended by the detector bank at the target

$\phi(E)$ = the incident neutron flux per unit energy at energy E

$\frac{\partial^2\sigma}{\partial\Omega\partial E'}$ = the double differential scattering cross section of the target (for neutrons incident at energy E, scattered through angle θ_s, to final energy E'.

$F(E,E')$ = the target transmission probability for once scattered neutrons

$\eta(E')$ = the detector efficiency for neutrons of energy E'

Δt = the interval of flight times measured, e.g. the window width of a multichannel time analyzer

(Note that vitreous silica is an isotropic system and thus the scattering is independent of the azimuthal scattering angle.)

Recall from Section 2.1 of Chapter II, the relationship between the double differential scattering cross section of the target and its scattering law is

$$\text{III-4} \qquad \frac{\partial^2\sigma}{\partial\Omega\partial E'} = \frac{1}{\hbar}\left(\frac{E'}{E}\right)^{\frac{1}{2}} S(K,\omega)$$

(Since we are concerned with a polyatomic scattering system, it is convenient to simplify the notation of Chapter II by including the neutron scattering lengths in the $S(K,\omega)$ of the above expression.) Noting that $E' = E - \hbar\omega$, Equation III-3 becomes

$$\text{III-5} \quad C(t) = N_o \frac{T}{\cos\beta} A_b \Delta\Omega \int d\omega \int dE\ \phi(E)\ F(E,E-\hbar\omega)\,\eta(E-\hbar\omega) \times S(K,\omega)\left(\frac{E-\hbar\omega}{E}\right)^{\frac{1}{2}} \delta\left[t - \frac{L}{(2E/m)^{\frac{1}{2}}} - \frac{L'}{(2(E-\hbar\omega)/m)^{\frac{1}{2}}}\right]\Delta t$$

In Section 2.2 of Chapter II it was shown that what one wishes to obtain from the experimental diffraction measurement is the structure factor of the target, i.e. the function

$$\text{III-6} \qquad \Gamma(K) = \int_{-\infty}^{\infty} S(K,\omega)\, d\omega$$

Consider now the differences between what is desired and what is actually measured. The integration indicated in III-6 is intended to be performed for all allowed energy transfers at a constant momentum transfer. In the experimental measurement the neutron detector performs an instrumental integration along a path of constant neutron

time of arrival. Loci of constant time of arrival in the $K - \hbar\omega$ plane which are characteristic of this experiment are shown in Figure 17 and it is apparent that the constant K condition is not satisfied. Also, it is obvious that the maximum possible energy transfer to the scattering system cannot exceed the energy of the incident neutron. From Equation III-5 one can see that each scattering event recorded in the experimental measurement is weighted by the expression

III-7 $$\phi(E)\ F(E,E-\hbar\omega)\ \eta\ (E-\hbar\omega)\left|\frac{E-\hbar\omega}{E}\right|^{\frac{1}{2}}$$

Although the functions in this weighting factor vary rather slowly, each event occurring at a different energy transfer receives a different weight in the integral.

Fortunately, our structure factor measurement is not seriously affected by these problems because the coherent neutron scattering by vitreous silica is predominantly elastic. In fact, most authors have agreed that in the conventional diffraction of thermal neutrons by solids it is reasonable to assume that the scattering is completely elastic (221)(222). This is the so-called "static approximation". In this case, $S(K,\omega) = \frac{d\sigma}{d\Omega}(K)\,\delta(\omega)$, and thus

III-8 $$\Gamma(K) = \int_{-\infty}^{\infty} S(K,\omega)\ d\omega = \frac{d\sigma}{d\Omega}$$

As a result, Equation III-5 reduces to the following form:

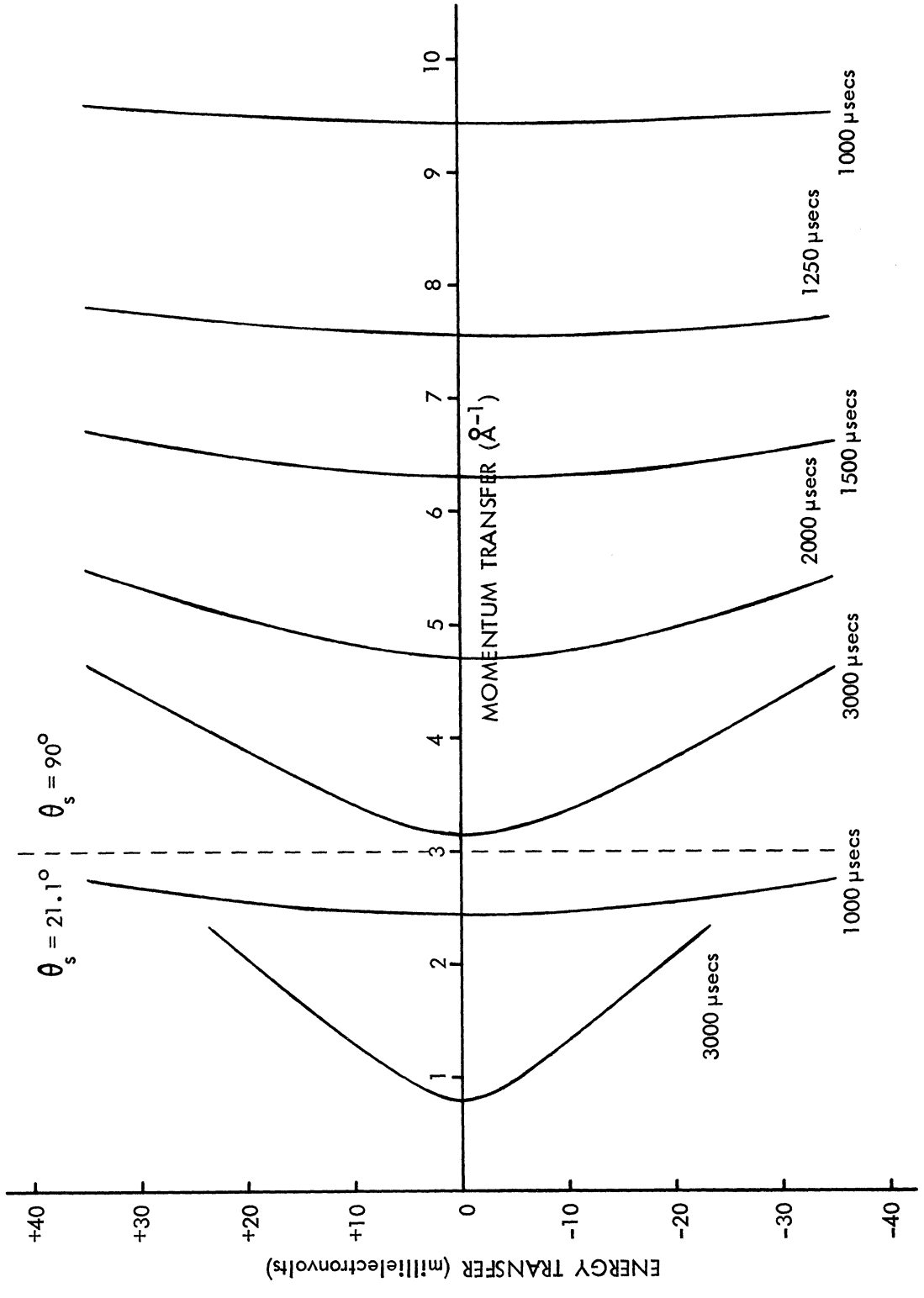

Figure 17. Loci of constant times-of-arrival for the time-of-flight diffraction measurement.

$$\text{III-9}\quad C(t) = N_o \frac{T}{\cos\beta} A_b \Delta\Omega \int dE\, \phi(E)\, F(E,E)\, \eta(E)\, \frac{d\sigma}{d\Omega} \times \delta\left[t - \frac{(L+L')}{(2E/m)^{\frac{1}{2}}}\right] \Delta t$$

If we define a new variable, $t' = \frac{(L+L')}{(2E/m)^{\frac{1}{2}}}$, then

$$\text{III-10}\quad C(t) = N_o \frac{T}{\cos\beta} A_b \Delta\Omega \int \phi(t')\, F(t',t')\, \eta(t')\, \frac{d\sigma}{d\Omega}\, \Delta t \times \delta(t - t') \frac{dE}{dt'}\, dt'$$

The t' integration of III-10 is straightforward and gives us the expression:

$$\text{III-11}\quad C(t) = \left[N_o \frac{T}{\cos\beta} A_b \Delta\Omega \phi(t)\, F(t,t)\, \eta(t)\, \frac{dE}{dt}\Big|_t \Delta t\right] \frac{d\sigma}{d\Omega}$$

where the neutron reciprocal velocity (time-of-flight) is $\tau = \frac{t}{(L+L')}$ and $\kappa = \frac{4\pi \sin(\theta_s/2)}{(h\tau/m_n)}$.

Every one of the bracketed factors in Equation III-11 may be either measured or calculated; however, in practice, a simpler and more accurate normalization is obtained through a comparison of the coherent scattering data to the intensity of scattering from an incoherent neutron scatterer in identical experimental conditions. A logical choice for the incoherent or reference scatterer in this experiment is vanadium. The coherent scattering cross-section for vanadium is only 0.048 barns, whereas the

incoherent scattering cross-section is 5.1 barns (223). Since the neutron scattering by the vanadium is also predominantly elastic, we may again invoke the static approximation and, in the same manner as above, derive the expression for the incoherent scattering count rate:

$$\text{III-12}\quad C'(t) = \left[N_o' \frac{T'}{\cos\beta'} A_b' \Delta\Omega' \phi'(t)\, F'(t,t) \eta'(t) \left.\frac{dE}{dt}\right|_t \Delta t\right] \frac{d\sigma}{d\Omega_V}$$

(The prime notation has been used to differentiate the factors relating to the incoherent scattering measurement from those of the coherent scattering measurement.)

The measurements are performed with the vanadium target mounted in the half of the sample cycler normally reserved for a dummy target. Both the vanadium and vitreous targets are 4" wide and 2" high. (As noted previously, the dimensions of the incident neutron beam are ¼" by 1¼".) The vitreous silica sample is inserted in the beam for a period of five minutes and is then replaced by the vanadium for an equal amount of time. The cycling of the two targets continues for the duration of the measurement.

Combining Equations III-11 and III-12, we obtain the following expression for the differential coherent scattering cross section of the vitreous silica:

$$\text{III-13}\quad \frac{d\sigma}{d\Omega} = \left[\frac{N_o' \frac{T'}{\cos\beta'} A_b' \Delta\Omega' \phi'(t)\, F'(t,t) \eta'(t)}{N_o \frac{T}{\cos\beta} A_b \Delta\Omega \phi(t)\, F(t,t) \eta(t)}\right] \frac{C(t)}{C'(t)} \frac{d\sigma}{d\Omega_V}$$

The angle between the direction of the incident beam and

the normal to the target surface, β, the area of the incident beam, A_b, the solid angle subtended at the target by the detectors, $\Delta\Omega$, and the detector efficiency, $\eta(t)$, are identical for both the coherent and incoherent scattering measurements. Furthermore, the cycling of the two targets should eliminate any effects from variations in the incident neutron flux. We see therefore that the above expression reduces to

$$\text{III-14} \qquad \frac{d\sigma}{d\Omega} = \left[\frac{C(t)}{C'(t)}\right]\left[\frac{N_o' T' F'(t,t) \frac{d\sigma}{d\Omega}_V}{N_o T F(t,t)}\right]$$

The calculation of the target transmission probabilities (or attenuation corrections) in Equation III-14 is straightforward and is discussed in Section 4.2 of Chapter IV.

The differential cross section of vanadium has been measured by Beyster (224). He has observed the neutron angular scattering distribution at 55 different energies ranging from 0.01 ev to 10 ev and at scattering angles of 30°, 45°, 60°, 90°, 120°, 135°, and 150°. The largest variation in the measured cross sections with angle is less than 10%. In addition, the integration of Beyster's cross sections agree to within 5% of the measured total cross section of vanadium.

The neutron energies transmitted by the two rotor system lie between 0.01 ev and 0.11 ev. Beyster's vanadium cross sections for these energies at scattering angles of

90^{o} and 30^{o} are shown in Figure 18. Since the variations of the cross sections will angle are so small, we have assumed that Beyster's 30^{o} vanadium data may be used to normalize our 21.1^{o} scattering angle data.

All of the scattering measurements were corrected for background effects. The range of the time-of-flight measurements was extended to both long and short times of arrival outside of the region in which the thermal neutron scattering from the targets was observed. The background was determined from the average count rates in these regions and subtracted from the measured count rates in the time range of interest to obtain C(t) and C'(t). Background measurements with the targets removed from the sample cycler indicated that the background was constant over the time range of interest. Data from time intervals where the background correction was an important contribution to the uncertainty were not used.

In the development of Equation III-14 we asserted that the neutron scattering is predominantly elastic. This claim can be substantiated with the aid of our double differential scattering cross section data (the results of the monochromator measurements which are described in Section 5.2, Chapter V). To illustrate the decrease in the scattering probability with increasing energy transfers, we calculate the function β , the fraction of the total scattering within the limits $\pm \hbar\omega$:

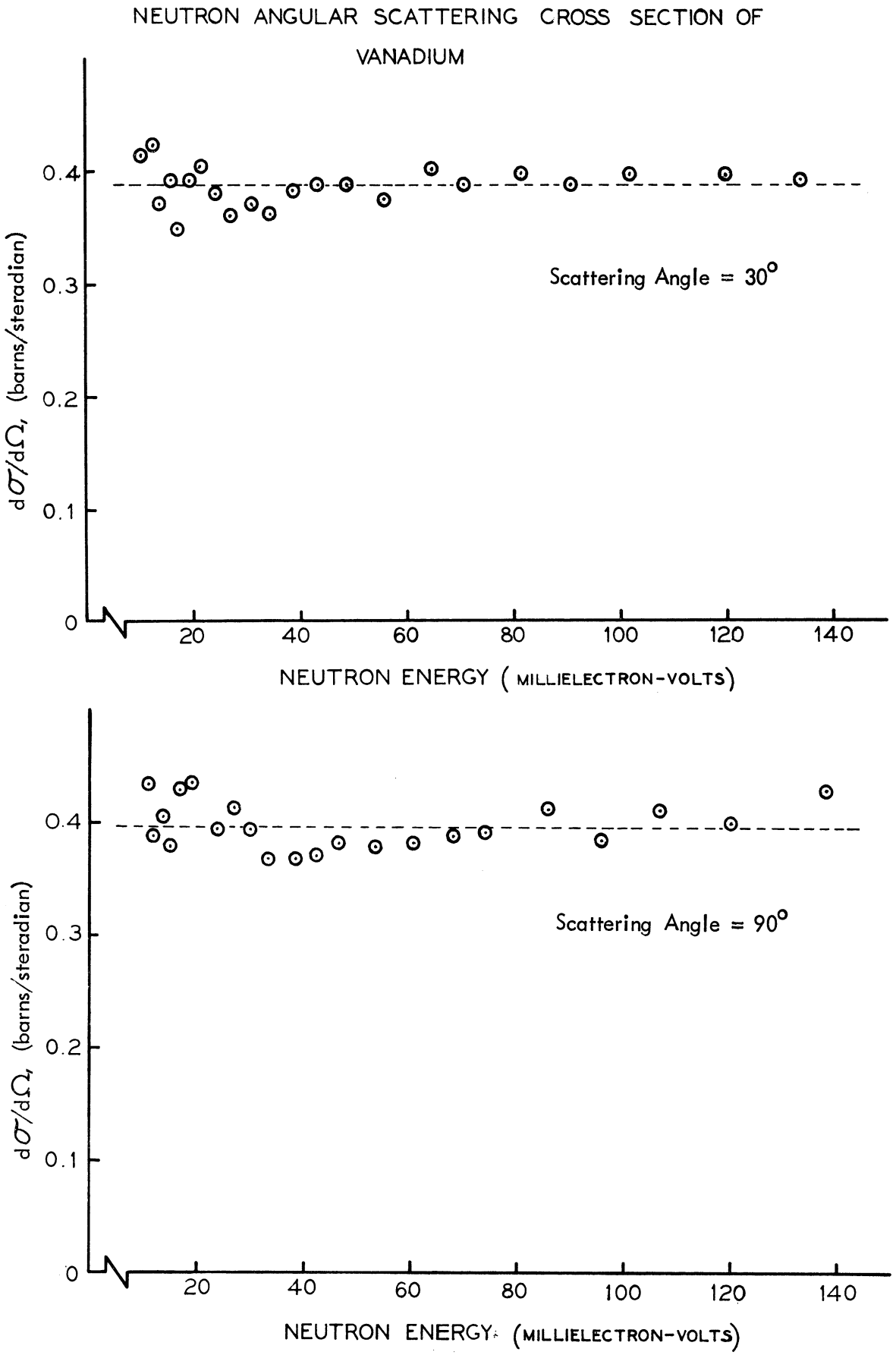

Figure 18. Single differential neutron scattering cross section of vanadium. (From Beyster (224).)

III-15 $$\beta = \int_{E-\hbar\omega}^{E+\hbar\omega} \frac{\partial^2\sigma}{\partial\Omega\partial E'}\, dE' \Big/ \int_{E-10meV}^{E+10meV} \frac{\partial^2\sigma}{\partial\Omega\partial E'}\, dE'$$

(To be precise, the limits of integration in the denominator of this expression should extend to the energy transfers at which the cross section goes to zero; however, poor counting statistics at large energy transfers and restrictions imposed by the experimental apparatus limit the effective range of the measurement. The cross section which we will use for this calculation decreases to less than 2% of its maximum value at energy transfers of ± 10 meV and therefore, the error introduced by neglecting the contributions to the total scattering probability at larger energy transfers should be negligible.)

A measurement of the vitreous silica cross section for scattering at an angle of 90° and an incident neutron energy of 34.3 meV has been employed for this demonstration. In Figure 19, values of β are plotted on the locus of the measurement in $\kappa - \hbar\omega$ space. The locus of a measurement with the two rotor configuration is also shown for the sake of comparison. One can see that more than 75 % of the scattering results in energy transfers of less than ± 3 meV. In fact, the minimal amount of broadening observed in the major (elastic) peak of the double differential cross section is due almost entirely to the resolution of the experimental apparatus rather than actual energy transfers.

Referring again to Figure 19, note that the path of

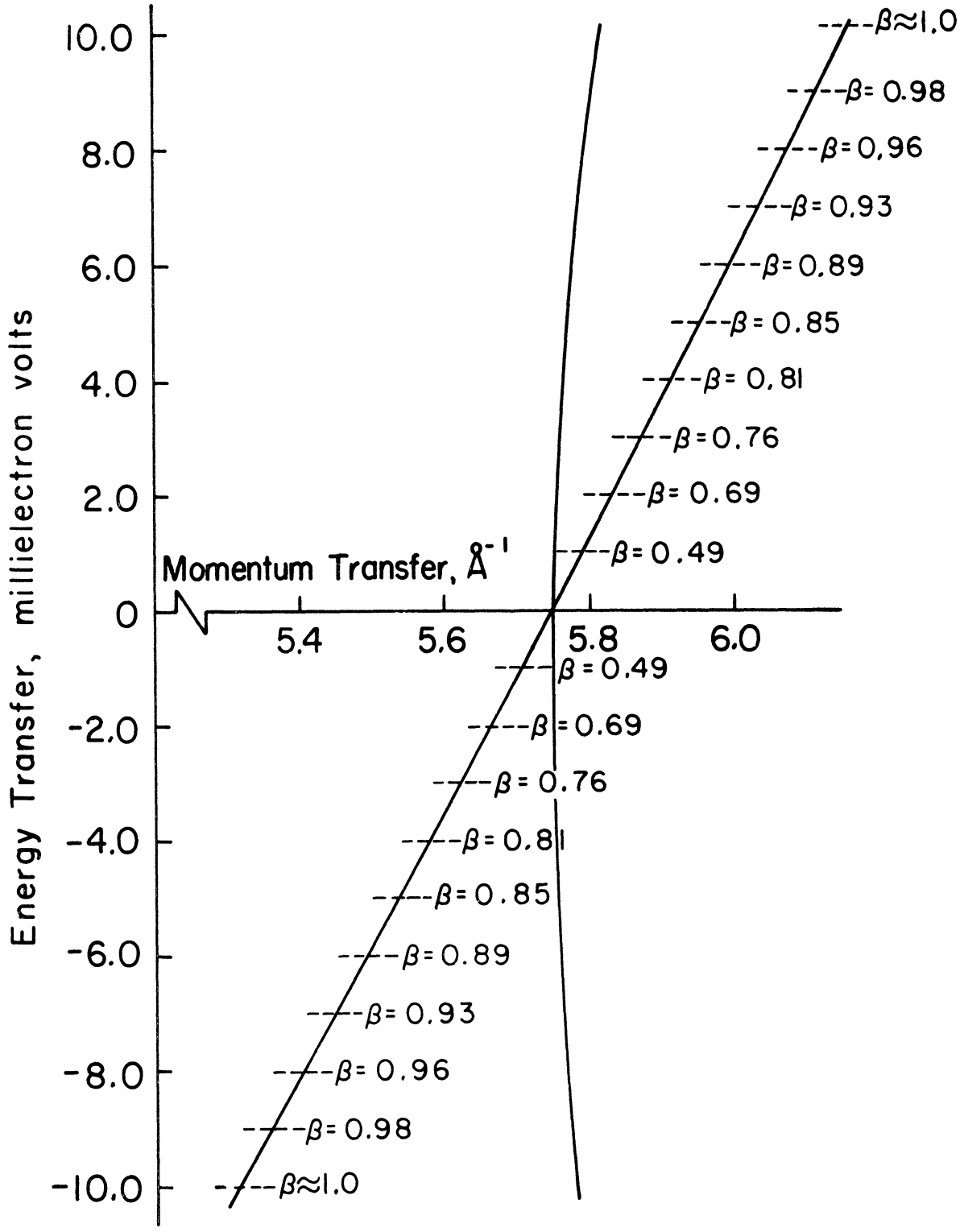

Figure 19. Fraction of the total neutron scattering by vitreous silica as a function of energy transfer.

the time-of-flight diffraction measurement with the two rotor configuration more nearly satisfies the constant momentum transfer condition than the comparable measurement with the monochromator. It is difficult to generalize and say that this condition is true for all momentum transfers for as was shown in Figure 17, the loci of the two rotor measurements vary considerably. However, let us briefly consider how the loci of these measurements are affected by the system's parameters and the choice of incident neutron energies and scattering angles.

It is relatively easy to show that if the locus of a time-of-flight measurement is to pass through the $\hbar\omega = 0$ axis tangent to the optimal measurement path of constant K (or K^2), the flight path lengths L and L' must be equal. In designing the experiment, one wants to position the target relative to the neutron source (rotor 2) and the detectors in such a manner that

$$\text{III-16} \qquad \left.\frac{d(K^2)}{d(\hbar\omega)}\right|_{\hbar\omega = 0} = 0$$

We rewrite Equation III-2 in the form

$$\text{III-17} \qquad \xi = \sqrt{\frac{2}{m_n}}\, t - \frac{L}{\sqrt{E}} - \frac{L'}{\sqrt{E'}} = 0$$

and the derivative is readily obtained (225) from the Jacobians:

$$\text{III-18}\qquad \frac{d(K^2)}{d(\hbar\omega)} = -\frac{\dfrac{\partial(K^2,\xi)}{\partial(E,E')}}{\dfrac{\partial(\hbar\omega,\xi)}{\partial(E,E')}} = -\frac{\det\begin{vmatrix} \dfrac{\partial(K^2)}{\partial E} & \dfrac{\partial\xi}{\partial E} \\ \dfrac{\partial(K^2)}{\partial E'} & \dfrac{\partial\xi}{\partial E'} \end{vmatrix}}{\det\begin{vmatrix} \dfrac{\partial(\hbar\omega)}{\partial E} & \dfrac{\partial\xi}{\partial E} \\ \dfrac{\partial(\hbar\omega)}{\partial E'} & \dfrac{\partial\xi}{\partial E'} \end{vmatrix}}$$

Since $E = E'$ for $\hbar\omega = 0$,

$$\text{III-19}\qquad \left.\frac{d(K^2)}{d(\hbar\omega)}\right|_{\hbar\omega = 0} =$$

$$= 2m_n \left.\frac{\dfrac{L'}{E'^{3/2}}\left(1 - \sqrt{\frac{E'}{E}}\cos\theta_s\right) - \dfrac{L}{E^{3/2}}\left(1 - \sqrt{\frac{E}{E'}}\cos\theta_s\right)}{\dfrac{L}{E^{3/2}} + \dfrac{L'}{E'^{3/2}}}\right|_{E = E'}$$

$$= \frac{2m_n}{(L + L')}(1 - \cos\theta_s)(L - L')$$

Thus, for all values of K, the condition for the constant K intercept at $\hbar\omega = 0$ is $L = L'$. It is also clear from Figure 17 that in attempting to make a measurement at a particular K, the curvature of the instrumental integration path is minimized when one chooses a combination of small θ_s and a high incident neutron energy. In addition to producing a better approximation to the desired constant K condition, a high incident neutron energy results in less of a variation in the data weighting function (Equation III-7).

3.3.2 CALIBRATION OF THE TIME-OF-FLIGHT DIFFRACTION MEASUREMENT

To this point in the description of the diffraction experiment, the errors which arise in the measurement of a neutron's time-of-flight have been ignored. For example, it has been implied that the trigger signal from the magnetic pickup on rotor 2 occurs at the exact instant when the rotor is in the open position. In practice this is not the case since it is virtually impossible to attain exact alignment of the rotor slot and the magnetic pickup position when the rotor housing is assembled. Another source of error is the measurement of the path lengths between the rotors, target, and detectors. The shielding around the neutron flight paths makes it difficult to physically measure these distances with the desired accuracy. Because of these and other sources of error, a technique to calibrate the time-of-flight scale has been developed.

At a given rotor speed, the range of neutron energies in the bursts transmitted by rotor 2 may be determined from Figure 16. A polycrystalline, coherent neutron scatterer with known atom plane spacings d_{pqr} is placed at the target position and the neutrons scattered from the incident beam are observed at a scattering angle θ_s. The wavelengths of the coherently scattered neutrons will lie within small bands centered about those λ's which satisfy the Bragg relation: $\lambda = 2d_{pqr}\sin(\frac{1}{2}\theta_s)$. If each coherent neutron

scattering peak observed in the time-of-flight distribution can be correctly associated with a particular Bragg reflection, the time-of-flight scale is calibrated and path lengths and timing errors are easily calculated.

The first step in the analysis of the calibration data is to fix the location of each coherent maxima in the neutron time-of-flight distribution: the i^{th} peak appears at channel number $\bar{N}_i = \sum N \cdot C_N / \sum C_N$ where C_N is the number of counts in the channel N corrected for background. The background is obtained by averaging the counts in a number of channels on each side of the coherent peak.

In order to express the relationship between the neutron wavelength λ_i and the time-of-flight analyzer channel $\bar{N}_i$, the following definitions are required. The triggering error which results from the misalignment of the magnetic pickup on rotor 2 is identified as δ_T. It is assumed that this error includes any error in the time delay unit which is interposed between the magnetic pickup and the time-of-flight analyzer (Figure 12). δ_T is positive if rotor 2 opens prior to the signal from the magnetic pickup. The time-of-flight analyzer is responsible for a timing error of $1.5\ \Delta t$. (Recall that Δt is the channel width of the time of flight analyzer.) This error is subtracted from the measured neutron time-of-flight because it represents a delay in the functioning of the time-of-flight analyzer after it receives its triggering signal. Since the distance

from rotor 2 to the target is L and the distance from the target to the detector plane is L', the coherently scattered neutrons in the peak centered at channel $\bar{N}_i$ will have a time-of-flight per unit path length of

III-20 $$\tau_i = (T_{delay} + \delta_T + (\bar{N}_i - 1.5)\,\Delta t)/(L + L')$$

If τ_i is in units of microseconds per meter, a conversion factor of 3.956×10^{-3} will give λ_i, the neutron wavelength in angstroms:

III-21 $$\lambda_i(\text{Å}) = 3.956 \times 10^{-3}\frac{(T_{delay} + \delta_T + (\bar{N}_i - 1.5)\,\Delta t)}{(L + L')}$$

Assuming that the coherent neutron peak at $\bar{N}_i$ is correctly identified as the diffraction from the planes with spacing d_{pqr}, the corresponding λ_i in III-21 is obtained from the Bragg equation: $\lambda_i = 2d_{pqr}\sin(\frac{1}{2}\theta_s)$. A plot of the λ_i's versus the corresponding $\bar{N}_i$'s will be linear. The slope of the plot is $(3.956\times10^{-3})\,\Delta t/(L + L')$; the channel width Δt is known, and therefore, the distance $(L + L')$ is determined. The intercept of the plot with the ordinate, $\bar{N} = 0$, gives us a number equal to

III-22 $$(3.956\times10^{-3})(T_{delay} + \delta_T - 1.5\,\Delta t)/(L + L')$$

T_{delay}, the delay time of the trigger pulse to the analyzer, the channel width Δt, and $(L + L')$ are all known, and therefore, we obtain the triggering error δ_T.

The entire calibration hinges on the correct identification of each coherent peak in the neutron time-of-flight distribution with a particular Bragg reflection. A description of the calibration for a measurement at the 90^{o} detector bank will illustrate how this assignment of the Bragg reflections takes place. The rotor speed for this measurement was 400 cycles per second. From Figure 16 it is determined that the approximate range of neutron energies in the bursts produced at this rotor speed extends from 20 meV to 85 meV. The equivalent range of neutron wavelengths is from 2.022 Å to 0.9810 Å.

An aluminum target was used as the calibration standard. The crystal structure of aluminum is cubic-close packed; the edge of the cubic unit cell has a length of 4.04145 Å (226). Thus, we have plane spacings of

$$d_{pqr} = \frac{4.04145\ \text{Å}}{(p^2+q^2+r^2)^{\frac{1}{2}}} \qquad \text{III-23}$$

The neutron wavelengths corresponding to the allowed coherent reflections at $\theta_s = 90^{o}$ are listed in Table III-2. A comparison of the wavelengths of the allowed Bragg reflections with the range of neutron wavelenths transmitted by the rotors at 400 cps indicates that as many as nine coherent scattering peaks might be observed in the time-of-flight distribution. However, since only seven peaks are observed in the actual measurement, one must determine which of the nine possible neutron wavelengths should be

TABLE III-2 NEUTRON DIFFRACTION MAXIMA OF ALUMINUM

Aluminum lattice constant = 4.04145 Å

$d_{pqr} = 4.04145\ \text{Å}/(p^2+q^2+r^2)^{1/2}$

p,q,r - no mixed indices allowed

$\lambda = 2\, d_{pqr} \sin(\Theta_s/2)$; Data tabulated below for $\Theta_s = 90^\circ$

plane	d (Å)	λ (Å)
111	2.33333	3.2998
200	2.02072	2.8577
220	1.42886	2.0207
311	1.21854	1.7233
222	1.16666	1.6499
400	1.01036	1.4289
331	0.92717	1.3112
420	0.90369	1.2780
422	0.82495	1.1666
333	0.77777	1.0999
440	0.71443	1.0104
531	0.68313	0.9661
442	0.67358	0.9526
620	0.63901	0.9037
533	0.61632	0.8716
622	0.60927	0.8616
444	0.58333	0.8250
711	0.56592	0.8003
642	0.54006	0.7638
553	0.52615	0.7441

assigned to the seven peaks. The matching of the appropriate wavelengths to the observed peaks is essentially a trial and error process. If the assignments are incorrect, the plot of λ_i versus $\bar{N}_i$ obviously will not be linear. When the correct assignments have been made, the data will appear as shown in Figure 20. The line indicated in this figure was fitted by a least squares analysis using the seven data points. The path lengths and triggering error are obtained from its slope and intercept in the manner described above.

In the foregoing discussion it was assumed that the scattering angle of the experiment is known prior to the calibration measurement. However, prior knowledge of the scattering angle is not required; if one wishes, the time-of-flight scale can be calibrated directly in terms of the desired units of momentum transfer. The magnitude of the momentum transfer of an elastically scattered neutron is $4\pi \sin(\frac{1}{2}\theta_s)/\lambda$. From the Bragg equation we know that $\sin(\frac{1}{2}\theta_s)/\lambda = 1/2d_{pqr}$ and therefore, $4\pi \sin(\frac{1}{2}\theta_s)/\lambda = 2\pi/d_{pqr}$. The calibration consists of simply matching each of the observed coherent scattering peaks with a particular d_{pqr}.

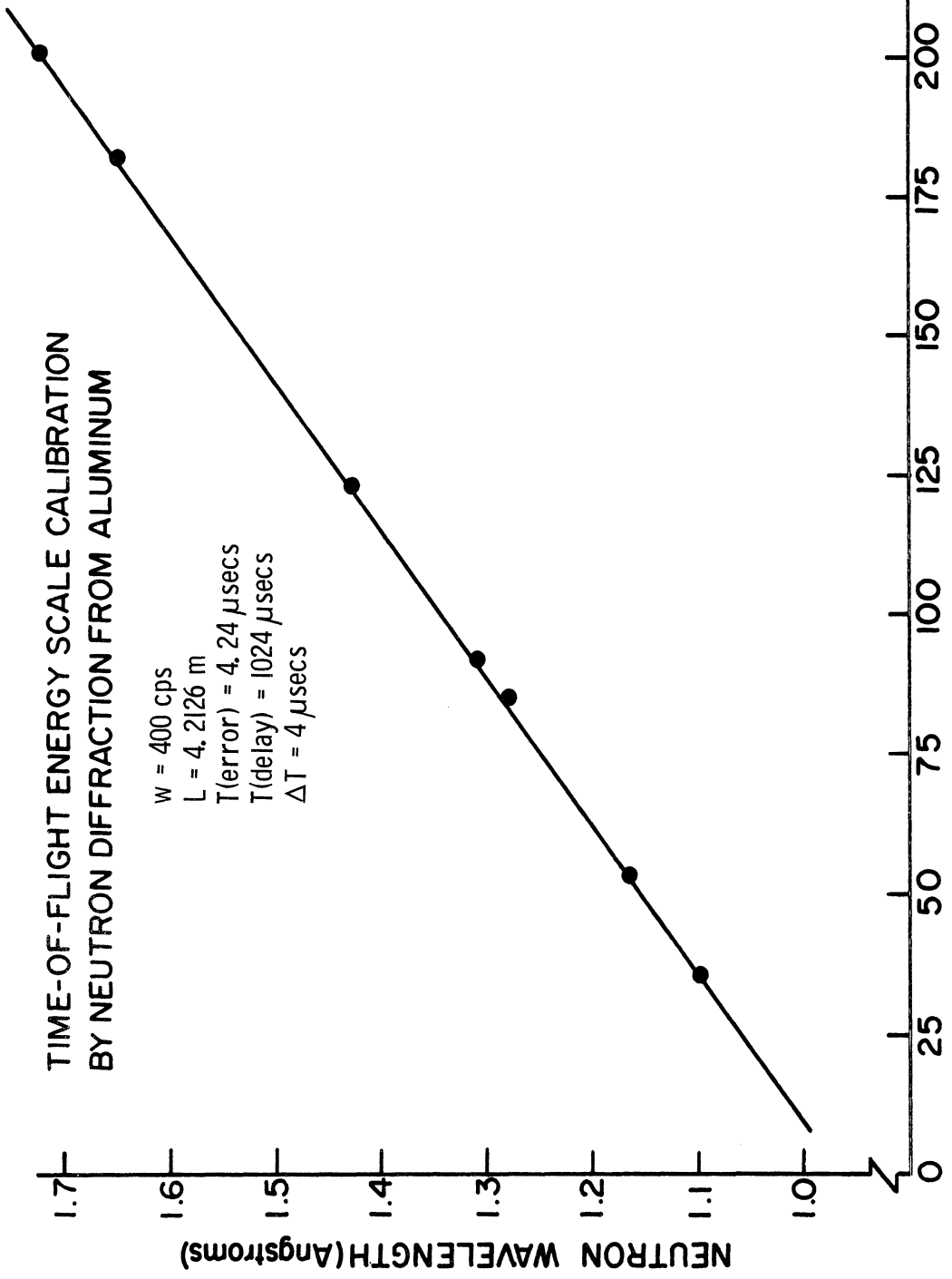

Figure 20. Neutron wavelengths of aluminum diffraction maxima as a function of time-of-flight analyzer channel.

3.3.3 RESOLUTION OF THE TIME-OF-FLIGHT DIFFRACTION EXPERIMENT

The resolution of the time-of-flight diffraction experiment is determined from the full widths at half maximum intensity of the aluminum diffraction maxima obtained in the calibration measurement. This data is presented in Figure 21.

In the region where the data from the bank of detectors at the 21.1° scattering angle overlaps the data from the 90° bank (~ 3 Å^{-1}), one can see that the resolution of the measurement at the 90° scattering angle is superior. This can be explained in part by the fact that the resolution of the measurements decrease with increasing rotor speed. In the region of the overlap, the data recorded at the 21.1° detector bank was obtained at a rotor speed of 480 cps; the data from the 90° bank was obtained at a rotor speed of 240 cps. However, Carpenter (233) has shown that the orientation of the detector plane relative to the direction of the scattered neutrons also contributes significantly to the resolution of the measurements.

As noted previously, elastically scattered neutrons with a time-of-flight per unit path length (reciprocal velocity) of τ arrive at a detector at time t:

$$t = \left[L + L'(\theta_s)\right]\tau \qquad \text{III-24}$$

where L is the distance from rotor 2 to the target and

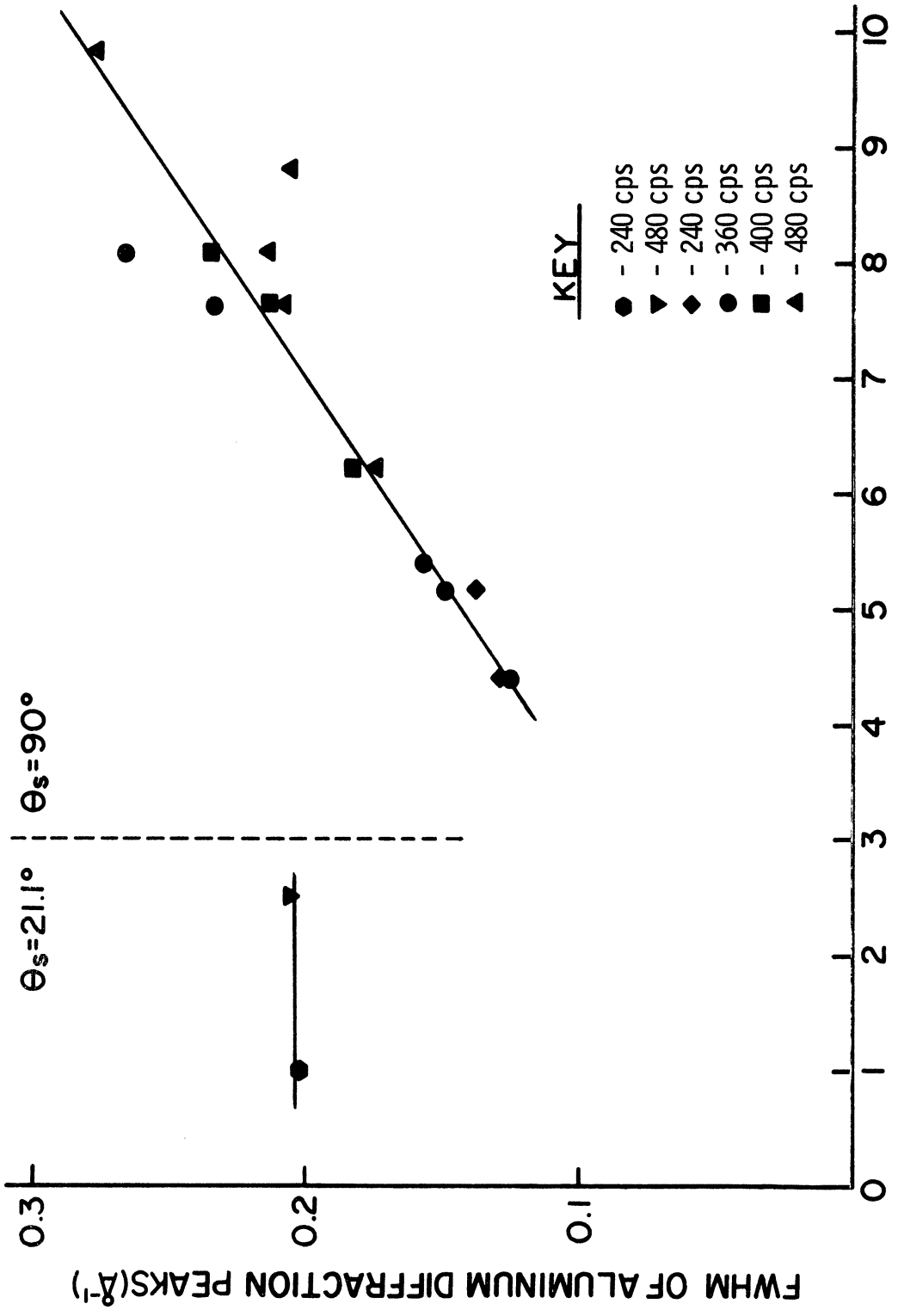

Figure 21. Resolution of the time-of-flight diffractometer.

$L'(\theta_s)$ is the distance from the target to the detector at scattering angle θ_s. Since the momentum transfer is

III-25 $$K = \frac{4\pi \sin(\frac{1}{2}\theta_s)}{(h\tau/m_n)}$$

we obtain the following expression for t as a function of K:

III-26 $$t = \frac{4\pi(m_n/h)\ \sin(\frac{1}{2}\theta_s)\ \left[L + L'(\theta_s)\right]}{K}$$

From III-26 it is clear that t may be made independent of θ_s for fixed K if:

III-27 $$\left[L + L'(\theta_s)\right]\ \sin(\tfrac{1}{2}\theta_s) = \text{constant} = L + L'(\pi)$$

For a fixed path length L, the locus of constant time of arrival is then

III-28 $$L'(\theta_s) = \frac{L + L'(\pi)}{\sin(\frac{1}{2}\theta_s)} - L$$

For the best possible resolution, the neutron detectors should be oriented tanget to this locus. The angle ϕ between the tangent to the locus and the incident beam direction is

III-29 $$\phi = \theta_s - \tan^{-1}\left[2\ L'(\theta_s)\ \tan(\tfrac{1}{2}\theta_s)/\ L + L'(\theta_s)\right]$$

For the system described here, $\phi = 11^\circ 11'$ at the $21^\circ 6'$ scattering angle and $\phi = 46^\circ 21'$ at the 90° scattering angle.

The diffraction measurements described here were performed with the detector plane at each scattering angle oriented perpendicular to the scattered neutron beam.

This means that the detectors at the 90° scattering angle would have to be rotated $46^{\circ}21'$ and the $21^{\circ}6'$ scattering angle detectors would have to be rotated $80^{\circ}5'$ to optimize the resolution. Unfortunately, these orientations were precluded by the manner in which the detectors were mounted and the physical arrangement of the shielding in the experimental area.

The effect of the non-optimum positioning of the detectors is apparent in Figure 21. As noted above, the resolution of the measurements should decrease with increasing rotor speed. While this effect is observed in the data from the 90° scattering angle, it is not observed in the data from the $21^{\circ}6'$ scattering angle. Since the misalignment of the detectors at the smaller scattering angle is much more severe than at 90°, this is the dominant factor in determining the resolution of the measurements at this angle.

Although the resolution of the measurements was not optimized, the quality of our data was not seriously affected. Corrections to the data for resolution broadening are described in Section 4.5.4 of Chapter IV and the differences between the corrected and uncorrected results are barely discernible.

3.3.4 TOTAL CROSS SECTION MEASUREMENT BY THE TIME-OF-FLIGHT TECHNIQUE

The total neutron cross section of vitreous silica was obtained through a series of transmission measurements. As in the diffraction experiment, the measurements were performed with the polychromatic thermal neutron pulses produced by the two rotor configuration. The transmission characteristics of the system (Figure 16) limited the range of the measurements to neutron energies between 10 meV and 110 meV.

The vitreous silica target was mounted in the sample cycler perpendicular to the direction of the incident neutron beam. The thermal neutron beam was monitored by a three inch diameter, parallel plate fission chamber mounted in the primary beam at a distance of 0.6432 meters beyond the target. The neutron sensitive surface of this detector is a 2 mg/cm^2 coating of uranium oxide (90% enriched U^{235}) on a 0.0625" aluminum window; its detection efficiency for 30 meV neutrons is $\sim 2 \times 10^{-3}$. The fission chamber was operated in the ionization region in order to discriminate against gamma and alpha background radiation.

The experimental measurement consisted of cycling the vitreous silica target in and out of the beam and recording the neutron time-of-flight distribution for each position. The period of each cycle was five minutes divided equally between the in-beam and out-of-beam target positions. The

only difference in the observed count rates for the two target positions should arise from the neutron attenuation by the target when it is in the beam: $\exp -(N_o \sigma(\tau)\, x)$. (N_o is the number of target nuclei per unit volume, $\sigma(\tau)$ is the total microscopic neutron cross section of the target as a function of the neutron time-of-flight per unit path length, and x is the target dimension parallel to the direction of the incident beam.) Any effect from variations in the incident neutron flux throughout the measurements is assumed to have been averaged out as a result of the cycling of the target. Other factors affecting the observed count rates such as the detector efficiency, are identical for measurements with or without the target in the beam. Thus, if $C_o(t)$ is the observed count rate with no target in the beam at a time t after rotor 2 opens, and $C_T(t)$ is the observed count rate with the target in the beam, the total microscopic neutron cross section as a function of the neutron time-of-flight per unit path length is

$$\text{III-30} \qquad \sigma = (1/N_o x)\, \ln(C_o(t)/C_T(t)) \; ; \; \tau = t/L_{2D}$$

L_{2D} is the length of the flight path from rotor 2 to the fission chamber.

Both $C_o(t)$ and $C_T(t)$ were corrected for contributions from the background count rates. The backgrounds for the time-of-flight distributions, with and without the target in the beam, were determined in exactly the same manner as

in the diffraction measurements. The range of the time scale of the measurements was extended to both long and short times t which lie outside of the region covered by the thermal neutron pulses. The average background was determined in these regions and subtracted from the measured count rates in the time range of interest. Because of the relatively low intensity of the neutron beam and the low detection efficiency of the fission chamber, the dead times of the detector and the time-of-flight analyzer were not significant factors in these measurements.

3.3.5 GEOMETRY OF THE TOTAL CROSS SECTION MEASUREMENT

Conditions of "good geometry" for a total cross section measurement require that the neutron detector subtends a small angle at the sample and vice versa. If the subtended angles are large, some of the neutrons scattered by the target will reach the detector and the correct contribution of the scattering cross section will not be included in the measured $\sigma(\tau)$.

In order to decrease the angle which the fission chamber subtends at the target position, a 40 mil cadmium sheet with a 3/8 inch diameter hole was mounted in the beam path directly in front of the fission chamber.

The angle which the target subtends at the detector decreases as the detector is moved further away from the target. Thus, if the geometry of the experiment is poor, one would expect to find that the measured total cross section varies with detector position. A simple transmission measurement was performed with the four rotor monochromator to determine if such an effect could be observed in this experiment. The physical arrangement of the target, collimators, and fission chambers was exactly the same as for the measurements with the two rotor configuration. (The monochromator measurements also served as a check on the results of the two rotor, polychromatic transmission measurements.)

For an incident neutron energy of 34.25 meV, the

target transmission measured by the fission chamber 0.6432 meters from the target was 0.832 ± 0.009; the target transmission measured simultaneously by a fission chamber 1.244 meters from the target was 0.830 ± 0.012. For other neutron energies, similar transmission measurements with the two fission chambers all agreed within the limits of the experimental errors. The magnitude of the errors in these measurements were comparable to those in the example cited above.

3.3.6 CALIBRATION OF THE TOTAL CROSS SECTION MEASUREMENT

The calibration of the time-of-flight scale in the total cross section measurement requires measurements with both the four rotor monochromator and the two rotor configuration. The neutron time-of-flight per unit path length as a function of analyzer channel N is

III-31 $$\tau = (T_{delay} + \delta_T + (N - 1.5)\Delta t)/(L_{2T} + L_{TD})$$

The delay time between the signal from the magnetic pickup and the triggering of the time-of-flight analyzer, T_{delay}, the triggering error, δ_T, and the timing error introduced by the time-of-flight analyzer, $-1.5\Delta t$, were defined in Section 3.3.3. L_{2T} is the distance from rotor 2 to the target and L_{TD} is the distance from the target to the fission chamber. The unknown factors in the above equation which are to be determined by the calibration are δ_T and $(L_{2T} + L_{TD})$.

The first step in the calibration is the measurement of several path lengths. This is accomplished with the monochromatic neutron bursts produced by the four rotor configuration. Straker (202) has described the technique of these measurements in detail and thus, the discussion here is confined to indicating what information one obtains. A fission chamber is mounted in the sample cycler at the target position and by an analysis of the relative times of arrival of monochromatic neutron pulses at the target

position and the positions of the other fission chambers in the primary beam path one is able to determine L_{4T} , the distance between rotor 4 and the target position, and L_{TD} , the distance between the target position and the fission chamber used for the transmission measurements. L_{24} , the spacing between rotors 2 and 4 , can be measured directly when the system is assembled. Thus we have $(L_{2T} + L_{TD}) = (L_{24} + L_{4T} + L_{TD})$.

The next step is the removal of rotor 4 from the system to form the two rotor configuration. In order to do this, the sample cycler and the fission chambers must first be removed from the beam path. Once rotor 4 is gone, the sample cycler and the fission chambers are returned to their former positions; brackets holding these items enable the original positions to be reproduced within ± 0.003 meters.

The final step requires that the calibration measurement previously described for the two rotor diffraction experiment be performed. This measurement gives us the triggering error δ_T , which, for a given rotor speed, is the same for both the diffraction and transmission measurements.

3.4 THE CRYSTAL SPECTROMETER

The maximum momentum transfer observed in the time-of-flight diffraction measurements was ~ 10 Å^{-1}. Through the use of the University of Michigan's triple axis crystal spectrometer it was possible to extend the range of the vitreous silica measurements to momentum transfers of ~ 14 Å^{-1}. The mechanical details of this spectrometer and its response to various idealized cross sections have been described in detail by Donovan (227) and Myers (228). The following discussion is confined to a brief description of the instrument and its use in the measurement of the silica diffraction pattern.

The triple axis crystal spectrometer is designed to fulfill the same functions as the mechanical monochromator facility, i.e. the instrument incorporates a means of monochromating a polychromatic neutron beam and a system capable of determining the energies and directions of neutrons scattered from the monochromatic beam by a target. Since the diffraction measurement does not require energy analysis of the scattered neutrons, the system is operated in the configuration shown in Figure 22.

The crystal spectrometer is sited at beam port "A" of the Ford Nuclear Reactor. As in the case of the mechanical monochromator facility, the front end of the spectrometer's primary collimator is extended through the pool water into a reentrant hole in the D_2O tank by means of a nitrogen-

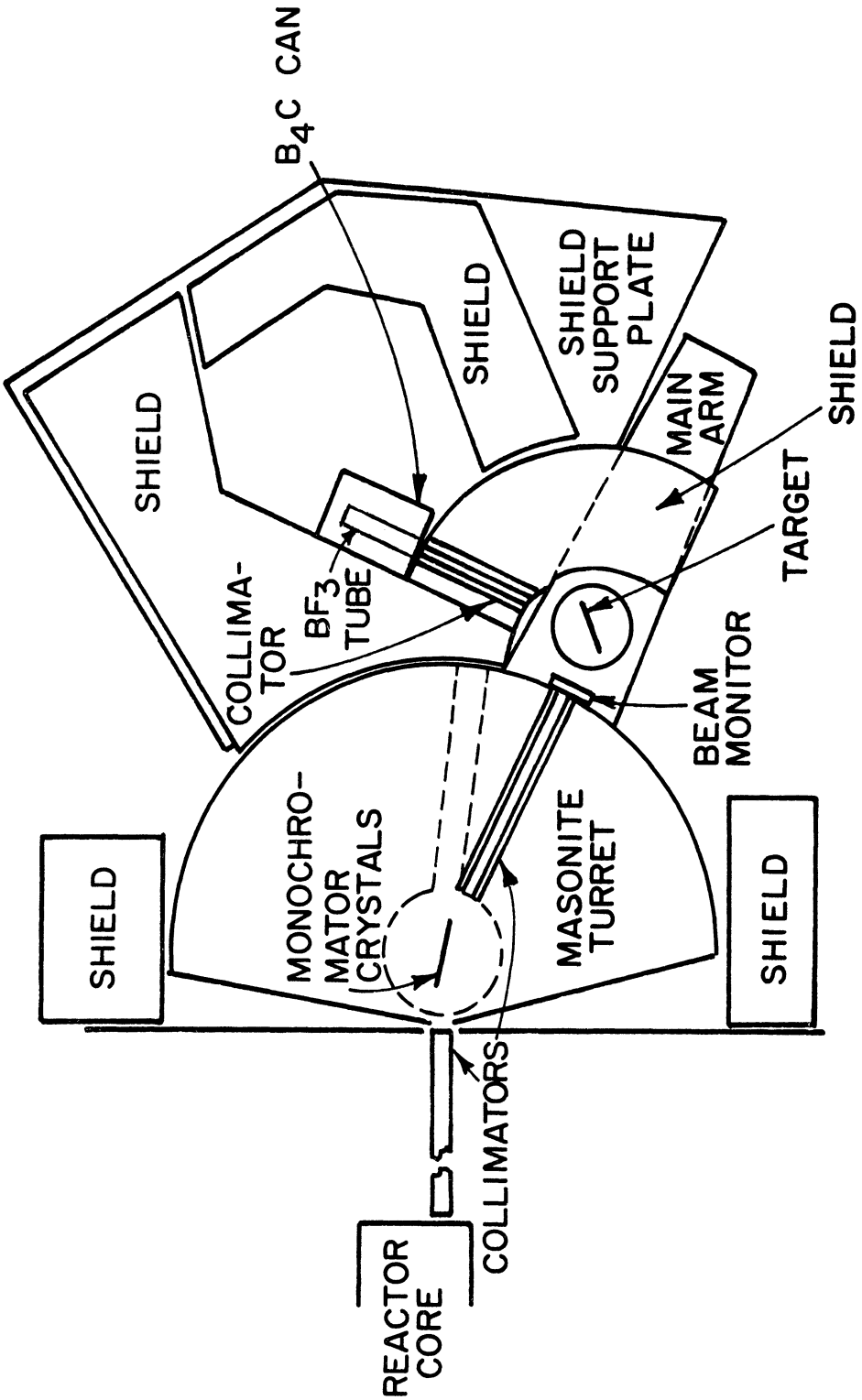

Figure 22. Schematic drawing of the triple axis crystal spectrometer used as a diffractometer.

filled stainless steel bellows (206). The neutron beam is collimated by a 120" Soller collimator with two 3" high by 0.905" wide slits. In the horizontal direction the maximum angular divergence of the beam is 25.9 minutes; the vertical divergence is 1.91 degrees.

The monochromatic beam is produced by the Bragg scattering of neutrons from the (200) planes of two copper crystals. These crystals are positioned so that the diffracted neutron beam is focused in the vertical direction at the target. The energies of the neutrons in this beam are varied by rotating the monochromator and shield. To reach the target the neutrons pass through a 40" collimator mounted in a beam port in the masonite turret shield. The slit in this collimator is 2" high by $\frac{1}{4}$" wide. The beam intensity at the target was between 1.5×10^6 and 2.0×10^6 neutrons per second.

The target is mounted on the main Bragg arm of the spectrometer at a distance of 52.5" from the monochromator. The Bragg arm moves in a 2:1 relationship with the monochromating crystals. This turning ratio is maintained with an accuracy of one minute in 90 degrees of rotation.

Neutrons scattered by the target were observed at a fixed scattering angle of $103^{\circ}34'$ by a 3" diameter, end window BF_3 tube. The detector was surrounded by a 20 mil sheet of cadmium and $2\frac{1}{2}$" of B_4C powder to shield against the stray neutron background; the detector efficiency is

III-32 $$\eta(E) = (0.919)\ (1 - \exp\left[-1.98(25.3/E)^{\frac{1}{2}}\right])$$

where E is the neutron energy in millielectronvolts. An 18" long Soller collimator with nineteen 0.125" wide slits was mounted in front of the detector; the distance between the front face of the collimator and the target was 6". The maximum horizontal angular divergence of the scattered neutron beam was 25.0 minutes, the vertical divergence was 7.5 degrees. The collimator-detector unit occupied the position normally occupied by the energy analysis crystal when the spectrometer is operated as a triple axis instrument.

The measurement was performed by varying the incident neutron energy and as noted above, observing the scattered neutron intensity at a fixed scattering angle. Momentum transfers ranging from ~ 7 Å^{-1} to ~ 14 Å^{-1} were observed. The intensity of the neutron beam incident on the target was monitored by a high transmission, parallel plate fission chamber. For each incident neutron energy, the data output of the spectrometer was the ratio C_2/C_1, C_2 scattering events detected by the BF_3 tube per C_1 monitor counts.

Several sources of experimental error must be considered and corrections applied to this data to obtain an accurate measure of $d\sigma/d\Omega$ for the target. One potential source of error is the fact that the neutrons diffracted by the copper crystals are not truly monoenergetic. The Bragg equation, $n\lambda = 2d \sin(\frac{1}{2}\theta_s)$, indicates that neutrons of wavelengths $\lambda, \lambda/2, \lambda/3$, etc., are diffracted by the crystals.

Fortunately, the source intensity, the crystal reflectivities, and the detector efficiencies all decrease with increasing neutron energy. Myers (228) has developed an expression for the "effective monitor efficiency" which takes all of these factors into consideration. He shows that, except for neutron energies below ~35 meV, the correction for the monitor efficiency is the only correction necessary to obtain the intensity of first order neutrons incident on the target. The minimum incident neutron energy in this experiment was 41.5 meV.

Another source of error is the fact that neutrons which have lost or gained energy in scattering from the target do not have an equal probability of detection. Also, the instrumental integration performed by the BF_3 tude does not occur along a locus of constant momentum transfer. Fortunately, these are not serious problems since the efficiency of the BF_3 tube varies slowly with energy, and as was shown previously, the neutron scattering by vitreous silica is predominantly elastic.

The major contribution to the background in these measurements comes from the incoherent scattering of neutrons by the copper monochromator crystals. This background is measured by rotating the crystals slightly off the Bragg condition. In cases where (1) the target was removed, and (2) cadmium was placed between the target and the detector, the count rates recorded by the BF_3 tube were negligible.

3.4.1 CALIBRATION OF THE CRYSTAL SPECTROMETER

Two calibrations are required: (1) the incident neutron energy as a function of the main Bragg arm position, and (2) the scattering angle at which the BF_3 detector is positioned.

Since the calibration of the main Bragg arm scale is well established from previous experiments, the main concern here is the measurement of the scattering angle. For this measurement the BF_3 detector is positioned as close as possible to the desired scattering angle and a ½" thick polycrystalline aluminum sample is mounted at the target position. The scattered neutron intensity from the aluminum is recorded as a function of the main Bragg arm position, i.e. the wavelengths of the neutrons incident on the target. As shown in Figure 23, the diffraction of neutrons by the (422), (400), (331), (420), and (333) crystal planes of the aluminum target produces large coherent peaks in the scattering data at positions of the main Bragg arm corresponding to neutron wavelengths λ_{hkl}. The scattering angle θ_s, which remains fixed throughout the measurements, is calculated from the Bragg relationship: $\lambda_{hkl} = 2d_{hkl}\sin(\frac{1}{2}\theta_s)$.

The calibration of the main Bragg arm scale, which is required for the θ_s measurement described above, is described in detail by Donovan (227). Briefly, the angular distribution of neutrons diffracted by the aluminum target is measured with the main Bragg arm fixed in one position. Coherent scattering peaks due to the diffraction of neutrons from the (111), (200), (220), and (311) crystal planes are

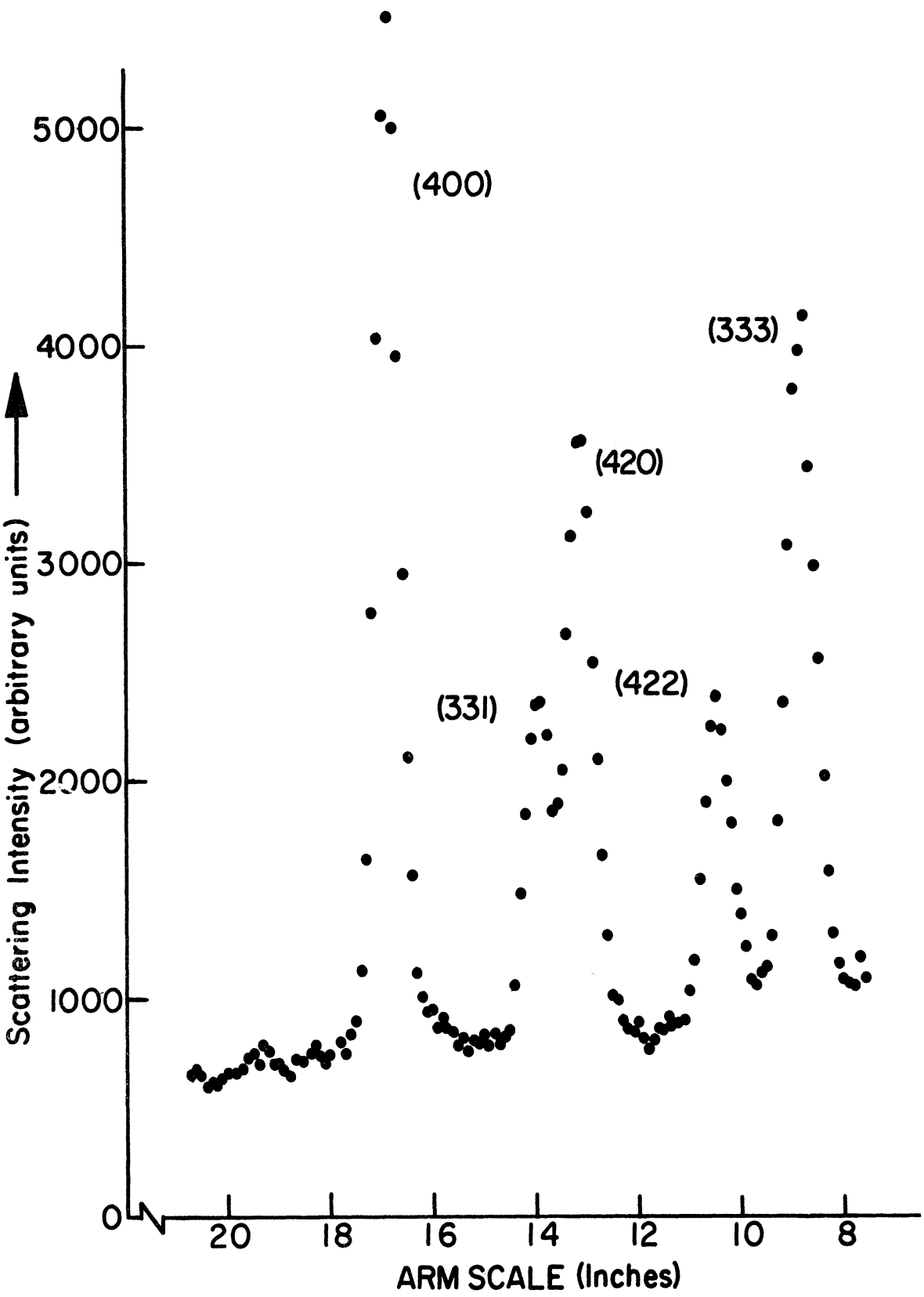

Figure 23. Aluminum diffraction maxima measured with the crystal diffractometer.

observed at the positions θ_{hkl} in the angular distribution. The neutron wavelength corresponding to the main arm setting at which the measurement is made is: $\lambda = 2d_{hkl}\sin(\frac{1}{2}\theta_{hkl})$. This measurement is repeated at several other positions of the main Bragg arm to complete the calibration.

It is apparent that the main arm calibration requires an accurate scale with which to measure the θ_{hkl}'s in the angular scattering distribution. The scattering angle measurement described at the beginning of this section cannot be used since it requires prior knowledge of the arm position-neutron wavelength relationship. However, there is no problem since any error in the angle scale is easily determined from the angular scattering data. For example, let us assume that the angle scale is in error by an amount $\delta\theta$; if the diffraction of neutrons from the (111) and (220) planes produce coherent maxima in the angular scattering distribution at scale readings of θ_{111} and θ_{220}, then

$$\text{III-32} \quad \lambda = 2d_{111}\sin\tfrac{1}{2}(\theta_{111}+\delta\theta) = 2d_{220}\sin\tfrac{1}{2}(\theta_{220}+\delta\theta)$$

The introduction of a trigonometric identity and a simple manipulation of III-32 gives the scale error:

$$\text{III-33} \quad \delta\theta = 2\arctan\left[\frac{d_{220}\sin(\frac{1}{2}\theta_{220}) - d_{111}\sin(\frac{1}{2}\theta_{111})}{d_{111}\cos(\frac{1}{2}\theta_{111}) - d_{220}\cos(\frac{1}{2}\theta_{220})}\right]$$

3.4.2 RESOLUTION OF THE CRYSTAL SPECTROMETER

The resolution function for a neutron diffraction measurement with a crystal spectrometer has been derived by Caglioti, et. al. (229)(230)(231). The resolution depends, in part, on the properties of the three collimators in the system. Since the collimators are of the Soller type, the horizontal angular divergence of the i^{th} collimator, α_i, is determined by the ratio s_i/l_i where s_i is the width and l_i is the length of the Soller element. For the primary collimator in the beam tube, $\alpha_1 = 7.54 \times 10^{-3}$ radians; for the collimator between the copper crystals and the target, $\alpha_2 = 6.25 \times 10^{-3}$ radians; for the collimator between the target and the BF_3 detector, $\alpha_3 = 6.94 \times 10^{-3}$ radians.

The collimating properties of Soller slit systems have been discussed by Sailor, et. al. (232), who point out that although the angular transmission function should be triangular, in practice, imperfections and critical reflection lead to a function which is more nearly Gaussian in shape. Therefore, it is assumed that the intensity of the incident neutron beam is reduced by a factor

III-34 $$A(\phi_i) = \exp -(\phi_i/\alpha'_i)^2$$

where ϕ_i is the angle made by the projection on the horizontal plane of any individual ray with the centerline of the i^{th} collimator, and $\alpha'_i = \alpha_i/2(\ln 2)^{\frac{1}{2}}$.

The resolution is also affected by the properties of the copper monochromating crystals. It is assumed that the monochromating crystal is composed of mosaic blocks, each individually perfect, oriented in a Gaussian distribution of the type

III-35 $$\Psi(\eta) = \Lambda \exp -(\eta/\beta')^2$$

where Λ depends on the properties of the crystal (232), η is the angular displacement from the mean of the projection of the normal to the reflecting planes of any block upon a horizontal plane, and β' is related to the full width at half maximum of the distribution β by the equation $\beta' = \beta/2(\ln 2)^{\frac{1}{2}}$. The measured value of β for the copper monochromating crystals is 13'. (227)

With the abovementioned assumptions, Caglioti shows that a diffraction peak centered at a scattering angle θ_s, has a Gaussian shape with the full width at half maximum, $W_{\frac{1}{2}}$, given by

III-36 $$W_{\frac{1}{2}}(\tfrac{1}{2}\theta_s, \theta_B) = \left[\frac{\alpha_1^2\alpha_2^2+\alpha_1^2\alpha_3^2+\alpha_2^2\alpha_3^2+4\beta^2(\alpha_2^2+\alpha_3^2) - 4a\alpha_2^2(\alpha_1^2+2\beta^2) + 4a^2(\alpha_1^2\alpha_2^2+\alpha_1^2\beta^2+\alpha_2^2\beta^2)}{\alpha_1^2+\alpha_2^2+4\beta^2}\right]^{\frac{1}{2}}$$

where the symbol a is the ratio

III-37 $$a = \frac{(\cot \theta_B)_{\text{monochromator}}}{(\cot \frac{1}{2}\theta_s)_{\text{target}}}$$

and θ_B is the Bragg angle setting of the copper monochromating crystals. The calculated resolution function for the crystal spectrometer, in units of momentum transfer (Å^{-1}), is shown in Figure 24.

In the scattering angle measurement, the coherent neutron scattering from the polycrystalline aluminum target produced three well-resolved diffraction maxima (Figure 22). The full width at half maximum intensity of each of these maxima was measured and compared with the widths obtained from Caglioti's expression. In Figure 24 one can see that the agreement of the measured and calculated widths is excellent for the limited range of momentum transfers in which the comparisons can be made.

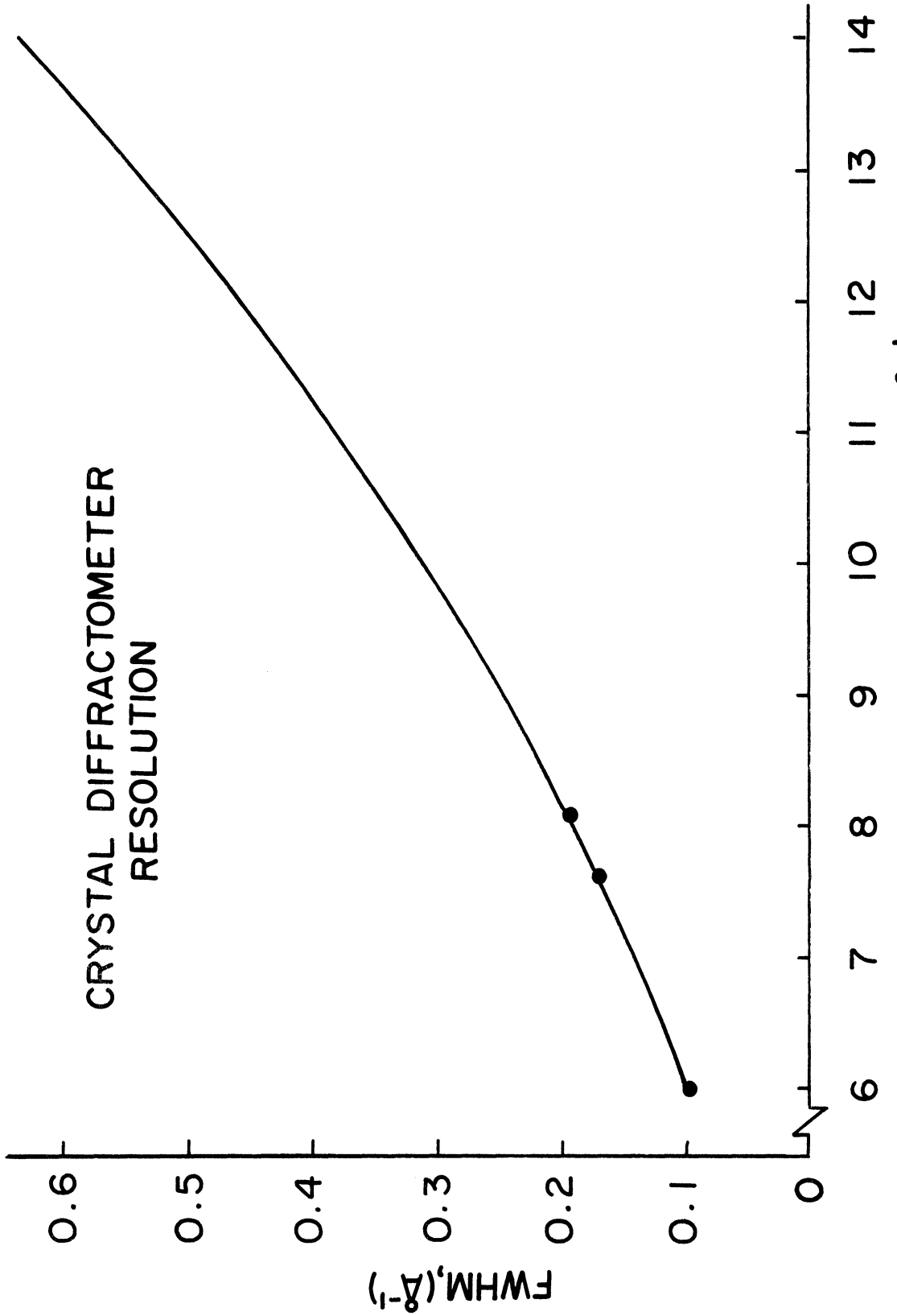

Figure 24. Resolution of the crystal diffractometer.

CHAPTER IV

4.1 THE TOTAL NEUTRON CROSS SECTION OF VITREOUS SILICA

As noted in Chapter III, the total neutron cross section of vitreous silica has been measured using the two rotor system, the four rotor monochromator, and the crystal spectrometer facility. The results of these measurements are shown in Figures 25 and 26.

The total neutron cross section, in terms of the sample's transmission of neutrons of a given energy, has been shown to be

IV-1 $$\sigma = (1/N_o x) \ln(1/T)$$

where T is the ratio of the transmitted neutron flux to the flux incident on the target. In designing an experiment to measure the total cross section, the sample thickness, x, should be chosen so that the transmission of the sample is between 0.7 and 0.2 (234). If the sample is too thick, the transmitted neutron flux is very weak and difficult to measure against the background. If the sample is very thin and the transmission is very large, the statistics of the measurement must be extremely good to accurately determine the difference between the incident neutron flux and the transmitted flux. The thickness of the sample used in the measurements taken with the crystal spectrometer and the two rotor system was 1.89 cm. Since the total neutron cross

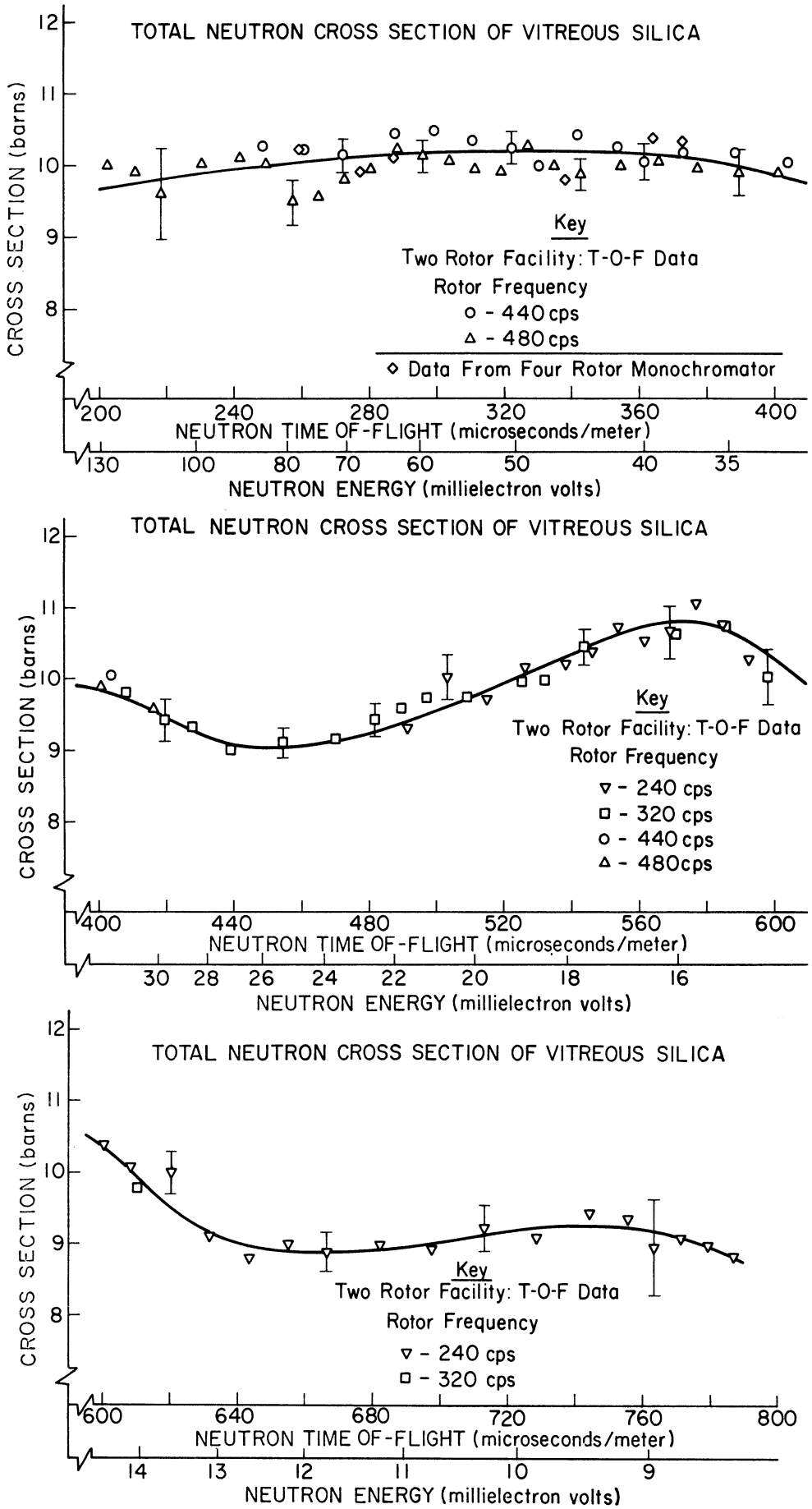

Figure 25. Total neutron cross section of vitreous silica obtained by time-of-flight measurement.

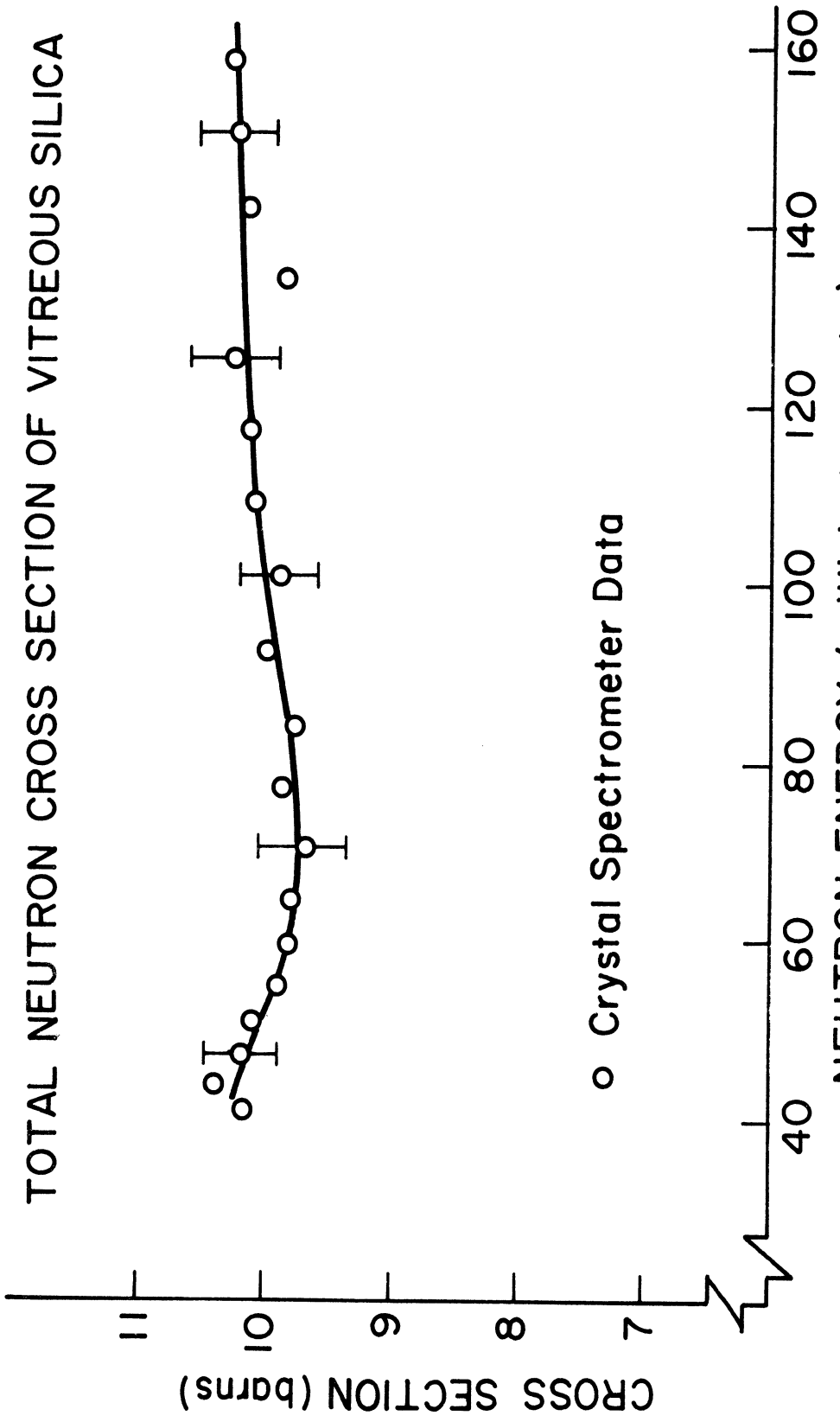

Figure 26. Total neutron cross section of vitreous silica obtained by crystal spectrometer measurement.

section of vitreous silica is of the order of 10 barns, the transmission of this sample is approximately 0.66. A thinner sample, 0.734 cm, was used in the measurements with the four rotor monochromator. Again assuming that the total cross section is ~10 barns, the transmission for this sample is T = 0.85.

The expression for the error in the total cross section for a given error in the measured transmission of the sample is obtained by differentiating Equation IV-1:

IV-2 $$d\sigma/\sigma = (1/\ln T)\,(dT/T)$$

In the case where the sample thickness is 1.89 cm, an error of one per cent in the transmission measurement gives rise to a two and one half per cent error in the cross section. On the other hand, a one per cent error in the transmission measurement for the 0.734 cm sample will give a six per cent error in the cross section.

The use of the thinner sample for the measurements with the four rotor monochromator was simply a matter of convenience. The transmission of this sample was measured in the course of the preparations of the inelastic neutron scattering experiments. In order that there would be comparable errors in all of the cross section measurements, longer counting times were allotted for the thin sample transmission measurements.

The primary reason for measuring the total cross section of vitreous silica was to obtain the necessary information

to correct the neutron scattering data for target attenuation effects. Previous measurements of this cross section by Melkonian (235) and Delaney and Weber (236), which are shown in Figure 27, were not considered to be adequate for this purpose. Although Delaney and Weber claim a probable error of 2% in their counting statistics, there is considerable scatter in their data. Measurements of the cross section for energies differing by less than one millielectronvolt vary by as much as a barn. Melkonian's cross section curve is generated from a relatively small number of measurements; for instance, the peak which he indicates at ~19 meV is defined by only one data point. The cross section data presented here represent at least five times as many measurements as Melkonian performed for the same range of neutron energies. Aside from the criticisms noted above, the lack of agreement in the results of Melkonian and Delaney and Weber was reason enough for obtaining additional cross section data.

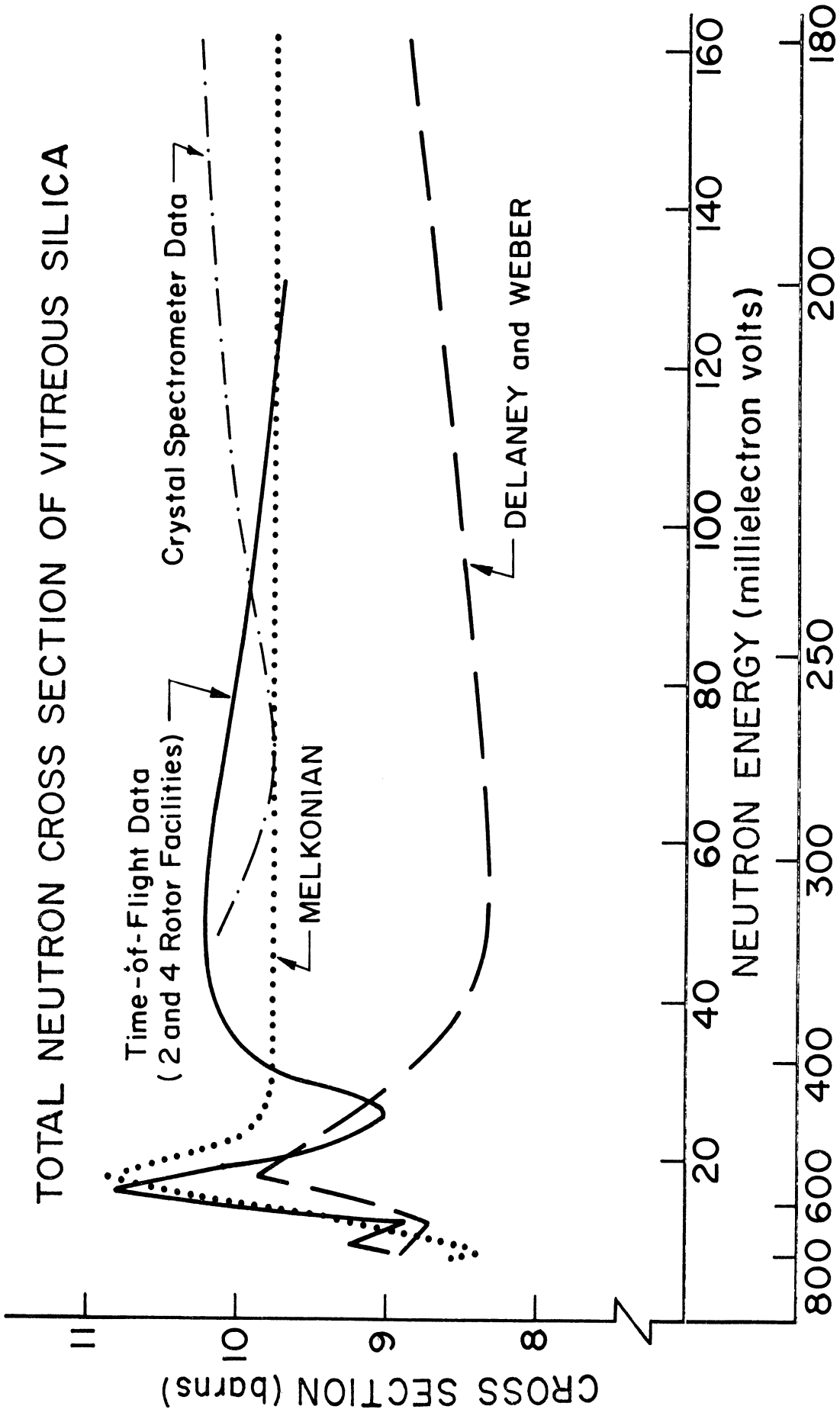

Figure 27. Comparison of measurements of the total neutron cross section of vitreous silica.

4.2 TARGET ATTENUATION CORRECTIONS

A correction to account for the scattering and absorption of the incident neutron beam and the singly scattered neutrons in the target was applied to the diffraction data. The target attenuation corrections, which are developed below, are for neutron scattering from a plane target. It is assumed that the flight paths of the neutrons incident on the target, the once scattered neutrons, and the normal to the target surface are coplanar. The more general case where neutrons emerge from the target at a given scattering angle but with different azimuthal angles (measured from the normal to the target surface) has been discussed by Striffler (237). The justification for the use of the simpler scattering geometry is that the incident neutron beam in the diffraction measurements was well collimated and the maximum azimuthal angles at which the neutron detectors are mounted are relatively small. At the 90° scattering angle of the two rotor facility, the maximum azimuthal angles of the detectors measured from the horizontal scattering plane are $+20^{\circ}$ and $-10^{\circ}45'$. The maximum angular deviations of the detectors at the $21^{\circ}6'$ scattering angle of the same facility are $\pm 6^{\circ}54'$ from the horizontal scattering plane. Calculations based on Striffler's formula indicate that the approximation that the once scattered neutrons emerge from the target in the horizontal scattering plane is acceptable for both banks of detectors. The coplanar assumption is well satisfied for

the diffraction measurements with the crystal spectrometer facility since the center line of the BF_3 detector which measures the scattered neutron intensity lies in the horizontal scattering plane.

The target attenuation calculation is straightforward: the product of the functions representing the probability of an incident neutron of energy E_o traveling a distance x in the target without attenuation to the point at which it is scattered through an angle θ_s and the probability of the once scattered neutron of energy E_f traveling a distance y to escape from the target without further interactions is integrated over all possible neutron paths in the target. This result is then divided by the average target thickness in the direction of the incident beam. The reciprocal of this calculation gives $F(E_o,E_f)$, the correction factor for the target attenuation. The target may be oriented so that the scattered neutrons are observed either in transmission or reflection. The path lengths x and y for the two different target geometries are shown in Figure 28. For the reflection geometry it is seen that

IV-3 $$y = x \tan\beta / \cos\theta_s(\tan\theta_s - \tan\beta)$$

and therefore

IV-4 $$(F^R(E_o,E_f))^{-1} = \int_0^{t/\sin\beta} \frac{\exp(-\sum(E_o)x)\ \exp(-\sum(E_f)x \tan\beta/\cos\theta_s(\tan\theta_s-\tan\beta))dx}{t/\sin\beta}$$

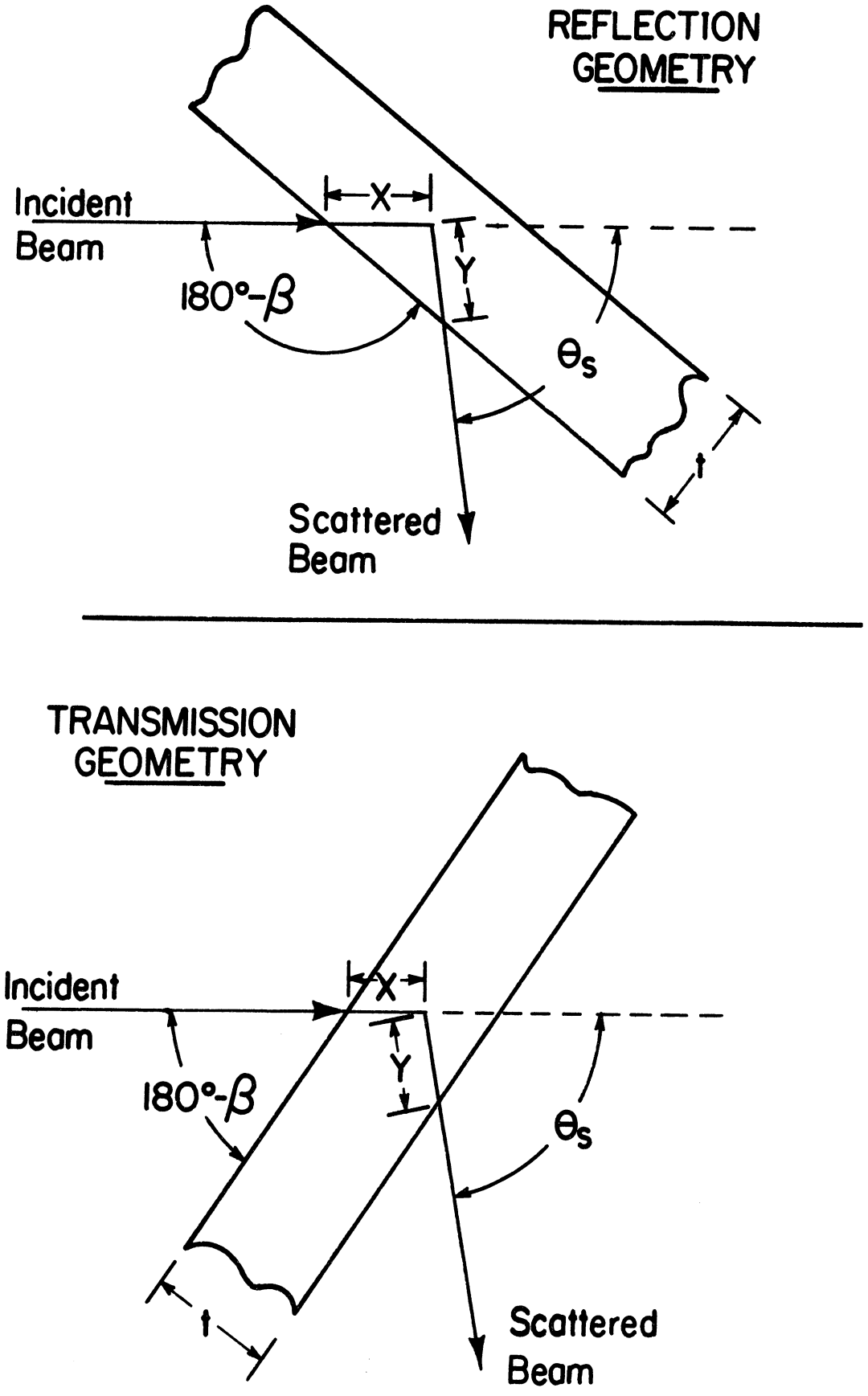

Figure 28. Target geometries for the diffraction measurements.

For the transmission geometry

$$\text{IV-5} \qquad y = (t/\sin\beta - x)/\sin\theta_s(\cot\theta_s - \cot\beta)$$

and

$$\text{IV-6} \qquad (F^T(E_o,E_f))^{-1} =$$

$$\int_o^{t/\sin\beta} \frac{\exp(-\sum(E_o)x)\exp(-\sum(E_f)([t/\sin\beta]-x)/\sin\theta_s(\cot\theta_s-\cot\beta))dx}{t/\sin\beta}$$

Equations IV-4 and IV-6 are integrated with the result that

$$\text{IV-7} \qquad F^R(E_o,E_f) = \frac{(\sum(E_o)X_R + \sum(E_f)Y_R)}{(1 - \exp(-\sum(E_o)X_R - \sum(E_f)Y_R))}$$

where $X_R = t/\sin\beta$

$Y_R = t/\cos\beta\cos\theta_s(\tan\theta_s - \tan\beta)$

and

$$\text{IV-8} \qquad F^T(E_o,E_f) = \frac{(\sum(E_o)X_T - \sum(E_f)Y_T)}{(\exp(-\sum(E_f)Y_T - \exp(-\sum(E_o)X_T)}$$

where $X_T = t/\sin\beta$

$Y_T = t/\sin\beta\sin\theta_s(\cot\theta_s - \cot\beta)$

In the calculation of the target attenuation corrections for the diffraction data it was assumed that the neutron scattering is elastic. This assumption is justified by the discussion in Section 3.3.2 of the preceding chapter and the fact that the total cross sections of both vitreous silica and vanadium are slowly varying functions. The total neutron cross section of vanadium, which was required for

the corrections of the measurements employing the vanadium target for the normalization of the scattered neutron intensity, was obtained from BNL-325 (90). The thickness of the vitreous silica target was 0.734 cm. and the vanadium target thickness was 0.318 cm.. The target orientations employed in the diffraction measurements along with the appropriate attenuation corrections calculated from Equations IV-7 and IV-8 are shown in Figure 29.

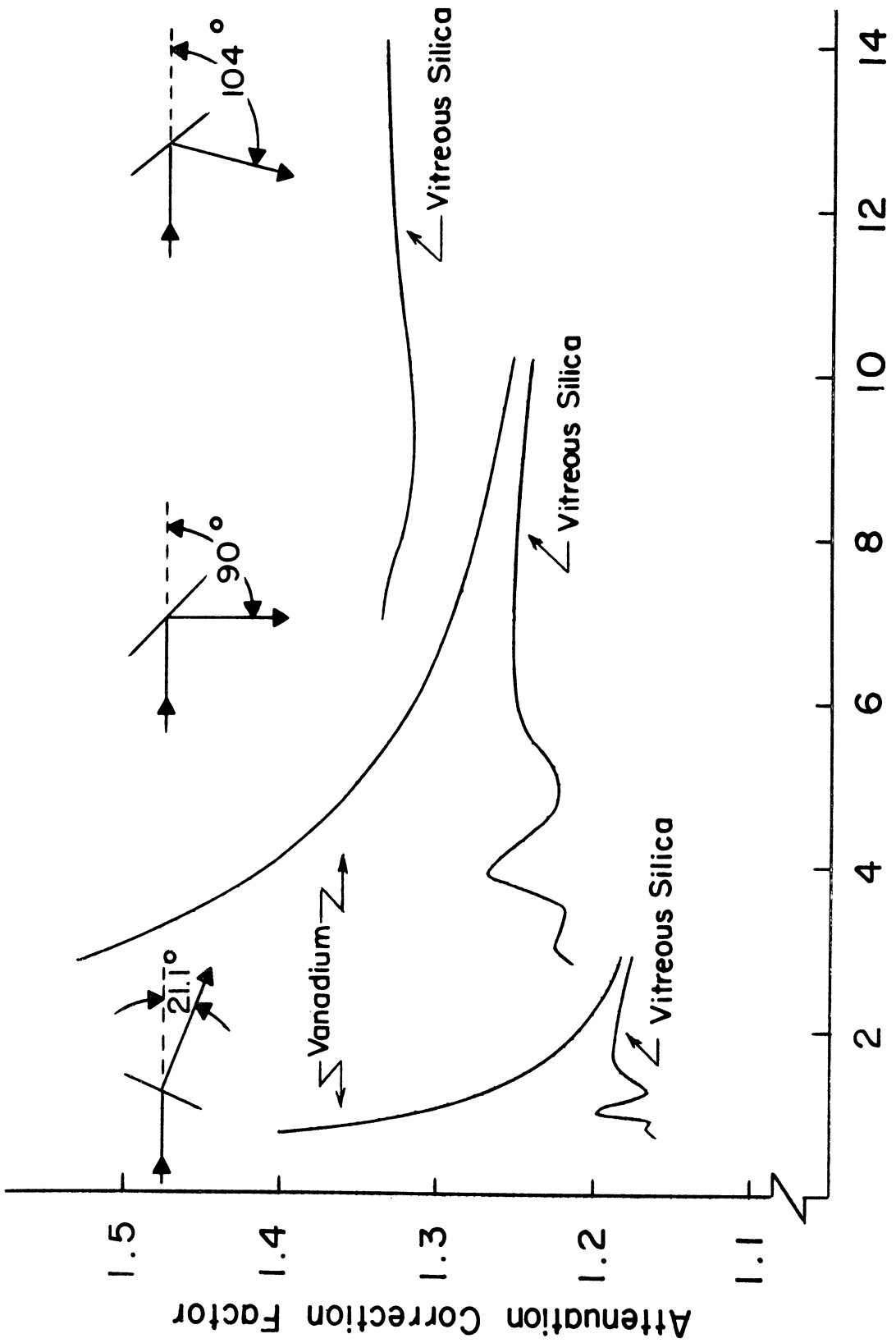

Figure 29. Target attenuation corrections for the diffraction measurements.

4.3 MULTIPLE SCATTERING

The determination of the scattering law and the structure factor of a target depends on the measurement of single scattering events. To this point in the discussion of the neutron scattering experiments there has been a tacit assumption that the scattered neutrons emerging from the target have undergone only one collision (or scattering event) in the target. However, the scattered neutron flux contains all orders of scattering and in some instances the experimental data must be corrected for the multiple scattering events. The multiple scattering contribution is difficult to calculate and impossible to completely separate from the scattered neutron spectrum by experimental techniques. In designing an experiment one attempts to reduce the effects of the multiple scattering by choosing a target which is thin in comparison to the mean free path of a neutron in the target material. In practice, the degree to which this criterion can be satisfied depends on the intensity of the incident beam: it is obvious that as the target thickness is decreased, a smaller number of the incident neutrons are scattered and the accumulation of a scattering spectrum with the desired statistical accuracy becomes more difficult. The present beam intensity of the University of Michigan's chopper facility makes extensive measurements with sample transmissions greater than 90% impractical.

Even in instances where it is possible to reduce the target thickness and still maintain a reasonably high scattered neutron flux, the number of singly scattered neutrons decreases more rapidly than the number of multiply scattered neutrons (238). Vineyard (238) has shown that the ratio of the intensities of the multiply scattered to once scattered neutrons can be reduced by the addition of a neutron absorber to the target. With a solid substance such as vitreous silica this might be accomplished by cutting the sample into small segments and assembling a target of alternate layers of cadmium sheet and the neutron scatterer. However, there was no attempt to do this in this experiment. Because of its brittle nature it is fairly difficult to cut vitreous silica into small pieces without a considerable amount of breakage. Furthermore, one must always be concerned with the possibility that the heat generated in grinding or cutting operations on glass will raise its temperature to a point where it is possible for devitrification to take place.

A number of general formulations of the multiple scattering problem have appeared in the literature. Vineyard (238) has provided expressions for calculating the multiple scattering of thermal neutrons in plane samples of infinite lateral extent. The formulae which he has derived are based on the assumptions that the scattering is elastic and that the angular distribution of primary scattered

neutrons, when averaged over a narrow angular range, is isotropic. The treatment of the multiple scattering problem in situations in which a scattering event generally results in a change in the neutron energy is obviously more complicated. The reader is referred to the work of Slaggie (239) (240) for a discussion of this problem.

Vineyard's expression for the twice scattered current of neutrons (neutrons/sec) per unit current incident on the sample is

$$J_2 = \frac{\sec\theta_o}{\Sigma_T^2} \exp(-\Sigma_T t \sec\theta) \int d\Omega \sigma_d(\underline{s},\underline{s}') \sigma_d(\underline{s}',\underline{s}_o) f(\theta') \qquad \text{IV-9}$$

where Σ_T = the total cross section (cm^{-1})

θ_o = the angle between the normal to the target surface and the incident beam

θ = the angle between the normal to the target surface and the scattered beam emerging from the target

t = the target thickness

$\sigma_d(\underline{s},\underline{s}')$ = the differential cross section for the scattering from the direction $\underline{s}'$ to the unit solid angle about direction $\underline{s}$.

The function $f(\theta')$ gives the probability that two scattering events will occur along the particular paths defined by θ_o, θ', and θ. (θ', like θ_o and θ, is measured from the

target normal.) For transmission through the sample ($\theta < \frac{\pi}{2}$):

$$\text{IV-10} \quad f(\theta') = \frac{\sec\theta'}{(\sec\theta_o - \sec\theta')} \times \left[R' \left[\frac{e^{\tau(\sec\theta - \sec\theta')} - 1}{(\sec\theta - \sec\theta')} \right] + \frac{e^{-\tau(\sec\theta_o - \sec\theta)} - 1}{(\sec\theta_o - \sec\theta)} \right]$$

and for reflection from the sample ($\theta > \frac{\pi}{2}$):

$$\text{IV-11} \quad f(\theta') = \frac{\sec\theta' \, e^{\tau \sec\theta}}{(\sec\theta_o - \sec\theta')} \times \left[R' \left[\frac{e^{\tau(\sec\theta - \sec\theta')} - 1}{(\sec\theta - \sec\theta')} \right] - \frac{e^{-\tau(\sec\theta_o - \sec\theta)} - 1}{(\sec\theta_o - \sec\theta)} \right]$$

where $\tau = \sum_T t$ and $R' = 1$ for $\theta' \leq \frac{\pi}{2}$; $R' = \exp(-\tau(\sec\theta - \sec\theta'))$ for $\theta' > \frac{\pi}{2}$.

The quasi-isotropic approximation enables one to replace each of the differential cross sections in Equation IV-9 with their average value, $\sigma/4\pi$. This substitution obviously simplifies the θ' integration.

The Vineyard formulae have been employed to estimate the multiple scattering contributions in the structure factor measurements. As in the determination of the target attenuation corrections, we are concerned with the scattering from two different targets - the coherent scatterer vitreous silica and the incoherent scattering vanadium reference target. On the basis of the discussion in Section 3.3.2, it is reasonable to assume that the scattering in these targets is primarily elastic.

Beyster (224) has shown that the assumption of isotropic scattering in the case of the vanadium target is excellent. On the other hand, the neutron scattering in vitreous silica is not isotropic and in this instance there must be some justification of the use of the quasi-isotropic approximation.

Cocking and Heard (241) have shown that Vineyard's formulae can be evaluated without invoking the quasi-isotropic approximation. Instead, the differential cross section as a function of the scattering angle is imposed on the calculation. (This cross section is, of course, directly proportional to the structure factor of the target.) As an example, Cocking and Heard calculated the multiple scattering current from a target of liquid lead, a coherent neutron scatterer. They discovered that the results which they obtained by using a realistic $\sigma_d(\underline{s},\underline{s}')$ function were almost exactly the same as those obtained by using the quasi-isotropic approximation. The reasons for the similarity in the results of the two calculations are discussed in their paper.

The second order scattering current from the vitreous silica target was calculated for the following experimental parameters: an incident neutron energy of E_o=65 meV, a scattering angle of $\theta_s = 90^o$, an angle between the incident beam and the normal to the target surface of $\theta_o = 45^o$, an angle between the scattered beam and the target normal of

$\theta = 135^{o}$, and $\sum_T t = 0.165$. Using a differential cross section which varies as the experimentally determined structure factor (Figure 45), the second order current was calculated to be 0.30×10^{-2} neutrons per second per unit current incident on the target. The use of the quasi-isotropic approximation, gave a second order current of 0.32×10^{-2} neutrons per second. This is consistent with the results of Cocking and Heard, i.e., the use of the quasi-isotropic approximation generally leads to a slight overestimate of the second order current. Therefore, it was concluded that the use of the quasi-isotropic approximation provides a satisfactory estimate of the multiple scattering by the vitreous silica target.

The second order currents from the vitreous silica and the vanadium targets have been calculated using the quasi-isotropic approximation. The results for three incident neutron energies at each scattering angle are listed in Table IV-1. (The momentum transfer at each energy and scattering angle is also provided to indicate the point in K-space which the calculation represents.)

Since the exact calculation of the third and higher orders of multiple scattering becomes exceedingly tedious, only the twice scattered neutron currents have been calculated. However, Vineyard has noted that in instances where target thickness is much less than one mean free path ($\sum_T t < 1$) the twice scattered component comprises most

of the multiple scattered intensity. Since the maximum value of $\Sigma_T t$ for the vitreous silica target was less than 0.175 and for the vanadium target was less than 0.240, this criterion is reasonably well satisfied in our measurements.

As noted at the beginning of this discussion, the Vineyard formulae are based on the assumption that the target is of infinite lateral extent. Cocking and Heard have shown how the effect of finite sample size may be taken into account. In a study of the multiple scattering from a liquid lead target ($\Sigma_T t = 0.1316$) they found that the finite sample correction reduces the calculated J_2 component by from 25% to 40% in comparison with the infinite sample case. The twice-scattered currents listed in Table IV-1 were not corrected for finite sample size and therefore, probably overestimate the multiple scattering.

The data in Table IV-1 indicates that the largest multiple scattering contribution comes from the vanadium target. The variation in these second order currents is of the order of 50%. However, the maximum ratio of the second order to first order scattering in the vanadium target is ~ 0.27. The second order currents from the vitreous silica target are smaller in magnitude and show less variation over the range of the measurement. The maximum ratio of the second order to first order currents for this target is 0.21. The correction of the scattering data for these second order contributions is discussed in Sections 4.4 and 4.5.

TABLE IV-1 The Second Order Scattered Neutron Current Structure Factor Measurements

Two Rotor Time-of-Flight Experiment

$\Theta_s = 21^\circ 6'$ $\Theta_o = 21^\circ 6'$ $\Theta = 0$

E_o(meV)	K(Å^{-1})	Vitreous Silica $J_2 \times 10^2$	Vanadium $J_2 \times 10^2$
15	0.99	0.28	0.48
65	2.05	0.27	0.34
115	2.73	0.26	0.28

$\Theta_s = 90^\circ$ $\Theta_o = 45^\circ$ $\Theta = 135^\circ$

E_o(meV)	K(Å^{-1})	Vitreous Silica $J_2 \times 10^2$	Vanadium $J_2 \times 10^2$
15	3.80	0.35	0.62
65	7.92	0.32	0.47
115	10.54	0.30	0.33

Crystal Spectrometer Experiment

$\Theta_s = 103^\circ 34'$ $\Theta_o = 38^\circ 13'$ $\Theta = 42^\circ 47'$

E_o(meV)	K(Å^{-1})	Vitreous Silica $J_2 \times 10^2$
50	7.72	0.35
100	10.92	0.34
150	13.37	0.36

4.4 THE DIFFERENTIAL SCATTERING CROSS SECTION

4.4.1 THE TWO ROTOR TIME-OF-FLIGHT MEASUREMENTS

The measurements of the differential scattering cross section of vitreous silica by the time-of-flight technique extend from a minimum momentum transfer of 0.8 $\mathring{A}^{-1}$ to a maximum of 10.2 $\mathring{A}^{-1}$. The raw data obtained with the two rotor configuration are reduced by means of the expression derived in Section 3.3.2 :

$$\text{III-28} \qquad \frac{d\sigma}{d\Omega} = \left[\frac{C(t)}{C'(t)}\right]\left[\frac{N_o' T' F'(t,t) \frac{d\sigma}{d\Omega_V}}{N_o T F(t,t)}\right]$$

The vanadium cross sections required for the normalization of the scattering intensity have been shown in Figure 18 ; the target geometries and the appropriate attenuation corrections are shown in Figure 29. The reduced data are presented in Figures 30, 31, and 32.

The derivation of Equation III-28 was based on the assumption that only single scattering events are observed. Since the measured flux includes all orders of scattering, a correction for the multiple scattering contribution must be considered.

For a given scattering angle, the only factors in the $d\sigma/d\Omega$ expression which will vary with the momentum transfer are the count rates and the target attenuation corrections. Equation III-28 is accordingly rearranged into the product of a constant and a K-dependent function:

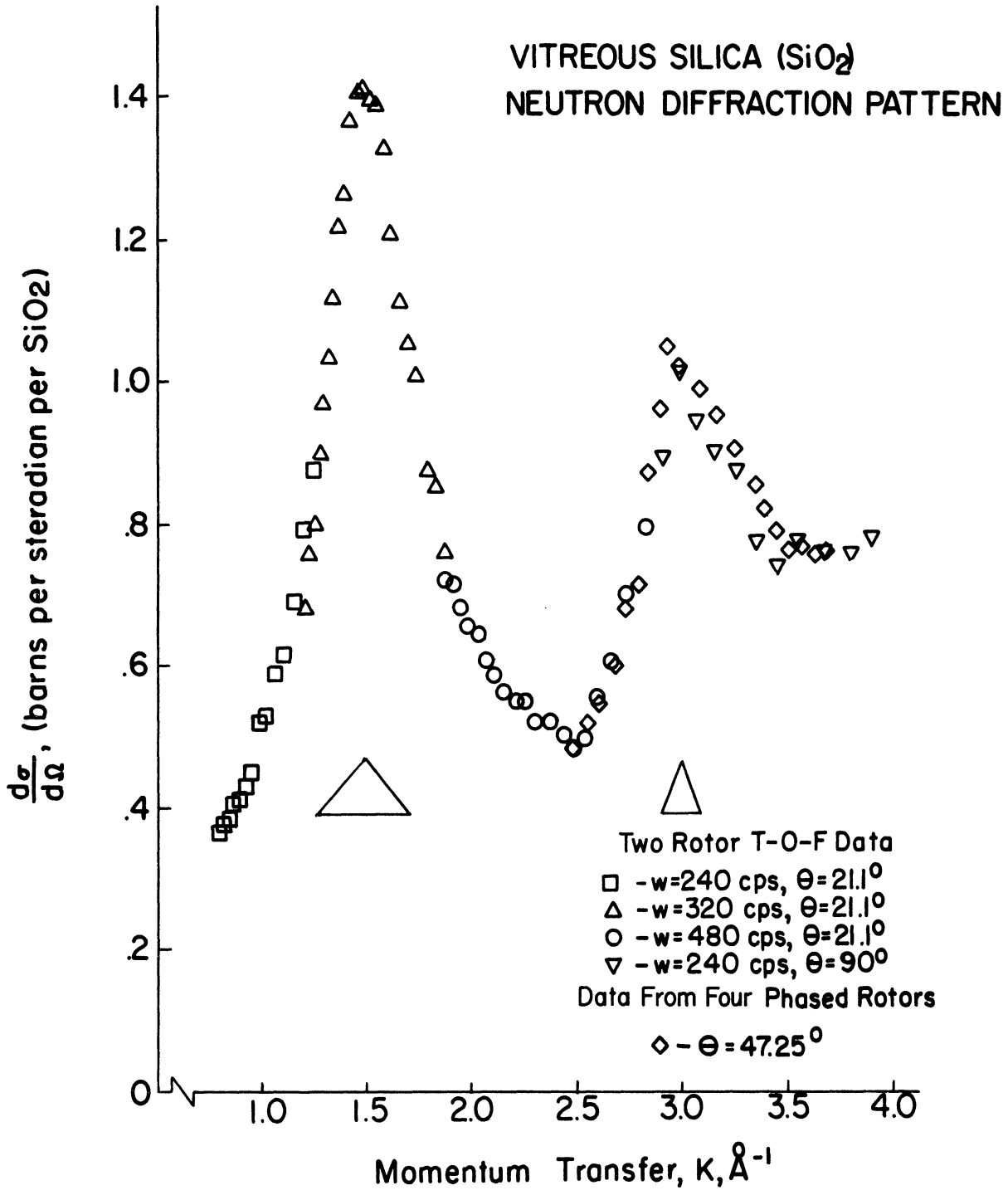

Figure 30. Single differential neutron scattering cross section of vitreous silica.

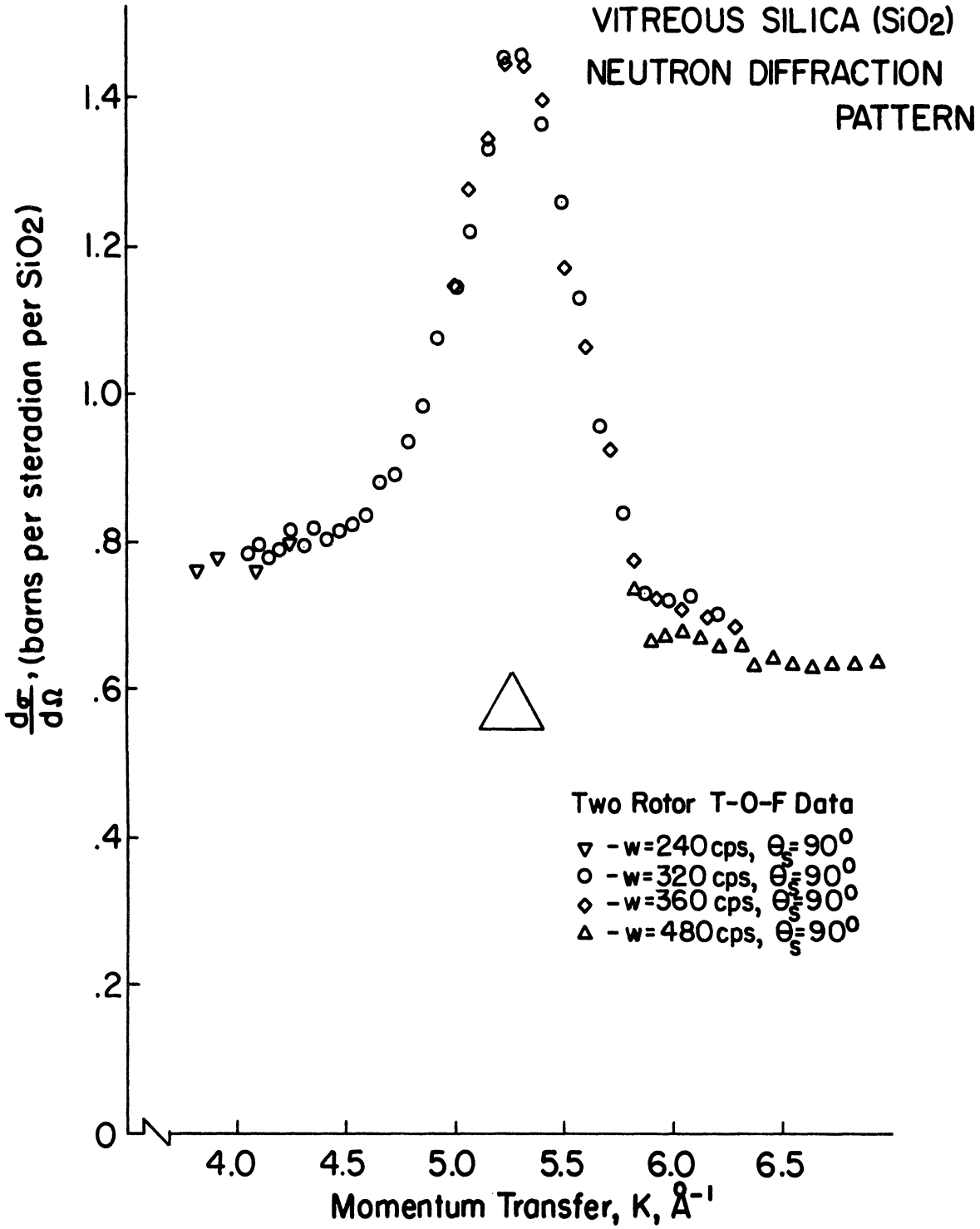

Figure 31. Single differential neutron scattering cross section of vitreous silica.

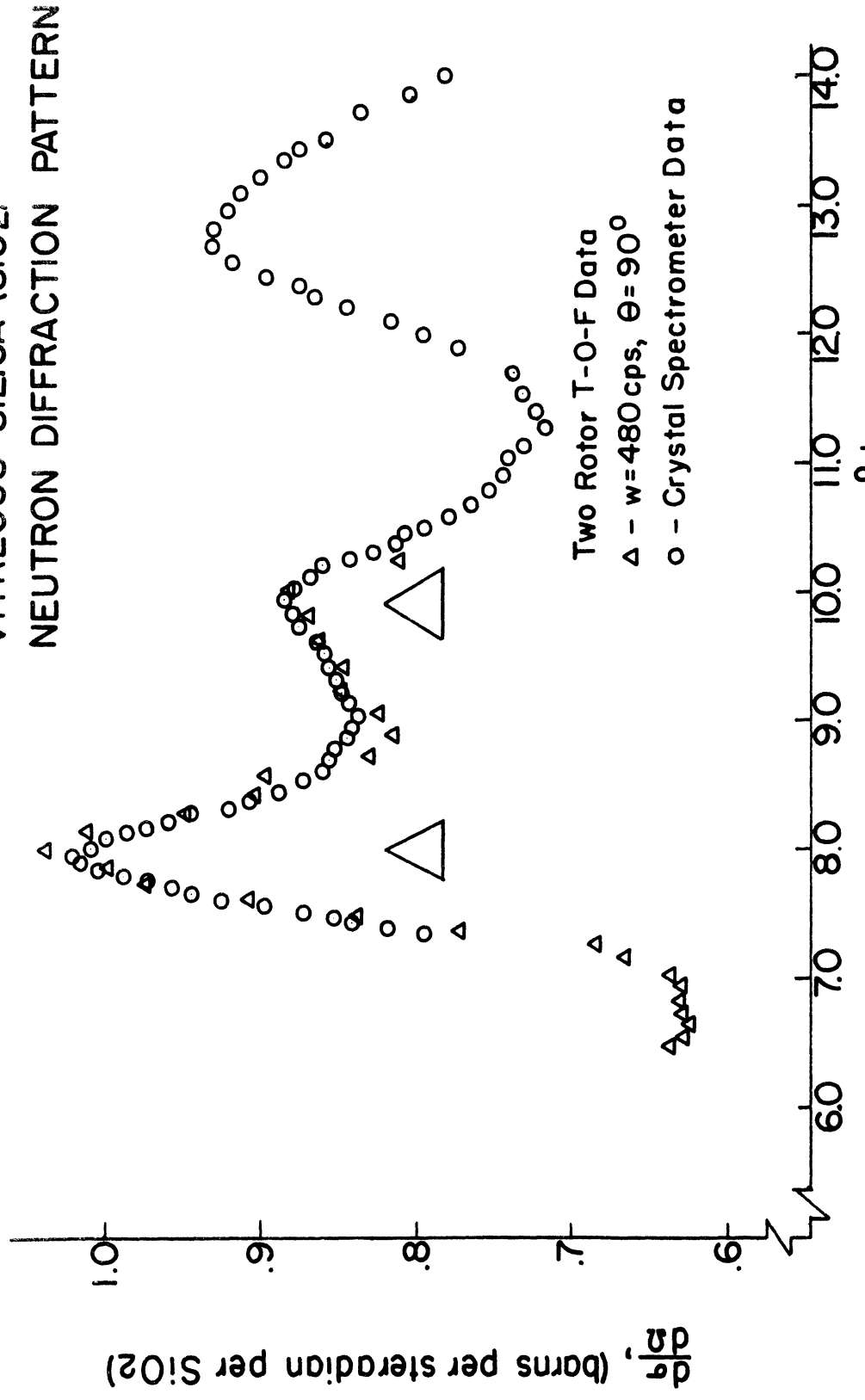

Figure 32. Single differential neutron scattering cross section of vitreous silica.

IV-12 $$\frac{d\sigma}{d\Omega} = \left[\frac{N_o' T' \frac{d\sigma}{d\Omega_V}}{N_o T}\right]\left[\frac{C(t)/F(t,t)}{C'(t)/F'(t,t)}\right]$$

The twice scattered neutron flux represents the major multiple scattering contribution (Section 4.3), and therefore it can be assumed that the count rates recorded in the cross section measurements are directly proportional to the sum of the first and second order scattering currents, J_1 and J_2. It follows that the experimentally derived $d\sigma/d\Omega$ varies with the momentum transfer according to the expression

IV-13 $$\frac{d\sigma}{d\Omega} = \text{constant} \times \left[\frac{J_1/F + J_2/F}{J_1'/F' + J_2'/F'}\right]$$

The (J_2/F) terms represent the errors introduced by the second order contributions to the observed scattering.

Values of (J_2/F) for both the vitreous silica and the vanadium measurements are provided in Table IV-2. The errors arising from the multiple scattering contribution to the vitreous silica data appear to be almost independent of the momentum transfer. In the case of the vanadium measurements, both the target attenuation corrections and the second order scattering currents decrease monotonically as the neutron energy increases. As a result, the multiple scattering error for the vanadium varies less than one would expect from the variation in the second order currents.

Although the K-dependence of the multiple scattering error is determined by the (J_2/F) terms, it is obvious that

TABLE IV-2 Multiple Scattering Errors in the Structure Factor Measurements

Two Rotor Time-of-Flight Experiment

$\Theta_s = 21°6'$ $\Theta_o = 21°6'$ $\Theta = 0$

E_o(meV)	$K(\AA^{-1})$	Vitreous Silica $J_2\times10^2$	Vitreous Silica $J_2\times10^2/F(E_o)$	Vitreous Silica J_2/J_1	Vanadium $J_2\times10^2$	Vanadium $J_2\times10^2/F(E_o)$	Vanadium J_2/J_1	S(K) % Error
15	0.99	0.28	0.23	0.22	0.48	0.36	0.26	3.2
65	2.05	0.27	0.23	0.22	0.34	0.28	0.24	1.6
115	2.73	0.26	0.22	0.21	0.28	0.24	0.23	1.6

$\Theta_s = 90°$ $\Theta_o = 45°$ $\Theta = 135°$

E_o(meV)	$K(\AA^{-1})$	Vitreous Silica $J_2\times10^2$	Vitreous Silica $J_2\times10^2/F(E_o)$	Vitreous Silica J_2/J_1	Vanadium $J_2\times10^2$	Vanadium $J_2\times10^2/F(E_o)$	Vanadium J_2/J_1	S(K) % Error
15	3.80	0.35	0.28	0.23	0.62	0.43	0.27	3.1
65	7.92	0.32	0.26	0.23	0.47	0.37	0.25	1.6
115	10.54	0.30	0.24	0.22	0.33	0.27	0.24	1.6

Crystal Spectrometer Experiment

$\Theta_s = 103°34'$ $\Theta_o = 38°13'$ $\Theta = 42°47'$

E_o(meV)	$K(\AA^{-1})$	Vitreous Silica $J_2\times10^2$	Vitreous Silica $J_2\times10^2/F(E_o)$
50	7.72	0.35	0.26
100	10.92	0.34	0.26
150	13.37	0.36	0.27

the actual magnitude of the error in $d\sigma/d\Omega$ depends on the relative intensities of the first and second order scattering currents. Representative values of J_2/J_1 and the resulting errors in $d\sigma/d\Omega$ (or S(K)) are included in Table IV-2. The most unfavorable multiple scattering situation results in an underestimate of the true $d\sigma/d\Omega$ by approximately 3.2%. In the most favorable situation, which occurs when the J_2/J_1 ratios for the vitreous silica and vanadium targets are nearly equal, the value of $d\sigma/d\Omega$ is underestimated by only 1.6%.

The calculation of the multiple scattering error for many momentum transfers would require a prohibitive amount of computer time. (The integral in the expression for J_2 must be evaluated by numerical techniques.) Therefore, the data have been adjusted for the multiple scattering in the following manner: all values of $d\sigma/d\Omega$ derived from Equation III-28 have been increased by 2.4%. This means that in all instances the multiple scattering error in the differential cross section should be less than 1%.

The technique of measuring the differential cross section with the two rotor configuration receives its most severe test at the point in K-space where the $21^{\circ}6'$ scattering angle data join the 90° scattering angle data (Figure 30). The measurements at these two angles differ in many respects. For example, at the $21^{\circ}6'$ scattering angle, a neutron must have an energy of 139 meV to produce a 3 Å^{-1} momentum transfer in an elastic collision; an elastic scattering

event producing the same momentum transfer at the 90° scattering angle requires an incident neutron energy of only 9 meV. In Figure 17 one can see that the loci of the measurements in the 3 $\mathring{A}^{-1}$ region of the $K - \hbar\omega$ plane are noticeably different for the two scattering angles. Figure 29 indicates that there are marked differences in the target attenuation corrections which are applied to the two sets of data. The width of the resolution function for the 21°6' measurement is roughly twice that of the 90° measurement (Section 3.3.4, Figure 21). The largest discrepancies in the multiple scattering contribution occur in the 3 $\mathring{A}^{-1}$ region.

The data matching problem is further complicated by the fact that the differential cross section of vitreous silica is sharply peaked in the region where the two measurements overlap. This means that the calibration of the momentum transfer scale for each of the two scattering angles must be precise. It is obvious that one also needs good counting statistics. However, in the final analysis, a successful matching of the two sets of data depends primarily on the validity of the assumptions and simplifications involved in the derivation of Equation III-28.

Having cited many of the differences in the two measurements and potential sources of error, it is satisfying to note that the data obtained at the two scattering angles are in good agreement. One is tempted to claim that this

result confirms the validity of Equation III-28. However, the region of overlap of the two sets of data in K-space is relatively limited and it could be argued that the observed agreement is simply a fortuitous coincidence. For this reason, it was decided that a measurement of $d\sigma/d\Omega$ in the 3 Å^{-1} region by a different experimental technique was desirable.

4.4.2 THE FOUR ROTOR MONOCHROMATOR MEASUREMENTS

Measurements performed with the four rotor monochromator configuration provided additional data for momentum transfers between ~ 2.5 Å^{-1} and ~ 3.6 Å^{-1}. In this experiment, the small bank of three detectors was positioned at a scattering angle of 47° 15'. The vitreous silica target was oriented so that the scattered neutrons were observed in transmission. The target orientation angle β (Figure 28) was 135°. The target attenuation correction for this geometry was obtained from Equation IV-8. The incident neutron beam was collimated with the same single slit collimator used in the measurements with the two rotor configuration (Section 3.3.1). The scattering intensity was normalized relative to intensity of the incident neutron beam. The incident beam intensity was monitored with a parallel plate fission chamber positioned directly after the collimator and approximately 11" from the target. The physical description and operating characteristics of this detector have been provided in Section 3.4.1 of Chapter III.

The differential cross section was measured for twenty different incident neutron energies in an interval between 20 meV and 42 meV. (In each instance the phasing of rotors 2 and 4 was adjusted to provide the neutron energy which would give the desired K at the 47° 15' scattering angle.) The characteristic loci of the monochromator measurements in the momentum-energy transfer plane are shown in Figure 51.

A comparison with Figure 17 indicates that, in general, the constant K condition is more nearly satisfied in the measurements with the two rotor configuration. However, this is not a serious problem since most of the scattering is confined to low energy transfers where the deviation from the constant K condition is quite small.

The neutron scattering spectra obtained with the monochromator are a measure of the double differential cross section $d\sigma/d\Omega dE$. After applying the appropriate corrections for the target attenuation, background, and the detector efficiency, the measured spectra were integrated to obtain the single differential cross section $d\sigma/d\Omega$. The background was measured by cycling the vitreous silica target with an empty target holder.

As noted above, the monochromator data were normalized by monitoring the intensity of the incident neutron beam. An absolute normalization was obtained by equating the $d\sigma/d\Omega$ measured with the monochromator to the vanadium normalized $d\sigma/d\Omega$ measured with the two rotor configuration at identical momentum transfers of 2.48 Å^{-1}. The statistical counting error for each of these measurements was less than 0.5 percent. In Figure 30 it is seen that the normalized monochromator data agrees quite well with the two rotor measurements at both the $21^{\circ}6'$ and the 90° scattering angles.

4.4.3 THE CRYSTAL SPECTROMETER MEASUREMENTS

The crystal spectrometer facility was employed to measure the differential cross section in the region of K -space between 7.35 $\mathring{A}^{-1}$ and 14.2 $\mathring{A}^{-1}$. Most of the details of these measurements have been discussed in Section 3.5.1 of Chapter III. The orientation of the target and the attenuation correction factor for this experiment are shown in Figure 29. (The same vitreous silica specimen was used in all of the differential cross section measurements.) As indicated in Section 3.5.1, the data are also corrected for the background, the efficiency of the fission chamber which monitors the incident beam intensity, and the efficiency of the BF_3 tube which measures the scattered neutron flux.

The crystal spectrometer measurement is similar to the mechanical monochromator measurement in that the intensity of the neutron scattering is normalized by means of the beam monitor. In this instance, the absolute normalization was obtained by equating the integrals of the $d\sigma/d\Omega$'s measured with the crystal spectrometer to the comparable data obtained in the two rotor, vanadium normalized measurements in the interval between 7.5 $\mathring{A}^{-1}$ and 8.5 $\mathring{A}^{-1}$:

$$\text{IV-14}\quad \left[\int_{7.5}^{8.5} \frac{d\sigma}{d\Omega}(K)\, dK\right]_{T\text{-}O\text{-}F} = C\left[\int_{7.5}^{8.5} \frac{d\sigma}{d\Omega}(K)\, dK\right]_{\text{Crystal Sp.}}$$

The factor C in the above expression is the normalization constant for the crystal spectrometer data. This range of

momentum transfers was chosen for the normalization because of the good counting statistics for both measurements and the fact that the resolution functions are very similar. (At a momentum transfer of 8 $\mathring{A}^{-1}$, the full width at half maximum intensity of the crystal spectrometer's resolution function is 0.19 $\mathring{A}^{-1}$; $W_{\frac{1}{2}}$ for the two rotor facility at the same momentum transfer is 0.22 $\mathring{A}^{-1}$.) The normalized data is shown in Figure 32.

There is no need to adjust the crystal spectrometer data for the multiple scattering contribution. The data in Table IV-2 indicates that the multiple scattering error is essentially constant for these measurements. As a result, the necessary correction is automatically included in the normalization constant obtained from Equation IV-14.

4.5 THE STATIC ATOM PAIR CORRELATION FUNCTION

4.5.1 THE BASIC EQUATION

The relationship between the static atom pair correlation function of a polyatomic system and its differential neutron scattering cross section was derived in Section 2.2 of Chapter II.

$$\text{II-32} \quad 4\pi r^2 \left[\bar{g}(r) - g_o\right] = \frac{2r}{\pi}\int_o^\infty K\, i(K) \sin Kr\, dK$$

$$\text{where} \quad i(K) = \frac{1}{\sum_t N_t b_t^2}\frac{d\sigma}{d\Omega} - 1$$

$$g(r) = \sum_t b_t \sum_{t'} N_{t'} b_{t'}\, g_{t't}(r) / \sum_t N_t b_t^2$$

$$g_o = \sum_t b_t \sum_{t'} N_{t'} b_{t'}\, n_t \,/ \sum_t N_t b_t^2$$

In order to simplify the notation in the following discussion, the differential scattering cross section, $\frac{d\sigma}{d\Omega}(K)$, will be identified as $I(K)$, and its limiting value at large K, $\sum_t N_t b_t^2$, as I_∞. The expression for $i(K)$ thus becomes

$$\text{IV-15} \qquad i(K) = \frac{I(K) - I_\infty}{I_\infty}$$

4.5.2 NORMALIZATION OF THE DATA

In many instances when the differential scattering cross section of a liquid or a noncrystalline solid is measured for the express purpose of obtaining a pair correlation function, the experiment is not designed in such a manner as to determine the absolute scattering intensity. In such cases where the scaling of the cross section measurement is arbitrary, it is necessary to normalize the data before the expression for the correlation function can be evaluated.

The differential neutron scattering cross section of vitreous silica reported here is scaled in terms of the absolute scattering intensity. Thus, in this instance there would appear to be no need to normalize the data for the correlation function calculation. However, one must recall that the calibration of this measurement is based on a comparison of the relative intensities of scattering from the vitreous silica and the vanadium reference. Obviously, the scaling of the vitreous silica measurement can only be as accurate as the measurement of the vanadium cross section. The only estimate of the error in the measurements of the vanadium cross sections by Beyster, et.al. (224), is that the integral of their differential cross section data agrees to within 5% of the measurement of the total scattering cross section.

In order to test the accuracy of the calibration by the vanadium reference technique (and the other corrections

applied to the data) one can make use of the fact that in the limit of large momentum transfers, I(K) should assume the constant value $\sum_t N_t b_t^2$. This is a necessary (but not sufficient) condition which the measurement must satisfy. Unfortunately, the technique of comparing the measured and calculated I_∞ 's is not applicable here since the single differential cross section of vitreous silica has not as yet assumed a constant value at K_{max} , the upper limit of the measurement. (Carraro, et.al. (88) report that there is evidence that the structure in the single differential cross section of vitreous silica persists at momentum transfers as large as 18 $\mathring{A}^{-1}$.)

J. Krogh-Moe (242) has suggested another method of checking the calibration of an absolute measurement and/or obtaining the required normalization of a measurement scaled in arbitrary units. The Krogh-Moe normalization is based on the fact that an atom in any system (solid, liquid, or gas) is excluded from the immediate vicinity of any other atom in the system. With this in mind, consider the behavior of the expression for the atom pair correlation function as r, the pair spacing, approaches zero. As r goes to zero, $\sin(Kr) \approx (Kr)$ and $\bar{g}(r)$ goes to zero. Equation II-32 reduces to

$$\text{IV-16} \qquad -2\pi^2 g_o = \int_o^\infty K^2 \left[\frac{I(K) - I_\infty}{I_\infty}\right] dK$$

from which one can extract the value of I_∞ in units consistent with the measured cross section, I(K). If the measurement of I(K) is scaled in arbitrary units, the solution of IV-16 for I_∞ provides the necessary normalization for the evaluation of the correlation function. If, on the other hand, the measurement is scaled on an absolute basis, the value of I_∞ derived from IV-16 should compare favorably with $\sum_t N_t b_t^2$.

The expression for the pair correlation function and the normalization calculation both call for integrations over the entire range of momentum transfers in which the function i(K) differs from zero. However, the experimental data is limited to a finite range of momentum transfers between $K_{min} = 0.8$ Å^{-1} and $K_{max} = 14.2$ Å^{-1}. The lack of data in the range between 0 and K_{min} is not a serious problem. In the normalization calculation, i(K) is multiplied by the square of the momentum transfer and thus, the contribution from the 0 to K_{min} region is extremely small. The evaluation of the pair correlation function is not prejudiced since the low K scattering data is sensitive only to long range order which is nonexistent in the non-crystalline target. Furthermore, because of the quality of the small angle vitreous silica data reported by Warren (26) and Weinberg (31), I(K) can be extrapolated to K = 0 with a minimum of error.

The lack of data in the region beyond K_{max} creates serious difficulties in the evaluation of $\bar{g}(r)$. This

problem is discussed in detail in Sections 4.5.5 and 4.5.6 . Fortunately, it is not as serious in the normalization calculation. If the upper limit of the integral in IV-16 is replaced by K_{max} and the equation is solved explicitly for I_∞, we have

$$\text{IV-17} \qquad I_\infty = \lim_{K_{max} \to \infty} \frac{3 \int_0^{K_{max}} K^2 I(K)\, dK}{K_{max}^3 - 6\pi g_o}$$

This expression was evaluated for values of K_{max} ranging from 10 Å^{-1} to the upper limit of our measurements, 14.2 Å^{-1}. The variation in the I_∞'s obtained from IV-17 was less than 2%. (The relative insensitivity of this normalization calculation to a reasonable choice of K_{max} has also been noted by Paalman and Pings (243).) Also, since our scattering data was normalized to an absolute scale, a direct comparison of $\sum_t N_t b_t^2$ and the I_∞ derived from IV-17 was possible. For $K_{max} = 14.2$ Å^{-1}, IV-17 gave a value of $I_\infty = 0.845$ barns/steradian/SiO_2 ; $\sum_t N_t b_t^2$ for vitreous silica is 0.86 barns/steradian/SiO_2 , a difference of only slightly more than 1%.

4.5.3 COMPUTATION OF THE FOURIER INTEGRAL

In order to compute the pair correlation function

$$\text{II-32} \qquad 4\pi r^2 \bar{g}(r) = 4\pi r^2 g_o + \frac{2r}{\pi}\int_0^\infty Ki(K)\, \sin Kr\, dK$$

it is necessary to transform the Fourier integral term into a sum over evenly spaced intervals of K. This transformation is accomplished in the manner suggested by Danielson and Lanczos (244).

Choosing a large, but finite momentum transfer K_o, it is assumed that in the region between $K = K_o$ and $K = \infty$, the product $Ki(K) = 0$. This makes it possible to write the integral term in a more convenient form by introducing the new independent variable

$$\text{IV-18} \qquad x = \frac{\pi}{K_o} K$$

letting

$$\text{IV-19} \qquad f(x) = Ki(K)$$

and making a linear change in scale of the parameter

$$\text{IV-20} \qquad t = \frac{K_o}{\pi} r$$

Thus,

$$\text{IV-21} \qquad \frac{2r}{\pi}\int Ki(K)\, \sin Kr\, dK = Ig(t) = \frac{2t}{\pi}\int f(x)\, \sin tx\, dx$$

Since the function f(x) is given only in the half range 0 to π, one can assume that $f(-x) = -f(x)$ in the range 0 to $-\pi$.

This means that f(x) is now an odd function which can be represented by a sum involving only sine terms. Therefore, let

$$\text{IV-22} \qquad f(x) = \sum_{j=1}^{2m} b_j \sin jx$$

where j is an integer and 2m is an even number sufficiently great so that the contribution to the sum from higher terms is negligible.

If f_n denotes the known values of f(x) at equidistant intervals $x_n = n(\pi/2m)$, the orthogonality property of the Fourier sum gives

$$\text{IV-23} \qquad \sum_{n=1}^{2m} f_n \sin jx_n = \frac{2m}{2} b_j \qquad \text{if } j = n$$

$$= 0 \qquad \text{if } j \neq n$$

Thus, from IV-23 one obtains the coefficients b_j at equidistant intervals and it follows that the desired integral, for integer values of t, can be represented as

$$\text{IV-24} \quad Ig(j) = jb_j = \frac{j}{m} \sum_{n=1}^{2m} f_n \sin\left[n \frac{j\pi}{2m}\right] \quad (j = 1, 2, \cdots, 2m)$$

Since there is no differential cross section data for momentum transfers greater than K_{max}, it would seem reasonable to set $K_o = K_{max}$. However, from Equation IV-20 and IV-24, it can be seen that the choice of K_o determines the increment in r at which the Fourier integral can be

evaluated, i.e., $\Delta r = \pi/K_o$. The choice of K_o must therefore be large enough so that the resulting Δr is sufficiently small to reveal the details of the structure in $\bar{g}(r)$. In the calculations described here, K_o is set equal to 112.2 Å^{-1} and thus $\Delta r = 0.028$ Å.

The increment ΔK in the numerical integration is taken to be 0.0137 Å^{-1} (m = 4096). The maximum increase or decrease in the measured I(K) in any interval $\Delta K = 0.0137$ Å^{-1} is 6%; on the average, $\Delta I(K)/\Delta K\big|_{\Delta K=0.0137\ \text{Å}^{-1}}$ is approximately 1%.

The nature of the error which is introduced by approximating the integral of II-32 by a sum has been studied by Ino (245). From his analysis he has drawn the following conclusion: if the function $4\pi r^2\left[\bar{g}(r) - g_o\right]$ can be regarded as practically zero for r greater than r_o, the approximation of the integral by a sum is very accurate if the increment ΔK of the summation is less than (π/r_o). For $\Delta K = 0.0137$ Å^{-1}, $r_o \approx 229$ Å, i.e., the increment in K chosen here for the numerical integration would be satisfactory even if one expected order in the structure of the vitreous silica at atom pair spacings as large as 229 Å.

Filipovich (246) has demonstrated that one is able to determine interatomic spacings more accurately from the positions of the maxima in $r\bar{g}(r)$ than from plots of either $\bar{g}(r)$ or $r^2\bar{g}(r)$. Thus, the result of the inversion of the measured I(K) of vitreous silica is presented in Figure 33 in the form of the function $4\pi r\bar{g}(r)$ versus r.

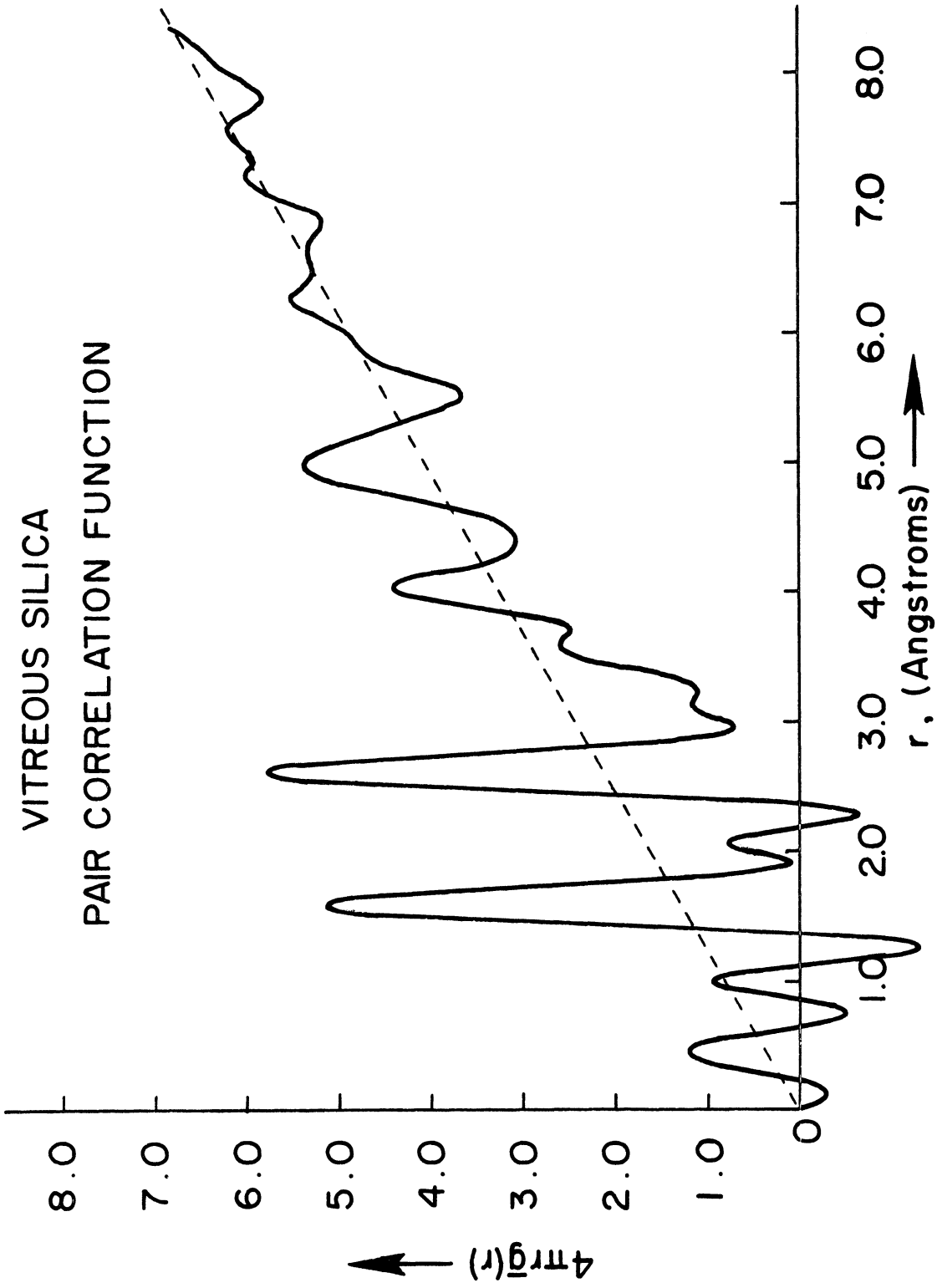

Figure 33. Atom pair correlation function of vitreous silica (no resolution correction).

4.5.4 THE RESOLUTION BROADENING CORRECTION

The widths of the peaks in the differential cross section of vitreous silica are considerably greater than the widths of the resolution functions of the time-of-flight and crystal diffractometers. However, the relatively small amount of resolution broadening in the data has not been ignored in the derivation of the pair correlation function. In Chapter III it was noted that the resolution of the I(K) measurements varies in an irregular manner. Although this variation probably would not produce gross errors in the atom pair correlation function, there is a possibility that some of the less pronounced features of $\bar{g}(r)$ could be affected.

The correction described here removes most, but not all of the resolution broadening from the data. The small amount of residual broadening, which is purposely left in the corrected I(K) data, is independent of the momentum transfer. The reason for this approach is as follows: the widths of the resolution functions of the two diffractometers are determined for the most part by experimental measurements. There is, of course, some error in these measurements. If one attempts to remove all of the resolution broadening from the data and inadvertently overestimates the broadening effect, it is extremely difficult to identify the spurious features which this error produces in the transform of the corrected I(K) function. The resulting atom pair correlation function

would very likely be less accurate than that which is obtained when the resolution effects are ignored. On the other hand, the effect of a constant width broadening function on the transformed function is readily understood.

The details of the resolution broadening correction are as follows: the observed cross section, $I_{obs}(K)$, is assumed to be the exact cross section I(K), broadened by a resolution function R(K,K'). This relationship is defined by the equation:

$$\text{IV-25} \qquad I_{obs}(K) = \int dK' \; R(K,K') \; I(K')$$

The resolution function R(K,K') is peaked at K = K' and has a width W(K). In order to effect the partial removal of the resolution broadening, R(K,K') is assumed to be the convolution of two functions, R_1 and R_2.

$$\text{IV-26} \qquad R(K,K') = \int dK'' \; R_1(K,K'') \; R_2(K'',K')$$

The broadening which arises from R_1 is that which is to be removed from the data, the contribution from R_2 is to remain. Since the resolution functions of the time-of-flight and crystal diffractometers can be approximated by Gaussian functions, the relationship between the widths of R, R_1 and R_2 is taken to be

$$\text{IV-27} \qquad W^2(K) = W_1^2(K) + W_2^2$$

Furthermore, in the calculations described here, W_2, the width of the R_2 function, is taken to be constant in K.

One now defines a new function, I_1, which is the exact differential cross section broadened by the constant width resolution function R_2.

$$\text{IV-28} \qquad I_1(K'') = \int dK' \; R_2(K'',K') \; I(K')$$

I_1 is, of course, also related to $I_{obs}(K)$ and is obtained from the solution of the expression for $I_{obs}(K)$ in terms of I_1 :

$$\text{IV-29} \qquad I_{obs}(K) = \int dK'' \; R_1(K,K'') \; I_1(K'')$$

The problem of correcting a continuous spectrum for the finite resolution of a spectrometer has been studied by Eckart (247) and he has derived an approximate solution for Equation IV-29 in a form which can be readily programmed for a computer calculation. The measured differential cross section $I_{obs}(K)$ is tabulated at equally spaced intervals of K: $K_n = n\Delta K$ and $I_{obs}(K_n) = I_n$. Assuming the resolution function is symmetric, the Eckart solution of Equation IV-29 reduces to the following expression:

$$\text{IV-30} \qquad I_1(K_n) = I_n - \left[\frac{W_1^2(K_n)}{(\Delta K)^2}\right]\left[I_{n+1} - 2I_n + I_{n-1}\right]$$

(For the details of the derivation of this expression the reader is referred to Eckart's paper.) The widths of the

resolution functions of the time-of-flight and crystal diffractometers are indicated in Figures 21 and 24. W_2, the width of the residual broadening function, is taken to be 0.08 Å^{-1}. $W_1(K)$ is, in turn, derived from Equation IV-27. For the sake of convenience, the momentum transfer interval chosen for the calculation is the same as that used in the evaluation of the Fourier transform of the data, 0.0137 Å^{-1}.

The atom pair correlation function derived from $I_1(K)$, the resolution corrected differential cross section, is shown in Figure 34. A comparison with the pair correlation function derived from the uncorrected cross section data, Figure 33, indicates that the effects of the resolution removal correction are limited to a narrowing of the first two peaks in the pair correlation function. The spacing of the peaks and the areas beneath them remain unchanged. For pair spacings greater than 3.0 Å, the correlation functions derived from the corrected and uncorrected data are virtually identical.

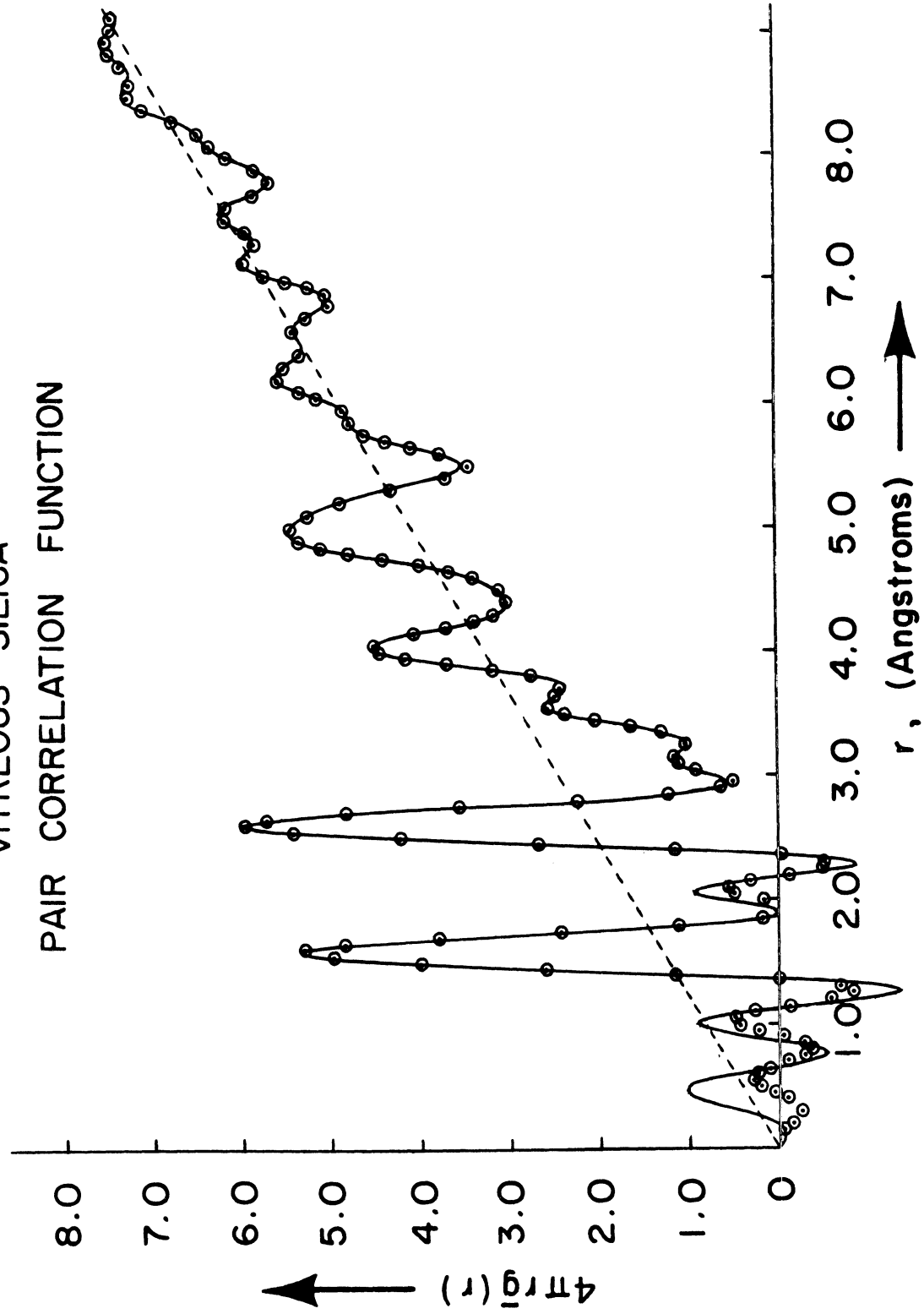

Figure 34. Atom pair correlation function of vitreous silica (with resolution correction).

4.5.5 ERROR ANALYSIS

The pair correlation function derived in the preceding pages must be carefully analyzed for the presence of spurious features before it can be accepted as the final result of the experiment. These effects, which are normally present in the transforms of experimental data, arise from errors in the measurement of I(K), unsuitable treatment of the various correction factors, and/or the termination of the data at a point in K-space where the function Ki(K) has not as yet gone to zero.

The ease with which one can identify the spurious maxima and minima in a correlation function depends in a large measure on the type of system being studied. The analysis of the correlation function of a monatomic liquid is relatively simple in that the errors generally produce secondary maxima which are noticeably sharper than the two or three bona fide maxima. On the other hand, the more complex structure of a molecular liquid or a noncrystalline polyatomic solid such as vitreous silica produces a correlation function in which real and spurious maxima and minima can be quite similar in appearance. In this situation the presence of errors in the correlation function can be detected most readily by the appearance of maxima at such low values of r that it is impossible for them to have any physical significance. As noted in the discussion of the Krough-Moe normalization, legitimate peaks in $4\pi r\bar{g}(r)$

cannot appear at r's smaller than the sum of the smallest pair of atomic radii involved. Also, in this instance a negative value of $4\pi r\bar{g}(r)$ has no physical significance and is indicative of errors in the transform. (If the nuclei of a polyatomic system have neutron scattering lengths of different signs, it is possible for $\bar{g}(r)$ to be less than zero; however, the scattering lengths of both oxygen and silicon are positive.)

In some instances it is possible to associate the spurious effects which one observes in the low r region with a particular type of error. For example, an erroneous peak in the Ki(K) function at K_e, when transformed, produces a general ripple in $4\pi r\bar{g}(r)$ with a period of $\Delta r_e = 2\pi/K_e$, the first maxima appearing at $r = \pi/2K_e$. (248) Conversely, a negative or overlooked peak at K_e produces a ripple with minima at the same sites.

Improper normalization of the I(K) data can also produce spurious oscillations in $4\pi r\bar{g}(r)$ at values of r close to zero. If there is a small fractional error in the normalization of the data, $\frac{\Delta I_\infty}{I_\infty}$, it is a simple matter to show that the corresponding error in the Ki(K) function is

$$\text{IV-31} \qquad \Delta[Ki(K)] = \left[\frac{\Delta I_\infty}{I_\infty}\right] Ki(K) + \left[\frac{\Delta I_\infty}{I_\infty}\right] K$$

The transform of the first term of this expression is simply the correct correlation function (ignoring the termination effects) multiplied by $\frac{\Delta I_\infty}{I_\infty}$, i.e., the error

in $4\pi r\bar{g}(r)$ appears as a shift in scale. The transform of the second term indicates that an additional error which is oscillatory in r is superimposed on the scaling error:

$$\text{IV-32} \qquad \frac{2}{\pi}\int_0^{K_{max}}\left[\frac{\Delta I_\infty}{I_\infty}\right] K\sin Kr \; dK$$

$$= \frac{2}{\pi}\left[\frac{\Delta I_\infty}{I_\infty}\right]\left[\frac{\sin(K_{max}r) - K_{max}r\cos(K_{max}r)}{r^2}\right]$$

It should be noted that the amplitude of the ripple created by a discrete error is relatively constant whereas the oscillatory contribution from a normalization error damps out quite rapidly as r increases.

In most instances, the major errors in experimental correlation functions result from the termination (or truncation) of the Fourier integral at a finite momentum transfer, $K = K_{max}$. The termination of the integration at K_{max} is equivalent to the Fourier transform of the product of $Ki(K)$ and the unit weighting function

$$\text{IV-33} \qquad M(K) = \begin{cases} 1 & \text{at } K \leq K_{max} \\ 0 & \text{at } K > K_{max} \end{cases}$$

Waser and Schomaker (249) have noted that the Fourier transform of the product of two functions is equal to the convolution (or folding) of the Fourier transforms of the separate functions. The cosine transform of the weighting function $M(K)$ is

$$\text{IV-34} \qquad T(r) = \text{const.}\ \frac{\sin K_{max}r}{r}$$

Thus, the function obtained from II-32 when the Fourier integral is terminated at K_{max}, $4\pi r\bar{g}'(r)$, is equal to the convolution of T(r) and the true correlation function, $4\pi r\bar{g}(r)$, the transform of Ki(K) for an infinite range of momentum transfers:

$$\text{IV-35} \quad 4\pi r\bar{g}'(r) = \frac{1}{\pi}\int_{-\infty}^{\infty} 4\pi u\bar{g}(u)\, T(r-u)\, du$$

$$= \frac{1}{\pi}\int_{-\infty}^{\infty} 4\pi u\bar{g}(u)\, \frac{\sin K_{max}(r-u)}{(r-u)}\, du$$

Now, to demonstrate the nature of the spurious effects which are introduced by the truncation of the K-integral, assume that there is a peak in the true correlation function at r_1, i.e. let

$$\text{IV-36} \quad 4\pi r\bar{g}(r) = \delta(r-r_1)$$

Substituting IV-36 in IV-35, it can be seen that

$$\text{IV-37} \quad 4\pi r\bar{g}'(r) = \frac{1}{\pi}\int_{-\infty}^{\infty} \delta(u-r_1)\, \frac{\sin K_{max}(r-u)}{(r-u)}\, du$$

$$= \frac{\sin K_{max}(r-r_1)}{\pi(r-r_1)}$$

This means that a peak which would have the appearance of a delta function in the true correlation function, in $4\pi r\bar{g}'(r)$ would appear as a broadened maximum, full width at half maximum of $3.78/K_{max}$, reduced in height to K_{max}/π. In addition, spurious minima with negative amplitudes of

$0.22\,K_{max}/\pi$ appear at $r_1 + 4.50/K_{max}$, spurious maxima of height $0.13\,K_{max}/\pi$ at $r_1 + 7.72/K_{max}$, and so on (243) (249).

Let us now analyze the correlation function which was derived from the resolution corrected I(K) data (Figure 34). Certain features of this function are relatively easy to identify as spurious, e.g., the minima centered at r_{min} = 0.76, 1.26, and 2.27 Å, and the maxima at r_{max} =0.50 and 1.02 Å. The smallest known distance between a silicon and oxygen atom in any form of silica is the 1.57 Å spacing found in Keatite (250); it follows therefore that the small maxima at 0.50 and 1.02 Å cannot be legitimate features of the correlation function. Since a negative value of $4\pi r\bar{g}(r)$ is physically impossible there is no question that the indicated minima are spurious.

The small maximum at r = 2.06 Å is tentatively identified as a spurious peak primarily because it occurs at the predicted location of a termination satellite. However, it should be noted that Richter, Breitling, and Herre (251) claim that a similar peak which they observe at r = 2.15 Å in their correlation function (derived from x-ray data) is real. Recall also that Strakna (177) has proposed a model in which the acoustic and dielectric losses in vitreous silica are attributed to the motion of oxygen atoms in elongated Si-O-Si bonds. If one accepts this hypothesis, the peak at r = 2.06 Å could be interpreted as the contribution from the Si-O pairs in these elongated

bonds.

At larger values of r the arguments for identifying certain small features of the correlation function as real are much more plausible. As a result it becomes increasingly difficult to distinguish the spurious maxima and minima from the legitimate. To illustrate this problem consider the two small maxima which appear at r = 3.15 and 3.50 Å. The analysis of the termination problem indicates that one might expect to find termination satellites of several of the major maxima at these positions: $r_{max} = 2.6 + 7.72/K_{max} =$ 3.15 Å, $r_{max} = 2.6 + 7.72/K_{max} + 2\pi/K_{max} = 3.6$ Å, and/or $r_{max} = 4.05 - 7.72/K_{max} = 3.5$ Å. On the other hand, the interpretation of the final results of this experiment in Chapter V will indicate that real maxima which can be associated with Si-Si and Si-O atom pairings also occur at these positions.

Fortunately, the ability to distinguish the spurious from the real features at the larger values of r is not crucial to this analysis. One should keep in mind that the ultimate goal of the error analysis is not simply to locate the spurious features in the correlation function but to identify their source. The indisputably spurious maxima and minima observed at the smaller values of r should be sufficient for this purpose.

The characteristics of the small r phenomena in our correlation function strongly indicate that they arise from

the termination problem. In Table IV-3 it is shown that the spurious maxima and minima appear at almost precisely the locations predicted for termination satellites of the major maxima at r = 1.6 and 2.6 Å. The techniques of suppressing these termination induced errors are discussed in Section 4.5.6.

TABLE IV-3 Termination Errors in the Pair Correlation Function

Predicted Locations of Termination Errors	Observed Locations of Spurious Features in $4\pi r\, g'(r)$
$r_{max} = 1.6 - 7.72/K_{max} - 2\pi/K_{max} = 0.60$ Å	$r_{max} = 0.50$ Å
$r_{min} = 1.6 - 4.50/K_{max} - 2\pi/K_{max} = 0.83$ Å	$r_{min} = 0.76$ Å
$r_{max} = 1.6 - 7.72/K_{max} = 1.05$ Å	$r_{max} = 1.02$ Å
$r_{min} = 1.6 - 4.50/K_{max} = 1.28$ Å	$r_{min} = 1.26$ Å
$r_{max} = 1.6 + 7.72/K_{max} = 2.15$ Å	$r_{max} = 2.06$ Å
$r_{max} = 2.6 - 7.72/K_{max} = 2.05$ Å	
$r_{min} = 2.6 - 4.50/K_{max} = 2.28$ Å	$r_{min} = 2.27$ Å

4.5.6 SUPPRESSION OF TERMINATION ERRORS

A number of different techniques of minimizing or completely eliminating the spurious maxima and minima in pair correlation functions have been discussed in the literature. As noted in Chapter I, one popular method of diminishing the termination effects is to multiply the integrand of the correlation function expression (II-32) by a suitable weighting or modification factor. For example, $\exp(-a K^2)$ is one such function often used for this purpose. The coefficient a, which has been called the arbitrary temperature factor, is usually chosen so that the resulting integrand of II-32 has a negligible value beyond K_{max}, the upper limit of the experimental measurement. (An extensive discussion of the application of modification factors to diffraction data is provided by Waser and Schomaker (249).) Although the application of a modification factor of this nature has the salutory effect of suppressing the termination induced features and spurious effects arising from errors in $I(K)$ at the larger K's, it also results in a general broadening of the features of the correlation function. This broadening effect has serious consequences for the small, but real maxima and minima: those in close proximity to the larger peaks can be seriously distorted and in some instances completely obscured. Therefore, the use of modification factors is considered to be unsuitable for the analysis of the vitreous silica data.

Kaplow, Strong, and Averbach (252) have proposed a trial and error smoothing process to eliminate the spurious detail introduced by the termination problem. Although this technique is not applied to the data reported here, it is of interest because it has been employed in one of the most recent and extensive diffraction studies of vitreous silica (40).

In order that the notation used here will be consistent with that of Kaplow, et.al. let

IV-38 $$G(r) = 4\pi r(\bar{g}(r) - g_o)$$

and

IV-39 $$F(K) = Ki(K)$$

To obtain the true function G(r) from the experimental data the authors employ two criteria: (1) a transform of G(r) must reproduce the measured function F(K); (2) in the absence of other errors, the function G(r) must be linear in the region below the first peak.

The correction procedure is described as follows: "A first approximation G^e is obtained by transforming the normalized data F^e for three or more termination points. The function G^e is corrected by following the trend of the successive termination effects and removing the obvious irregularities and the oscillations below the first peak. The corrected function G^c is then transformed to produce

the function F^c, which may be compared with the experimental function F^e. F^c and F^e will differ in two ways: (1) they may be different in the region $0 < K < K_{max}$, indicating that the function G^c is not consistent with the experimental data, and (2) the function F^c will extend beyond K_{max}, since it is computed from G^c rather than measured experimentally. In general, F^c will not coincide with F^e on transforming the first trial value of G^c, but it is usually not obvious how G^c should be changed from an observation of $(F^e - F^c)$.

The new value F^c is then terminated at K_{max} and transformed to give a new distribution function. This distribution function contains a termination error, which is obtained by subtraction and used to correct the experimental function G^e. The corrected G^e may be compared with G^c and the comparison will indicate the alteration required in G^c. The procedure is repeated until the match is arbitrarily good. The transform of the final G^c is used to extend F^e. At this point we have a function $F(K)$, which matches the experimental values up to K_{max}, and extends beyond K_{max} to large values of K. This extended function may then be transformed to give a final value of $G(r)$ which is free from spurious detail, and consistent with the experimental data."

This correction technique is considered to be unacceptable for the following reasons: (1) In practice it is difficult to 'see through' a transform and predict the

effect on $F(K)$ of small adjustments in $G(r)$ or vice versa. In the case of vitreous silica the $G(r)$ and $F(K)$ functions have a considerable amount of structure. Even when the calculations described above are programed for a computer, the number of iterations required to produce a convincing fit is prohibitive. (2) The correction process begins with an attempt to identify the spurious features of G^e, particularly at the larger values of r, by evaluating the transform of F^e for different values of K_{max}. Those features which vary with the choice of K_{max} are judged to be spurious. In practice we have found that the differences in the values of K_{max} must be quite large (~ 3 Å^{-1}) to observe significant variations. This analysis is complicated by the fact that the shapes of the real peaks in G^e are also sensitive to the choice of K_{max}. As K_{max} decreases there is a considerable broadening effect which alters the appearance of the smaller, but real features - especially those which occur in the immediate vicinity of one of the larger peaks. Furthermore, even if a small feature is truly spurious and is observed to shift in position as K_{max} is varied, this does not preclude the possibility that a real peak is also present in the same general vicinity. The error identification technique employed by Kaplow, et.al. does not have the sensitivity required to determine if there are real features in close proximity to the spurious. (3) Kaplow, et.al. state that the final G^c is used to

extend F^e beyond the K_{max} of the experimental measurement. This extended function is subsequently transformed to obtain the final result, G(r). It should be obvious that the extended portion of the F^e function, which is generated according to the instructions provided above, is in no way unique. The transform of an artificial extension of the experimental data can hardly be expected to provide us with a more accurate representation of the true correlation function.

The technique of removing the termination effects which has been employed in this report is similar to one proposed by Warren (253). The analysis begins with the familiar integral equations relating the pair correlation function and the differential scattering cross section:

$$\text{IV-40} \qquad K i(K) = \int_0^\infty 4\pi r(\bar{g}(r) - g_o) \sin Kr \; dr$$

and

$$\text{IV-41} \qquad 4\pi r(\bar{g}(r) - g_o) = \frac{2}{\pi}\int_0^\infty K i(K) \sin Kr \; dK$$

Recall that as a result of the termination of the experimental measurement at K_{max} we obtain the function $\bar{g}'(r)$ from the inversion of our data:

$$\text{IV-42} \qquad 4\pi r(\bar{g}'(r) - g_o) = \frac{2}{\pi}\int_0^{K_{max}} K i(K) \sin Kr \; dK$$

The substitution of IV-40 in IV-42 provides an equivalent expression for $\bar{g}'(r)$ in terms of $\bar{g}(r)$:

IV-43 $$4\pi r(\bar{g}'(r) - g_o) = \frac{2}{\pi}\int_o^{K_{max}} \sin Kr \int_o^{\infty} 4\pi r'(\bar{g}(r') - g_o) \sin Kr'\, dr'\, dK$$

Evaluating the K-integral we have

IV-44 $$\int_o^{K_{max}} \sin Kr \sin Kr'\, dK = \int_o^{K_{max}} \tfrac{1}{2}\left[\cos K(r - r') - \cos K(r + r')\right] dK = \frac{K_{max}}{2}\left[j_o(K_{max}[r - r']) - j_o(K_{max}[r + r'])\right]$$

where $j_o(x) = \frac{\sin x}{x}$, the spherical Bessel function of order zero

Therefore, it follows that

IV-45 $$4\pi r(\bar{g}'(r) - g_o) = \frac{K_{max}}{\pi}\int_o^{\infty}\left[j_o(K_{max}[r - r']) - j_o(K_{max}[r + r'])\right] \times 4\pi r'(\bar{g}(r') - g_o)\, dr'$$

The integration of the g_o term is straightforward and IV-45 reduces to

IV-46 $$4\pi r\bar{g}'(r) = \frac{K_{max}}{\pi}\int_o^{\infty}\left[j_o(K_{max}[r - r']) - j_o(K_{max}[r + r'])\right] \times 4\pi r'\, \bar{g}(r')\, dr'$$

This is the basic expression employed in our removal of the

termination effects.

The details of the correction are as follows: by a trial and error fitting process one attempts to generate the true correlation function $4\pi r'\bar{g}(r')$, which, when substituted in IV-46, reproduces $(4\pi r\bar{g}'(r))_{exp}$, the truncated transform of the experimental data. In the fitting process it is convenient to represent $4\pi r'\bar{g}(r')$ as a series of scalar delta functions, i.e.,

$$\text{IV-47} \qquad 4\pi r'\bar{g}(r') = \sum_{n=0} G_n \delta(r'-r_n)$$

where $r_n = (n + \frac{1}{2})\Delta r$. Δr is a suitably small interval in r chosen to provide the necessary detail in features of the corrected function. (For the work reported here, $\Delta r = 0.10$ Å). Substituting IV-47 in IV-46 we have

$$\text{IV-48} \qquad 4\pi r\bar{g}'(r) = \frac{K_{max}}{\pi}\int_0^{\infty}\left[j_0(K_{max}[r-r'])- j_0(K_{max}[r+r'])\right] \times \sum_{n=0} G_n \delta(r'-r_n)\, dr'$$

$$= \frac{K_{max}}{\pi}\sum G_n\left[j_0(K_{max}[r-r_n])-j_0(K_{max}[r+r_n])\right]$$

Thus, one generates a set of the G_n coefficients, calculates $4\pi r\bar{g}'(r)$ by means of IV-48, and compares this result with $(4\pi r\bar{g}'(r))_{exp}$. If the match is not satisfactory, the G_n's are adjusted and a new $4\pi r\bar{g}'(r)$ function is calculated. The iterative process of adjusting the G_n's continues until one is able to satisfactorily reproduce $(4\pi r\bar{g}'(r))_{exp}$.

One of the major advantages of the technique described

above is that the corrected function which one is attempting to generate is related directly to the function being fitted rather than its Fourier transform. The adjustments in the G_n's required to produce a given change in $4\pi r\bar{g}'(r)$ are much more obvious than the alterations one would have to make in the $K\,i(K)$ function to produce the equivalent result. Also, note that the j_o's in IV-48 are functions which damp out rather rapidly. For the K_{max} of the measurement reported here, j_o decreases to less than 0.14 of its maximum value at $r \pm 0.55$ Å. This means that the response in $4\pi r\bar{g}'(r)$ to an adjustment of one of the G_n's is confined to a very small interval in r.

The results of the application of this termination correction technique to our vitreous silica data are shown in Figures 34 and 35. Recall that our best estimate of $(4\pi r\bar{g}'(r))_{exp}$ is represented by the solid curve in Figure 34. The termination corrected function, $4\pi r\bar{g}(r)$, is shown in Figure 35. The function $4\pi r\bar{g}'(r)$, obtained from the corrected correlation function shown in Figure 35, is represented by the solid data points in Figure 34.

The almost exact matching of the two functions in Figure 34 indicates that the spurious features in our best estimate of $(4\pi r\bar{g}'(r))_{exp}$ are due almost entirely to the termination problem. The very slight mismatch in the small r region is attributed to the small amount of uncorrected resolution broadening which remains in the I(K)

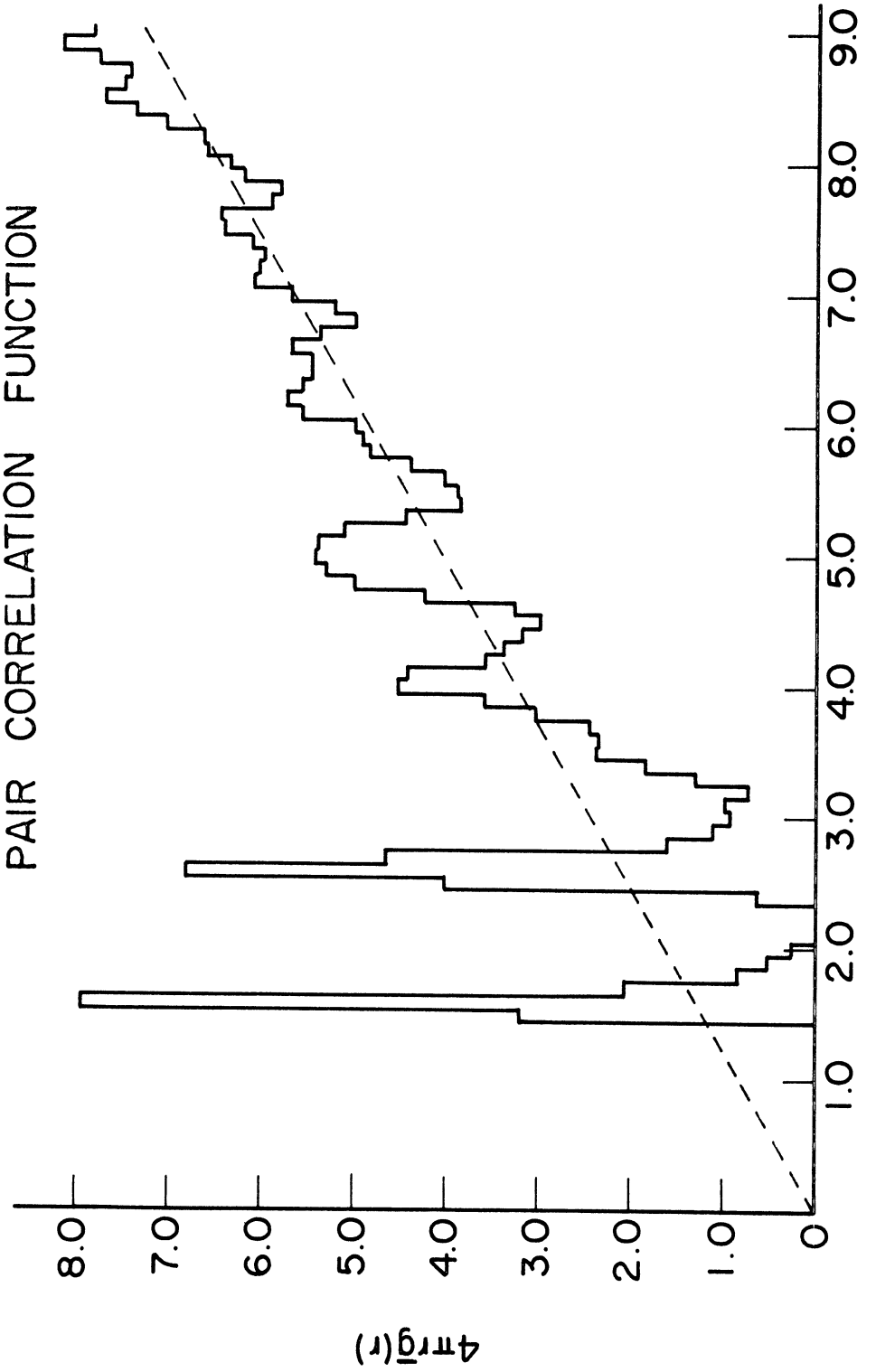

Figure 35. Atom pair correlation function of vitreous silica (with corrections for resolution and termination effects).

data (Section 4.5.4). A comparison of the correlation functions derived from the I(K) data before and after the resolution correction, Figures 33 and 34 respectively, indicates that the amplitudes of the spurious features in the small r region are sensitive to this correction. The effect of the partial removal of the resolution broadening is most apparent in the behavior of the first spurious maximum which shows a marked decrease in size and a tendency to shift closer to the predicted position of the first termination satellite (Table IV-3).

Although the foregoing discussion has dealt exclusively with the computation of the pair correlation function, one should remember that it is possible to analyze the data by still another technique - the direct comparison of the measured cross section with the theoretical cross sections of various models. Indeed, Waser and Schomaker (249) indicate that one generally uses the results of the correlation function calculation to narrow the choice of possible models and structural parameters and then analyzes the remaining possibilities by comparing the measured and theoretical cross sections. The obvious inference is that the latter technique provides a more sensitive method of analysis.

Unfortunately, the technique of comparing measured and theoretical cross sections does not enable one to circumvent the termination problem. The relationship

between the differential scattering cross section and the pair correlation function of a model is defined by IV-40:

$$\text{IV-40} \quad \left[Ki(K)\right]_M = \int_0^\infty \left[4\pi r(\bar{g}(r)-g_o)\right]_M \sin Kr \; dr$$

Although this expression calls for integration over an infinite range of r's, the specification of atom pairings and spacings for a model must of necessity be limited to a finite range. Therefore, what one actually calculates is the function

$$\text{IV-49} \quad \left[Ki(K)\right]'_M = \int_0^{r_{max}} \left[4\pi r(\bar{g}(r)-g_o)\right]_M \sin Kr \; dr$$

where r_{max} is the maximum atom pair spacing specified for the model. (In those few instances where models of the structure of vitreous silica have been described in explicit terms, r_{max} is generally less than 13 Å.) Since the truncation of the r-integral at r_{max} can be expected to produce spurious effects, a comparison of $\left[Ki(K)\right]'_M$ with the measured function, $\left[Ki(K)\right]_{exp}$, is unsatisfactory and very apt to be misleading.

Fortunately, the spurious, termination induced features in $\left[Ki(K)\right]'_M$ can be suppressed by exactly the same technique employed above in the correction of the pair correlation function. The expression for $\left[Ki(K)\right]'_M$ in terms of the error free function $\left[Ki(K)\right]_M$ is derived from IV-49 and IV-41:

$$\text{IV-50}\quad \left[Ki(K)\right]'_M = \int_0^{r_{max}} \left[4\pi r(\bar{g}(r)-g_o)\right]_M \sin Kr \; dr$$

$$= \frac{2}{\pi}\int_0^{r_{max}} \sin Kr \int_0^{\infty} \sin K'r \left[K'i(K')\right]_M \, dK' \, dr$$

$$= \frac{r_{max}}{\pi}\int_0^{\infty} \left(J_o\left[r_{max}(K-K')\right] - J_o\left[r_{max}(K+K')\right] \right) \times \left[K'i(K')\right]_M \, dK'$$

By the trial and error fitting process one generates the function $\left[K'i(K')\right]_M$ which, when substituted in IV-50, reproduces the function $\left[Ki(K)\right]'_M$ derived from IV-49. The function which satisfies this condition is the most accurate representation of the theoretical cross section of the model which can be derived from the information at hand.

As an example let us assume that we have a model whose pair correlation function is exactly like that shown in Figure 35. r_{max} in this instance is 9 Å. From IV-49 we derive the function $\left[Ki(K)\right]'_M$. This result is represented by the triangular points in Figure 36; the measured function for the vitreous silica, $\left[Ki(K)\right]_{exp}$, is represented by the solid curve in the same figure. Since the correlation function we are dealing with was originally derived from $\left[Ki(K)\right]_{exp}$, the close match which is observed between $\left[Ki(K)\right]_{exp}$ and $\left[Ki(K)\right]'_M$ is expected. However, there are also some rather apparent discrepancies which must be

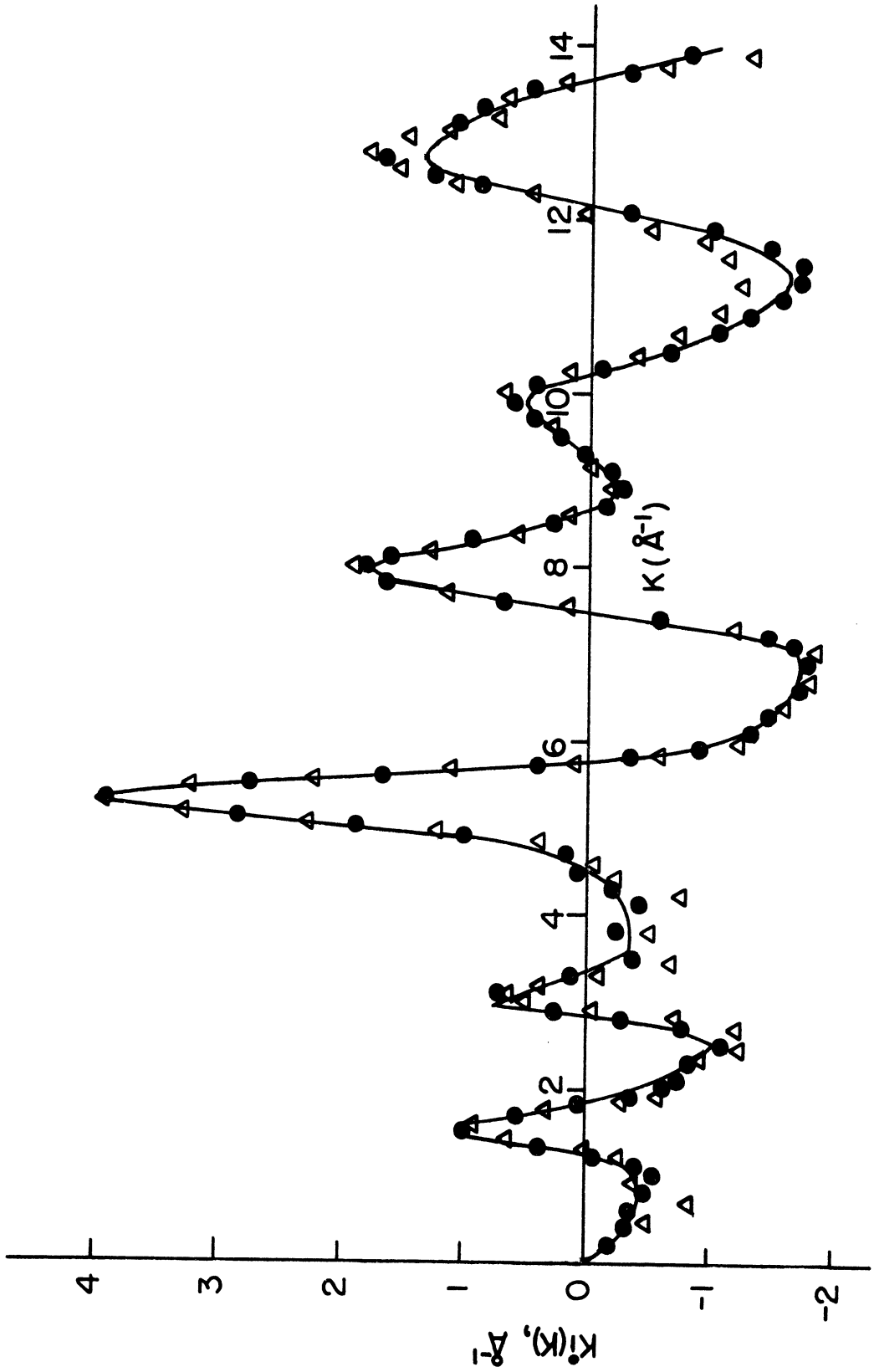

Figure 36. $K\left[\frac{I(K) - I_\infty}{I_\infty}\right]$ versus K for vitreous silica.

explained. As noted above, the most probable source of these discrepancies is the presence of spurious termination effects in $[Ki(K)]'_M$.

In the usual analysis the next step would be the solution of IV-50 for the error free function $[K'i(K')]_M$. However, in this case the trial and error solution process is unnecessary. If Figure 35 is indeed an accurate representation of the true correlation function, one should be able to reproduce the function $[Ki(K)]'_M$ derived from IV-49 by substituting $[Ki(K)]_{exp}$ for $[K'i(K')]_M$ in IV-50. The result of this calculation is represented by the solid data points in Figure 36. Observe that the $[Ki(K)]'_M$ functions derived from IV-49 and IV-50 are in excellent agreement. This confirms that our best estimate of the correlation function of vitreous silica is free from spurious termination satellites and completely consistent with $[Ki(K)]_{exp}$.

CHAPTER V

5.1 INTERPRETATION OF THE STRUCTURE DATA

We begin the interpretation of the experimental results with an analysis of the atom pair correlation function. If we were dealing with a monatomic substance, the analysis of a distribution function of this nature would be relatively straightforward. When there is only one possible type of atom pairing, the number of atom pairs at various spacings in the structure is determined simply by integrating the areas under the maxima in the function $4\pi r^2 \bar{g}(r)$. The interpretation of the pair correlation function of a polyatomic system obviously is more complicated. In the case of vitreous silica, there are three possible atom pairings to consider: silicon-oxygen, oxygen-oxygen, and silicon-silicon. This means that a peak in Figure 35 could be the product of a single type of atom pairing or a combination of two or even three different types of atom pairs with similar interatomic spacings.

In Chapter I we discussed Henninger's (40) proposal of identifying atom pairings by forming the ratio of the pair correlation functions derived from x-ray and neutron data. This technique was not employed here because it is useful only for identifying well resolved maxima produced by a single type of atom pair. When a peak in the pair correlation function involves more than one type of atom pairing, the ratio provides neither the identities nor the

relative numbers of the different pairs. (Other criticisms of this technique were noted in Section 1.3.13 .)

Since there is no exact method of identifying which atom pairs produce a given peak in $\left[4\pi r\bar{g}(r)\right]_{exp}$, the the analysis of the data must rely rather heavily on our knowledge of the structures of the crystalline silicas. This use of the crystal data is justified by the many common physical properties which suggest the presence of short range similarities in the structures of the crystalline and vitreous silicas.

The first peak in the pair correlation function is identified as the contribution of the nearest neighbor silicon-oxygen pairs. Inspection of Figures 34 and 35 indicates that the mean silicon-oxygen spacing lies within one or two percent of 1.60 Å. The slight skewing of the peak towards larger spacings suggests the possibility of a distribution of silicon-oxygen spacings similar to the 1.58 Å to 1.69 Å range observed in beta-cristobalite. The minimum separation of the nearest silicon and oxygen atoms in a crystalline silica is the 1.52 Å spacing in beta-tridymite; the maximum spacing is the abovementioned 1.69 Å in beta-cristobalite.

It is a well established fact that each silicon atom in the crystalline silicas has four oxygen atoms as its nearest neighbors; the nearest neighbors of each oxygen atom are two silicons. If the same correlation occurs in vitreous silica, the integration of the area under the first peak in

$4\pi r^2 \bar{g}(r)$ should give a value of 2.23 :

$$\text{V-1} \quad \int_{1\text{st peak}} 4\pi r^2 \bar{g}(r)\, dr =$$

$$= \int 4\pi r^2\, dr \; \frac{\sum_t (b_{coh})_t \sum_{t'} N_{t'} (b_{coh})_{t'} g_{t't}(r)}{\sum_t N_t (b^2_{coh})_t}$$

$$= \int 4\pi r^2\, dr \; (b_{coh})_O (b_{coh})_{Si} \left[\frac{N_{Si} g_{Si-O} + N_O g_{O-Si}}{N_O (b^2_{coh})_O + N_{Si} (b^2_{coh})_{Si}} \right]$$

$$= 2.23$$

where $\int 4\pi r^2\, dr\, g_{O-Si} = 2$

$\int 4\pi r^2\, dr\, g_{Si-O} = 4$

$n_O = N_O/V = 0.0442$ atoms/Å^3

$n_{Si} = N_{Si}/V = 0.0221$ atoms/Å^3

$(b_{coh})_O = 0.577 \times 10^{-12}$ cm

$(b_{coh})_{Si} = 0.42 \times 10^{-12}$ cm

The value derived from the integration of the experimental function in the region between r = 1.4 Å and r = 2.1 Å is 2.38, a difference of less than 7%. By way of comparison, Henninger, et.al. (40) find that the integral of the first maximum in their correlation function exceeds the expected number of Si-O pairs by 25%.

The prominent second peak in $4\pi r\bar{g}(r)$ is identified as the contribution of the nearest oxygen neighbors in the

structure. The indicated mean O-O spacing is 2.60 Å. (The minimum and maximum O-O spacings in the crystalline silicas, 2.45 Å and 2.74 Å respectively, both occur in beta-cristobalite.) From the Si-O and O-O spacings we obtain the angle β(O-Si-O) :

$$\text{V-2} \quad \beta(\text{O-Si-O}) = \arccos\left[\frac{2R_{\text{Si-O}}^2 - R_{\text{O-O}}^2}{2R_{\text{Si-O}}^2}\right]$$

$$= \arccos\left[\frac{2(1.60)^2 - (2.60)^2}{2(1.60)^2}\right] = 109^\circ$$

If each silicon atom lies in the center of a regular tetrahedron formed by the four nearest neighbor oxygens, the expected value of β(O-Si-O) is $109^\circ 28'$.

In every known crystalline silica but one, the SiO_4 tetrahedra link together only at their vertices. The sole exception is Silica W, a low density microfibrous crystalline phase of silica in which the neighboring tetrahedra share common edges. If the SiO_4 tetrahedra in vitreous silica also link at their vertices, there will be a total of six nearest neighbor oxygen-oxygen pairs. The integral of the second peak in $4\pi r^2 \bar{g}(r)$ would be expected to have a value of 4.74 :

$$\text{V-3} \quad \int_{\text{2nd peak}} 4\pi r^2 \bar{g}(r)\, dr = \int 4\pi r^2\, dr \left[\frac{(b_{\text{coh}}^2)_O N_O\, g_{\text{O-O}}}{N_O(b_{\text{coh}}^2)_O + N_{Si}(b_{\text{coh}}^2)_{Si}}\right]$$

$$= 4.74$$

where $\int 4\pi r^2 \, dr \, g_{O-O} = 6$

Integration of the experimental function between r = 2.35 Å and r = 2.95 Å gives a value of 4.94 . The difference between the measured and expected pair densities is approximately 3.5 % . Again by way of comparison, Henninger, et.al. (40) find that their pair correlation function overestimates the expected number of O-O pairs by 14 % .

In determining the number of O-O pairs represented by the second peak we have our first encounter with the problem of overlapping maxima in the pair correlation function. Fortunately, the O-O peak is so much larger than its neighbor that even with the overlap at the larger pair spacings one can still obtain an accurate measure of the number of nearest neighbor oxygen-oxygen pairs.

The next maximum in the pair correlation function, the rather small feature immediately adjacent to the O-O peak, is identified as the contribution of the nearest silicon-silicon neighbors in the structure. The mean Si-Si spacing lies between 3.05 Å and 3.10 Å . This means that the mean angle of linkage between neighboring SiO_4 tetrahedra,

$$\text{V-4} \qquad \ominus(\text{Si-O-Si}) = \arccos\left[\frac{2R^2_{\text{Si-O}} - R^2_{\text{Si-Si}}}{2R^2_{\text{Si-O}}}\right] ,$$

is between 145° and 151°. In the following discussion it is tentatively assumed that $\ominus(\text{Si-O-Si}) = 148^\circ$.

Since the neighboring SiO_4 tetrahedra link at their

vertices rather than sharing common edges or joining face to face, one would expect that integration of the third peak in $4\pi r^2\bar{g}(r)$ would indicate the presence of four nearest neighbor silicon-silicon pairs, i.e. ,

$$\text{V-5} \qquad \int_{\text{3rd peak}} 4\pi r^2\bar{g}(r)\,dr = \int 4\pi r^2\,dr\left[\frac{(b_{coh}^2)_{Si}N_{Si}\,g_{Si\text{-}Si}}{N_O(b_{coh}^2)_O + N_{Si}(b_{coh}^2)_{Si}}\right]$$

$$= 0.84$$

where $\int 4\pi r^2\,dr\,g_{Si\text{-}Si} = 4$

(The expectation of four Si-Si pairs at this spacing also assumes that the structure of vitreous silica is a continuous network of interconnected silicon and oxygen atoms in which the number of nonbridging oxygen atoms is relatively insignificant.) An accurate integration of the Si-Si peak is quite difficult due to its small size and the fact that it is not well resolved. As an alternative, let us consider the total integral of $4\pi r^2\bar{g}(r)$ in the region between r = 0 and r = 3.35 Å . An interatomic spacing of 3.35 Å should be large enough to include all of the nearest neighbor Si-O, O-O, and Si-Si pairs and yet be small enough to preclude significant contributions from the next nearest neighbors in the structure, the Si-(2nd)O and O-(2nd)O pairs. The expected value of the integral is

$$\text{V-6} \qquad \int_0^{3.35} 4\pi r^2\bar{g}(r)\,dr = \underbrace{2.23}_{\text{Si-O}} + \underbrace{4.74}_{\text{O-O}} + \underbrace{0.84}_{\text{Si-Si}} = 7.81$$

The integral of the experimental function gives a value of 8.55, approximately 9.5 % greater than expected. Some of this discrepancy can undoubtably be attributed to O-(2nd)O pairs with spacings less than 3.35 Å . One should also recall that the largest termination satellites and the oscillating contribution from normalization errors occur at the smaller values of r.

Most of the pair correlation functions of vitreous silica which have appeared in the literature indicate that in the region between r = 3.4 Å and r = 4.4 Å there is a single broad maximum centered at r = 4.0 Å. In this work it has been determined that there are two maxima in this region: one at r = 3.6 Å and one at r = 4.05 Å. Only Lorch (89), who reports maxima at r = 3.6 Å and r = 4.05 Å, has obtained similar results. The reason for this discrepancy is that although the 3.6 Å peak is a real feature found in almost every pair correlation function derived from neutron data, it is invariably identified as a spurious termination satellite and suppressed. Such is the case in the work of Carraro (88) and Henninger (40). In each instance the transform of their neutron data clearly indicates the presence of a peak at r = 3.6 Å prior to adjustments for termination effects; yet, in the"corrected" transforms the peak has disappeared. In Chapter IV it was shown that the point at which a spurious termination satellite appears in the pair correlation function depends on the maximum

momentum transfer in the experimental measurement. K_{max} in Carraro's measurement was $\sim 18.2\ \text{Å}^{-1}$, in Henninger's, $\sim 12.9\ \text{Å}^{-1}$, and in our measurement $\sim 14.2\ \text{Å}^{-1}$. Since the position of the peak in question is insensitive to this very large range of K_{max}'s, it can hardly be a termination satellite.

The character of the pair correlation function in the region between r = 3.3 Å and r = 4.3 Å is determined almost exclusively by the distribution of the Si-(2nd)O and the O-(2nd)O atom pairs. To illustrate the many different positions which these atoms can assume we employ a model of two regular SiO_4 tetrahedra sharing a common oxygen atom. As shown in Figure 37, the common or linking oxygen atom locates the origin of a rectangular Cartesian coordinate system. It is convenient to orient the coordinate axes so that $Si^{(1)}$, $Si^{(2)}$, and $O^{(1)}$, the three atoms which define the linking angle Θ, all lie in the x-y plane. In Table V-1 the coordinates of the nine atoms in the linked tetrahedra are described by four parameters: R, the nearest neighbor silicon-oxygen spacing; Θ, the linking angle of the tetrahedra; ϕ_1 and ϕ_2, the angles describing the rotations of the tetrahedra about the axes $O^{(1)}$-$Si^{(1)}$ and $O^{(1)}$-$Si^{(2)}$. Each silicon-(2nd)oxygen spacing is determined by specifying R, Θ, and either ϕ_1 or ϕ_2. For example, the spacing between the atoms $Si^{(2)}$ and $O^{(2)}$ is

$$V\text{-}7 \qquad R\left[Si^{(2)} - O^{(2)}\right] = \left[\frac{11}{3}R^2 - \frac{8}{3}R^2\cos\Theta - \frac{2(8)^{\frac{1}{2}}}{3}R^2\sin\Theta\cos\phi_1\right]^{\frac{1}{2}}$$

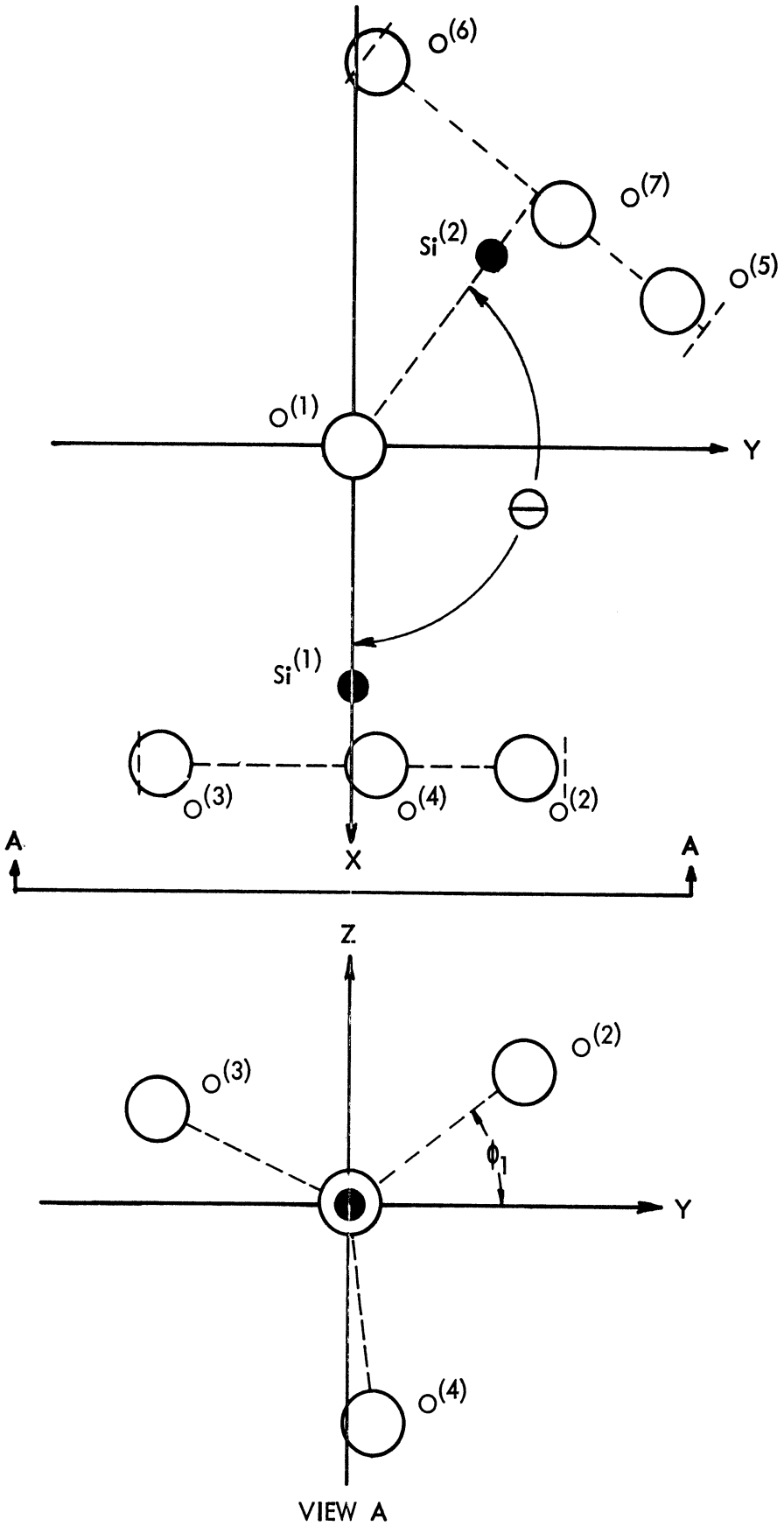

Figure 37. Coordinate system for two regular SiO_4 tetrahedra linked by a common oxygen atom.

TABLE V-1 Coordinates of the Atoms of Two Regular SiO_4 Tetrahedra Linked by a Common Oxygen Atom

$Si^{(1)}$	$X = R$ $Y = 0$ $Z = 0$
$Si^{(2)}$	$X = R\cos\Theta$ $Y = R\sin\Theta$ $Z = 0$
$O^{(1)}$	$X = 0$ $Y = 0$ $Z = 0$
$O^{(2)}$	$X = (4/3)\,R$ $Y = (\sqrt{8}/3)\,R\cos\phi_1$ $Z = (\sqrt{8}/3)\,R\sin\phi_1$
$O^{(3)}$	$X = (4/3)\,R$ $Y = (\sqrt{8}/3)\,R\cos(\phi_1 + 120^\circ)$ $Z = (\sqrt{8}/3)\,R\sin(\phi_1 + 120^\circ)$
$O^{(4)}$	$X = (4/3)\,R$ $Y = (\sqrt{8}/3)\,R\cos(\phi_1 + 240^\circ)$ $Z = (\sqrt{8}/3)\,R\sin(\phi_1 + 240^\circ)$
$O^{(5)}$	$X = (4/3)\,R\cos\Theta + (\sqrt{8}/3)\,R\cos\phi_2\sin\Theta$ $Y = (4/3)\,R\sin\Theta - (\sqrt{8}/3)\,R\cos\phi_2\cos\Theta$ $Z = (\sqrt{8}/3)\,R\sin\phi_2$
$O^{(6)}$	$X = (4/3)\,R\cos\Theta + (\sqrt{8}/3)\,R\cos(\phi_2 + 120^\circ)\sin\Theta$ $Y = (4/3)\,R\sin\Theta - (\sqrt{8}/3)\,R\cos(\phi_2 + 120^\circ)\cos\Theta$ $Z = (\sqrt{8}/3)\,R\sin(\phi_2 + 120^\circ)$
$O^{(7)}$	$X = (4/3)\,R\cos\Theta + (\sqrt{8}/3)\,R\cos(\phi_2 + 240^\circ)\sin\Theta$ $Y = (4/3)\,R\sin\Theta - (\sqrt{8}/3)\,R\cos(\phi_2 + 240^\circ)\cos\Theta$ $Z = (\sqrt{8}/3)\,R\sin(\phi_2 + 240^\circ)$

In Figure 38 the various R[Si-(2nd)O]'s are plotted as a function of ϕ for a silicon-oxygen spacing of R = 1.60 Å and a linking angle of $\Theta = 148^{\circ}$. (The error flags indicate the range in values of R[Si-(2nd)O] for variations in Θ of $\pm 3^{\circ}$.) The oxygen-(2nd)oxygen spacings are functions of all four of the parameters, e.g., the spacing between the atoms $O^{(2)}$ and $O^{(5)}$ is given by the expression:

V-8 $$R\left[O^{(2)} - O^{(5)}\right] =$$

$$\frac{4R}{3}\left[3 - (2)^{\frac{1}{2}}\sin\theta(\cos\phi_1 + \cos\phi_2) - \cos\theta(2 - \cos\phi_1\cos\phi_2) - \sin\phi_1\sin\phi_2\right]^{\frac{1}{2}}$$

Several of the R[O-(2nd)O]'s are plotted in Figure 39 for different combinations of ϕ_1 and ϕ_2.

There have been numerous suggestions that the structure of vitreous silica can be described as a network of SiO_4 tetrahedra in which the angles ϕ_1 and ϕ_2 are uniformly distributed from 0 to 360°. Warren (26), for one, has stated that "the orientation of one tetrahedral group with respect to a neighboring group about the connecting Si-O-Si bond can be practically random." Dean and Bell (254) make a similar claim: "each tetrahedral unit can lie in any position formed by rotating it about the bond joining its central silicon atom to the bridging oxygen." However, it can be shown that the distribution of Si-(2nd)O and O-(2nd)O pairs derived from a random rotation model does not agree with the measured pair correlation function.

The distribution functions for ϕ_1 and ϕ_2 in the random

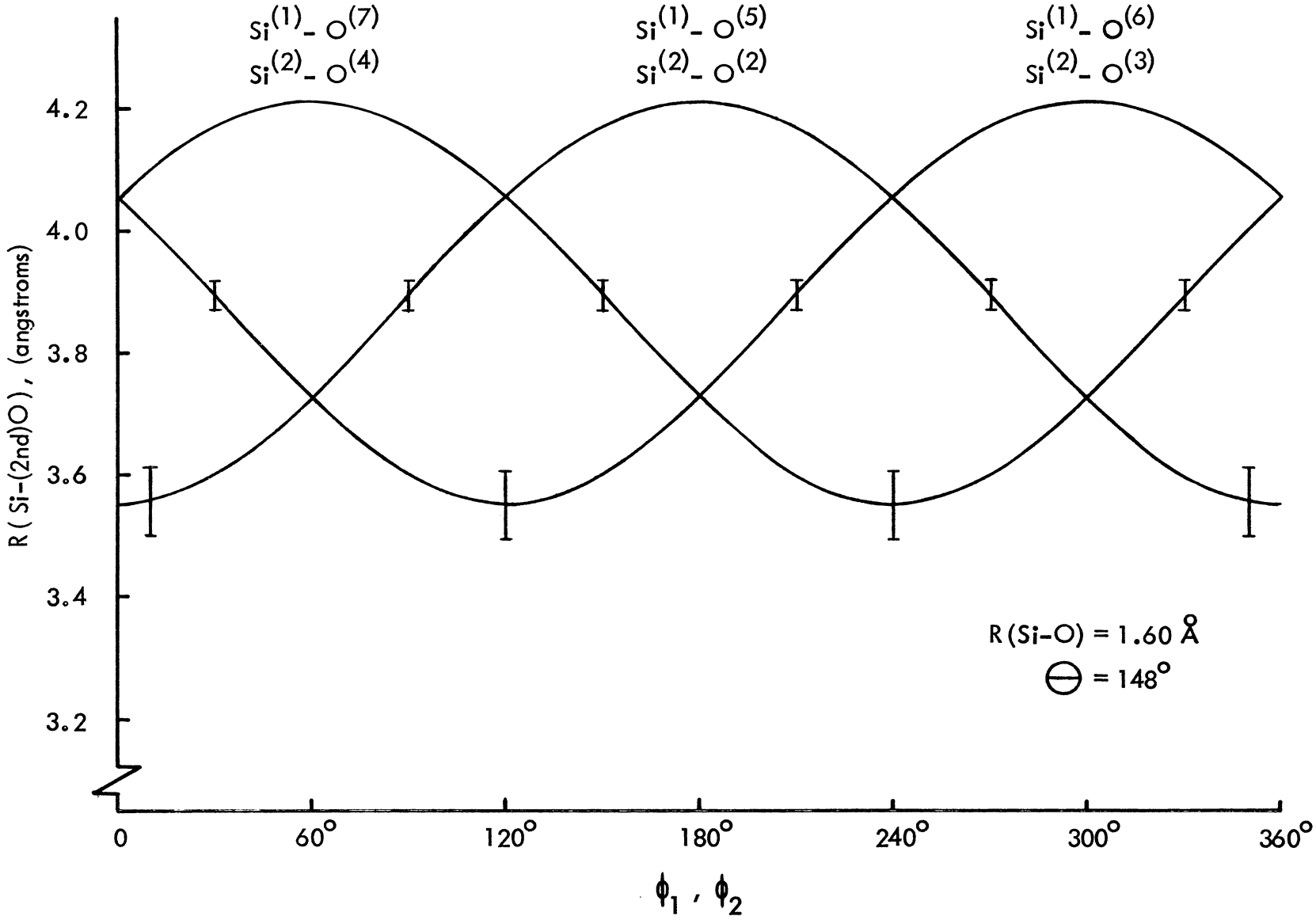

Figure 38. Silicon - (2nd)oxygen spacings.

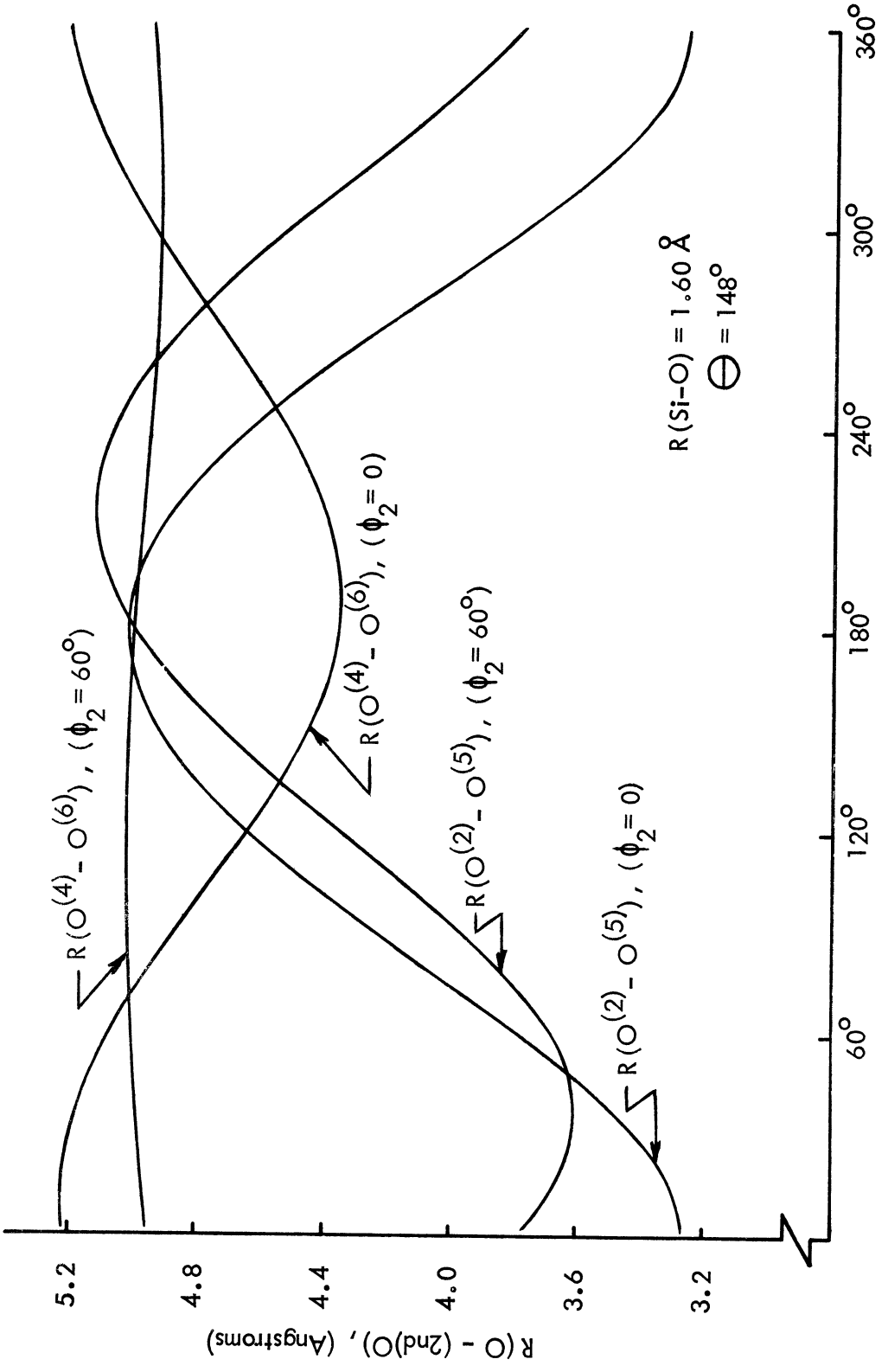

Figure 39. Oxygen - (2nd)oxygen spacings.

rotation model, $P_1(\phi_1)$ and $P_2(\phi_2)$, are constants of magnitude $1/2\pi$ per radian. Assuming for the moment that the structure parameters R and Θ are constants, the distribution of the Si-(2nd)O pairs in the model, P'(R'), is derived from the relationship:

$$\text{V-9} \qquad P'(R') = \int_0^{2\pi} P_1(\phi_1)\, d\phi_1\ \delta\left[R' - R_1(\phi_1)\right]$$

The function $R_1(\phi_1)$ in the argument of the delta function is the expression for the spacing between the atoms Si[(2)] and O[(2)]. (Since the SiO_4 tetrahedra are assumed to be regular in shape, the distribution function derived from $R_1(\phi_1)$ and $P_1(\phi_1)$ will represent all of the Si-(2nd)O pairs in this structure. Likewise, the expression for the spacing of a single O-(2nd)O pair can be used to derive the distribution function for all of the O-(2nd)O pairs in the model.) The delta function has the property

$$\text{V-10} \qquad \delta\left[f(x)\right] = \frac{1}{\left|\frac{\partial f}{\partial x}\right|_{x_o}}\ \delta(x - x_o) \quad \text{where } f(x_o) = 0 ,$$

and therefore the expression for P'(R') reduces to

$$\text{V-11} \qquad P'(R') = P_1(\phi_1)\ \frac{1}{\left|\frac{\partial R_1}{\partial \phi_1}\right|}$$

$$= \frac{1}{2\pi}\left|\frac{2\left[\frac{11}{3}R^2 - \frac{8}{3}R^2\cos\theta - \frac{2(8)^{\frac{1}{2}}}{3}R^2\sin\theta\cos\phi_1\right]^{\frac{1}{2}}}{\frac{2(8)^{\frac{1}{2}}}{3}R^2\sin\theta\sin\phi_1}\right|$$

The Si-(2nd)O distribution function is plotted in Figure 40

for values of R = 1.60 Å and Θ = 148°.

The distribution of O-(2nd)O pairs in the random rotation model is derived from the expression:

$$\text{V-12} \qquad P''(R'') = \int_0^{2\pi}\int_0^{2\pi} P_{12}(\phi_1,\phi_2)\, d\phi_1 d\phi_2 \;\; \delta\left[R'' - R_2(\phi_1,\phi_2)\right]$$

The silicon-oxygen spacing and the tetrahedra linking angle, R and Θ, are again assumed to be constants; $R_2(\phi_1,\phi_2)$ is the expression for the spacing between atoms $O^{(2)}$ and $O^{(5)}$; $P_{12}(\phi_1,\phi_2)$, the joint probability distribution function for ϕ_1 and ϕ_2, is equal to $\left[1/2\pi\right]^2$. The derivation of an explicit expression for P"(R") similar to V-11 is difficult; however, a satisfactory approximation of P"(R") is readily obtained by averaging the integrand of V-12 over finite intervals and computing the distribution of R" 's numerically:

$$\text{V-13} \qquad P''(R'') = \frac{\Delta\phi_1\Delta\phi_2}{(2\pi)^2} \sum_n \sum_m D\left[R'' - R_2(n\Delta\phi_1, m\Delta\phi_2)\right]$$

$$\text{where} \quad D(r) = \begin{cases} 1 & \text{for } -\frac{\Delta r}{2} < r \leqslant \frac{\Delta r}{2} \\ 0 & \text{otherwise} \end{cases}$$

Increments in the rotation angles of $\Delta\phi_1 = \Delta\phi_2 = 10^\circ$ provide a sample of 1296 R" 's. The distribution of O-(2nd)O spacings derived from this sample is shown in Figure 41.

In any silica structure in which the SiO_4 tetrahedra link at their vertices, i.e., share only one common oxygen atom, the number of silicon-oxygen and oxygen-oxygen second

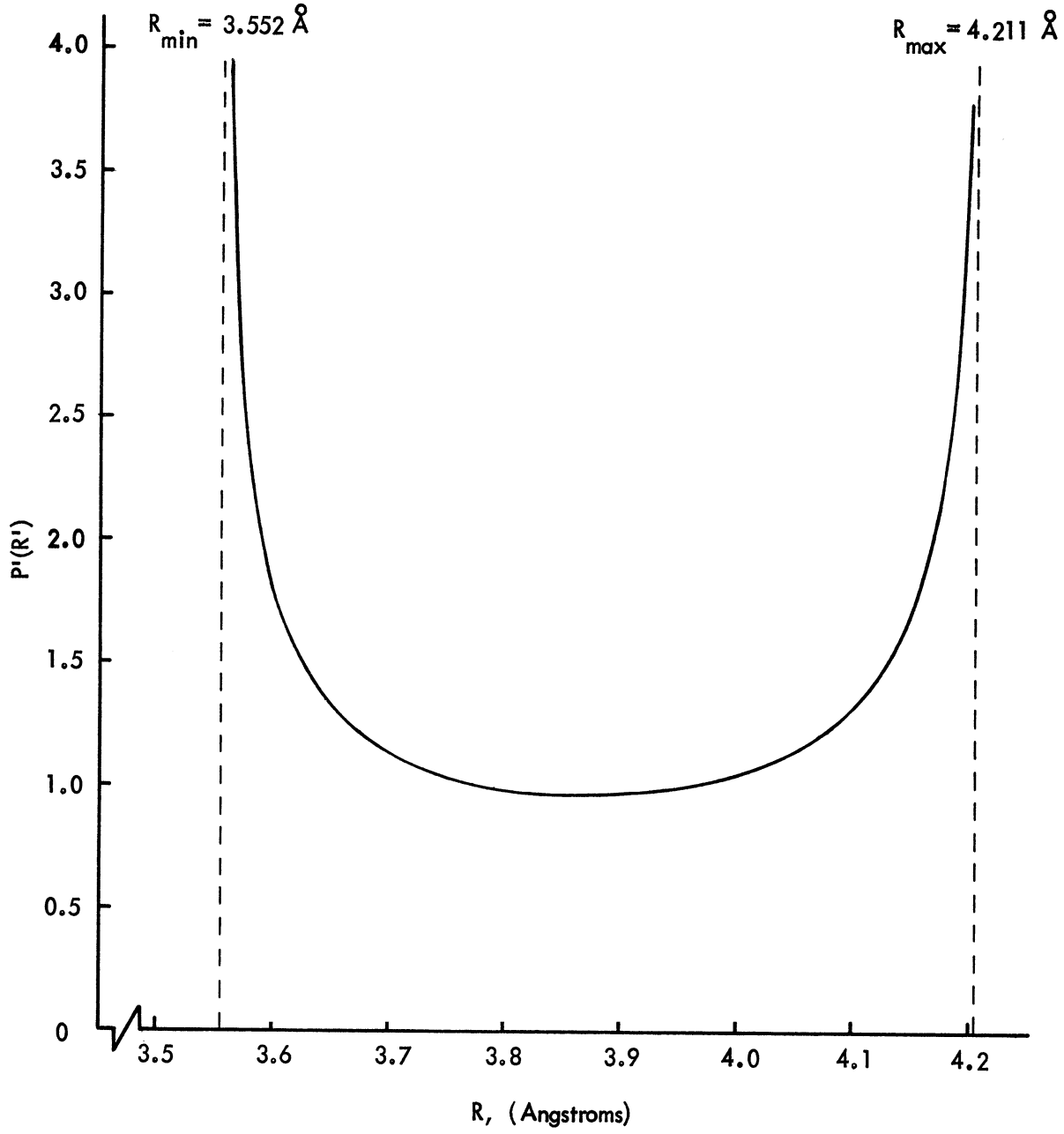

Figure 40. Distribution of silicon - (2nd)oxygen spacings for randomly oriented SiO_4 tetrahedra.

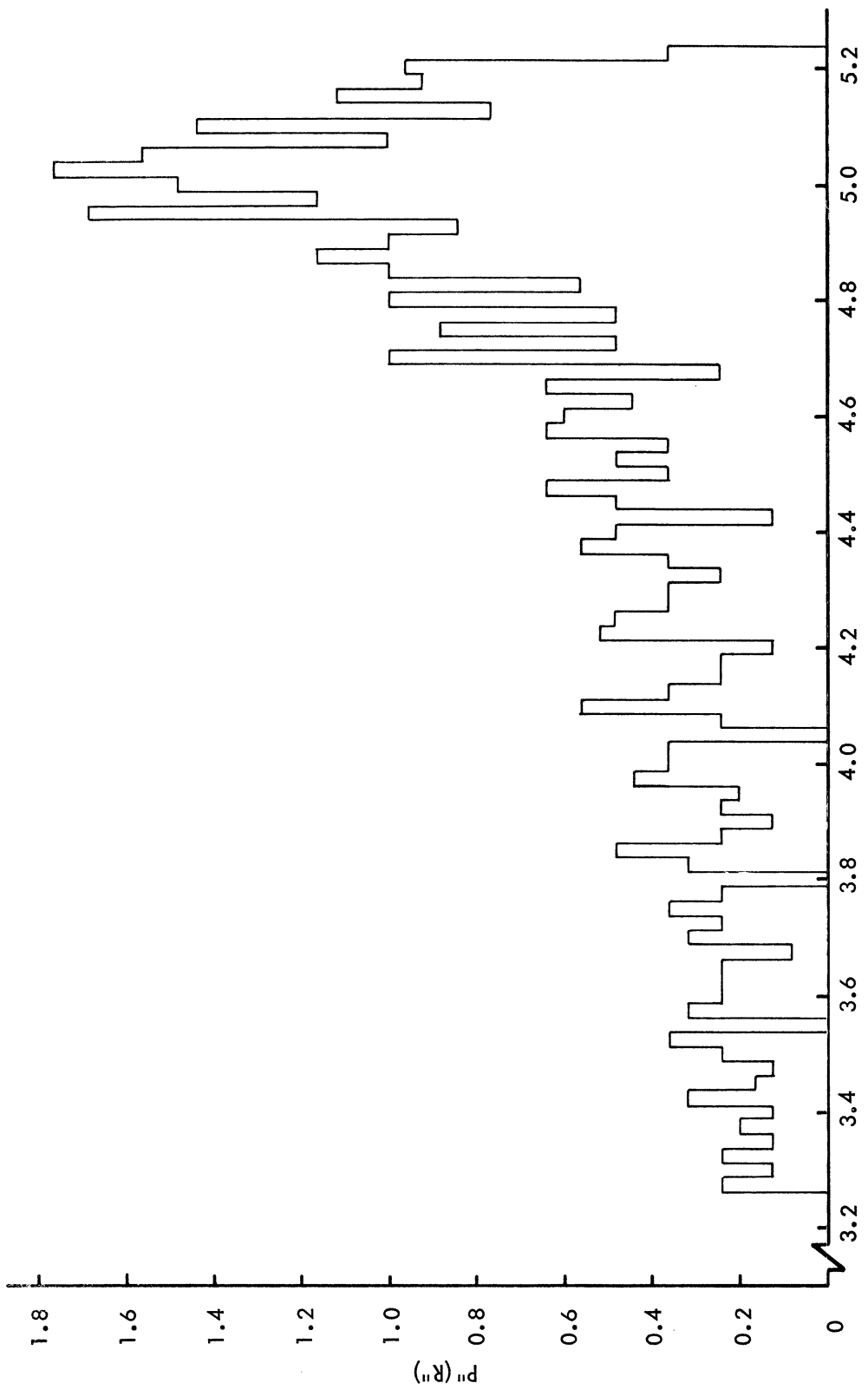

Figure 41. Distribution of oxygen - (2nd)oxygen spacings for randomly oriented SiO_4 tetrahedra.

nearest neighbors are:

V-14
$$\int 4\pi r^2 \, dr \, g_{O-(2nd)O} = 18$$

$$\int 4\pi r^2 \, dr \, g_{O-(2nd)Si} = 6$$

$$\int 4\pi r^2 \, dr \, g_{Si-(2nd)O} = 12$$

We obtain $\left[4\pi r\bar{g}(r)\right]_{rrm}$, the pair correlation function of the random rotation model, by distributing these atom pairs as indicated in Figures 40 and 41. The comparison of the model and the measured functions in Figure 42 is limited to pair spacings less than ~4.3 Å. At larger spacings one would have to consider the possibility of contributions from the Si-(2nd)Si and O-(3rd)O atom pairs.

Figure 42 clearly indicates that the random rotation model is unsatisfactory. The model's most obvious shortcomings are: (a.) the pair densities in the region between r = 3.25 Å and 3.8 Å are too high, (b.) the pair densities between r = 3.8 Å and 4.25 Å are too low, and (c.) the prominent peak at ~4.2 Å occurs at too large a spacing. No reasonable changes in the silicon-oxygen spacing R, and/or the tetrahedra linking angle Θ can correct these defects.

It might be argued that satisfactory agreement with the measured function could be obtained if the model allowed for distributions in R and Θ. The effect of these refinements would be a nonuniform broadening of the more prominent maxima in $\left[4\pi r\bar{g}(r)\right]_{rrm}$. The greatest amount of broadening

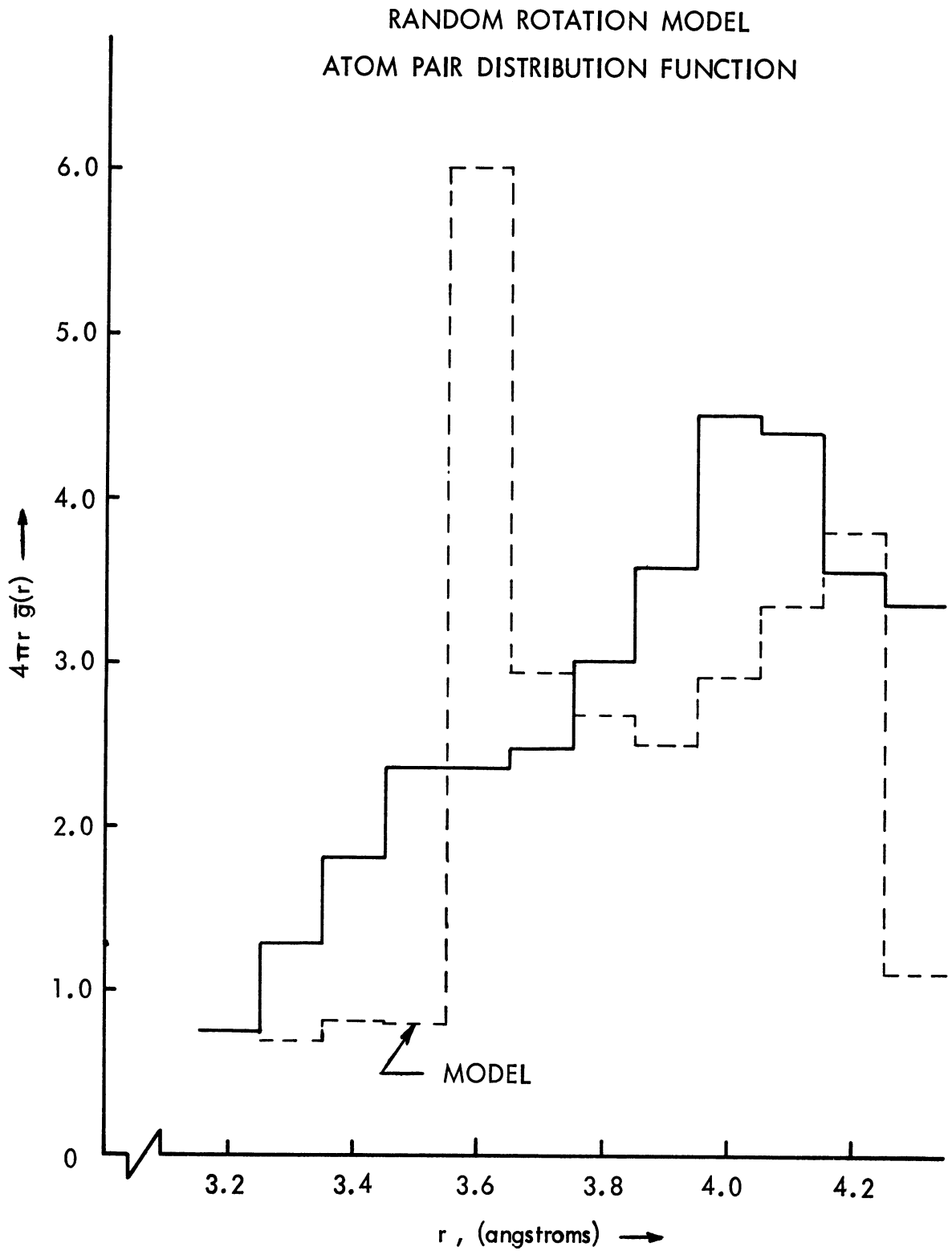

Figure 42. Atom pair correlation function for a random tetrahedra rotation model of vitreous silica.

would occur at the smaller pair spacings. If the linking angle Θ assumed values between $148^{o} \pm 10^{o}$, the minimum Si-(2nd)O spacings in the model would range between 3.351 Å and 3.729 Å ; the distribution of the maximum Si-(2nd)O spacings for the same Θ's is much narrower, 4.186 Å to 4.213 Å . Also, the broadening of a peak at the smaller spacings is relatively symmetric whereas at the larger spacings the broadened maxima tend to skew toward smaller r's.

A uniform broadening of the prominent peak at 3.6 Å and skewing of the 4.2 Å feature towards smaller pair spacings would undoubtably improve the appearance of $\left[4\pi r\bar{g}(r)\right]_{rrm}$. However, there are no distributions of R and Θ compatible with the widths of the Si-O and Si-Si maxima in $\left[4\pi r\bar{g}(r)\right]_{exp}$ which can produce satisfactory agreement between a refined $\left[4\pi r\bar{g}(r)\right]_{rrm}$ and the measured pair correlation function. We conclude that adjacent SiO_4 tetrahedra in vitreous silica must have preferred orientations.

The simplest nonrandom ϕ arrangement of the SiO_4 tetrahedra is one in which the angles ϕ_1 and ϕ_2 are unique. Assuming that these angles are univalued, we find that the most satisfactory distribution of the Si-(2nd)O and O-(2nd)O pairs is obtained from the configuration $\phi_1 = 40^{o}$ and $\phi_2 = 343^{o}$ (-17^{o}) . A comparison of the uni-ϕ model and the measured pair correlation function is shown in Figure 43.

A cursory examination of Figures 42 and 43 might suggest that the uni-ϕ model isn't much of an improvement

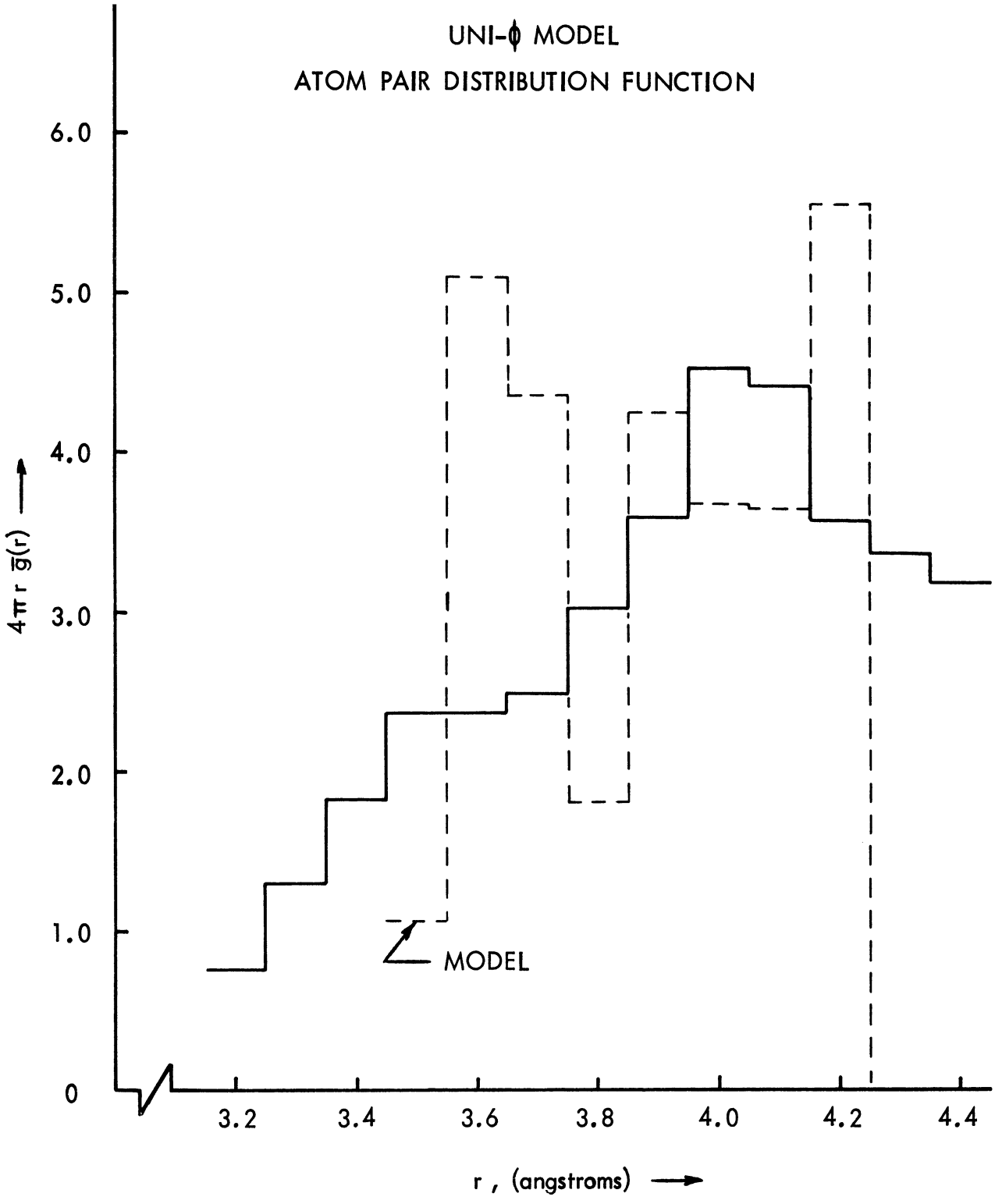

Figure 43. Atom pair correlation function for the uni-ϕ model of vitreous silica.

on the random rotation structure. However, the comparison in Table V-2 shows that in terms of both the total integral of $4\pi r^2\bar{g}(r)$ and the distribution of the atom pairs, the uni-ϕ configuration is a much superior model. Since the Si-O, O-O, and Si-Si maxima in $\left[4\pi r\bar{g}(r)\right]_{exp}$ are not delta functions, a realistic model would have to include some provision for distributions in R, Θ, ϕ_1, and ϕ_2. Distributions in these parameters will broaden the maxima in $\left[4\pi r\bar{g}(r)\right]_{\text{uni-}\phi}$ and agreement with $\left[4\pi r\bar{g}(r)\right]_{exp}$ in even greater detail can be expected.

The inability of the random rotation model to reproduce the measured distribution of the Si-(2nd)O and O-(2nd)O pairs ruled out this structure possibility; on the other hand, the fact that the uni-ϕ configuration produces a reasonable distribution of these atoms does not prove that this model correctly describes the short range structure of vitreous silica. If it is possible to reproduce the experimental results (for atom spacings up to $r \approx 4.25$ Å) with a single orientation of the nearest neighbor SiO_4 groups, it seems reasonable to expect that satisfactory agreement could be obtained from a model with two or more preferred orientations, i.e., a structure in which the angles ϕ_1 and ϕ_2 are neither single valued nor completely random. One serious weakness in our modeling technique is that in considering only the distribution of the Si-(2nd)O and O-(2nd)O pairs, we have completely

TABLE V-2 Model and Measured Atom Pair Densities in Vitreous Silica

	$\int_{3.25}^{3.80} 4\pi r^2 \bar{g}(r)\, dr$	$\int_{3.80}^{4.25} 4\pi r^2 \bar{g}(r)\, dr$	$\int_{0}^{4.25} 4\pi r^2 \bar{g}(r)\, dr$
Measurement	4.22	7.10	19.44
Uni-ϕ Model	4.17	7.29	19.27
Random Rotation Model	4.56	5.64	18.01

ignored the influence of the total network on the orientation of the nearest neighbor SiO_4 groups. To claim that a model of the structure is unique, two criteria must be satisfied: (1.) the model must be able to reproduce the measured pair correlation function for all values of r, and (2.) it must be shown that no other configuration can produce satisfactory agreement with the experimental results.

Tilton (65), Ordway (255), Bell and Dean (93) (254), and King and Evans (63) (256) have attempted to model the structure of vitreous silica by physically constructing large networks of tetrahedral units. This technique appears to be the most satisfactory method yet devised for generating a realistic set of atomic coordinates for a large sample. The efforts of Bell and Dean, and King and Evans, in particular, are quite promising.

Tilton's work was described in Section 1.3.10 of Chapter I. Recall that he assembles five-membered rings of symmetric tetrahedra to form pentagonal-dodecahedral configurations. We find that the atom pair density distribution derived from this model is completely at odds with our experimental results. The comparison in Table V-3 indicates the lack of agreement between the model and measured pair densities for pair spacings less than 4.25 Å. As the pair spacings increase, the discrepancies become even more apparent. Robinson's version of this structure,

TABLE V-3 Pentagonal-Dodecahedral Models and Measured Atom Pair Densities in Vitreous Silica

	$\int_{3.25}^{3.80} 4\pi r^2 \bar{g}(r)\, dr$	$\int_{3.80}^{4.25} 4\pi r^2 \bar{g}(r)\, dr$	$\int_{0}^{4.25} 4\pi r^2 \bar{g}(r)\, dr$
Measurement	4.22	7.10	19.44
Tilton's Model	0	11.43	19.24
Robinson's Model	0	11.43	19.24

the distorted or textured pentagonal-dodecahedron, was described in Section 1.3.11. Even though his distortion of the dodecahedron alters some of the atom spacings, there is no discernible improvement in the pair density distribution. Dean and Bell (254) have also calculated a pair correlation function for a pentagonal-dodecahedral model. They report that the agreement between the model and experimental data is poor for pair spacings less than 5.0 Å and that it is "especially bad" beyond 5.0 Å.

The models constructed by Ordway, Bell and Dean, and King and Evans are based on the continuous random network concepts of Zachariasen and Warren (Sections 1.3.3 and 1.3.4). Ordway (255) reports that he has constructed a random network of 300 tetrahedral units. From the experience derived in assembling this structure, he has attempted to formulate a unique set of rules for generating random networks. These rules govern modeling decisions such as the site at which each additional SiO_4 unit is attached to the network, the positions to which the other three vertices of the newly attached tetrahedron are rotated, and the formation of bonds at these vertices. Unfortunately, since he has not as yet published a pair correlation function or any other quantitative description of his model, there is no means of assessing the quality of this work.

Bell and Dean have assembled a number of models, each

containing up to about 600 atoms. One of their first reported efforts was a random network in which the tetrahedra linking angles ranged from 120° to 160° with a mean, $\bar{\Theta}$, of approximately 140°. This model was found to be unsatisfactory because its density was some 20 to 25 percent above the experimental value. In a more recent paper (254) they have presented a pair correlation function for a random network model in which the mean tetrahedra linking angle is "around 150°". Although the small size and inadequate labeling of the curves in the paper hinder comparisons, the spacings, shapes, and relative intensities of the maxima in this model's pair correlation function appear to agree quite well with our experimental results.

The largest reported model is the random network of 651 tetrahedra constructed by King and Evans (63). Because of its size, the coordinates of the 1,953 atom sites in this structure were measured with surveyor's transits. (Accurate measurement of atom coordinates in a large three dimensional model with a mechanical probe is virtually impossible. The optical measuring technique employed by King and Evans was developed by Ordway (257).) The authors estimate that 1,200 of the model's atoms are representative of the interior silica structure. These fall within a sphere roughly 18 Å in diameter. For atom pair spacings greater than 12 Å, the density of the model appears to be essentially constant.

The tetrahedra in the King and Evans model were linked together by bent springs. As the springs were inserted into the model the angles at which they were bent, i.e., the Si-O-Si bond angles, had a gaussian distribution with a mean value of 163°. However, because the springs were flexible and allowed readjustment of the structure as the construction proceeded, the final distribution of Si-O-Si angles in the model turned out to be substantially different. The final distribution of Θ's, shown superimposed on the initial distribution in Figure 44, has a mean value of 156° and is decidedly nongaussian.

Even though the value of $\bar{\Theta}$ in the King and Evans model was reduced from an initial 163° to 156°, it is still too large. Figure 45 shows the lack of agreement between the model's neutron differential scattering cross section and our experimental data. Also, the average density of the model, 2.08 g/cm^3, is approximately 5.5 percent too low.

One of the most surprising and unfortunate aspects of the modeling efforts described in the literature is the almost complete absence of quantitative details. As noted above, Ordway offers no particulars about his model beyond stating that it is "an amorphous network of 300 tetrahedra with no unshared vertices". The model assembled by Bell and Dean, whose pair correlation function apparently agrees well with our results, is described simply as having a mean tetrahedra linking angle of "about 150°". Even such basic

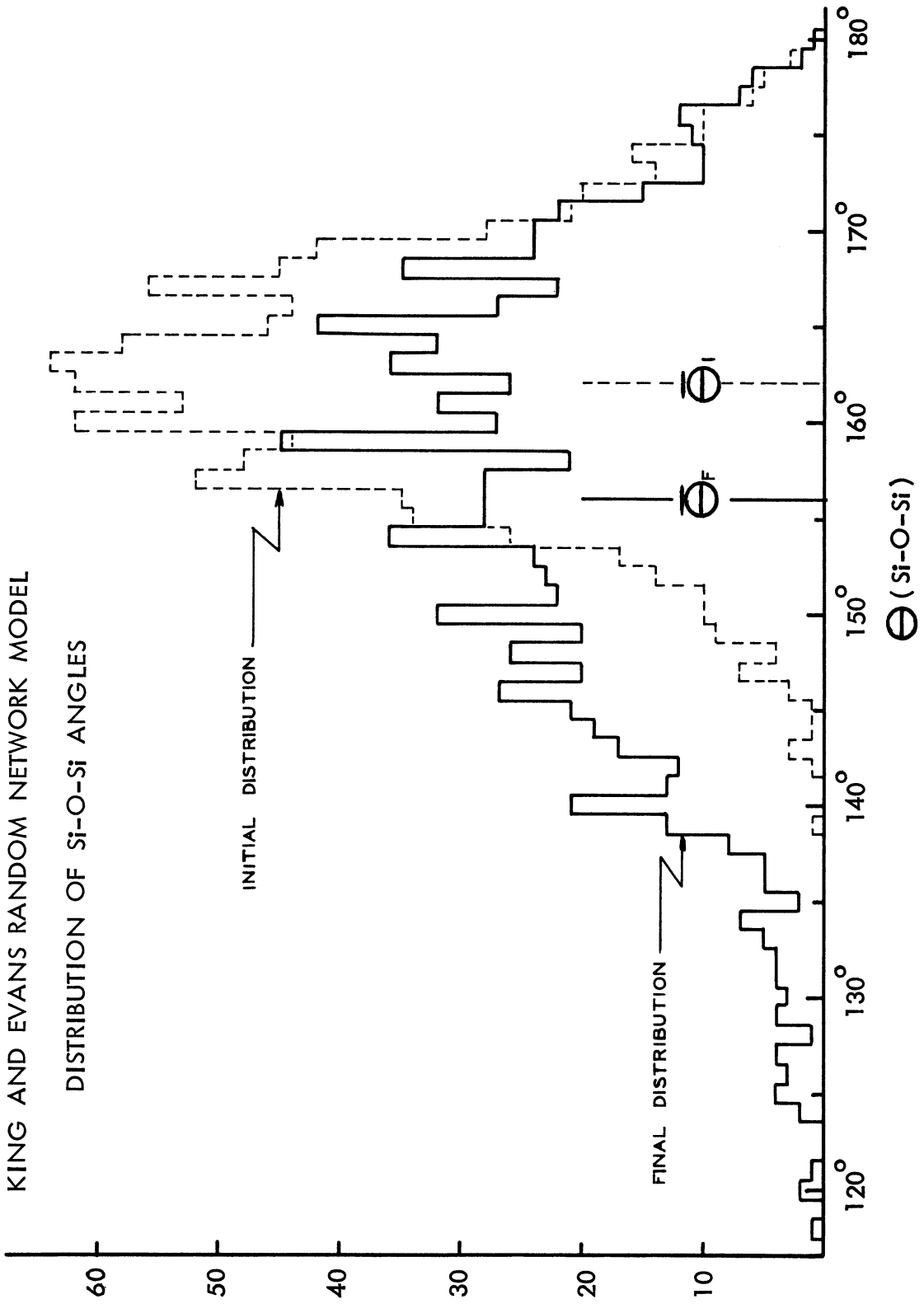

Figure 44. Initial and final distributions of Si-O-Si angles in the King and Evans model of vitreous silica.

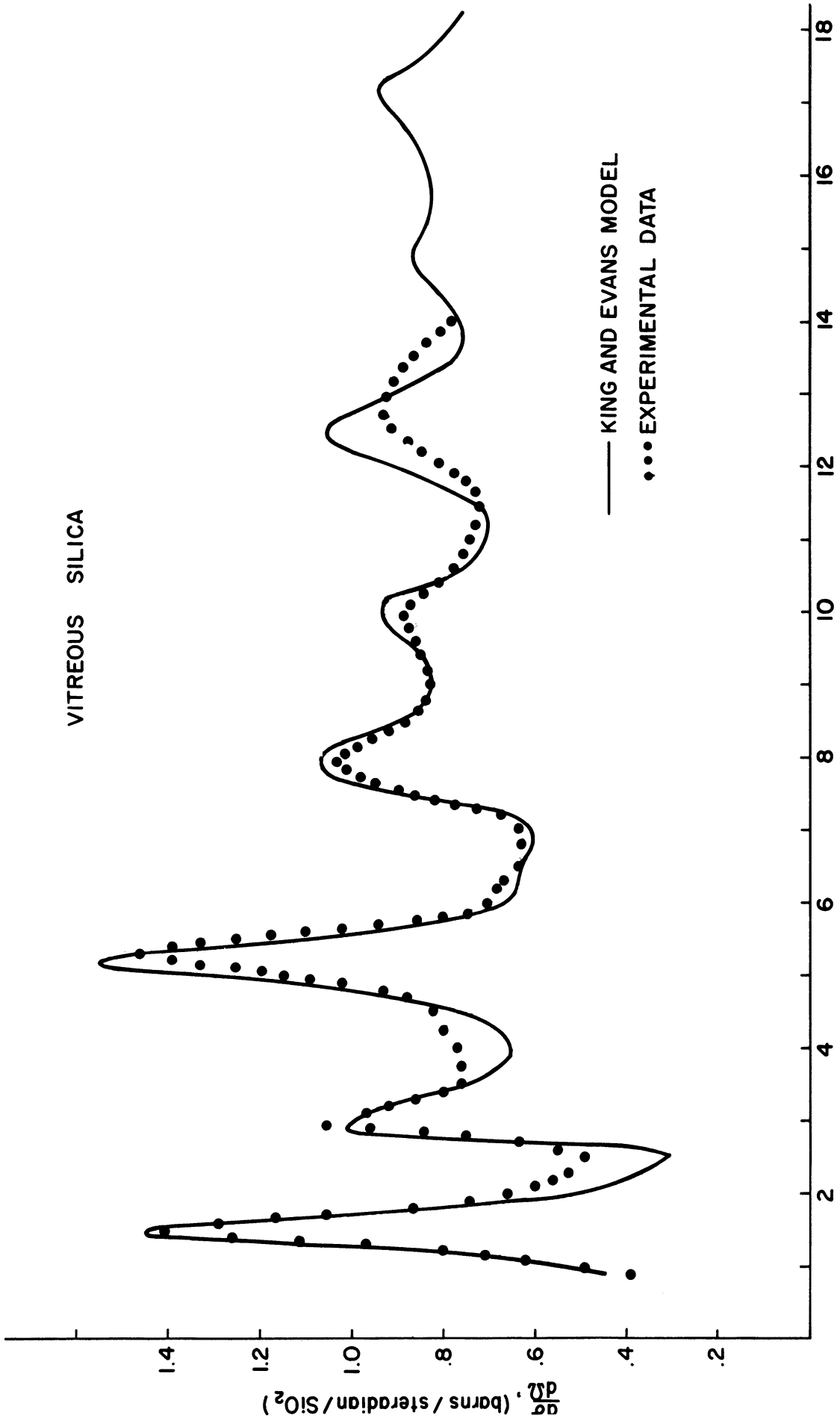

Figure 45. Comparison of the single differential neutron scattering cross section for the King and Evans model and the experimental cross section data.

information as the average model density is omitted. The final value of $\bar{\Theta}$ and the distribution of Θ's in the King and Evans model, which we obtained through a private communication with the authors, were never published.

It is pointless for the model maker to demonstrate that his model can reproduce an experimental diffraction pattern and/or an atom pair correlation function if no further details are provided. It is information such as the distribution of the Si-(3rd)Si atom pairs which is meaningful to the theoretician attempting to explain the physical properties of vitreous silica. The composite of all of the atom pair distributions is virtually useless for this purpose. Since the rationale of model building is to aid in the identification of which atom pairs produce the different maxima in the pair correlation function, the minimum model description should include the average density and the distributions in R, Θ, ϕ_1, and ϕ_2, the structure parameters defining the short range atom orientations.

Throughout this work we have noted the possibility that the short range orientations of the atoms in one or more of the crystalline silicas might be similar to those in vitreous silica. In order to resolve the question of which of the crystalline forms is most nearly like vitreous silica we have calculated the neutron coherent cross sections for the crystalline silicas. These cross sections, in addition to the reported crystalline structure parameters, are

compared with our experimental results.

The coherent elastic scattering cross section of a polycrystalline target is given by the expression (182):

$$\text{V-15} \qquad \left\langle \frac{d\sigma^{coh}}{d\Omega} \right\rangle = \frac{n^2 V}{2} \sum_{hkl} \frac{F_{hkl}^2}{\tau_{hkl}^2} \delta(K - 2\pi\tau_{hkl})$$

V is the volume of the crystal, n is the number of unit cells in the crystal per unit volume, hkl are the Miller indices of the crystal plane defined by the reciprocal lattice vector τ_{hkl}, and F_{hkl} is the structure factor of the crystal's unit cell. The structure factors were calculated using a computer program suggested by Busing, Martin, and Levy (258) and the silica structure data compiled by Wyckoff (259).

The polycrystalline scattering cross sections are useful for several reasons. As noted in Chapter IV, there are many potential sources of error in deriving the pair correlation function from the scattering data. The calculated cross sections provide a means of comparing the crystal data with our experimental results prior to evaluating the Fourier transform. Also, because of the size and complexity of the unit cells of some of the crystalline silicas, it is difficult to describe and compare the atom orientations in terms of such simple structure parameters as R, Θ, ϕ_1, and ϕ_2. In these instances a comparison of scattering cross sections is the

most satisfactory method of testing the possibility of structural similarities.

The principal known crystalline phases of silica are cristobalite, quartz, tridymite, keatite, coesite, silica W, and stishovite. Tridymite is usually found to be an intimate mixture of two structures - tridymite S and tridymite M - which are sometimes identified as independent phases. Several of these phases are readily eliminated from consideration. For example, it was noted previously that silica W, the least dense of the silicas at 1.96 g/cm^3, is the only known phase in which the SiO_4 tetrahedra share common edges. Its nearest neighbor spacings, R_{Si-O}= 1.87 Å and R_{Si-Si}= 2.58 Å, differ markedly from those observed in vitreous silica. At the other end of the density spectrum is the crystalline phase stishovite. Although there is speculation that the coordination of oxygens about the silicon atoms in this silica is six rather than the normal four, little structure data is available. However, the fact that the 4.35 g/cm^3 density of stishovite is almost twice that of vitreous silica would appear to rule out the possibility of any structural similarities.

The second most dense silica is coesite at 3.01 g/cm^3. The SiO_4 groups in coesite have two different shapes. In some of the tetrahedra the silicon-oxygen spacings range between 1.60 Å and 1.63 Å and the oxygen-oxygen spacings between 2.61 Å and 2.67 Å; in the other tetrahedra the

variations in these nearest neighbor spacings are 1.60 - 1.62 Å and 2.60 - 2.66 Å. The two SiO_4 groups, in turn, join into two different ring shapes - each consisting of four tetrahedra. With this structure the check for similarities with vitreous silica is best accomplished through a comparison of the scattering cross sections. At low momentum transfers the largest maximum in the scattering cross section of coesite occurs at ~ 2.0 Å^{-1}. Prominent maxima also appear at 1.8, 2.7, 2.8, 3.6, and 4.0 Å^{-1}. Since the first three maxima in the cross section of vitreous silica are located at ~ 1.5, 2.95, and 5.25 Å^{-1}, the two structures are not similar.

The crystalline silica keatite is of special interest because it exhibits a slightly negative thermal dilatation. A negative thermal dilatation of the same order of magnitude is observed in vitreous silica. The density of keatite (2.50 g/cm^3) is intermediate to that of cristobalite (2.32 g/cm^3) and quartz (2.66 g/cm^3). According to Shropshire, Keat, and Vaughan (250), the keatite structure is based on four-fold spirals of corner linked SiO_4 tetrahedra. These spirals are linked together by additional tetrahedra each of which shares its corners with tetrahedra in the four different spirals. As in the case of coesite, there are two slightly different SiO_4 groups in the unit cell. The nearest neighbor spacings in the tetrahedra which form the spirals are $R_{Si-O} = 1.58 - 1.61$ Å and

R_{O-O} = 2.51 - 2.64 Å. In the tetrahedra which link the spirals together, R_{Si-O} = 1.57 - 1.61 Å and R_{O-O} = 2.51 - 2.67 Å. Also, three different Si-O-Si bond angles are observed in keatite: $\Theta_1 = 155^{\circ}49'$, $\Theta_2 = 149^{\circ}22'$, and $\Theta_3 = 155^{\circ}17'$. The smallest of these angles lies well within the limits of error for the value of $\bar{\Theta}$ derived from our vitreous silica data. On the other hand, Θ_1 and Θ_3 are too large for reasonable agreement with the data. Although the maxima in the cross sections of keatite and vitreous silica do not differ as markedly as was the case with coesite, discrepancies are observed. There are prominent peaks in the keatite cross section at momentum transfers of ~ 1.4 and ~ 1.6 $Å^{-1}$. These would correspond fairly well with the 1.5 $Å^{-1}$ peak in the glass data. However, the keatite cross section also exhibits strong maxima at ~ 2.0, 2.7, and 3.3 $Å^{-1}$.

Silica W, stishovite, keatite, and coesite exist in only one form. On the other hand, quartz can exist in two phase modifications, tridymite S in six, tridymite M in three, and cristobalite in two.

The structures of the six modifications of tridymite S and the three modifications of tridymite M have not been determined, but, according to Sosman (260), it is likely that they are closely related to one another. Wyckoff (259) suggests that the structure of one of the high temperature forms of tridymite S, probably tridymite S-IV, is hexagonal.

If we use the coordinate system described in Figure 37 and Table V-I, the orientation of adjacent tetrahedra in the unit cell is described by the parameters R = 1.52 Å, $\Theta = 180^{\circ}$, and $\phi_1 = \phi_2 = 0$. It is quite apparent that this configuration has nothing in common with our description of the short range structure in vitreous silica.

The structures of the high and low temperature modifications of quartz are closely related. The unit cells are hexagonal, each contains three silicon and six oxygen atoms, and the difference in the respective cell dimensions is less than two percent. The SiO_4 tetrahedra in low-quartz are not quite regular in shape, but very nearly so, with an average silicon-oxygen spacing of 1.61 Å. This compares with a regular Si-O spacing in high-quartz of 1.62 Å. The Si-O-Si bond angle in low-quartz is 144°; in high-quartz, $\Theta = 146^{\circ}$. Although the R's and the Θ's in the quartz structures differ very little from the values of $\bar{R}$ and $\bar{\Theta}$ derived from the vitreous silica data, a comparison of the scattering cross sections in Figure 46 indicates that the structures are not similar. The probable explanation is that in the quartz structures the orientation of the tetrahedra about the Si-O-Si bond, described by the angles ϕ_1 and ϕ_2 in our simplified coordinate system, are very different from those most commonly occurring in vitreous silica.

The unit cell of the high temperature modification of

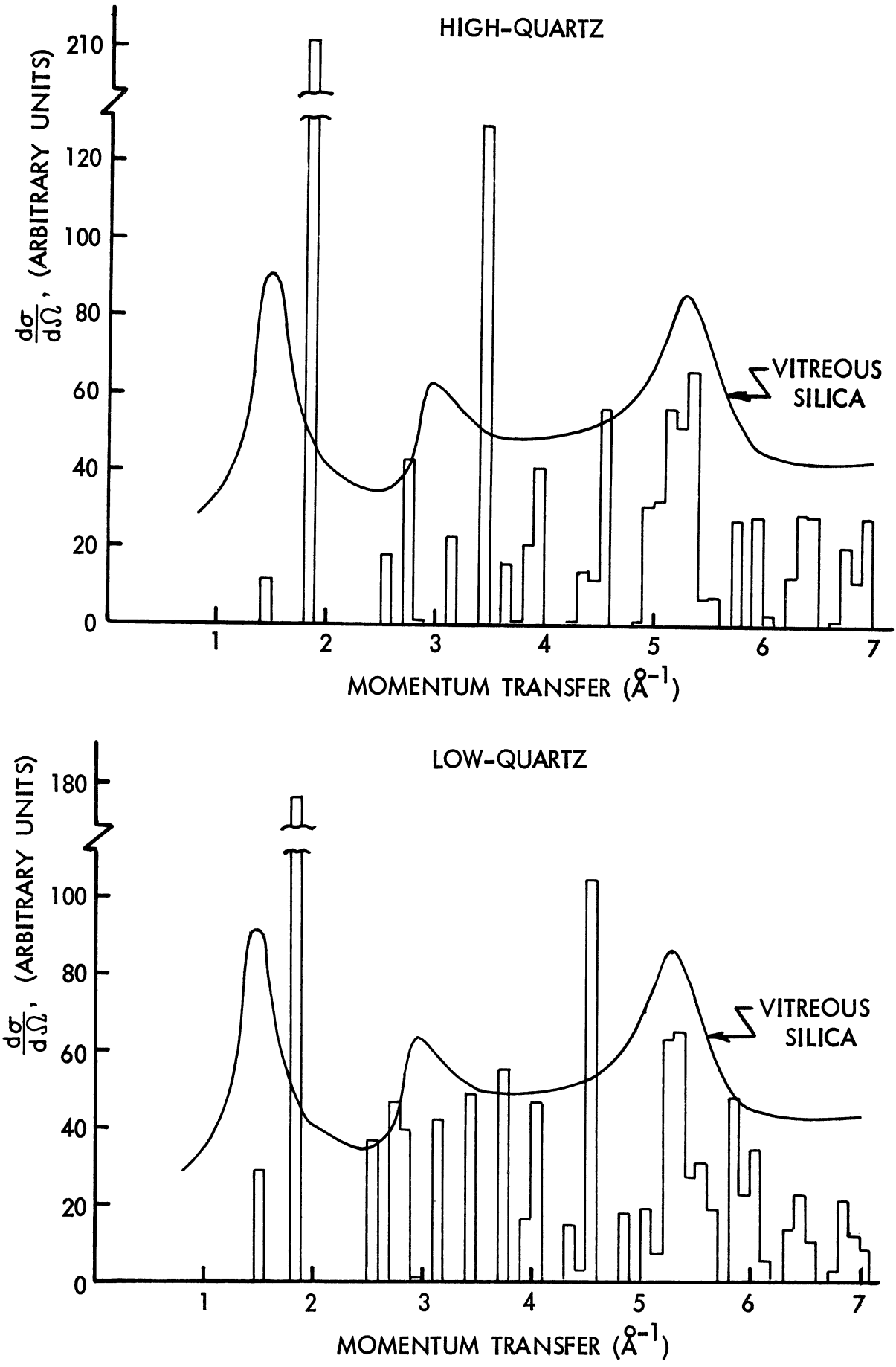

Figure 46. Comparison of the single differential neutron scattering cross sections of vitreous silica and quartz. (The cross sections are plotted on different intensity scales.)

cristobalite is cubic, containing eight silicon and sixteen oxygen atoms. The exact positions of the atoms within the unit cell are not well established. Wyckoff (261) has described a simple, highly symmetrical arrangement. He indicates that the SiO_4 tetrahedra are regular in shape with silicon-oxygen spacings of 1.55 Å and oxygen-oxygen spacings of 2.53 Å. The tetrahedra linking angle, Θ, is 180° and the orientations of the tetrahedra about the Si-O-Si bonds are described by the angles $\phi_1 = 0$ and $\phi_2 = 60°$. Barth (262) has proposed a more complicated arrangement. In Barth's structure the tetrahedra are highly irregular with silicon-oxygen spacings ranging between 1.58 Å and 1.69 Å and oxygen-oxygen spacings between 2.45 Å and 2.74 Å. Some of the Si-O-Si bond angles are 180°, the others 136°. If the Wyckoff description is correct, it is evident that the structures of high-cristobalite and vitreous silica are not similar. On the other hand, maxima in the scattering cross section derived from Barth's structure correspond well with the major features of the glass cross section. (See Figure 47.)

Sosman (260) suggests that the differences in the Barth and Wyckoff structures might be due to the manner in which they prepared their samples. Cristobalite samples are never perfectly crystalline. The degree of crystallinity in a given specimen is very sensitive to (1.) the temperature at which the cristobalite was originally formed

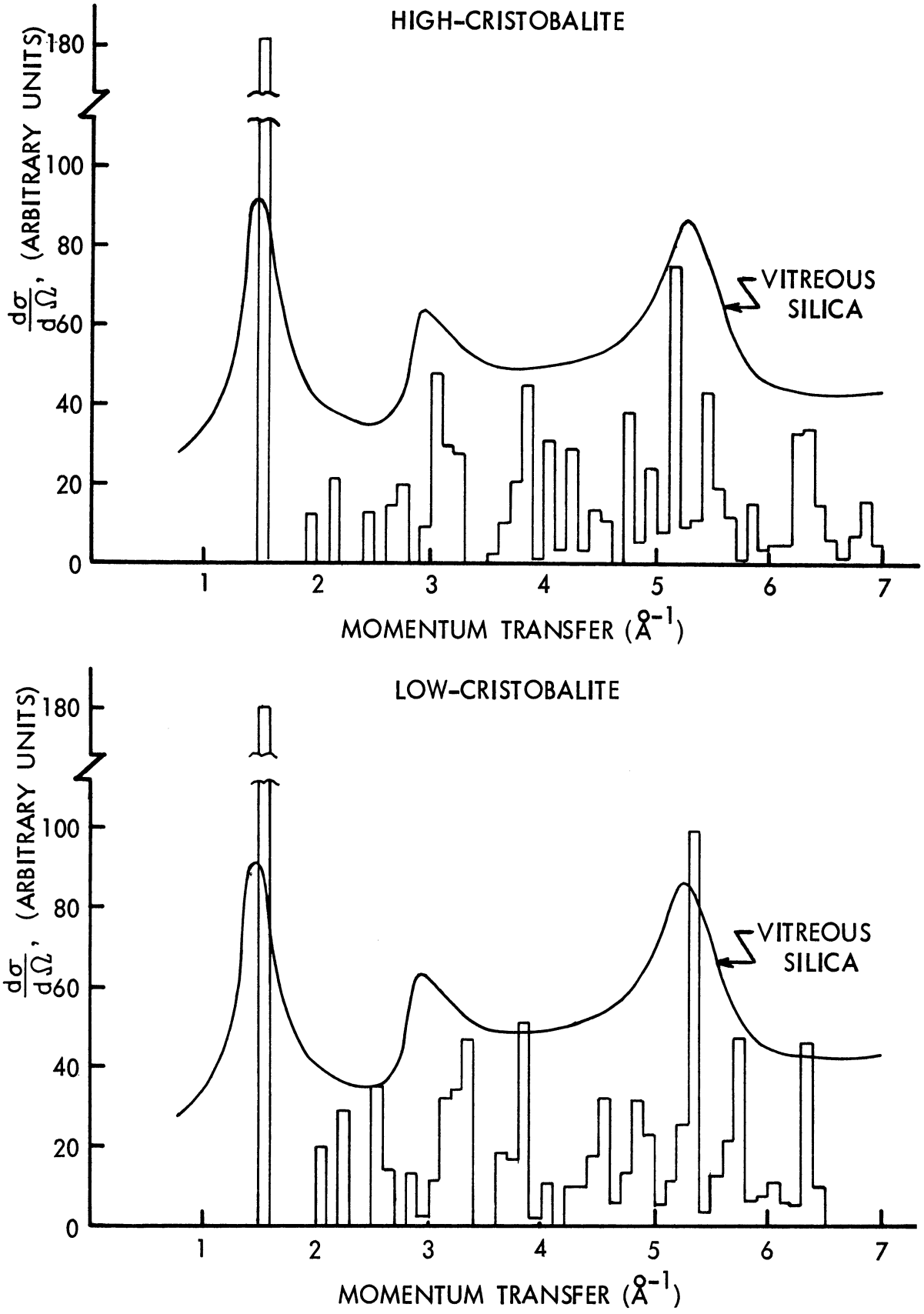

Figure 47. Comparison of the single differential neutron scattering cross sections of vitreous silica and cristobalite. (The cross sections are plotted on different intensity scales.)

or at which it has been brought to a near-permanent state by heating for a long period of time; and (2.) the kind of silica from which it was originally prepared. This uncertainty about the true structure of high-cristobalite is unfortunate. Since cristobalite is the stable crystalline phase at the temperatures that vitreous silica solidifies, and its density, 2.211 g/cm^3 at 430°C, is almost exactly that of vitreous silica, one might well expect to find marked similarities in the two structures.

The remaining silica to be considered is the low temperature modification of cristobalite. The structure of low-cristobalite, like that of quartz, is helical (260). The unit cell contains four silicon atoms, eight oxygen atoms, and is tetragonal pseudocubic. Its dimensions are $a = 4.9733$ Å and $c = 6.9262$ Å (259). The SiO_4 tetrahedra in low-cristobalite are not quite regular in shape due to a 2.58-2.63 Å variation in the oxygen-oxygen spacings. Although our simplified coordinate system for corner-linked tetrahedra assumes that the tetrahedra are regular, the positions of near neighbors in the low-cristobalite lattice can be described by the parameters $R = 1.59$ Å, $\Theta = 148°$, $\phi_1 = 53°$, and $\phi_2 = 355°$ $(-5°)$ with an average error in the first and second nearest neighbor spacings of less than 0.02 Å. Note the close resemblance to our description of the vitreous silica: $\bar{R} = 1.60$ Å, $\bar{\Theta} = 148°$, $\bar{\phi}_1 = 40°$, and $\bar{\phi}_2 = 343°$ $(-17°)$. Also, the comparison of scattering

cross sections in Figure 47 shows that the major maxima in the low-cristobalite cross section agree well with the maxima in the glass cross section. We conclude that, of those silicas whose structures are well established, low-cristobalte is the crystalline phase most similar to vitreous silica.

5.2 INELASTIC NEUTRON SCATTERING SPECTRA OF VITREOUS SILICA

Inelastic neutron scattering spectra of vitreous silica were measured at scattering angles of 21.2°, 47.25°, and 90°, with incident neutron energies ranging from a minimum of 18.0 meV to a maximum of 45.5 meV. These spectra were obtained by cycling one of the 0.290" thick vitreous silica targets described in Section 3.1 with an empty target holder. The cycle period was eight minutes divided between six minutes of scattering by the target and two minutes of background counting. The measurements were all performed at room temperature ($\sim 26^{\circ}$C). A MAD language program written for the University of Michigan's IBM 7090 computer was used to process the data. This program, DATANAL 3 (263), incorporates a channel by channel background subtraction, corrections for detector efficiency, and a linear smoothing over 3, 5, or 9 channels. (The smoothing feature of the program was not used for the vitreous silica data.) Sample spectra from each of the three scattering angles are presented in Figures 48, 49, and 50.

The most interesting result of our measurements is that in almost every spectrum we observe prominent, clearly resolved coherent scattering maxima at energy transfers of $\sim \pm$ 4.6 meV (~ 37 cm^{-1}). In Figure 51 we have traced the loci of the spectra measurements in the $K - \hbar\omega$ plane and plotted the positions at which these low frequency maxima appear. The scattering data also shows evidence of inelastic coherent maxima at energy transfers of $\sim \pm$ 9 - 10 meV

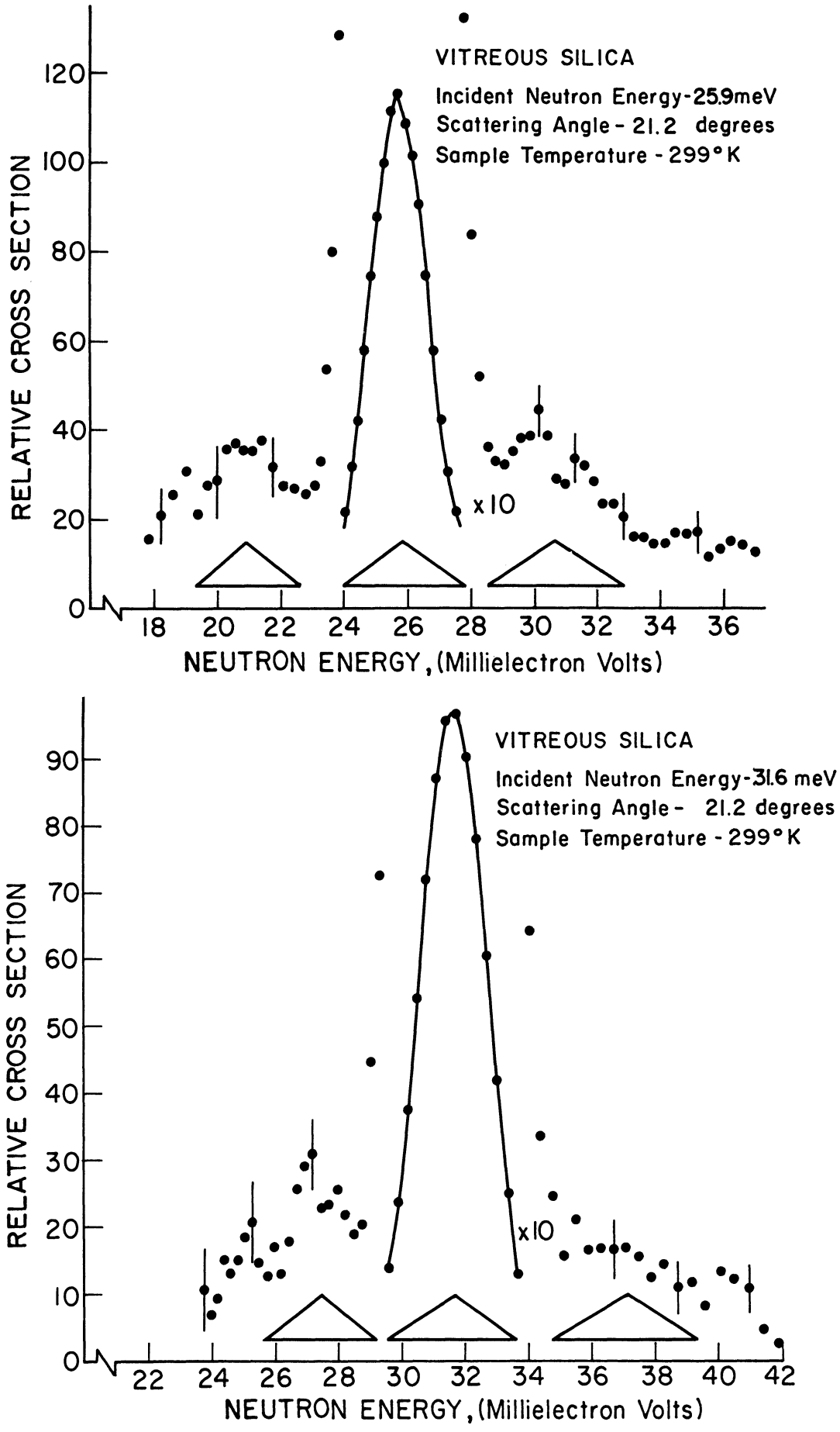

Figure 48. Inelastic neutron scattering spectra of vitreous silica for $\theta_s = 21.2^{\circ}$.

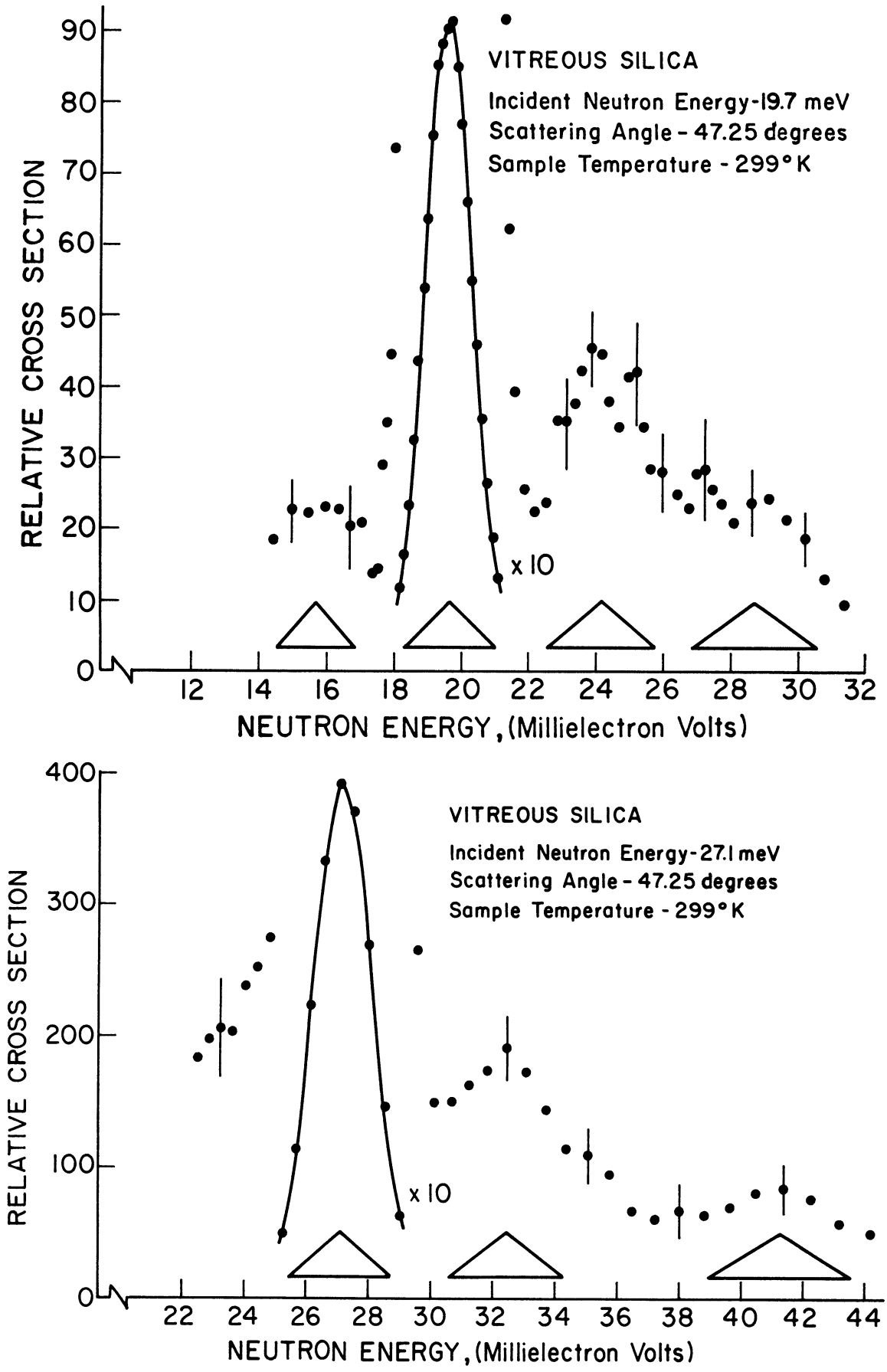

Figure 49. Inelastic neutron scattering spectra of vitreous silica for $\theta_s = 47.25^{\circ}$.

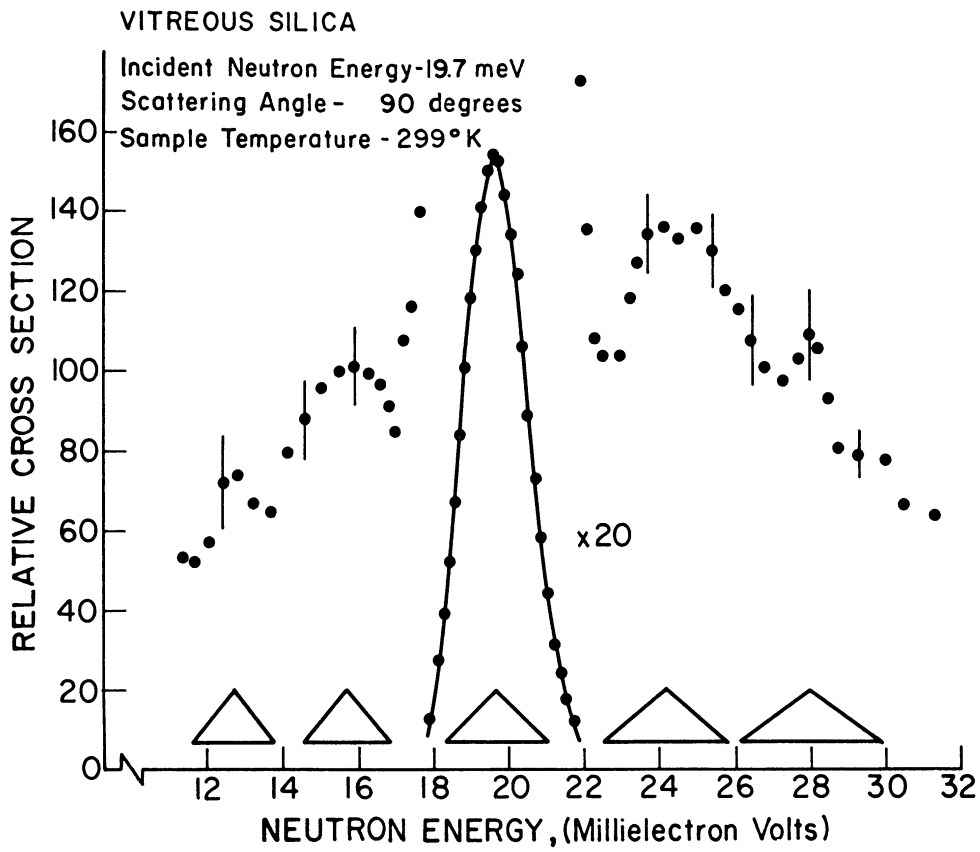
VITREOUS SILICA
Incident Neutron Energy-19.7 meV
Scattering Angle - 90 degrees
Sample Temperature - 299°K
RELATIVE CROSS SECTION
0
20
40
60
80
100
120
140
160
x20
12
14
16
18
20
22
24
26
28
30
32
NEUTRON ENERGY, (Millielectron Volts)

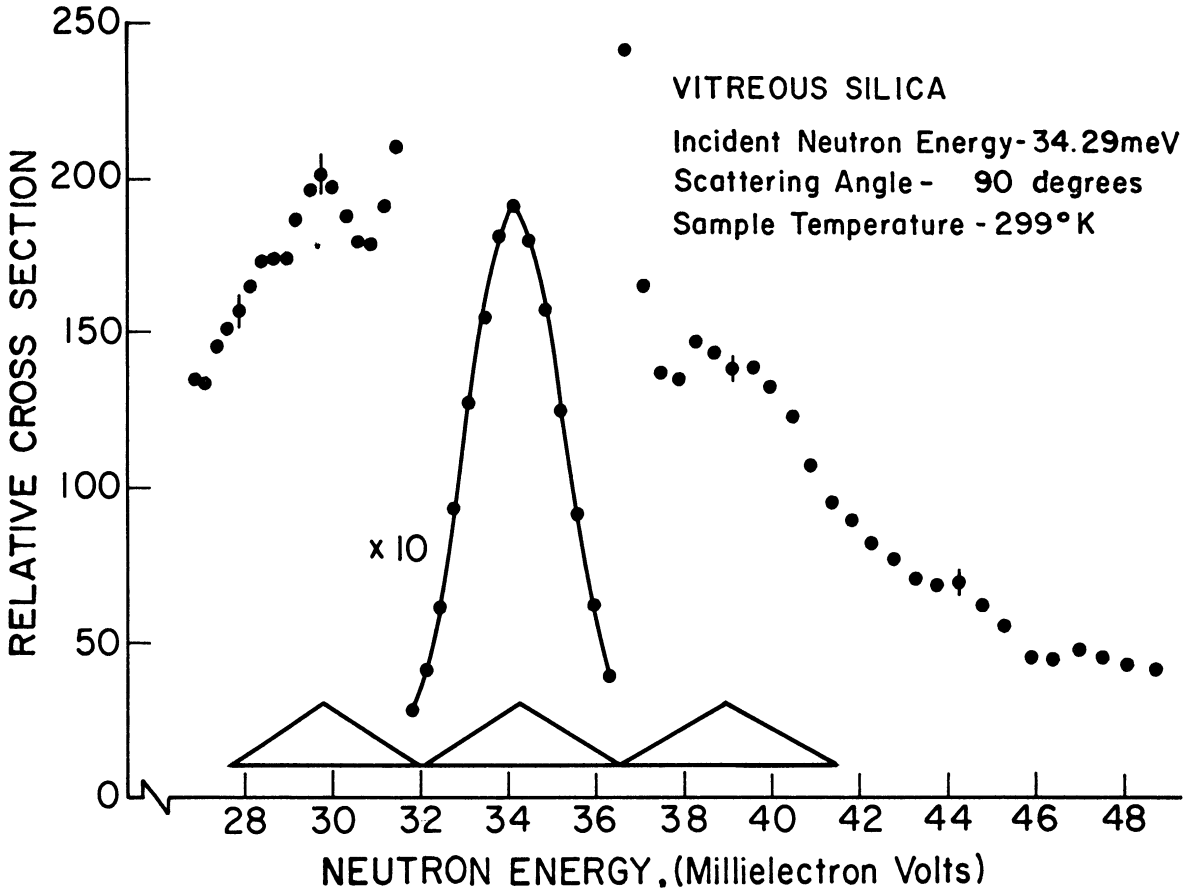
VITREOUS SILICA
Incident Neutron Energy-34.29meV
Scattering Angle - 90 degrees
Sample Temperature - 299°K
RELATIVE CROSS SECTION
0
50
100
150
200
250
x 10
28
30
32
34
36
38
40
42
44
46
48
NEUTRON ENERGY, (Millielectron Volts)

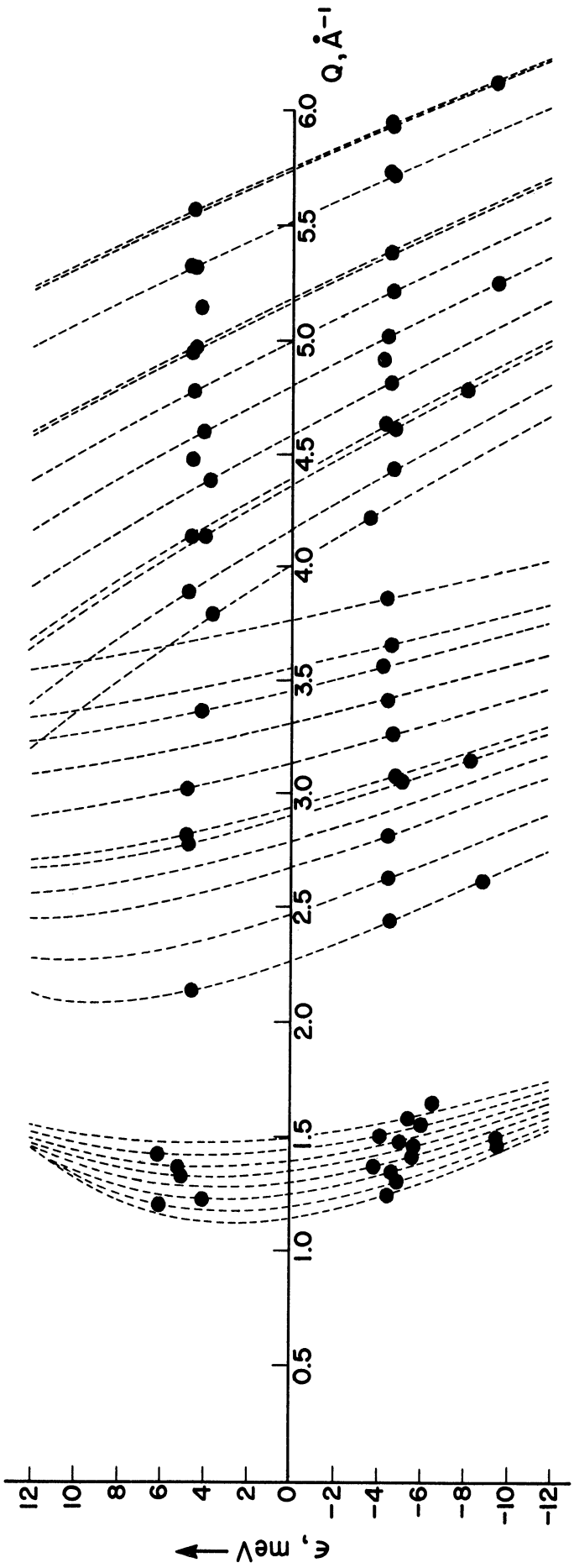

Figure 51. Locations of maxima in the vitreous silica cross section. Dashed curves represent the loci of the measurements for different incident neutron energies and scattering angles.

($\sim$73 - 81 cm^{-1}); however, these peaks do not appear as persistently, nor are they as clearly delineated as the $\sim \pm$ 4.6 meV maxima. The scattering cross section generally tends to decrease with increasing energy transfers. This factor, and experimental limitations such as the intensity of the incident neutron beam, restrict the effective range of our investigations to the lower frequencies ($\omega < 100$ cm^{-1}) of the target's vibrational spectrum.

As noted in Section 1.4.3, the only other inelastic neutron scattering data available for comparison with our results are the cold neutron measurements of Egelstaff (120) and Leadbetter (121). One of Leadbetter's spectra is shown in Figure 6 (page 87); one can see that there are no marked low frequency scattering maxima in this data. Leadbetter himself describes the $\omega < 50$ cm^{-1} region of his spectra as containing "smeared out, ill-defined shoulders". Egelstaff reports that he observes scattering maxima at energy transfers of 2 meV (16 cm^{-1}), 4 meV (32 cm^{-1}), 13 meV (105 cm^{-1}), and 39 meV (315 cm^{-1}). In his paper he has provided three examples of his measurements: spectra obtained at scattering angles of 45° and 75° for a sample temperature of $350^{\circ}C$, and one 45° scattering angle measurement for a sample temperature of $20^{\circ}C$. Only in the $350^{\circ}C$ data can one find reasonably well defined maxima. While the reported peaks at 13 meV and 39 meV are clearly visible, what structure there is in the region $\omega < 50$ cm^{-1} is best characterized by the Leadbetter description, i.e. ill-defined shoulders. Also, it should be

noted that none of the Egelstaff spectra include any indication of the resolution of the measurement or of the counting statistics.

Attempts to describe the atomic motions and calculate the vibrational frequency spectrum of vitreous silica were discussed in Section 1.4.4 . The most detailed model and calculation for vitreous silica which is available is the work by Bell, Bird, and Dean (137). The vibrational frequency spectrum which they have derived is based on the atomic geometry of a random network model (of ~600 atoms) and a central and non-central nearest neighbor harmonic force field. In a discussion of the results of this calculation, Dean (264) was questioned about the nature of the vibrational spectrum at low frequencies. He responded as follows: "First, it is not possible to get a good representation of the long wavelength modes of a material from calculations based upon modes of only limited size. Secondly, our force-constant model is fairly simplified - for there is little point in attempting to use a sophisticated force-constant model in this first attempt to understand the nature of atomic vibrations in vitreous silica. Consequently, we are unable to say anything about the low frequency region (say, 0 to 100 cm^{-1}) where weak forces may have a considerable influence. The calculated spectrum becomes meaningful above about 100 wave numbers."

In the absence of a realistic model (or models), we must consider methods of extracting information directly

from the scattering data. One of the possibilities mentioned in Section 2.3 was the use of the Egelstaff cross section extrapolation technique. Recall that for a fixed energy transfer, we have the expression

$$\text{II-41} \qquad \lim_{K \to 0} \left[\frac{d^2\sigma}{d\Omega dE} K^{-2} \right] = b_{coh}^2 \frac{k}{k_0 6NM\omega} \frac{g(\omega)}{\exp(\hbar\omega/k_B T) - 1}$$

Thus, one might hope to obtain some indication of the shape of the target's frequency distribution function and an estimate of the fraction of normal modes with the frequencies in question.

Unfortunately, there are a number of problems, both experimental and theoretical, which seem to indicate that the Egelstaff technique would not be satisfactory for analysis of the glass data. According to Haywood and Thorson (265), experimental problems such as multiphonon and multiple scattering effects, and extrapolation of the $\left[d^2\sigma/d\Omega dE\right]/K^2$ expression from values of K where the $S_d(K,\omega)$ contribution is still significant, are likely to produce significant errors in the $g(\omega)$ function. The most serious problem, however, is theoretical. As was pointed out in Section 2.3, the $g(\omega)$ function obtained from Equation II-41 is the true frequency distribution function only in the special case where the target material has a Bravais lattice with cubic symmetry. It is quite apparent that such a description is not even remotely applicable to the structure of vitreous silica. Since there is no clear interpretation of the $g(\omega)$ function derived from II-41 when

the target is a diatomic non-crystalline solid, we cannot justify the use of this mode of analysis.

The lowest frequency cooperative thermal excitations in all solid systems are acoustic waves (long wavelength phonons). In Section 2.3 we discussed the possibility that the coherent structure in the inelastic neutron scattering spectra of vitreous silica might be analyzed for evidence of an average frequency - wavenumber relationship (i.e., phonon dispersion relation) for these acoustic modes. Indeed, this is exactly the manner in which Leadbetter has interpreted his vitreous silica data.

In addition to measurements of the inelastic neutron scattering spectra of vitreous silica, Leadbetter's work includes scattering studies of polycrystalline samples of low-quartz and low-cristobalite. No evidence of structure is found in the $\omega < 50$ cm^{-1} region of the quartz spectra; on the other hand, very prominent maxima appear in this region of the low-cristobalite spectra. Leadbetter interprets these maxima in the low-cristobalite data as evidence of a directionally averaged, very highly disperse acoustic branch. The top of the branch is described as being spread between 30 - 50 cm^{-1} and it is claimed that there is a maxima in $g(\omega)$ at ~40 cm^{-1}. The low-cristobalite results are in turn compared with the glass data: "For $\omega < 50$ cm^{-1} there are very significant differences in the spectra. In particular the peak at ~40 cm^{-1} in cristobalite is almost completely smeared out in the vitreous silica,

where it exists only as an ill-defined shoulder, and there is appreciable scatter at energy transfers below the low-energy cutoff for cristobalite." This ill-defined, low frequency structure in the glass spectra is " to be understood as originating from a much broadened transverse acoustic branch of the spectrum closely similar to that observed in cristobalite." Furthermore, Leadbetter states that "the transverse acoustic waves are very highly damped in the glass, and the phonon groups are so broadened that it is somewhat doubtful whether a phononlike description of these excitations is meaningful."

Leadbetter's explanation of the low frequency structure in the neutron data is unsatisfactory for a number of reasons. In the first place, he completely ignores the results of another study of vitreous silica which he coauthored with Flubacher, Morrison, and Stoicheff (119). The work by Flubacher, et. al. included measurements of the heat capacity and the Raman and Brillouin spectra. The anomalous behavior of the low temperature heat capacity of vitreous silica was discussed in Section 1.5 . The Brillouin spectrum measurement provided a method of determining elastic wave velocities at a frequency of $\sim 10^{10}$ c/sec. A comparison of the Brillouin results with wave velocities obtained from acoustic measurements at a frequency of $\sim 10^{7}$ c/sec indicated that the dispersion of the lattice waves in vitreous silica is not significant up to a frequency of at least 5×10^{10} c/sec. Flubacher, et.al.

offered the following comment: "We cannot rule out the possibility that disorder in the lattice may introduce anomalous features into the acoustic spectrum at higher frequencies; the comparison of the results of Brillouin scattering and ultrasonic experiments shows only that the velocity of the acoustic waves is constant in the frequency range 10^7 to 5×10^{10} c/sec. Nevertheless there seems to be little justification for invoking such features in the region where the wavelengths of the acoustic waves are in excess of 100 Å (i.e. $\nu \sim 5 \times 10^{11}$ c/sec)." On the other hand, the Raman spectrum exhibited an intense continuum extending from ~ 560 cm^{-1} to at least 8 cm^{-1}. (The low frequency Raman scattering by vitreous silica is confirmed by Krishnan (116) who was able to follow the continuum down to ~ 30 cm^{-1}.) Therefore, Flubacher, Leadbetter, et.al. concluded that the low frequency acoustic modes of vitreous silica behave normally, i.e. show no evidence of dispersion, and the heat capacity anomaly is due to "optical modes of unusually low frequency". Without any reference to this earlier work, Leadbetter now claims that "the unusually high heat capacity of vitreous silica is due to the presence of a highly disperse and much broadened (transverse) acoustic branch of the spectrum."

The general appearance of the neutron cross section for one-phonon events in a coherent scattering polycrystal was described in Section 2.3 . Recall that if the acoustic waves in the target can be characterized as purely transverse

and purely longitudinal, the scattering contribution from the longitudinal modes peaks at $K = 2\pi\tau \pm q_L$ and goes to zero at $K = 2\pi\tau$; the contribution from the transverse modes has a broad maximum at $K \approx 2\pi\tau$ and goes to zero at $K = 2\pi\tau \pm q_T$ (See Figure 9, page 146). As a result, peaks or sharp breaks in the scattering spectra of a polycrystal within the limits $2\pi\tau - q \leq K \leq 2\pi\tau + q$ are almost invariably due to the longitudinal phonons (186)(187). Since Leadbetter's glass data shows no peaks or even sharp breaks in the $\omega < 50$ cm^{-1} region, there is no direct evidence that the scattering he observes results from neutron interactions with either longitudinal or transverse acoustic modes.

The fact that there are relatively sharp low frequency scattering maxima in our vitreous silica data means that we are in a much better position than Leadbetter to judge if this scattering originates from acoustic modes. We have another advantage in that our thirty-three inelastic scattering spectra measurements cover a range of momentum transfers from ~ 1.1 Å^{-1} to ~ 6.0 Å^{-1}. The $K - \hbar\omega$ loci of Leadbetter's six cold neutron scattering spectra are all concentrated in the vicinity of the first diffraction maxima ($K \approx 1.5$ Å^{-1}). Also, with a cold neutron source one can only measure energy gain spectra (i.e. energy transfers from the scatterer to the incident neutrons); the scattering spectra reported in this work are the first neutron data showing both the energy losses and gains in the scattering

by vitreous silica.

Experimental dispersion relations for coherent scattering polycrystals have usually been derived from data in the second Brillouin zone. (For a liquid or a non-crystalline solid, the region of K - space in the vicinity of the first maximum in $S(K)$ is the equivalent of the second Brillouin zone.) Measurements in the first Brillouin zone ($\tau = 0$) generally cannot be extended to small enough values of K to produce a satisfactory dispersion curve. On the other hand, as momentum and energy transfers increase, the discontinuities in the coherent scattering spectra which can be attributed to individual phonon excitations are obscured by scattering contributions from the increasing number of reciprocal lattice points and vibrational modes which can satisfy the momentum and energy conservation conditions. Indeed, as K increases, the form of the coherent cross section approaches that for incoherent scattering (186).

We have examined the low frequency structure in our data and can find no evidence of a dispersion relation for acoustic phonons. What we see appears to be scattering by a vibrational mode independent of K superimposed on the scattering contribution of the acoustic phonons. For almost all of the momentum transfers scanned in these measurements, the maxima in the scattering spectra appear at $\sim \pm 4.6$ meV. The only noticeable deviation from this pattern occurs in the immediate vicinity of the first peak in the structure

factor (Figure 51, $K \sim 1.5\ A^{-1}$) and, as noted above, this is exactly where we would expect to observe the coherent effects of the acoustic modes. Due to the breadth of the $1.5\ A^{-1}$ diffraction peak, it is highly unlikely that the acoustic phonons could produce sharp discontinuities in the scattering spectra. However, their effect is observed through the apparent broadening and shifts in the maxima of the dominant K - independent mode in this low K region. As the momentum transfers increase, what structure there is in the scattering contribution of the acoustic phonons is rapidly smoothed out and the K - independent character of the dominant low frequency mode becomes evident.

If the scattering spectra of a polycrystal were to exhibit structure similar to that in our vitreous silica data, it would probably be attributed to an optical phonon mode. However, in a non-crystalline solid the concept of lattice waves or phonons is applicable only to the extremely long wavelength acoustic motions of the system. In his study of the vibrational spectra of glass-like disordered chains, Dean (132) indicates that spatial localization of the vibrational modes is a necessary consequence of the presence of disorder in a system. We conclude that there is a local configuration of atoms repeated throughout the structure of vitreous silica which gives rise to a low frequency atomic motion. The plot of the inelastic scattering maxima in the $K - \hbar\omega$ plane clearly indicates that this mode produces a peak in the vibrational spectrum

of vitreous silica at a frequency of $\sim 1.11 \times 10^{12}$ cps (~ 37 cm^{-1}). The marked similarity of the short range structure of vitreous silica and low-cristobalite, and the fact that Leadbetter observes prominent neutron scattering maxima at ~ 40 cm^{-1} in his low-cristobalite data strongly indicates that almost identical motions must occur in both systems.

Other than a satisfactory method for treating the dynamics of a non-crystalline solid, nothing would be a greater aid to our understanding of vitreous silica than a knowledge of the atomic motions in low-cristobalite. The similarities of these two silicas have been noted above and throughout this work. Unfortunately, low-cristobalite exists only in the form of an opaque polycrystal. The type of scattering study which can provide information about the amplitudes, directions, and phases of the motions of the atoms within the unit cell of a crystalline system requires a target in the form of a single crystal. The polycrystalline form of low-cristobalite has also prevented the measurement of its Raman and Brillouin spectra, elastic constants, thermal expansivity, dielectric and acoustic attenuation characteristics, and other physical properties. Thus, in many respects we know even less about low-cristobalite than the vitreous silica.

5.3 THE EXPERIMENTAL RESULTS AS RELATED TO THE HEAT CAPACITY ANOMALY AND THE ACOUSTIC AND DIELECTRIC LOSSES

Our intention here is to offer several examples of how the results of the neutron measurements relate to efforts to explain the heat capacity anomaly and the acoustic and dielectric losses in vitreous silica.

Due to the measurements and analysis of Anderson and Bömmel (172), the acoustic and dielectric losses in vitreous silica have been attributed to a thermally activated structural relaxation. The most ambitious effort to model this phenomena, indeed, the only model which includes a reasonable amount of quantitative detail is the work by Strakna (177). As noted in Section 1.6, Strakna associates the losses with a specific defect, an elongated Si-O-Si bond with two equilibrium positions for the bridging oxygen atom. The following is an excerpt from his arguments: "An Si-Si separation centered at about 3.86 Å will result in two "anomalous" Si-O distances - one peaked at 1.74 Å and the other at 2.12 Å. If this defect occurs in at least a few percent of the total number of Si-O-Si bonds, then an x-ray radial distribution curve with sufficient resolution should show peaks at 3.86, 1.74, and 2.12 Å. Figure 7 shows an x-ray radial distribution curve of SiO_2 taken from a study by Richter, et al.(251). Notice that peaks appear approximately where predicted in Table I with the exception of the 1.74 Å peak which apparently isn't resolved from the large normal Si-O peak at 1.6 Å."

"An estimation of the relative population of anomalous to normal Si-O-Si bonds can be found by comparing the areas of the respective peaks on the x-ray distribution curve of Fig. 7. According to this comparison, an exceptionally large proportion, 20% to 30% of the total number of Si-O-Si bonds, are elongated."

Strakna has made an unfortunate choice in using the Richter, et al. results to support his claims. The shapes and intensities of the most prominent maxima in this distribution function are significantly different from those in other distribution functions derived from x-ray data and the peak which appears at 2.12 Å is undoubtably spurious. We have examined the pair correlation function derived from our neutron data and can find no evidence of the elongated Si-O-Si bonds. Furthermore, in Strakna's model it is assumed that the normal (unelongated) Si-O-Si bond angles are $\sim 180^{\circ}$; in this work we have shown that $\overline{\Theta}$(Si-O-Si) is $\sim 148^{\circ}$. Since the model is not consistent with the structure data, we conclude that Strakna's explanation of the structural relaxation is incorrect.

The inelastic neutron scattering measurements provide important new information with regard to the heat capacity anomaly. As noted in Section 1.5, Flubacher, et al. (119) have fit their low-temperature heat capacity data using a frequency distribution function which combines a Debye spectrum for the contribution from the acoustic modes and three Einstein oscillator terms (Equation I-13, page 120).

The three Einstein terms have characteristic wavenumbers of 9, 22, and 40 cm^{-1} and represent respectively 0.008, 0.2, and 1.4% of the total number of modes. The difficulty of deriving an accurate representation of $g(\omega)$ solely from analysis of the heat capacity data has been noted by Leadbetter (149): "The assumption of harmonic oscillators is not necessarily correct, nor must it be construed that that there are necessarily three sharp peaks in $g(\omega)$; but the thermodynamic data alone can give no more detailed information about the nature or distribution of the energy states involved." Our neutron measurements provide direct experimental confirmation of a peak in the frequency spectrum at 37 cm^{-1}. The results of Flubacher, Leadbetter, et.al., indicate that the motion(s) giving rise to this 37 cm^{-1} peak must account for practically 90% of the low-frequency modes producing the excess heat capacity of vitreous silica. Also, since an almost identical peak appears in the vibrational frequency spectrum of low-cristobalite, we conclude that most of the excess heat capacity of vitreous silica is not a direct consequence of the aperiodic nature of the glass structure.

REFERENCES

1. Morey, G. W., The Properties of Glass (Reinhold, New York, 1954), p. 28
2. American Society for Testing Materials, Standards, Part 3, p. 953 (1955)
3. Jones, G. O., Glass (Wiley, New York, 1956), p. 2
4. Prins, J. A., in Physics of Non-Crystalline Solids ed. by J. A. Prins (Wiley, New York, 1965), p. 1
5. Stevels, J. M., in Physics of Non-Crystalline Solids ed. by J. A. Prins (Wiley, New York, 1965), p. 497
6. Mackenzie, J. D., Modern Aspects of the Vitreous State, Vol. 1, ed. by J. D. Mackenzie (Butterworths & Co., London, 1960), p. 1
7. Secrist, D. R., and J. D. Mackenzie, in Modern Aspects of the Vitreous State ed. by J. D. Mackenzie (Butterworths & Co., London, 1964), Vol. 3, p. 149
8. Knipping, F. P., and M. von Laue, S. B. bayer Akad. Wiss., 315 (1912)
9. Bragg, W. H., Proc. roy. Soc. Ser. A 88, 428 (1913)
10. Debye, P., Ann. Phys. 461, 809 (1915)
11. Ehrenfest, P., Proc. Acad. Sci. Amst. 23, 1138 (1915)
12. Parmelee, C. W., G. L. Clark, and A. E. Badger, J. Soc. Glass Technol. 13, 285 (1929)
13. Clark, G. L., and C. R. Amberg, J. Soc. Glass Technol. 13, 290 (1929)

14. Zoltai, T., and M. Buerger, Z. Kristal. 114, 1 (1960)

15. Randall, J. T., H. P. Rooksby, and B. S. Cooper, Z. Kristal. 75, 196 (1930)

16. Scherrer, P., Nachr. Gotting. Ges. 1918, p.98

17. Lebedev, A. A., Trans. State Optical Institute 2, No. 10 (1921)

18. Zachariasen, W. H., J. Amer. Chem. Soc. 54, 3841 (1932)

19. Morey, G. W., J. Amer. Ceram. Soc. 17, 315 (1934)

20. Warren, B. E., J. Amer. Ceram. Soc. 17, 249 (1934)

21. Sosman, R. B., The Phases of Silica (Rutgers University Press, New Brunswick, N. J., 1965)

22. Valenkov, N. N., and E. A. Porai-Koshits, Nature 137, 273 (1936); Z. Kristal. 95, 195 (1936)

23. Randall, J. T., The Diffraction of X-rays and Electrons by Amorphous Solids, Liquids, and Gases (Chapman and Hall, New York, 1934)

24. Eckstein, B., in Physics of Non-Crystalline Solids ed. by J. A. Prins (Wiley, New York, 1965), p. 77

25. Urnes, S., in Modern Aspects of the Vitreous State ed. by J. D. Mackenzie (Butterworths & Co., London, 1960), Vol. 1, p. 10

26. Warren, B. E., J. Appl. Phys. 8, 645 (1937)

27. Warren, B. E., H. Krutter, and Morningstar, J. Amer. Ceram. Soc. 19, 202 (1936)

28. Warren, B. E., and J. Briscoe, J. Amer. Ceram. Soc. 21, 49 (1938)

29. Bragg, W. H., and W. L. Bragg, The Crystalline State (Bell & Sons, London, 1933), p. 189

30. Chemical Engineers' Handbook, Third Edition (McGraw Hill Book Co., 1950)

31. Weinberg, D. L., J. Appl. Phys. 33, 1012 (1962)

32. Debye, P., and H. Menke, Phys. Z. 31, 797 (1930)

33. Zernike, F., and J. A. Prins, Z. Phys. 41, 184 (1927)

34. Debye, P., Physik. Z. 28, 135 (1927)

35. Fournet, G., Bull. Soc. Franc. Mineral. Crist. 74, 39 (1951)

36. Bienenstock, A., and B. G. Bagley, J. Appl. Phys. 37, 4840 (1966)

37. Cartz, L., Nature 180, 1115 (1957)

38. Riley, D. P., in Non-Crystalline Solids ed. by Fréchette (Wiley, New York, 1960), p.26

39. International Tables for X-ray Crystallography

40. Henninger, E. H., R. C. Buschert, and L. Heaton, J. Phys. Chem. Solids 28, 423 (1967)

41. Finbak, C., Acta Chem. Scand. 3, 1279 (1949)

42. Klug, H. P., and L. E. Alexander, X-ray Diffraction Procedures (Wiley, New York, 1954), p. 608

43. Grjotheim, K., Glass Ind. 38, 201 (1958)

44. Petrashen, M. I., and E. A. Porai-Koshits, J. Exptl.-Theoret. Phys. (USSR) 21, 887 (1951)

45. Warren, B. E., J. Amer. Ceram. Soc. 24, 256 (1941)

46. Westbrook, J. H., J. Amer. ceram. Soc. 41, 433 (1958)

47. German, H., Diplom-Arbeit, Humboldt Universitat, Berlin (1961)

48. Eckstein, B., in Physics of Non-Crystalline Solids ed. by J. A. Prins (Wiley, New York, 1965), p. 77

49. Evstropyev, K. S., in The Structure of Glass (Consultants Bureau, New York, 1958), Vol. 1, p. 9

50. Lebedev, A. A., Bull. Acad. Sci. USSR, phys. ser. 4, No. 4 (1940)

51. Porai-Koshits, E. A., in The Structure of Glass (Consultants Bureau, New York, 1958), Vol. 1, p. 25

52. Oberlies, F., Naturwissenshaften 43, 224 (1956)

53. Prebus, A. F., and J. W. Michener, Ind. Eng. Chem. 46, 147 (1954)

54. Warshaw, J., J. Amer. Ceram. Soc. 43, 4 (1960)

55. Zarcycki, J., and R. Mezard, Phys. Chem. Glasses 3, 163 (1962)

56. Shelyubsky, V. I., in The Structure of Glass (Consultants Bureau, New York, 1958), Vol. 1, p. 169

57. Sosman, R. B., The Phases of Silica (Rutgers University Press, New Brunswick, N. J., 1965), p. 315

58. King, S. V., Nature 213, 1112 (1967)

59. Bernal, J. D., Proc. Roy. Soc. A 280, 299 (1964)

60. Dean, P., Nature 210, 257 (1966)

61. Simon, I., in Modern Aspects of the Vitreous State ed. by J. D. Mackenzie (Butterworths, London, 1960), Vol. 1, p. 120

62. Cartz, L., Zeit. Krist. 120, 241 (1964)

63. Evans, D. L., and S. V. King, Nature 212, 1352 (1966)

64. Oberlies, F., and A. Dietzel, Glastech. Ber. 39, 37 (1957)

65. Tilton, L. W., J. Res. Natl. Bur. Std. 59, 139 (1957)

66. Hicks, J. F. G., Science 155, 459 (1967)

67. Robinson, H. A., J. Phys. Chem. Solids 26, 209 (1965)

68. Babcock, C. L., S. W. Barber, and K. Fajans, Ind. Eng. Chem. 46, 161 (1954)

69. Doborzynski, D., Bull. intern. acad. polon. sci., Classe sci. math. nat. 1938A, p. 153

70. Zarcycki, J., J. Trav. Congr. int. Verre IV (Paris, 1956), p. 323

71. Bagdyk'yants, G. O., and A. G. Alekseev, The Structure of Glass (Consultants Bureau, New York, 1960), Vol. 2, p. 198

72. Patterson, A. L., Phys. Rev. 56, 195 (1944)

73. Bauer, S. H., in Non-Crystalline Solids ed. by Fréchette (Wiley, New York, 1960), p. 53

74. Ackermann, L., Optik 3, 47 (1948)

75. König, H., Optik 3, 419 (1948)

76. Maxwell, L. R., and V. M. Mosley, Phys. Rev. 47, 330 (1935)

77. McClurg, G. O., J. Chem. Phys. 20, 1398 (1952)

78. Shishakov, N. A., J. Phys. Chem. 23, 889 (1949)

79. Weyl, W. A., and E. C. Marboe, The Constitution of Glasses: A Dynamic Interpretation (Interscience Publishers, New York, 1964), Vol. II, Part 1, p. 634

80. Porai-Koshits, E. A., in The Structure of Glass (Consultants Bureau, New York, 1958), Vol. 1, p. 25

81. Hartlief, G., Z. Anorg. Chem. 238, 353 (1938)

82. Simon, I., Phys. Rev. 103, 1587 (1956)

83. Zarzycki, J., Verres et. Refr. 11, 3 (1957)

84. Norman, N., private communication cited by Tilton (65)

85. Warren, B. E., private communication cited by Robinson (67)

86. Milligan, W. O., H. A. Levi, and W. Peterson, Phys. Rev. 83, 226 (1956)

87. Breen R. J., R. M. Delaney, P. J. Persiani, and A. H. Weber, Phys. Rev. 105, 517 (1957)

88. Carraro, G., M. Domenici, and T. Zucca, in Physics of Non-Crystalline Solids ed. by J. A. Prins (Wiley, New York, 1965), p. 152

89. Lorch, E., J. Phys. C: Solid St. Phys. 2, 229 (1969)

90. Hughes, D. J., and R. B. Schwartz, Neutron Cross Sections (Second Edition), Brookhaven National Lab. Report No. BNL-325 (1958)

91. Sosman, R. B., The Phases of Silica (Rutgers University Press, New Brunswick, N. J., 1965), p. 327

92. Douglas, R. W., and J. O. Isard, J. Soc. Glass Technol. 35, 206 (1951)

93. Bell, R. J., and P. Dean, Nat. Phys. Lab. Math. Rep., Ma. 62, (1967)

94. Coblentz, W. W., Investigations of Infra-Red Spectra (Carnegie Institute of Washington, D.C., 1908), Parts V and VII

95. Reinkober, O., Ann. Phys. 34, 343 (1911)

96. Raman, C. V., Ind. J. Phys. 2, 387 (1928)

97. Raman, C. V., and K. S. Krishnan, Ind. J. Phys. 2, 398 (1928)

98. Pringsheim, P., and N. Rosen, Z. Physik 50, 741 (1928)

99. Hollaender, A., and J. W. Williams, Phys. Rev. 34, 380 (1929); 38, 1739 (1931)

100. Simon, I., in Modern Aspects of the Vitreous State ed. by J. D. Mackenzie (Butterworths,London, 1960), Vol. 1, Chap. 6

101. Bobovich, Ya. S., and T. P. Tulub, Sov. Phys. Usp. 66, 1 (1958)

102. Gross, E. F., and Romanov, Z. Physik 55, 744 (1929)

103. Markin, E. P., V. V. Obukhov-Denisov, T. A. Sidorov, N. N. Sobolev, and V. P. Cheremisinov, The Structure of Glass (Consultants Bureau, New York, 1960), Vol. 2

104. Barnes, R. B., Phys. Rev. 39, 562 (1932)

105. Simon, I., and H. C. McMahon, J. Chem. Phys 21, 23 (1953)

106. Lippencott, E. R., A. Van Valkenburg, C. E. Weir, and E. N. Bunting, J. Res. nat. Bur. Stand. 61, 61 (1958)

107. Matossi, F., and H. Bluschke, Z. Phys. 108, 295 (1938)

108. Reitzel, J., J. Chem. Phys. 23, 2407 (1955)

109. Gouq-Jen Su, N. F. Borrelli, and A. R. Miller, Phys. Chem. Glasses 3, 167 (1962)

110. Florinskaya, V. A., and R. S. Pechenkina, The Structure of Glass (Consultants Bureau, New York, 1958), Vol. 1, p. 55

111. Plendl, J. N., and L. C. Mansur, J. Phys. Chem. Solids 28, 1589 (1967)

112. Hanna, R., J. Amer. Ceram. Soc. 48, 595 (1965)

113. Gross, E. F., and V. A. Kolesova, The Structure of Glass (consultants Bureau, New York, 1958), Vol. 1, p. 45

114. Gross, E. F., and M. Romanov, Z. Physik 55, 744 (1929)

115. Kujumzelis, T. G., Z. Physik 100, 221 (1936)

116. Krishnan, K. S., Proc. Ind. Acad. Sci. 37A, 377 (1958)

117. Harrand, M., Compt. rend. hebd. Seanc. Acad. Sci. 238, 784 (1954)

118. Lord, Jr., R. C., private communication cited in ref.(68)

119. Flubacher, P., A. J. Leadbetter, J. A. Morrison, and B. P. Stoicheff, J. Phys. Chem. Solids 12, 53 (1959)

120. Egelstaff, P. A., in Physics of Non-Crystalline Solids ed. by J. A. Prins (Wiley, New York, 1965), p. 127

121. Leadbetter, A. J., J. Chem. Phys. 51, 779 (1969)

122. Adams, R. V., and R. W. Douglas, Glastech Ber. 32K, 12 (1959)

123. Heaton, H. M., and H. Moore, J. Soc. Glass Tech. 41, 3 (1957)

124. Mattossi, F., J. Chem. Phys. 17, 679 (1949)

125. Venkateswarlu, K., and S. Sundaraum, J. Chem. Phys. 23, 2365 (1955)

126. Dennison, D. M., Astrophys. J. 62, 84 (1925); Schaefer, C., Z. Physik 60, 586 (1930)

127. Saksena, B. D., Trans. Faraday Soc. 57, 242 (1961)

128. Herzberg, G., Infrared and Raman Spectra of Polyatomic Molecules (Van Nostrand, New York, 1946), p. 182

129. Su, G. J., N. F. Borrelli, and A. R. Miller, Phys. Chem. Glasses 3, 167 (1962)

130. Wadia, W., and L. S. Balloomal, Phys. Chem. Glasses 9, 115 (1968)

131. Stepanov, B. I., and A. M. Prima, Optiko i Spek. 4, 734 (1958); 5, 15 (1958)

132. Dean, P., Proc. Phys. Soc. 84, 727 (1964)

133. Anderson, O. L., in Physics of Non-Crystalline Solids ed. by J. A. Prins (Wiley, New York, 1965), p. 179

134. Dyson, F. J., Phys. Rev. 92, 1331 (1953)

135. Schmidt, H., Phys. Rev. 105, 425 (1957)

136. Lieb, E. H., and D. C. Mattis, Mathematical Physics in One Dimension (Academic Press, New York, 1966)

137. Bell, R. J., N. F. Bird, and P. Dean, J. Phys. C (Proc. Phys. Soc.) 1, 299 (1968)

138. Dean, P., and M. D. Bacon, Proc. R. Soc. A 283, 64 (1965)

139. Zarzycki, J., and F. Naudin, Verres Refract. 14, 113 (1960)

140. Simon, I., J. Amer. Ceram. Soc. 40, 150 (1957)

141. Weyl, W. A., and E. C. Marboe, The Constitution of Glasses: A Dynamic Interpretation (Interscience Publishers, New York, 1962), Vol. I, p. 287

142. Krishnan, R. S., Proc. Ind. Acad. Sci. (A) 37, 382 (1953)

143. Saksena, B. D., Proc. Phys. Soc. London 72, 9 (1958)

144. Scott, J., and S. Porto, Phys. Rev. 161, 903 (1967)

145. Shapiro, S., D. C. O'Shea, and H. Z. Cummins, Phys. Rev. Letters 19, 361 (1967)

146. Harrand, M., Compt. rend. 238, 784 (1954)

147. Sosman, R. B., The Phases of Silica (Rutgers University Press , New Brunswick, New Jersey, 1965), p. 126

148. Spitzer, W. G., and D. A. Kleinman, Phys. Rev. 121, 1324 (1961)

149. Leadbetter, A. J., Phys. Chem. Glasses 9, 1 (1968)

150. Rosenstock, H. B., J. Phys. Chem. Solids 23, 659 (1962)

151. Born, M., and K. Huang, Dynamical Theory of Crystal Lattices (Oxford University Press, 1954), Chap. II

152. Debye, P., Ann. d. Phys. (4) 39, 789 (1912)

153. Leibfried, G., and G. Ludwig, Solid State Phys. 7, 275 (1961)

154. Blackman, M., Handbuch der Physik 7, [illegible] (1955)

155. Anderson, O. L., J. Phys. Chem. Solids 12, 41 (1959)

156. Westrum, E. F., Jr., IV^{me} Congrès International du Verre, Paris (1956); unpublished results cited by A. J. Leadbetter and J. A. Morrison, Phys. Chem. Glasses 4, 188 (1963)

157. Koga, I., Phys. Rev. 109, 1467 (1958)

158. McSkimin, H. J., J. Appl. Phys. 24, 988 (1953)

159. Anderson, O. L., and G. J. Dienes, in Non-Crystalline Solids ed. by V. D. Frechette (Wiley, New York, 1960), p. 449

160. Fine, M. E., J. Appl. Phys. 25, 402 (1954)

161. White, G. K., and J. A. Birch, Phys. Chem. Glasses 6, 85 (1965)

162. Smyth, H., H. Skogen, and W. Harsell, J. Amer. Ceram. Soc. 36, 327 (1953)

163. Dank, M., and S. W. Barber, J. Chem. Phys. 23, 597 (1955)

164. Tarasov, V. V., Zh. fiz. Khim. 27, 744 (1953)

165. DeSorbo, W., Acta Metallurgia 2, 274 (1954)

166. Nernst, E., Handbuch der Physik 10, 314 (1926)

167. Antoniou, A. A., and J. A. Morrison, J. Appl. Phys. 36, 1873 (1965)

168. Leadbetter, A. J., and J. A. Morrison, Phys. Chem. Glasses 4, 188 (1963)

169. Marx, J. W., J. M. Sivertsen, J. Appl. Phys. 24, 81 (1953)

170. McSkimin, H. J., J. Appl. Physics 24, 988 (1953)

171. Fine, M. E., J. Appl. Physics 25, 402 (1954)

172. Anderson, O. L., and H. E. Bömmel, J. Amer. Ceram. Soc. 38, 125 (1955)

173. Stevels, J. M., Glastech. Ber. 26, 227 (1953)

174. Bömmel, H., W. P. Mason, and A. W. Warner, Phys. Rev. 102, 64 (1956)

175. Volger, J., J. M. Stevels, and C. Van Amerongen, Phillips Research Reports 10, 260 (1955)

176. Mason, W. P., Physical Acoustics and Properties of Solids (Van Nostrand, Princeton, N. J., 1958)

177. Strakna, R. E., Phys. Rev. 123, 2020 (1961)

178. Clark, A. E., and R. E. Strakna, Phys. Chem. Glasses 3, 121 (1962)

179. Primak, W., Phys. Rev. 110, 1240 (1958)

180. Lomer, W. M., and G. G. Low, in Thermal Neutron Scattering ed. by P. A. Egelstaff (Academic Press, London, 1965), p.1

181. Turchin, V. F., Slow Neutrons (D. Davey, New York, 1965)

182. Summerfield, G. C., J. M. Carpenter, and N. A. Lurie, Introduction to the Theory of Slow-Neutron Scattering, to be published.

183. Fermi, E., Ricerca scient. 7, 13 (1936)

184. Van Hove, L., Phys. Rev. 95, 249 (1954)

185. Gurevich, I. I., and L. V. Tarasov, Low-Energy Neutron Physics (Wiley, New York, 1968), p. 500

186. Egelstaff, P. A., Atomic Energy Research Establishment Reports No. AERE N/R 1164, 2 (1958); AERE 4101, 4 (1962)

187. Cocking, S. J., and Z. Guner, in Inelastic Scattering of Neutrons in Solids and Liquids, Vol. I (IAEA, Vienna, 1963), p. 237

188. Larsson, K. E., and U. Dahlborg, Physica 30, 1561 (1964)

189. Cocking, S. J., and P. A. Egelstaff, Phys. Letters 16, 130 (1965); J. Phys. C (Proc. Phys. Soc.) 1, 507 (1967)

190. Randolph, P. D., and K. S. Singwi, Phys. Rev. 152, 99 (1966)

191. Dorner, B., T. Plesser, and H. Stiller, Physica 31, 1537 (1965)

192. Cocking, S. J., in Inelastic Scattering of Neutrons in Solids and Liquids, Vol. I (IAEA, Vienna, 1963), p. 227

193. Sköld, K., and K. E. Larsson, Phys. Rev. 161, 102 (1967)

194. Singwi, K. S., Physica 31, 1257 (1965); Phys. Rev. 136, 969 (1964)

195. Egelstaff, P. A., Atomic Energy Research Establishment Report No. AERE R4101 (1962)

196. Cocking, S. J., Adv. Phys. 16, 189 (1967)

197. Egelstaff, P. A., in Inelastic Scattering of Neutrons in Solids and Liquids (IAEA, Vienna, 1961), p. 25

198. Gurevich, I. I., and L. V. Tarasov, Low-Energy Neutron Physics (Wiley, New York, 1968), p. 485

199. Kagan, Yu., Zh. eksp. teor. Fiz. 42, 1375 (1962)

200. Boller, B., Corning Glass Works, private communication

201. Egelstaff, P. A., S. J. Cocking, and T. K. Alexander, in Inelastic Scattering of Neutrons in Solids and Liquids (IAEA, Vienna, 1961), p. 165

202. Straker, E. A., Doctoral Thesis, The University of Michigan, 1965

203. Technical Progress Report on Neutron Cross Section and Spectra Studies, 1964, Atomic Energy Commission Contract No. AT(11-1)-917 (unpublished)

204. Technical Progress Report on Neutron Cross Section and Spectra Studies, 1965, Atomic Energy Commission Contract No. AT(11-1)-917 (unpublished)

205. The Ford Nuclear Reactor, Description and Operation, Michigan Memorial Phoenix Project, Phoenix Memorial Laboratory, 1962 (unpublished)

206. Bullock, J. B., E. A. Daniels, and J. S. King, ANS Transactions 8, 302 (1965)

207. Hughes, D. J., and R. B. Schwartz, Neutron Cross Sections (Second Edition), Brookhaven National Lab. Report No. BNL-325 (1958)

208. Carpenter, J. M., Doctoral Thesis, The University of Michigan, 1963

209. Marseguerra, M., and G. Pauli, Nuc. Inst. Methods 4, 140 (1959)

210. Pickles, J. R., and R. Hazlewood, Atomic Energy Research Establishment Report No. AERE/X/PR/2357 (1960)

211. Royston, R. J., Nuc. Inst. Methods 30, 184 (1964)

212. Sampson, T. E., Some Resolution Calculations For The University of Michigan Phased Rotor Velocity Selector, unpublished (1966)

213. Stedman, R., AECL Report No. CRRP-931 (1960)

214. Lurie, N. A., Doctoral Thesis, The University of Michigan, 1969

215. Wraight, L. A., Atomic Energy Research Establishment Report No. AERE M.833 (1960)

216. Little, R. I., A Four Input Adapter for the TMC Model CN-110/211 Analyzer, PTR-548 (1961)

217. Lurie, N. A., Maintenance Manual - TOFA Quadapter For The TMC Model CN-1024 Analyzer, unpublished (1968)

218. Sample Holder and Cycler, The University of Michigan Mechanical Monochromator, unpublished (1965)

219. Straker, E. A., Master's Thesis, The University of Michigan, 1962

220. Zweifel, P. F., and J. M. Carpenter, in Inelastic Scattering of Neutrons in Solids and Liquids (IAEA, Vienna,1961), p.199

221. Placzek, G., Phys. Rev. 86, 377 (1952)

222. Vineyard, G., Phys. Rev. 110, 999 (1958)

223. Dolling, G., and A. D. B. Woods in Thermal Neutron Scattering ed. by P. A. Egelstaff (Academic Press, London, 1965), p. 210

224. Beyster, J. R., private communication

225. Kaplan, W., Advanced Calculus (Addison-Wesley, Cambridge, 1952), p. 94

226. Handbook of Chemistry and Physics (39th Edition) (Chemical Rubber Publishing Co., Cleveland, Ohio, 1958), p.2470

227. Donovan, J. L., Doctoral Thesis, The University of Michigan, 1964

228. Myers, W. R., Doctoral Thesis, The University of Michigan, 1965

229. Caglioti, G., A. Paoletti, and F. P. Ricci, Nuc. Inst. Methods 3, 223 (1958)

230. Caglioti, G., A. Paoletti, and F. P. Ricci, Nuc. Inst. Methods 9, 195 (1960)

231. Caglioti, G., and F. P. Ricci, Nuc. Inst. Methods 15, 155 (1962)

232. Sailor, V. L., H. L. Foote, H. H. Landon, and R. E. Wood, Rev. Sci. Inst. 27, 26 (1956)

233. Carpenter, J. M., Nuc. Inst. Methods 47, 179 (1967)

234. Hoag, J. B., Nuclear Reactor Experiments (Van Nostrand, Princeton, New Jersey, 1958), p. 147

235. Melkonian, E., Phys. Rev. 76, 1744 (1949)

236. Delaney, R. M., and A. H. Weber, in Non-Crystalline Solids ed. by Frechette (Wiley, New York, 1960), p. 96

237. Striffler, C. E., Master's Thesis, The University of Michigan, 1964

238. Vineyard, G., Phys. Rev. 96, 93 (1954)

239. Slaggie, E. L., in Neutron Thermalization and Reactor Spectra (IAEA, Vienna, 1968), Vol. I, p. 311

240. Slaggie, E. L., Nuc. Sci. Eng. 30, 199 (1967)

241. Cocking, S. J., and C. R. T. Heard, Atomic Energy Research Establishment Report No. AERE-R 5016 (1965)

242. Krogh-Moe, J., Acta Cryst. 9, 951 (1956)

243. Paalman, H. H., and C. J. Pings, Rev. Mod. Phys. 35, 389 (1963)

244. Danielson, G. C., and C. Lanczos, J. Franklin Inst. 233, 365 (1942); 233, 435 (1942)

245. Ino, T., J. Phys. Soc. Japan 12, 495 (1957)

246. Filipovich, V. N., J. Tech. Phys. (USSR) 26, 409 (1956)

247. Eckart, C., Phys. Rev. 51, 735 (1937)

248. Furukawa, K., Rep. Prog. Phys. 25, 396 (1962)

249. Waser, J. and V. Schomaker, Rev. Mod. Phys. 25, 671 (1953)

250. Shropshire, J., P. P. Keat, and P. A. Z. Vaughn, Z. Kristallogr. 112, 409 (1959)

251. Richter, H., G. Breitlung, and F. Herre, Naturwiss. 40, 621 (1953)

252. Kaplow, R., S. L. Strong, and B. L. Averbach, Phys. Rev. 138, A1336 (1965)

253. Warren, B. E., X-Ray Diffraction (Addison-Wesley, Reading, Mass., 1969), p. 127

254. Dean, P., and J. Bell, New Scientist 45, 104 (1970)

255. Ordway, F., Science 143, 800 (1963)

256. King, S. V., Nature 215, 615 (1967); private communication

257. Ordway, F., Rev. Sci. Inst. 36, 1156 (1965)

258. Busing, W. R., K. O. Martin, and H. A. Levy, ORNL-TM-305 (1962); ORNL-TM-306 (1964)

259. Wyckoff, R. W. G., Crystal Structures (Second Edition), (Interscience(Wiley), New York, 1964), Vol. I, p. 312

260. Sosman, R. B., The Phases of Silica (Rutgers University Press, New Brunswick, New Jersey, 1965), Chapter 13

261. Wyckoff, R. W. G., Amer. J. Science 9, 448 (1925); Z. Kristal. 62, 189 (1925)

262. Barth, T. F. W., Amer. J. Science 23, 350 (1932)

263. DATANAL 3 -- A Time-of-Flight Neutron Scattering Data Reduction Program for the University of Michigan Mechanical Monochromator (unpublished report, Department of Nuclear Engineering, University of Michigan)

264. Dean, P., Proceedings of the International Conference on Statistical Mechanics (1968) reprinted in J. Phys. Soc. of Japan 26, Supplement, 20 (1969)